



HAL
open science

On the fracture of solar grade crystalline silicon wafer

Lv Zhao

► **To cite this version:**

| Lv Zhao. On the fracture of solar grade crystalline silicon wafer. Mechanics [physics.med-ph]. Université de Lyon, 2016. English. NNT : 2016LYSEI134 . tel-02004451

HAL Id: tel-02004451

<https://theses.hal.science/tel-02004451>

Submitted on 1 Feb 2019

HAL is a multi-disciplinary open access archive for the deposit and dissemination of scientific research documents, whether they are published or not. The documents may come from teaching and research institutions in France or abroad, or from public or private research centers.

L'archive ouverte pluridisciplinaire **HAL**, est destinée au dépôt et à la diffusion de documents scientifiques de niveau recherche, publiés ou non, émanant des établissements d'enseignement et de recherche français ou étrangers, des laboratoires publics ou privés.



INSA

N°d'ordre NNT : 2016LYSEI134

THESE de DOCTORAT DE L'UNIVERSITE DE LYON
opérée au sein de
l'Institut National des Sciences Appliquées de Lyon

Ecole Doctorale N° ED162
MECANIQUE, ENERGETIQUE, GENIE CIVIL, ACOUSTIQUE

Spécialité de doctorat :
Discipline : Mécanique – Génie Mécanique – Génie Civil

Soutenue publiquement le 08/12/2016, par :
Lv ZHAO

ON THE FRACTURE OF SOLAR GRADE CRYSTALLINE SILICON WAFER

Devant le jury composé de :

GRAVOUIL Anthony	Professeur des Universités	INSA Lyon	Président
PAGGI Marco	Professore Associato	IMT Lucca	Rapporteur
PARDOEN Thomas	Professeur des Universités	UCLouvain	Rapporteur
CHABLI Amal	Directrice de Recherche	CEA-INES	Examinatrice
ALBARET Tristan	Maître de Conférences	Université Lyon 1	Invité
NELIAS Daniel	Professeur des Universités	INSA Lyon	Directeur de thèse
MAYNADIER Anne	Maître de Conférences	FEMTO-ST	Co-directrice

Département FEDORA – INSA Lyon - Ecoles Doctorales – Quinquennal 2016-2020

SIGLE	ECOLE DOCTORALE	NOM ET COORDONNEES DU RESPONSABLE
CHIMIE	CHIMIE DE LYON http://www.edchimie-lyon.fr Sec : Renée EL MELHEM Bat Blaise Pascal 3 ^e étage secretariat@edchimie-lyon.fr Insa : R. GOURDON	M. Stéphane DANIELE Institut de Recherches sur la Catalyse et l'Environnement de Lyon IRCELYON-UMR 5256 Équipe CDFA 2 avenue Albert Einstein 69626 Villeurbanne cedex directeur@edchimie-lyon.fr
E.E.A.	ELECTRONIQUE, ELECTROTECHNIQUE, AUTOMATIQUE http://edeea.ec-lyon.fr Sec : M.C. HAVGOUDOUKIAN Ecole-Doctorale.eea@ec-lyon.fr	M. Gérard SCORLETTI Ecole Centrale de Lyon 36 avenue Guy de Collongue 69134 ECULLY Tél : 04.72.18 60.97 Fax : 04 78 43 37 17 Gerard.scorletti@ec-lyon.fr
E2M2	EVOLUTION, ECOSYSTEME, MICROBIOLOGIE, MODELISATION http://e2m2.universite-lyon.fr Sec : Safia AIT CHALAL Bat Darwin - UCB Lyon 1 04.72.43.28.91 Insa : H. CHARLES Safia.ait-chalal@univ-lyon1.fr	Mme Gudrun BORNETTE CNRS UMR 5023 LEHNA Université Claude Bernard Lyon 1 Bât Forel 43 bd du 11 novembre 1918 69622 VILLEURBANNE Cédex Tél : 06.07.53.89.13 e2m2@univ-lyon1.fr
EDISS	INTERDISCIPLINAIRE SCIENCES-SANTE http://www.ediss-lyon.fr Sec : Safia AIT CHALAL Hôpital Louis Pradel - Bron 04 72 68 49 09 Insa : M. LAGARDE Safia.ait-chalal@univ-lyon1.fr	Mme Emmanuelle CANET-SOULAS INSERM U1060, CarMeN lab, Univ. Lyon 1 Bâtiment IMBL 11 avenue Jean Capelle INSA de Lyon 696621 Villeurbanne Tél : 04.72.68.49.09 Fax :04 72 68 49 16 Emmanuelle.canet@univ-lyon1.fr
INFOMATHS	INFORMATIQUE ET MATHEMATIQUES http://infomaths.univ-lyon1.fr Sec : Renée EL MELHEM Bat Blaise Pascal 3 ^e étage infomaths@univ-lyon1.fr	Mme Sylvie CALABRETTO LIRIS – INSA de Lyon Bat Blaise Pascal 7 avenue Jean Capelle 69622 VILLEURBANNE Cedex Tél : 04.72. 43. 80. 46 Fax 04 72 43 16 87 Sylvie.calabretto@insa-lyon.fr
Matériaux	MATERIAUX DE LYON http://ed34.universite-lyon.fr Sec : M. LABOUNE PM : 71.70 –Fax : 87.12 Bat. Saint Exupéry Ed.materiaux@insa-lyon.fr	M. Jean-Yves BUFFIERE INSA de Lyon MATEIS Bâtiment Saint Exupéry 7 avenue Jean Capelle 69621 VILLEURBANNE Cedex Tél : 04.72.43 71.70 Fax 04 72 43 85 28 Ed.materiaux@insa-lyon.fr
MEGA	MECANIQUE, ENERGETIQUE, GENIE CIVIL, ACOUSTIQUE http://mega.universite-lyon.fr Sec : M. LABOUNE PM : 71.70 –Fax : 87.12 Bat. Saint Exupéry mega@insa-lyon.fr	M. Philippe BOISSE INSA de Lyon Laboratoire LAMCOS Bâtiment Jacquard 25 bis avenue Jean Capelle 69621 VILLEURBANNE Cedex Tél : 04.72 .43.71.70 Fax : 04 72 43 72 37 Philippe.boisse@insa-lyon.fr
ScSo	ScSo* http://recherche.univ-lyon2.fr/scso/ Sec : Viviane POLSINELLI Brigitte DUBOIS Insa : J.Y. TOUSSAINT viviane.polsinelli@univ-lyon2.fr	Mme Isabelle VON BUELTZINGLOEWEN Université Lyon 2 86 rue Pasteur 69365 LYON Cedex 07 Tél : 04.78.77.23.86 Fax : 04.37.28.04.48

*ScSo : Histoire, Géographie, Aménagement, Urbanisme, Archéologie, Science politique, Sociologie, Anthropologie

*The opportunity is prepared for the person that has
the best preparation.*

Remerciements

Tout d'abord, je tiens à remercier professeur Daniel Nélias pour m'avoir proposé l'opportunité d'aborder cette thématique intéressante, et aussi pour m'avoir fourni constamment des ressources techniques et humaines durant ma thèse. La confiance, les discussions, les encouragements ainsi que la patience qu'il m'a apportés sont des éléments indispensables sans lesquels cette thèse n'aurait pas terminé avec succès. A grand merci s'adresse à maître de conférences Anne Maynadier pour son encadrement le long des 3 ans. J'apprécie bien les aides et conseils qu'elle a données sur le plan expérimental. En plus, son enthousiasme, sa rigueur sur les travaux de recherche m'ont appris les caractères nécessaires pour pouvoir mener à bien un projet scientifique. Particulièrement, je remercie docteur Didier Bardel pour son intervention durant la dernière année de thèse, ses aides et suggestions constantes m'ont permis d'améliorer la qualité de mes travaux, surtout sur l'interprétation des résultats. J'ai bien apprécié la liberté et la flexibilité que mes encadrants m'ont laissées, celles-ci m'ont permis d'explorer le monde inconnu sans contrainte.

Je tiens à remercier aussi tous les collaborateurs durant ma thèse: dans le cadre du projet DEMOS, C. Belouet et F. De Moro de l'entreprise Solarforce qui nous ont fourni les éprouvettes MCSi et RST; dans le cadre du projet d'EquiPex DURASOL, P. Messaoudi et F. Medlege du CEA-INES qui ont effectué la découpe des wafers Si pour obtenir des éprouvettes jumelles, B. Marie (CEA-INES) qui a effectué les mesures de diffraction des rayons X et aussi les mesures d'EBSD, D. Binésti et M. Van Iseghem de l'EDF avec qui nous avons eu des discussions fructueuses. L'Agence Nationale de la Recherche (ANR) est particulièrement remerciée pour son financement partiel à travers du projet d'EquipeX DURASOL.

Les remerciements s'adressent aux membres de jury: prof. T. Pardoën et prof. M. Paggi en tant que rapporteur, prof. A. Gravouil et directrice de recherche A. Chabli en tant qu'examinateur, et aussi maître de conférences T. Albaret en tant qu'invité. J'ai vraiment apprécié les discussions qu'on a eues lors de la soutenance.

Je tiens à remercier A. Soulot, F. Legrand, P. Chaudet, P. Valverde, qui m'ont fourni des supports techniques. Leurs disponibilités, leur expertise m'ont permis de réaliser les études expérimentales dans la direction désirée. Particulièrement, je veux remercier Dr. Y. Gaillard de l'institut FEMTO-ST pour les mesures AFM.

Je tiens à remercier les collègues du laboratoire avec qui j'ai vécu un environnement dynamique et amical: N. Blal, T. Elguedj, N. Tardif, A. Bel-Brunon, D. Campello, Y. Zhang, K.E. Koumi, D. Campello, J. Marty, K. Amuzuga (Pipo), C. Zhang, S. Chen, S. Zhu, W. Gao, Y. Lu, W. Ye, D. Liu, W. Zhu, M. Wang, L. Yao, J. Xie, H. Xiong, S. Gao, J. Wang, B. Liang, D. Wang, F. Fekak, A. E. Sondé, I. Azehaf, C. Robitaille, A. Chemin, J. Blaizot, S. Lacroix, N. Azzeggagh, H. Jerby, L. Roux, N. Lion, A. Balan, T. Beyer, G. Coudouel, T. Jailin, C. Pettavino. Un merci particulier s'adresse à Eric (M. Taro) avec qui j'ai eu plein de discussions à propos de plein de sujets tant scientifique que quotidien pendant les 2 premières années de thèse.

Finalement, je veux exprimer mes remerciements sincères à mes membres de famille, tout d'abord ma femme Ting pour son support constant et inépuisable durant ces 3 dernières années, ensuite mes parents et deux frères pour leur support et encouragement, finalement ma fille Yicheng pour sa tolérance (imposée ;-)) d'avoir un papa chargé.

Abstract

The solar grade crystalline silicon occupies an important position in photovoltaic (PV) technology. It is indeed the most common active material for electrical generation. The profitability of silicon solar cells is a critical point for the PV market and it requires improved electrical performance, lower wafer production costs and enhancing reliability and durability of the cells. Innovative processes are emerging that provide thinner wafers with less raw material loss. But the induced crystallinity and distribution of defects compared to the classical wafers are unclear. It is therefore necessary to develop methods of microstructural and mechanical characterization to assess the rigidity and mechanical strength of these materials. Particularly for durability issue, the fundamental understanding of fracture behavior of solar cells and particularly of the brittle material that constitutes the wafer is crucial. In this direction, we will improve our knowledge of the causes and modes of cracking in the silicon wafers in order to finally be able to avoid them or at least to take them into account when designing the next solar cells generations. Nevertheless, the literature in this direction remains too rare and inaccuracies remain. For example, the community has not yet described with certainty the failure mode of multi-crystalline silicon (MCSi) : does it break in a transgranular or intergranular way and why ?

In this work, 4-point bending tests were performed under quasi-static loading. This allowed to conduct both the stiffness estimation and the rupture study. A high speed camera was set up in order to track the fracture process thanks to a 45°tilted mirror. Fractographic analysis were performed using confocal optical microscope, scanning electron microscope and atomic force microscope. Electron Back-Scatter Diffraction and Laue X-Ray diffraction were used to explore the relationship between the microstructural grains orientations/textures of our material and the observed mechanical behavior. Jointly, finite element modeling and simulations were carried out to provide auxiliary characterization tools and help to understand the involved fracture mechanism.

Thanks to the experiment-simulation coupled method, we have assessed accurately the rigidity of silicon wafers stemming from different manufacturing processes. A fracture origin identification strategy has been proposed combining high speed imaging and post-mortem fractography. Fracture investigations on silicon single crystals have highlighted the deflection free (110) cleavage path, the high initial crack velocity, the velocity dependent crack front shape and the onset of front waves in high velocity crack propagation. The investigations on the fracture of multi-crystalline wafers demonstrate a systematic transgranular cracking. Furthermore, thanks to twin multi-crystalline silicon plates, we have addressed the crack path reproducibility. A special attention has been paid to the nature of the cleavage planes and the grain boundaries barrier effect. Finally, based on these observations, an extended finite element model (XFEM) has been carried out which fairly reproduces the experimental crack path.

KEY WORDS: Solar grade silicon wafer, 4-point bending, material rigidity, fracture, crack velocity, extended finite element model (XFEM).

Résumé

Le silicium cristallin occupe une position clé dans la technologie photovoltaïque (PV). Il est en effet le matériau actif permettant la génération électrique le plus répandu. La rentabilité des cellules à base de silicium est donc un point essentiel pour le marché photovoltaïque et cela passe notamment par l'amélioration du rendement électrique, la baisse des coûts de production des wafers ainsi que par le renforcement de la fiabilité/durabilité des cellules. Des procédés innovants émergent, qui permettent d'obtenir des wafers de plus en plus minces avec moins de perte de matière première. Cependant la cristallinité et la répartition des défauts générés sont mal connues. Il est donc nécessaire de mettre en place des méthodes de caractérisation microstructurales et mécaniques afin de statuer sur la rigidité ou la tenue mécanique en service de ces matériaux. Dans ce contexte, la compréhension fine du comportement à la rupture des cellules et particulièrement du matériau fragile qui constitue le wafer est primordiale. C'est à cette condition que nous améliorerons notre connaissance des causes et des modes de fissuration des wafers au sein des modules PV afin de les éviter ou au moins de les prendre en compte lors de la conception. Néanmoins, les recherches dans cette direction restent trop peu nombreuses et des imprécisions subsistent. Par exemple, le silicium multi-cristallin (MCSi) rompt-il de manière intra-granulaire ou inter-granulaire ?

Dans ce travail, des essais de flexion 4 points ont été effectués afin de caractériser à la fois la rigidité et la rupture. Afin de capturer le processus de rupture fragile en flexion, une caméra rapide a été utilisée conjointement à un miroir incliné à 45° . Des analyses fractographiques quasi systématiques ont été menées par microscopie optique confocale, microscopie électronique à balayage ainsi que microscopie à force atomique. Ces techniques ont permis d'étudier à faibles échelles les causes et caractéristiques de la rupture dans les wafers Silicium PV. La diffraction d'électrons rétrodiffusés (EBSD) et la diffraction par rayon X (DRX) de Laue ont été utilisées afin d'explorer le lien entre les orientations cristallographiques de nos matériaux et les comportements observés. Conjointement, des modélisations et simulations numériques (par la méthode des éléments finis) ont été mis en place afin de fournir des outils de caractérisation auxiliaires et d'aider à comprendre les mécanismes de rupture mis en jeux.

Grâce à ce couplage expériences-modélisations/simulations numériques, une caractérisation fiable de la rigidité des wafers issus de différents procédés de fabrication a pu être effectuée. Une stratégie d'identification de l'origine de la rupture est également proposée alliant imagerie rapide et fractographie post mortem. L'étude de la rupture du silicium, dans le cas monocristallin, a mis en évidence la stabilité du clivage sur les plans (110), la grande vitesse d'amorçage de la fissure, la dépendance de la forme du front de fissure à la vitesse de propagation ainsi que l'apparition de "Front Waves" pour les fissures à très grande vitesse de propagation. L'étude de la rupture des wafers multi-cristallins démontre une fissuration systématiquement intra-granulaire. De plus, des éprouvettes jumelles (même géométrie, même microstructure) ont permis l'étude de la répétabilité du chemin de fissuration : une attention particulière a été portée à la nature des plans de

clivage, ainsi que l'effet de barrière des joints de grains. Enfin, soutenue par ces observations, une modélisation par la méthode des éléments finis étendus (XFEM) est proposée. Elle permet, connaissant la géométrie des grains et leur orientation, de reproduire le chemin de fissuration observé expérimentalement sur une éprouvette multi-cristalline.

MOTS CLÉS: Wafer en silicium de qualité photovoltaïque, flexion à 4-point, rigidité du matériau, rupture, vitesse de propagation de fissure, modèle éléments finis étendu (XFEM).

Contents

Contents	i
List of Figures	v
List of Tables	xv
Introduction	1
1 Basic knowledge on crystalline silicon	5
1 Crystallographic structure of silicon	7
2 Lattice defects	8
3 Brittle-ductile transition	11
4 Application : solar cell	13
5 Mechanical investigations on solar grade silicon	15
2 Mechanical characterizations for solar grade silicon wafers	19
1 Introduction	21
2 Material presentation	23
2.1 Manufacturing processes	23
2.2 Grain orientation distribution	26
2.3 Thickness variation and surface roughness	29
3 Experimental and numerical methods for determination of elastic stiffness	30
3.1 Experimental set up	30
3.2 Finite element modeling	32
3.3 Characterization of Young's modulus with relative error correction	37
4 Investigation on crack propagation mode and fracture origin	38
4.1 Crack propagation mode analysis	38
4.2 Identification of fracture origin	41
4.3 Weibull distribution	46
5 Discussion	48
5.1 Identification of the Young's modulus	48
5.2 Fracture investigation	49
6 Conclusion and remarks	50
7 Outlook	51

3	Fracture in single crystalline silicon	55
1	Introduction	57
2	Experimental procedure	62
3	Crack velocity	63
3.1	Steady state velocity	65
3.2	Initial velocity	66
3.3	Global crack stability	70
3.4	Summary on the crack velocity	71
4	Crack front determination	73
4.1	Wallner lines shapes	73
4.2	Crack front evolution	75
5	High velocity surface marks	77
5.1	Special surface marks characteristics	78
5.2	Velocity correlation	80
5.3	Special surface marks origin	80
6	Discussion	85
6.1	Stability of (110) cleavage	86
6.2	Crack initiation behavior	86
6.3	Crack velocity correlated crack front shape	87
6.4	Presence of front waves for high speed crack	88
7	Conclusion	88
8	Outlook	88
4	Fracture in multi-crystalline silicon	91
1	Introduction	93
2	Materials and experimental methods	97
2.1	Multi-crystalline silicon plates	97
2.2	Bending tests with high speed imaging technique	98
3	Intergranular or transgranular fracture	100
3.1	Crack overlapping twin boundary	100
3.2	Zigzag crack path along grain boundary	101
4	Fracture path reproducibility	103
4.1	Inconsistent path	103
4.2	Consistent path	108
5	Crack velocity in multi-crystal	110
5.1	Fracture stress	111
5.2	Crack propagation velocity	111
6	Cleavage plane investigation	114
6.1	Fractography analysis	114
6.2	Cleavage plane identification with grain orientation	115
6.3	Fracture energy assessment	121
7	Grain and twin boundaries crossing	124
7.1	Misorientation characterization	124

7.2	Grain boundaries crossing	126
7.3	Twin boundaries crossing	130
8	Fracture modeling	133
8.1	Cohesive-XFEM method	133
8.2	Damage initiation model	134
8.3	Simulation	137
9	Discussion	140
9.1	Transgranular crack	140
9.2	Reproducibility of the fracture	141
9.3	Fracture path	142
9.4	Crack velocity and grain boundary effect	142
10	Conclusion	143
General conclusions and prospects		145
A	Silicon plasticity	149
1	Introduction	149
2	Specimens and experimental setup	150
3	Experimental procedure and results	152
3.1	Reproducibility and comparison with existing results	152
3.2	Effects of temperature	153
3.3	Effects of strain rate	154
4	Discussion and conclusion	155
5	Perspectives	157
B	Euler rotation matrix	159
C	Pole figures and inverse pole figures	161
1	Stereographic projection	161
2	Pole figures	162
3	Inverse pole figures and texture analysis	162
D	Fracture mode	165
E	Common crystallographic axis of both grains separated by grain boundary	167
Bibliography		169

List of Figures

1	Sketch of an unframed PV module (left) and the exploded view of the PV laminate at the edge of two neighboring solar cells[EIT 10].	1
2	PV modules undergoing (thermo-)mechanical sollicitation in service (a). The cracking of silicon wafers reducing the electrical efficiency (b), the black areas revealed by electroluminescence correspond to the electrically inactive regions [KÖN 14].	2
1.1	Crystalline structure of silicon : deviated face-centered cubic system.	7
1.2	Equivalent crystal structures for a cubic symmetry system.	8
1.3	Crystal point defects. Vacancy (a), and interstitial (b) and substitutional (c).	9
1.4	Line defects in a crystal. Edge dislocation (a), and screw dislocation (b). The bold straight lines stand for the dislocation lines, the long arrows represent the shear stress driving the dislocation's motion, the short arrow indicate the direction of Burgers vector b [MOR].	10
1.5	Surface defects in a crystal. 2D representation of grain boundary (a), and twin boundary (b).	11
1.6	Dependence of BDT temperature on the applied strain rate : $\dot{\epsilon}_1=1.3 \times 10^{-6}/s$, $\dot{\epsilon}_2=2.6 \times 10^{-6}/s$, $\dot{\epsilon}_3=5.2 \times 10^{-6}/s$, $\dot{\epsilon}_4=1.3 \times 10^{-5}/s$, $\dot{\epsilon}_5=2.6 \times 10^{-5}/s$. Points marked with circles, triangles and squares correspond respectively to 'brittle', 'transition' and 'ductile' tests [SAM 89].	12
1.7	P-N junction formation in silicon, with intentional doping process [HER 82].	14
1.8	Schema on the solar cell function [HER 82].	15
1.9	Solar grade silicon wafer (a), and ready-for-use unencapsulated solar cell (front side view) (b). The surface dimension is $156 \times 156 \text{ mm}^2$	16
2.1	Commonly recognized fracture causes in silicon wafer. The wire sawing induced micro-cracks as revealed by [MÖL 05] (a), and the inclusion cluster as shown in [SØI 04] (b).	23
2.2	MCSi specimens manufacturing process (a) and a look at the representative grain shapes (specimen size : $50 \times 50 \times 0.17 \text{ mm}^3$) (b).	24
2.3	RST specimens manufacturing process (a) and a look at the representative grain shapes (specimen size : $50 \times 50 \times 0.09 \text{ mm}^3$) (b).	25
2.4	Single crystalline specimens manufacturing process (a) and a look at the representative specimen (specimen size : $50 \times 50 \times 0.19 \text{ mm}^3$) (b).	27

2.5	MCSi grain orientation distribution. Color coded map of the grain orientations measured by the Laue X-ray diffraction on a standard wafer (a) and pole figures over one part of the wafer (containing 60 grains) for 011 directions (b) and 111 directions (c).	28
2.6	RST grain orientation distribution. Color coded map (left) where Y corresponds to the drawing direction. Inverse pole figure (right),	28
2.7	Thickness variation of the studied silicon plates investigated by optical microscopy. Para. signifies the direction parallel to the drawing direction, perp. stands for the direction perpendicular to the drawing direction, mono represents mono-crystalline silicon.	29
2.8	Surface roughness of the three kinds of silicon plates. RST plates (a), MCSi plates (b) and single crystalline silicon plates (c).	30
2.9	4-point bending test	31
2.10	Parametric modeling assisted by Matlab code	33
2.11	The modeling of MCSi and RST plates in FE analysis. Voronoi tessellation method (a), MCSi modeling with Voronoi tessellation (b) and RST modeling with long strips for the two loading configurations, longitudinal (c) and transverse (d).	34
2.12	Comparaison of numerical and experimental force-deflection curves on a 193 μm thick single crystalline wafer under 4-point bending	35
2.13	Relative error determination based on [0.1 – 0.3] mm deflection interval for stiffness calculation. Influence of the plate thicknesses (a) and influence of the friction coefficient (b). The straight lines denote the average of the assessed relative errors.	36
2.14	Artificial texture of RST plates for the stiffness characterization using the FE model : inverse pole figure for the grain direction (RD) and inverse pole figure for the perpendicular direction (TD)	37
2.15	Representative experimental and numerical stress-strain curves for MCSi and RST plates	38
2.16	4-point bending with mirror.	39
2.17	MCSi plate before (left) and after (right) cracking.	40
2.18	RST plate before (left) and after (right) cracking with grains perpendicular to the tension direction.	41
2.19	The grain boundary shape on the upper surface (a) and fracture surface of RST plate crack with grains perpendicular to the tension direction (b).	41
2.20	RST plate before (left) and after (right) cracking with grains parallel to the tension direction.	42
2.21	Wallner lines shape under bending. The schematic showing the generation of Wallner lines (a), and the observation of the Wallner lines on the fracture surface (b).	43
2.22	Optical image of the $(11\bar{1})$ fracture surface of single crystalline silicon under 4 point bending. The dotted line represents approximately the crack front shape.	43

2.23	First cracks marked in two consecutive images for MCSi plate with (left) the last image before cracking and (center) the first image after cracking. Why these are the first cracks is coming from analysis by image subtraction (right). The two black vertical lines in the right image reveal the punch rollers' positions.	44
2.24	MCSi fracture source identification. Crack surface pointing out the initiation locality (b), and fracture surface on the same crack as in (b) pointing out further propagation direction (a).	45
2.25	First crack marked in two consecutive images for RST plate with (left) the last image before cracking and (center and right) the first image after cracking. The two black vertical lines in the right image reveal the punch rollers' positions.	45
2.26	RST fracture source identification with grains parallel to the punch rollers. Crack surface pointing out the initiation locality (a), and fracture surface on the same crack as in (a) pointing out further propagation direction (b).	46
2.27	Elimination of possible fracture roots thanks to determined crack propagation directions. Important local thickness variation (a) possible inclusions (b). The horizontal arrows indicate the crack propagation directions.	46
2.28	Crack surface of a RST plate with grains elongated along the direction perpendicular to the punch rollers	47
2.29	Weibull distributions of both MCSi plates and RST plates in the two loading configurations	48
2.30	Fracture cause identification for single crystalline silicon wafer. The high speed camera points out the first crack (a) and the fractography highlights the initiation point (b). The two black lines denote the punch rollers in (a).	52
2.31	New insights on crack surface in single crystalline silicon. (111)–(110) deflection revealed in (a)–(d) and the special shape of Wallner lines in (a). The horizontal arrows indicate the crack propagation directions at different spots on the same crack surface including the initiation point.	53
2.32	The Wallner lines shape found in literature [SHE 04b].	53
3.1	The crack velocity profile after initiation. (110) cleavage conducted by uni-axial tensile tests using 'potential drop' method [CRA 00] (a), and fracture investigations performed with 3 point bending tests using 'potential drop' method [SHE 04b] (b), (111) cleavage simulated with molecular dynamic model [BUE 07] (c).	58
3.2	Cleavage plane deflection from (110) to [100] [PÉR 00a].	59
3.3	The (110)–(111) deflection observed in [SHE 03b]. The 3-point bending set up is presented on the top, and the deflection results are presented at the bottom of the figure (the sub-figures are extracted from [SHE 03b]).	60

3.4	The (110)-(111) deflection observed in [CRA 00] for a crack velocity higher than 3000 m/s. The central (major) part of the crack is (110) plane while local (111) planes can be observed in the hackle region (the sub-figures are extracted from [CRA 00]).	61
3.5	The crack front shape under bending, the dotted line denotes the atomic debonding path [SHE 04b].	61
3.6	Surface roughness measurement conducted with a profilometer. The wire sawing traces can be revealed on the mono-crystalline silicon wafer. . . .	62
3.7	Two strategies for pre-crack introduction.	62
3.8	Experimental set up of 4 point bending tests equipped with a tilted mirror and a high speed camera.	63
3.9	The measured crack propagating velocities with respect to the fracture stress, each point corresponds to one test.	64
3.10	Crack propagation tracked by high speed camera and highlighted thanks to wavelet denoising. Cases for crack steady state velocities of 1400 m/s, 2000 m/s, 2600 m/s, 3000 m/s, 3300 m/s, 3600 m/s (a)-(f). The yellow bar stands for the uncertainty of the crack tip position. Number 1 denotes the first image revealing the crack propagation and number 0 is the image just before.	65
3.11	Crack velocity profiles measured as a function of the crack length.	66
3.12	Two different precrack front shapes in accordance with the two precracking strategies. Crack propagation <2900m/s initiates from long elliptical precrack (a) and crack propagation > 2900m/s starts from short straight precrack (b). The dimension can be referred to the specimen's thickness <i>i.e.</i> 190 μm	67
3.13	Finite element analysis of SERR at crack initiation. Geometry of the analyzed structure loaded by pure bending (a), snapshots on the modeled pre-crack with elliptical front shape (b) and pre-crack with tilted straight front shape (c) corresponding to the experimental pre-cracks as presented in FIG. 3.12(a) and FIG. 3.12(b).	68
3.14	Energy release rate at crack initiation (assessed in this study) and propagation (reported in [CRA 00]) with respect to different steady state velocities.	68
3.15	Initiation velocity versus propagation velocity. The straight line represents the assumed case such that the propagation velocity is equal to the initiation velocity.	69
3.16	Fractographic determination of crack initiation state. Snapshot of correlation between the surface marks and the steady state velocity with massive studies (a), the fractography at initiation spot for the crack with steady state velocity of 3600 m/s (b).	71

3.17	Crack surface topographies for the rapid propagation case of 3600 m/s. (a), topographic surface of the primary crack that initiates from the pre-crack. (b), topographic surface of the secondary crack that initiates underneath the punch roller.	72
3.18	Crack surface for different propagating velocities. Representative for velocity below 2000 m/s (a), representative for velocity between 2000-2800 m/s (b), representative for velocity between 2800-3000 m/s (c), representative for velocity beyond 3000 m/s (d), comparison of the former 4 shapes as well as the shape in [SHE 03a, SHE 04b] with <1700 m/s (e). Solid lines denote the Wallner lines and the thin dotted lines stand for the atomic debonding path. The dimension can be referred to the specimen's thickness <i>i.e.</i> 190 μm	74
3.19	Comparison between the experimentally observed Wallner lines and composed ones following FIG. 3.20(a).	76
3.20	Crack front determination : method and results. The generation of Wallner lines from surface defects (a), method for recovering the crack front shape from Wallner lines and the surface waves (b), the real crack front shapes for different crack propagation velocities (c). The front for rapid crack presents curvature jump while that for slow crack is smooth.	77
3.21	Special surface marks on (110) plane for a rapid propagation (3600 m/s). Optical images showing different marks at different loci (a). Local details obtained with SEM are illustrated in (b)-(d), which correspond to the framed regions in parallelogram, ellipse and triangle, respectively. The crack propagation direction is from the left to the right.	78
3.22	SSM characteristics imaged with AFM measurements. Spacing and amplitude of the SSM and the Waller lines along the straight dotted lines in the three following subfigures (a), central surface traces in the same region of FIG. 3.21(b) (b), surface instabilities & SSM in the same region of FIG. 3.21(c) (c), lower surface traces in the same region of FIG. 3.21(d) (d).	79
3.23	The SSM with respect to the crack velocity. The correlation with different steady state velocities (a), the SSM evolution in the transitory phase of a rapid crack (3600 m/s) (b), the onset position established with (a) (c), and the the tilt angle of the SSM established with (a) (d). For figures without scale bar, the dimension can be referred to the specimen's thickness <i>i.e.</i> 190 μm	81
3.24	Analysis of the FW origin and generation process. The relationship between the local velocity v_l and the macroscopic propagation velocity v , t_f is the local tangent of the crack front (a), the local velocity plots for several propagation velocities (b), the red mark on the vertical axis indicates that the velocity fluctuation appears at approximately 2500 m/s for all cases, while the two red marks on the horizontal axis show that the fluctuation onset height varies between 0.34h to 0.6h.	83

3.25	Real scale schema on the FW generation and propagation, the trace is compared with the experimentally observed SSM. Case for 2800 m/s (a), and case for 3600 m/s (b).	84
3.26	SERR and SERR gradient distribution along the crack front. Dynamic toughness extracted from [CRA 00] 3.26(a), the SERR distribution from the lowest point to the asymptotic point along the crack front (b) and the corresponding SERR gradient distribution with respect to the local crack velocity along the same path (c). The dimension can be referred to the specimen's thickness <i>i.e.</i> 190 μm .	85
3.27	A case without pre-crack showing deflection from (111) to (110) plane under contact force perturbation. The dimension can be referred to the specimen's thickness <i>i.e.</i> 190 μm .	87
4.1	Ridge nucleated from the dislocation perturbation on the crack front. Optical microscope micrograph of a slightly etched (110) fracture surface (a), optical photograph of the (110) surface, with the quarter-elliptical crack front (note the large perturbations-free zone) (b), AFM micrograph of a small perturbation resulting from interaction with a single perturbation (velocity vector from right to left) (c), and large perturbation resulting from interaction with several adjacent dislocations (velocity vector from left to right)(d) [BER 14].	93
4.2	Reported crack along the grain boundary rather expected as a twin boundary [POP 13].	94
4.3	Bond trapping effect numerically revealed in intergranular crack [MÖL 14]. (112) plane cleavage in a single crystal and the crack path is smooth (a), fracture along (112) symmetrical tilt grain boundary (STGB) but the crack penetrates in the crystals and propagates on (111) planes with higher material toughness.	95
4.4	Grain boundary crossing behaviors in tensile configuration [CHE 07b]. The crossing takes place with one breakthrough point (a), and the crack overcomes the grain boundary with multiple breakthrough points (b). The propagation directions are from the left to the right in (a) and from the top to the bottom in (b).	96
4.5	Twin boundary characteristic. The color coded map (a) and the corresponding pole figures (b). The red straight line denotes the twin boundary supposed perpendicular to the specimen's surface as presented in the color code map, the blue curved line represents the the projection of the real twin boundary obtained with the symmetry of the poles.	98
4.6	Sub-grains in multi-crystalline silicon. The sub-grains optically revealed in the studied specimens (a), sub-grain boundary accommodated by dislocations [NAK 09] (b).	99

4.7	Schema of the experimental set up : a tilted mirror is put under the specimen to allow the camera to view the tensile surface. The grain boundaries can be distinguished in the mirror thanks to the different light reflections with respect to different grain orientations.	99
4.8	A particular case showing an overlap of the crack on a twin boundary. The crack path revealed by a macroscopic image with a zoom exhibiting the overlap on a boundary (a) and the corresponding fractography on the crack-boundary overlap portion (b). The red and pink lines highlight the Wallner lines and the surface instabilities in (b).	101
4.9	False grain boundary overlap. The observation of the crack path at a relatively large scale reveals a grain boundary overlap (a), while a zigzag crack path can be seen at a smaller scale indicating that the crack does not really superimpose the grain boundary (b), the crack surface morphology under optical microscope (c). The horizontal arrows in (a) indicate the tensile direction, the others point out the crack propagation direction. . . .	102
4.10	Crack paths of twin plates 1-1 and 1-2. The fracture paths differ from the beginning but share consistency in several grains. The specimen's dimension is $50 \times 50 \text{ mm}^2$, the crack propagates in up-down direction.	104
4.11	Crack paths of twin plates 2-1 and 2-2. The discrepancy in the fourth grain lead to totally different crack paths thereafter. The specimen's dimension is $50 \times 50 \text{ mm}^2$, the crack propagates in up-down direction.	105
4.12	Crack paths of twin plates 3-1 and 3-2. The inconsistency occurs at the third grain, with totally different crack directions. The crack propagates in up-down direction.	106
4.13	Crack paths and fracture surface morphologies in grain 3 of twin plates 3-1 and 3-2. Reconstruction of the two different paths (indicated as ① and ②) in grain number 3 containing sub-grains (a), the two paths form an angle of 23° on the surface of the specimen. Tilt angles of the cleavage planes ① and ② related to the specimen's surface (b), the two cross sections follow the dotted lines in (a). Crack surface morphology (indicated as path ①) in twin plate 3-1 where dislocation induced marks are likely to exist (c), crack surface morphology (indicated as path ②) in twin plate 3-2 (d), the surface instabilities indicate that the cleavage plane of path ② is (111). The propagation direction is from left to right in (c) and (d). . . .	107
4.14	Crack paths of twin plates 4-1 and 4-2. The fracture paths are nearly the same. The specimen's dimension is $50 \times 50 \text{ mm}^2$, the crack propagates in up-down direction.	109
4.15	Crack paths of twin plates 5-1 and 5-2. The crack paths are perfectly the same according to optical observation on surface. The specimen's dimension is $50 \times 50 \text{ mm}^2$, the crack propagates in up-down direction.	110
4.16	The stress-strain curves of the two twin specimens : twin plates 5-1 and 5-2	111

4.17	Cracking process of twin plate 5-1. The first image presents the completely fractured plate, the yellow line highlights the entire fracture path and the dashed blue lines indicate the punch roller positions. The second image corresponds to the subtraction between the first photo after cracking and the last photo before cracking, thus the first observation of the crack. The rest images are the following subtraction results. The yellow marks spot the crack tip positions in sequential subtractions.	112
4.18	Crack propagation velocity associated to the grains in twin plate 5-1. Mean crack propagation velocity measured with high speed camera images (a), and indication of the crack tip positions (b). G denotes grain and GB the grain boundary. Refer to FIG. 4.19 for the grain numbering.	113
4.19	Fractographies on all the fracture involved grains for twin plate 5-1. The numbers represent the crossing order of the crack through the grains from the beginning to the end, the grain 9 owns many twins.	115
4.20	Fractographies on all the fracture involved grains for twin plate 5-2. The numbers represent the crossing order of the crack through the grains from the beginning to the end, the grain 9 owns many twins.	116
4.21	Angular color map of grain orientation distribution measured with Laue X-ray diffraction. The three angles γ , β , α denote the rotations around the axes x, z, y, sequentially.	117
4.22	Pole figure taking a crack plane as the stereographic projection plane. DPP denotes a perpendicular direction to the cleavage plane, DIP (any) direction in the cleavage plane.	119
4.23	Low energy cleavage planes in silicon, the four (111) planes constitute a tetrahedron. A (110) plane contains one [110], two [111] and two [112] directions (a), a (111) plane contains three [110] and three [112] directions (b), a (112) plane contains one [110] and one [111] direction (c). . .	119
4.24	Cleavage plane orientation in sample's coordinate system.	120
4.25	Cleavage plane investigation with pole figures ($\{110\}$ -blue circles, $\{111\}$ -red squares and $\{112\}$ -green triangles families) taking the cleavage plane as the projection plane. The pole figures (a), (b), (c), (d), (e), (f) are based on the cleavages planes of grains 3, 7, 8, 9 ₁ , 9 ₂ , 11 (see FIG. 4.20), respectively.	121
4.26	Schematic drawing for grain boundary misorientation : the hatched plane denotes the grain boundary ; l and n represent the common crystallographic axis of both grains and the normal vector to the boundary plane, respectively ; θ represents the misorientation.	125
4.27	Fractography on the grain boundaries crossing (crack runs from the left to the right)	127
4.28	SEM images for grain crossing details. The crossing locality from the grain 2 to 3 (a) and the crossing locality from the grain 4 to 5 (b).	128
4.29	Correlation between the CLMIS and the crossing shape. The light color points correspond to the twin boundaries that will be detailed in section 7.3.129	129

4.30	Schematized process on the "V" crossing mechanism at a grain boundary, grain A and grain B are the two adjacent grains, the numbers address the successive advancing. This crossing behavior correlates a low twist angle between the two cleavage planes.	130
4.31	Schematized process on the "X" crossing mechanism at a grain boundary crossing, grain A and grain B are the two adjacent grains, the numbers address the successive advancing. This crossing behavior correlates a high twist angle between the two cleavage planes.	130
4.32	Theoretical twin boundary crossing from the up to down. Two tetrahedrons with a common face of a (111) plane, the initial cleavage plane is (111) (a), the preferential plane ahead of the twin boundary is either the (111) plane (b), or the (110) (c), two tetrahedrons with a common face of (111) plane, the initial cleavage plane is (110) (d), the preferential plane ahead the twin boundary is either the (110) (e) or the (111) plane (f). The two short parallel lines in (a) and (d) indicate the intersection between the two cleavage planes with a color correspondence in (a)-(c) and another in (d)-(e).	131
4.33	Twin boundary crossing. Surface observation of the twins (a), topographies on the twin boundary crossings in θ_2 (b) and from θ_3 to θ_4 (c), as spotted by the dashed circle and the dashed square in (a). The measured CLMISs are 2° and 33° for (b) and (c), respectively.	132
4.34	The principle of the XFEM with phantom nodes [ABA 13].	134
4.35	Different coordinate systems involved in the fracture modeling. GCS denotes global coordinate system, LCS (equivalent to CCS) stands for local coordinate system and DCCS denotes deviated crystal coordinate system.	136
4.36	Typical linear traction-separation response.	137
4.37	Grain modeling of the twin plate 5-1 (a), boundary conditions and mesh on the modeled specimen (b).	138
4.38	Comparison of the crack path between the experiment (a) and the simulation (b). The experiment was conducted in bending condition and the simulation was performed in tensile condition.	139
A.1	Specimens cut from thin silicon wafer.	151
A.2	Firstly activated slip systems.	151
A.3	Experimental set up at high temperature.	152
A.4	Comparison between the specimens cut from two directions.	153
A.5	Comparison between the results in the literature and in this study	154
A.6	Temperature effect.	154
A.7	Strain rate effect.	155
A.8	Plastic deformation localized at the contact region in literature work [WAL 00].	156
A.9	Deformed specimen with a zoom on the cross section morphology.	156
A.10	Influences of the temperature (a) and the strain rate (b) on the yield points.	157

List of Figures

C.1	Stereographic projection, example of [100] directions.	161
C.2	Pole figure, example of [100] poles.	162
C.3	Inverse pole figure. The full figure with 24 equivalent "triangle" parts (a) and the retained "triangle" figure representing the sample's coordinate system (ND, RD and TD) (b).	163
D.1	Three elementary fracture modes.	165

List of Tables

- 1.1 Miller indices 7
- 2.1 Parameters of experimental set up (mm) 31
- 2.2 Weibull parameters with 90% confidence intervals for MCSi and RST plates 47

- 4.1 MCSi twin plates for fracture reproducibility investigation 103
- 4.2 Angles between low energy cleavage planes in silicon. 108
- 4.3 Orientations of the grains crossed by the crack in the twin plate 5-1. . . . 118
- 4.4 Cleavage plane orientation expressed with ϕ_1 and ϕ_2 in the twin plate 5-1 120
- 4.5 Fracture toughness of low energy crystal planes in silicon. 122
- 4.6 Energy review on the fracture planes in the twin plate 5-1. 123
- 4.7 Grain boundary misorientations based on the Laue X-ray diffraction measurements 126
- 4.8 Comparison of the cleavage planes between the experiment and the simulation 140

Introduction

Since greenhouse warming is a worldwide concern, and the global energy consumption is predicted to increase substantially every year, exploitation of clean and renewable solar energy has become critical. Among the three most popular solar technologies : photovoltaic (PV), concentrating solar power, solar thermal energy, PV solar power-based on solar cells-occupies the key position. Nowadays, the majority of solar cells are made of silicon, mainly because of its abundance¹. As shown in FIG. 1, the solar cells are embedded in a laminate structure (PV module) as center-pieces. The PV modules are then assembled into solar panels in order to provide high voltage. Some PV cells are based on other active materials such as amorphous silicon or smart polymers, however, these alternative PV technologies will not be mature at least for the coming decade [NAK 09]. According to up-to-date information provided by Fraunhofer ISE [Fra16], PV technologies based on crystalline silicon account for about 93% of the total production in 2015, among this, multi-crystalline silicon occupies about 69%.

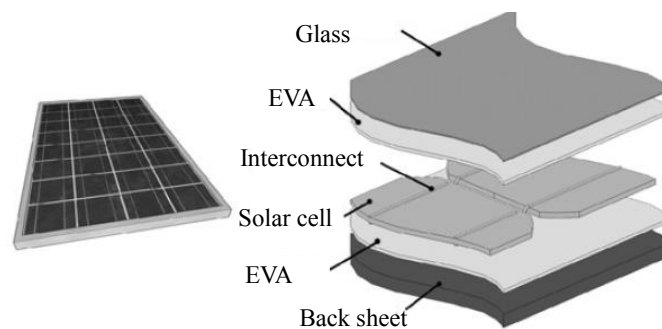


FIGURE 1: Sketch of an unframed PV module (left) and the exploded view of the PV laminate at the edge of two neighboring solar cells[EIT 10].

In the development of solar cell technology, the electrical efficiency, being the most important factor on the profitability of solar energy, received the major concern and was subject to most of the scientific investigations by acting on some physico-chemical parameters. The world record for lab cell efficiency is 25.6% based on mono-crystalline silicon technology and 20.8% based on multi-crystalline silicon technology [Fra16]. Meanwhile,

1. Silicon makes up 27.7% of the Earth's crust and is the second most abundant element in the crust, with only oxygen having a greater abundance (46%) [EMM 75].

in the last 10 years, the efficiency of average commercial silicon modules increased from about 12% to 17%, showing an encouraging growth [Fra16]. Besides, the efficiency gap between the lab and commercial solar cells shows the potential improvements that can be made.

Beyond the electrical efficiency improvement, the research on cheaper manufacturing process, reliability as well as durability of PV products are important issues which should be carefully considered in the solar energy development.

- Classical silicon wafers are fabricated with ingot cast solidification technology, associated with slicing process using wire saw. This manufacturing process can ensure a good flatness of the wafer, but the main drawbacks are the material loss due to the cutting width which reaches almost 50% and the relative important wafer thickness. From an economical point of view, these disadvantages finally impact the profitability knowing that the fabrication cost of silicon wafers represents up to 40% of the total cost of a PV module [MÖL 05]. In this direction, advanced manufacturing processes for thinner silicon wafers increasingly emerge. Most aim to directly produce properly sized wafers (especially, with adequate thickness), eliminating most of the cutting operations.
- Another important issue that the PV products confront is the reliability and durability. Actually many silicon wafers break during the manufacturing process before the integration in PV cells. Post-manufacturing cracks created during transportation, installation or service can significantly decrease the efficiency of PV modules [KÖN 11b, PAG 14]. An example, given in FIG. 2, shows the (thermo-)mechanical solicitation induced cracking at the level of silicon wafers.

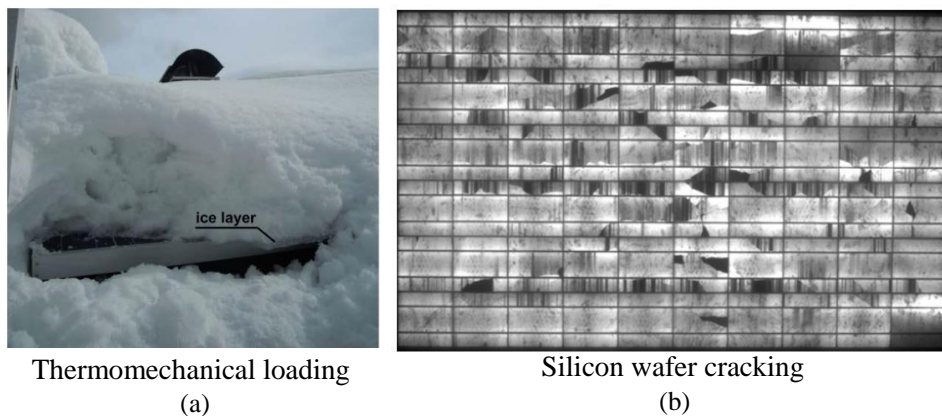


FIGURE 2: PV modules undergoing (thermo-)mechanical solicitation in service (a). The cracking of silicon wafers reducing the electrical efficiency (b), the black areas revealed by electroluminescence correspond to the electrically inactive regions [KÖN 14].

Within the French National Research Agency (ANR) funded project DEMOS, the company Solarforce develops Ribbon on Sacrificial Templates (RST) process to fabricate

slicing free multi-crystalline silicon wafers. This process produces Si wafers almost two times thinner than the classical wafers. Along with the development of this novel technology, LaMCoS-INSA de Lyon, as a partner, was involved in the characterization of the elastic properties and in the study of the defects as well as their origin which reduce mostly the mechanical strength. Moreover, for the purpose of enhancing the reliability and durability of global solar technology, the ANR funded project EquiPeX Durasol was launched in order to lengthen the lifetime as well as to guarantee good energetic performance of the solar equipment. This ANR project regroups many research units from electrical, physical, chemical to mechanical fields. The LaMCoS-INSA de Lyon is charged to perform fundamental investigations on the fracture behavior from the silicon wafer (material) scale to the solar cell scale.

The present work is concerned by the two projects mentioned above. We focus on Si wafers instead of solar cells in this work, knowing that the reliability and the durability of PV modules are mainly endangered by the outright fracture of the embedded brittle Si wafers. Even though the fracture behavior of (solar grade) crystalline silicon has been substantially studied in the literature, there are still some key open questions and challenges, such as : fair fracture root identification methodology, acceleration phase of the fracture process, the cleavage plane selection in function of the crack velocity, fracture path in the multi-crystal, impact of various material defects on the crack trajectory.

The present work is based on fracture tests in combination with high speed imaging technique, characterization tools such as microscopy, Atomic Force Microscope (AFM), Electron Back-Scatter Diffraction (EBSD), Laue X-ray diffraction, and modeling by Finite Element method. The manuscript develops in the following way :

- The first chapter deals with the basic knowledge on crystalline silicon, which includes the crystallographic structure, lattice defects, brittle-ductile transition, and the solar grade silicon. Previous mechanical investigations are also discussed.
- The second chapter aims at characterizing the material stiffness and understanding the fracture mode as well as fracture origin of RST and classical silicon wafers. The proposed experimental and numerical methods are applicable to silicon wafers with innovative manufacturing processes. The outlook in this chapter highlights several interesting fracture phenomena which promote the investigations in chapters 3 and 4.
- The third chapter carries out detailed investigation on the (110) silicon cleavage which is the main fracture mode of mono-crystalline silicon wafer in PV modules. The investigation gives insight to several unknown fracture behaviors in silicon, such as fracture stability, crack front evolution with the crack velocity, specific surface traces (appearance of front waves).
- The fourth chapter focuses on the fracture behavior of multi-crystalline silicon. First, we discuss more in detail the fracture mode (inter- or trans-granular). Then, based on twin specimens, we investigate the crack path reproducibility, the cleavage

planes, and the barrier effect of grain boundaries. Finally a fracture model is elaborated allowing to reproduce the experimental crack path in multi-crystals. This indicates that the fracture in the solar silicon wafers is predictable.

- Finally, we come out the general conclusions, followed by a discussion and some prospects.

Chapter 1

Basic knowledge on crystalline silicon

Solar cells develop increasingly, while one important issue—the mechanical strength and service life lengthening of solar cells—is often overlooked. Yet this issue is necessary for economic sustainability of the PV technology and deserves careful investigations. Today, the most widely used solar cells are composed of crystalline silicon wafers (monocrystalline : a single silicon crystal or multi-crystalline : aggregate of a couple of single crystals separated by grain boundaries). The principal failure of solar cell is related to the wafer cracking (partial or total) which reduces the electrical performance or outright leads to the dysfunction of the cell. In this first chapter, the basic knowledge on the crystalline silicon and its application in solar cell are addressed. The first part deals with the characteristic crystallography of silicon, followed by an introduction of the essential material defects that may weaken the mechanical strength. The third part highlights the specific brittle-to-ductile transition on the mechanical behavior. The last part focuses on the principle of solar cell, previous mechanical investigations are also discussed.

Contents

1	Crystallographic structure of silicon	7
2	Lattice defects	8
3	Brittle-ductile transition	11
4	Application : solar cell	13
5	Mechanical investigations on solar grade silicon	15

1 Crystallographic structure of silicon

In solid state, silicon can be either amorphous or crystalline. Crystalline silicon has a diamond structure, which is a deviation of face-centered cubic (fcc) system. The crystal lattice is illustrated in FIG. 1.1. Each atom shares 4 valence electrons with the other atoms. The difference from a real fcc is that in an unit cell, in addition to the 8 atoms at the top and the 6 atoms at the center of the faces, there are 4 "extra" atoms situated at the centroid of 4 tetrahedrons. Each tetrahedron is formed by 3 in-face atoms and 1 top atom (see FIG. 1.1).

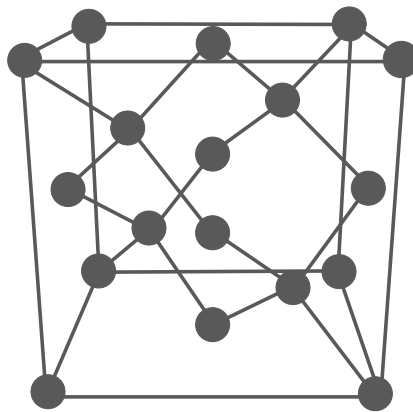


FIGURE 1.1: Crystalline structure of silicon : deviated face-centered cubic system.

The cubic symmetry of silicon leads to equivalent crystallographic directions and planes. Following Miller indices (see TAB. 1.1), a single direction (plane¹) associated with h, k, l ² in any order and for any sign of each belongs to the same direction (plane) family defined by positive h, k and l . The most widely studied directions (planes) of silicon are $[100]$ ($\{100\}$), which are used to define the elastic constants for cubic symmetry system, $[111]$ ($\{111\}$) and $[110]$ ($\{110\}$), which correspond to the cleavage planes in crystalline silicon.

TABLE 1.1: Miller indices

Notation	Interpretation
$(h k l)$	single crystal plane
$\{h k l\}$	equivalent planes (plane family)
$\langle h k l \rangle$	single crystal direction
$[h k l]$	equivalent directions (direction family)

1. Following the Miller indices, a crystallographic plane is defined with its normal direction.
2. Inverse x, y and z -intercepts of planes, h, k and l are reduced to 3 integers having the same ratio.

When positioning a silicon single crystal in the sample's coordinate system, we have 24 equivalent possibilities due to the symmetry of cubic structure, which leads to 24 equivalent descriptions of a grain's orientation. As can be noticed in FIG. 1.2, the single crystal has 6 equivalent $[100]$ directions. Upon bonding the crystal directions to the sample's coordinate system, we have 6 possibilities to align with x axis, then 4 possibilities to align with y , the third crystal direction will be fixed systematically along z axis (the sample's coordinate system obeys right-hand rule). Therefore, we can obtain $6 \times 4 = 24$. This multi-equivalence can also be elucidated with Miller indices. Considering three different indices h, k, l , there are 6 ways to arrange the order : $h k l, h l k, k h l, k l h, l h k, l k h$. For each arrangement, we have 4 possibilities to assign the sign. Taking the order arrangement $h k l$ for instance, we can have $h k l, -h k l, h -k l, h k -l$. Thus, for an equivalent direction or plane, 24 descriptions come out.

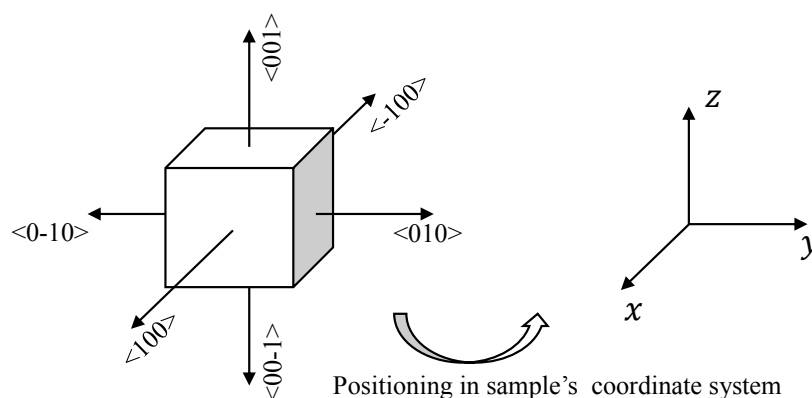


FIGURE 1.2: Equivalent crystal structures for a cubic symmetry system.

Since the atom density differs from one crystallographic direction (plane) to another, the physical properties of a silicon single crystal manifest anisotropic characteristics, such as elastic constants, thermal expansion coefficients, surface energies, electrical resistivity [HUL 99]. This anisotropic feature dominates particularly the fracture behavior, as will be mentioned in detail in chapter 3.

2 Lattice defects

Like all other crystals, the silicon lattice is never perfect and contains crystal defects induced by the manufacturing process.

- Point defects

For brief descriptions : when an atom is removed from the perfect crystal lattice, a vacancy is formed, as shown in FIG. 1.3(a); if a host or a foreign atom sits in a normally unoccupied site or interstice, a selfinterstitial occurs, as can be noticed

in FIG. 1.3(b); when a foreign atom comes to substitute a host atom at its original site, this point defect is called substitutional.

Crystalline silicon is grown from the melt state (solidification). Due to the low diffusive mobility of the intrinsic³ point defects, *i.e.* vacancies, selfinterstitials, many of the defects thermodynamically at equilibrium concentration at the freezing point are 'frozen in' the crystal during cooling phase. Depending on the temperature gradient close to the freezing interface and the time at high temperatures, point defect agglomerates can be formed, too. Reviews of Falster et al. [FAL 00a, FAL 00b] give an overview of intrinsic point defects in CZ (Czochralski, the most popular manufacturing process for silicon) silicon. Due to imperfect insulation, as grown crystals, whatever the method is used, also contain foreign atoms, like oxygen, nitrogen and carbon. These atoms promote usually the generation of interstitials or substitutional defects. Particularly, in order to realize some expected electric performances like making silicon based semiconductor devices, some dopants (elements from groups III and V of the periodic table of elements) are intentionally added into the silicon crystals. The dopants act as substitutionals, as will be discussed in section 4 of this chapter.

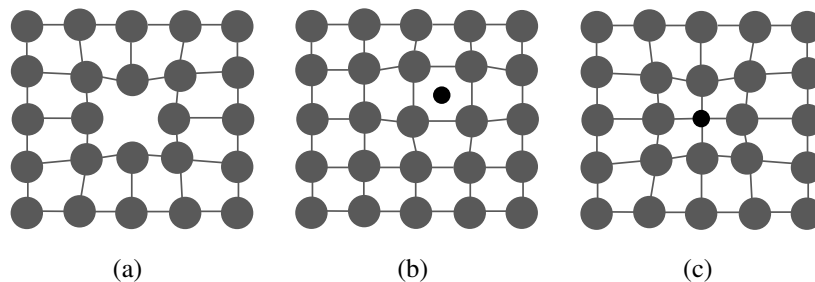


FIGURE 1.3: Crystal point defects. Vacancy (a), and interstitial (b) and substitutional (c).

- Line defects

Line defects are mainly dislocations. Two elementary types of dislocation exist : edge dislocation and screw dislocation. An edge dislocation is a defect where an extra half-plane of atoms is introduced mid way through the crystal. The locus of defective points (termed dislocation line) produced in the lattice by the dislocation lie along a line, as highlighted by the bold straight line in FIG. 1.4(a). When subject to important shear stress, the edge dislocation moves forward on the shear plane and causes the top half of the crystal to move with respect to the bottom half, as can be seen in FIG. 1.4(a). The upper part finally slides over the lower by a lattice vector distance **b**, called Burgers vector⁴, when the dislocation arrives at a free

3. Intrinsic means that the defects are due to host atoms instead of foreign atoms. In reverse, we use extrinsic.

4. The shortest lattice vectors that are allowed as Burgers vectors are $\frac{1}{2} \langle 110 \rangle$, *i.e.* half the diagonal of

surface. For the edge dislocation, the Burgers vector is directed perpendicular to the dislocation line (see FIG. 1.4(a)). A screw dislocation is much harder to visualize. The motion of screw dislocation is also a result of shear stress, the particularity is that the dislocation line is parallel to the Burgers vector but the movement is perpendicular to the Burgers vector, as can be noticed in FIG. 1.4(b). In the real crystal lattice, the most of the dislocations have mixed feature, *i.e.* the combination of edge and screw dislocations. Particularly, in silicon, the main dislocations are 60° dislocations (the dislocation line and Burgers vector make an angle of 60°) and screw dislocations [HOR 58].

In intrinsic silicon crystal, the main origin of dislocations is the thermal stresses due to thermal gradients during temperature transients in cooling phase, or mismatch stresses caused by heavily doped areas in combination by high temperatures. Moreover, the silicon crystal may also contain what is called geometrically necessary dislocations (GNDs). The concept of GNDs was introduced by [NYE 53] and [ASH 70] to account for the gradients of plastic strain induced by the deformation. This kind of dislocations are also present at grain boundaries to accommodate the misorientation [NAK 09].

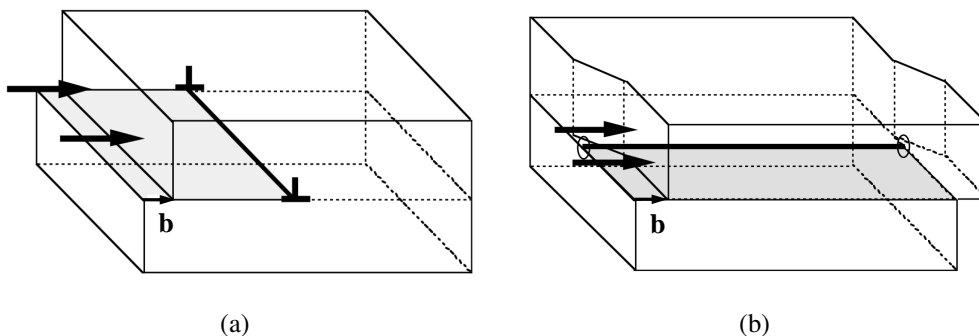


FIGURE 1.4: Line defects in a crystal. Edge dislocation (a), and screw dislocation (b). The bold straight lines stand for the dislocation lines, the long arrows represent the shear stress driving the dislocation's motion, the short arrow indicate the direction of Burgers vector **b** [MOR].

- Planar defects

Without considering the disorder of the atomic arrangement⁵ at the free surface (interface between the crystal and the gas or liquid), the main surface defects in a poly-crystal are grain boundary, twin boundary and stacking faults. As illustrated in FIG. 1.5(a), grain boundaries are internal surfaces that separate individual grains whose crystallographic orientations mismatch. While twin boundaries are present

a cube face or one of the short edges of the tetragonal cell. These vectors are equal to the shortest distance between two equivalent atoms [HOR 58].

5. At free surface, the crystal undergoes relaxation and reconstruction [BAT 75].

inside one grain and change the grain orientation such that the lattice structures are symmetric with respect to the twin interfaces (see FIG. 1.5(b)).

Stacking faults are also planar defects inside the grain. A crystal is constructed by the stacking of close-packed planes in a well defined order...ABCABC.... A stacking fault appears wherever the local stacking sequence does not obey the intrinsic order, such as ...ABCBABC... occurs with extra B plane in the middle constituting a stacking fault. In silicon stacking, faults are along (111) atomic planes. A silicon lattice may contain an extra atomic plane; this stacking fault is called extrinsic. If an atomic plane is missing, the stacking fault is intrinsic. Most stacking faults in silicon are of the extrinsic type [TIL 15].

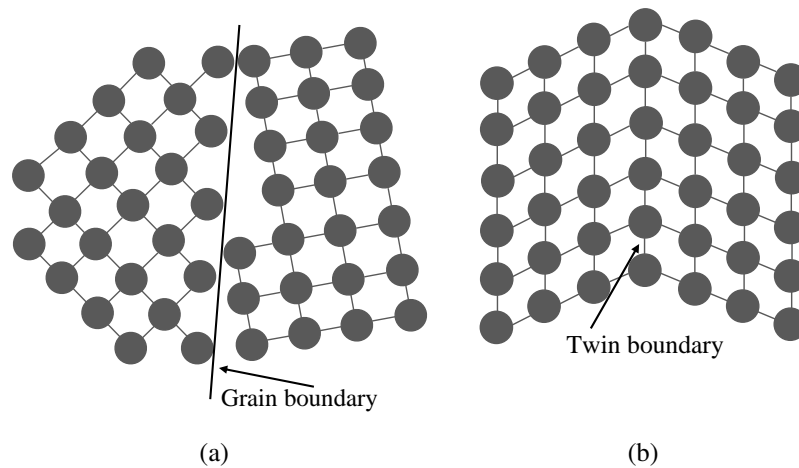


FIGURE 1.5: Surface defects in a crystal. 2D representation of grain boundary (a), and twin boundary (b).

- Volume defects

Volume defects in crystals are three-dimensional aggregates of atoms, *i.e.* precipitates or voids. In silicon, the precipitates depend on the dissolved elements during the growth. The mostly encountered precipitates are SiO_x -, SiC, Si_3N_4 [NAK 09], their characteristic size can be up to $50 \mu\text{m}$. The precipitates or voids are usually harmful for the device's performance and mechanical strength. It is why particular efforts have been (and will always be) made in order to reduce the solute atoms in silicon and then prevent the precipitates formation during the fabrication process of crystals.

3 Brittle-ductile transition

At room temperature, crystalline silicon is a fully brittle material since the dislocations are immobile because of the strong covalent forces. When the material is solicited,

the stress concentrates at crack tip locations or close to other defects and then reaches the intrinsic strength to nucleate catastrophic cracking with no appreciable plastic deformation [LAW 80]. However, when the temperature rises up to a certain value, a brittle-ductile transition (BDT) occurs. The latter has been firstly revealed in 1960s [PEA 57, PAT 63] and then received a lot of investigations [JOH 75, YON 78, SAM 89, HIR 89, BRE 92].

In order to precisely capture the BDT, the investigations were widely conducted with fracture tests [JOH 75, SAM 89, BRE 92]. When the material becomes ductile, the dislocations accommodate the high stress gradient near the crack tip and blunt the crack front [LIN 86]. Thus, the fracture strength is higher than that at room temperature. Since plastic deformation of silicon is sensitive to the loading rate (visco-plasticity), the BDT temperature depends on the applied strain rate—the greater the strain rate is, the higher the BDT, as presented in FIG. 1.6. It has been measured around 560° at a low strain rate of $1.3 \times 10^{-6}/s$, which represents $\frac{2}{3} T_m$ (melting temperature), as revealed in FIG. 1.6.

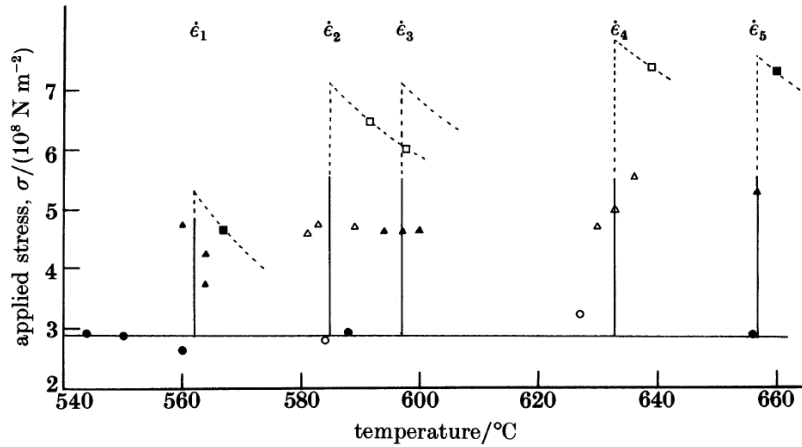


FIGURE 1.6: Dependence of BDT temperature on the applied strain rate : $\dot{\epsilon}_1=1.3 \times 10^{-6}/s$, $\dot{\epsilon}_2=2.6 \times 10^{-6}/s$, $\dot{\epsilon}_3=5.2 \times 10^{-6}/s$, $\dot{\epsilon}_4=1.3 \times 10^{-5}/s$, $\dot{\epsilon}_5=2.6 \times 10^{-5}/s$. Points marked with circles, triangles and squares correspond respectively to 'brittle', 'transition' and 'ductile' tests [SAM 89].

The BDT temperature is higher than most of service temperatures of silicon based systems, like microelectromechanical systems (MEMS) and solar cells. It means that the centerpiece of these systems (silicon) remains brittle with no room for plasticity. However, most of crystalline silicon manufacturing processes are based on the solidification of the molten silicon. During the solidification, *i.e.* temperature decreases from T_m to room temperature, any thermal stress would lead to plastic deformation so that the solid silicon undergoes more or less residual stresses as a function of the severity of the thermal stress. This plastic deformation induced residual stresses will increase the material brittleness and thus reduce the mechanical resistance.

The plastic behavior of silicon is very different from metals which manifest a single yield point. A silicon crystal involves a deficit of mobile dislocations, the initial dislocation density being on the order of magnitude of 10^8 m^{-2} [SUM 80], thus subject to an

external loading, the limited dislocation motion cannot accommodate the imposed strain rate, leading to an apparent elastic behavior until an explosive dislocation multiplication occurs which allows the relief of the flow stress and the occurrence of a yield drop (for reviews, see [ALE 69]). In this work, a series of 4-point bending tests have been carried out at elevated temperatures in order to characterize the yield drop behavior as well as the strain hardening. This part has not been completed and is presented in Appendix A.

4 Application : solar cell

Intrinsic silicon is a pure semiconductor, which is almost an insulator due to a large band gap (the energy difference between the top of the valence band and the bottom of the conduction band). In a pure semi-conductor, an entering photon with enough energy can extract an electron out of the valence band and makes it a free electron in the conduction band. This in turn leaves a positive hole in the valence band. However, no resulting electric current can be obtained since the promoted electrons and holes will recombine very soon.

When doping of intrinsic silicon impurity atoms from group III (acceptors) and group V (donors), we will get extra free holes and extra electrons, respectively, as shown in FIG. 1.7a. Correspondingly, we will get P-type (P means positive) semiconductor in which the majority carriers are holes and the minority carriers are electrons as well as N-type (N means negative) semiconductor in which the majority carriers are electrons and the minority carriers are holes. The widely used acceptors and donors are boron and phosphorus elements in solar grade silicon. When N-type and P-type layers join together, the electrons will diffuse from N-side to fill holes in P-side. Thus, positive charge begins to build on N-side and negative charge begins to set up on the P-side, forming what is termed P-N junction (see FIG. 1.7b) at the joining interface. Once the junction has fully built, a barrier will be created for the electrons moving from N-side to P-side due to the negative charge at P-side. For the same reason, the diffusion of the holes from N-side to P-side will be stopped due to the positive charge at N-side (see FIG. 1.7c).

As schematized in FIG. 1.8, when a photon promotes an electron to the conduction band at P-side, it can subsequently pass through the P-N junction into N-side instead of instantly re-combining with a hole. This is why a solar cell can generate the photo current (voltage).

A solar cell is the smallest independent unit of solar power production. It is obtained from a silicon wafer after a series of processing such as doping, metallization of the two surfaces, surface texturing and eventually encapsulation with EVA. In PV market, we have essentially two kinds of silicon wafers, mono-crystalline silicon wafers and multi-crystalline silicon wafers. Both kinds of materials are of high purity, which reaches 99.99999% or 7N (N stands for nines) [MOR 03]. The mono-crystalline Si has a better electrical performance since there are no grain boundaries, while it is much more expensive than the multi-crystalline silicon. The main drawback of the multi-crystalline Si is the presence of lattice defects such as grain boundaries, twin boundaries and sub-grain boundaries which reduce the electrical efficiency. However, because of its low

1. Basic knowledge on crystalline silicon

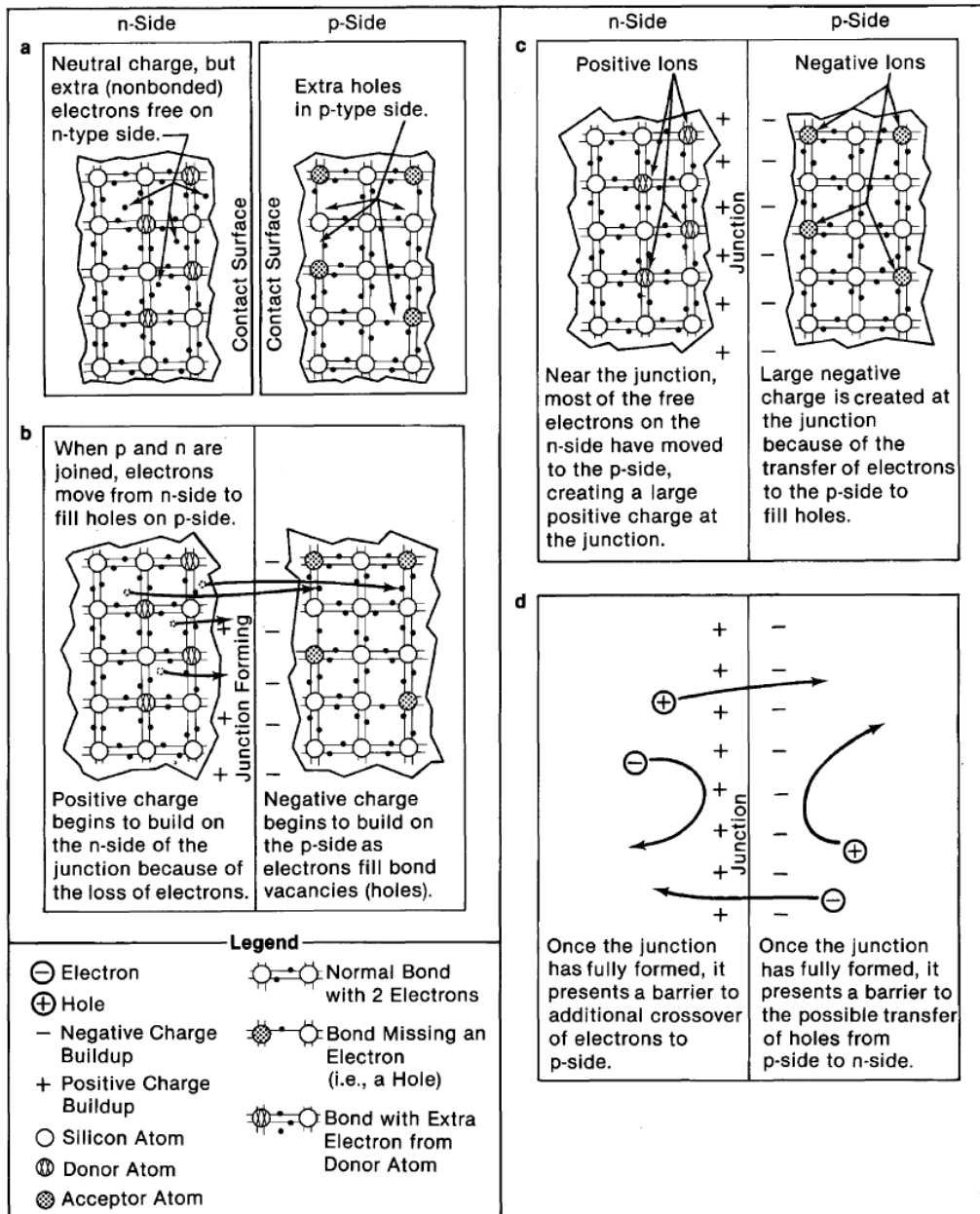


FIGURE 1.7: P-N junction formation in silicon, with intentional doping process [HER 82].

fabrication cost, the multi-crystalline silicon dominates in the PV market.

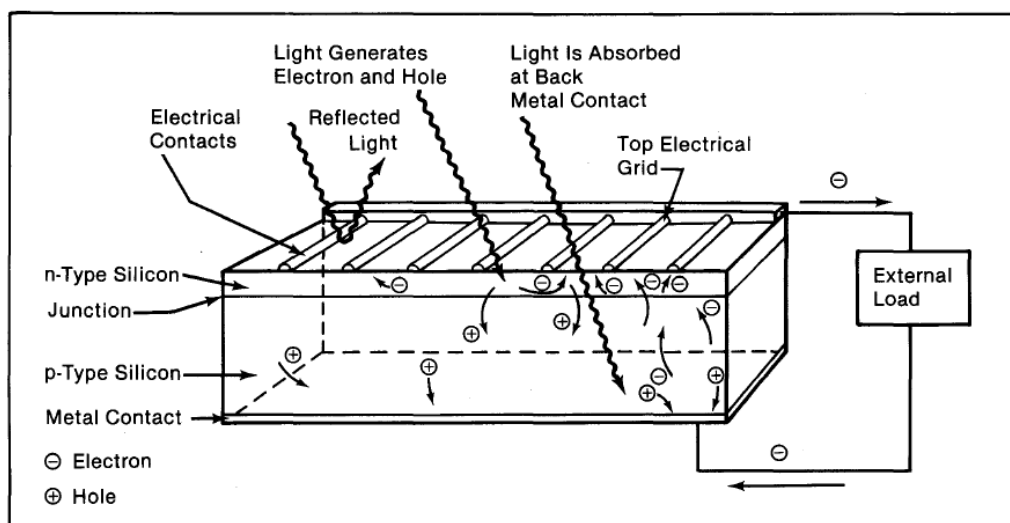


FIGURE 1.8: Schema on the solar cell function [HER 82].

5 Mechanical investigations on solar grade silicon

A comparison between a standard solar grade silicon wafer and a solar cell is illustrated in FIG. 1.9. After introducing dopants in the bulk and subsurface layer (to form P-N junction) of silicon wafer, the latter is already able to produce photo current, as presented in the last section. In order to more efficiently collect the electrons, the wafer is metallized at both surfaces, one (back side) is coated with a continuum aluminum paste, the other (front side) is covered with well spaced aluminum or silver thin conductors (called fingers). Moreover, when the solar cells are integrated in a PV module, they are interconnected with each other by larger conductors (called busbars), as can be noticed in FIG. 1.9(b). The fingers are deposited by screen printing technique, while the busbars are soldered at spaced points (see FIG. 1.9(b)). The mechanical failure of a solar cell is mainly related to brittle cracking of the center-embedded silicon wafer, given that the all around metallization material is ductile, which is more resistant than the brittle silicon against the external solicitation.

Whereas the improvement of the energetic efficiency of solar cells has captured since many years most of the efforts from the scientific community, mainly chemists and physicists, little is known about the thermo-mechanical strength and the fracture behavior of crystalline silicon plates, in itself or when embedded in a ready-for-use solar cell, under static or dynamic loading.

It should be noted firstly that crystalline silicon bulk (the case for solar grade silicon) barely undergoes fatigue problem. The cracking or microcracking occurs only when external loading instantaneously exceeds the nominal fracture strength, even in moist air and water [CHE 80, LAW 81]. However, there is much more evidence that cyclically-stressed, micronscale silicon thin films (the case for microelectromechanical systems) can crack prematurely under high-cycle fatigue loading [CON 92, MUH 01, ARS 99].

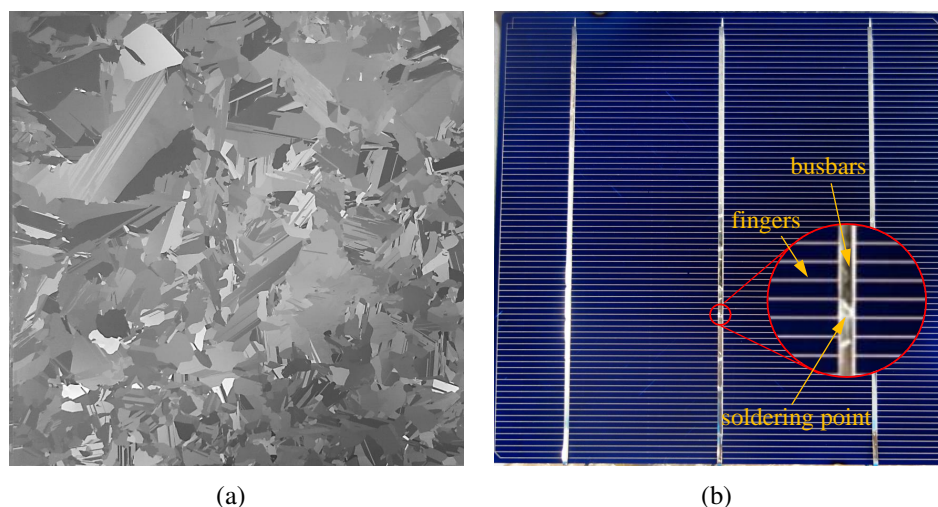


FIGURE 1.9: Solar grade silicon wafer (a), and ready-for-use unencapsulated solar cell (front side view) (b). The surface dimension is $156 \times 156 \text{ mm}^2$.

This sub-critical failure been latter been explained by the sequential formation of SiO_2 layer which is much less resistant than Si [MUH 02a, MUH 02b]. This "reaction-layer fatigue" mechanism is only significant in thin films where the critical crack size for catastrophic failure can be reached by a crack growing within extremely the tiny (nanoscale) oxide layer [MUH 02b]. This is the reason why in PV industry, the slow crack growth (fatigue) issue is not considered when evaluating the reliability of Si wafer upon design.

At the wafer scale, the former works were mainly based on Weibull distribution in order to analyze statistically the characteristic fracture strength and its scatter, relative to a given manufacturing process. Funke et al. [FUN 04] carried out biaxial tests to investigate the fracture stress of different kinds of wafers with or without chemical etching, the authors came out with distinguished critical strengths corresponding to different manufacturing and etching processes. Popovich et al. [POP 11, POP 13] highlighted, with 4-point bending tests, the effect of the crystallinity on the wafer resistance. They concluded, in addition, that the crack can propagate along the grain boundaries. Echizenya et al. [ECH 11] evaluated the bending strength of polycrystalline silicon wafers via Weibull distribution, they highlighted the dependence of the wafer strength on the slicing process, which might induce more or less micro-cracks on the wafer surface. Jagailoux et al. [JAG 16] proposed photoelasticity technique to measure the residual stress inside crystal silicon wafers, they evaluated the residual stresses induced by both crystal growth thermal gradient and the wire sawing process. The value has been found in the average of 1 to 14 MPa. Moreover, Brun and Melkote [BRU 09] elaborated a systematic approach to assess the breakage of crystalline silicon wafers via analysis of the total stress state in the wafer during handling and transport. The authors considered that the knowledge on the stress and the crack size allowed to assess the fracture initiation. But in practice, the determination of critical crack size is not straightforward and needs heavy works. Over the years,

the investigations on fracture origin are rare to see, no sophisticated method was available yet at the wafer scale. An interesting work was performed by [KLU 14] which did spot the fracture origin for as-cut single crystalline silicon wafers. However, this work was based on 3-point bending tests, where the crack would initiate underneath the contact line while the defects elsewhere were much less solicited. A more pertinent method should introduce a wide uniform deformation field so that all kinds of defects undergo the same stress.

At solar cell scale, in addition to statistical studies based on massive fracture tests, other monitoring techniques like electroluminescence were widely used to assess defects non visible to the naked eye. Blakers and Armour [BLA 09] showed, with repeated flexure, that either the solar cells broke immediately or they were unaffected by multiple flexing. This conclusion indicates that the brittle fracture in silicon is instantaneous as soon as the critical stress is reached. Meanwhile, there is no fatigue process when the load results in a smaller stress. Kajari-Schröder et al. [KAJ 11] and Köntges et al. [KÖN 11a] provided a statistic crack distribution over the solar cells in PV modules. Their analysis on the spatial distribution and orientation of micro cracks offers valuable insight into the causes of micro cracks if the PV module is subject to a uniform mechanical load. Sander et al. [SAN 13] investigated the crack pattern in encapsulated solar cells based on 4-point bending tests. The authors highlighted a dependence of the fracture strength values with the busbars orientation. The same conclusion has been obtained in [KAU 14]. Bending tests on flexible PV modules with initial cracks in silicon cells have also been performed in [PAG 14]. In that case, the role of fracture on the electric response was for the very first time monitored using the electroluminescence technique during the deformation process (for both monotonic and cyclic loading). They showed that in spite of the very brittle nature of silicon, due to action of the encapsulating polymer and residual thermo-elastic stresses, cracked regions can recover the electric conductivity when crack closure takes place upon mechanical unloading. Kohler et al. [KOH 14] performed photo- and electroluminescence analysis to locate defects such as material inhomogeneities or cracks, they observed defect clusters which seem to nucleate from large grain boundaries. Wen and Yin [WEN 12] performed electronic speckle pattern interferometry to rapidly identify cracks in PV cells. The advantage of this technique with respect to electroluminescent imaging is that it allows to distinguish between different types of cracks, such as chevron-shaped, broken electrical connections, surface cracks and through cracks. Particularly, Paggi et al. [PAG 13] proposed for the first time, a multi-physics and multi-scale computational approach to study the evolution of microcracking in polycrystalline silicon solar cells and its effect on the electric response of PV modules. In this study, only intergranular cracking was considered.

From the reviewed previous investigations, it can be noticed that there is barely any work devoted to assess the fundamental fracture mechanism in silicon in the PV community. Yet crystalline silicon manifests many particular fracture behaviors, such as in-plane fracture anisotropy on (110) cleavage plane [EBR 99, PÉR 00b], phase transformation induced crack tip blunting and the consequent crack velocity threshold [BUE 07], crack instabilities due to dopants and dislocations [SHE 08, KER 13, SHI 02]. These particu-

1. Basic knowledge on crystalline silicon

larities, as will be further mentioned in chapter 3 and 4, eventually limit the formulation of definitive explanations on the crack behavior in monocrystalline silicon with classical linear elastic fracture mechanics. Moreover, the basic knowledge of fracture mechanism of silicon can guide the modeling direction, mainly the crack propagation mode (intergranular or transgranular) and fracture path in multi-crystalline silicon wafer, especially as modeling is the research tendency in the PV community. Therefore, in this work, we focus our attention only on silicon wafer scale, and we aim to enrich the fundamental knowledge on the fracture mechanisms for both monocrystalline and multi-crystalline materials.

Chapter 2

Mechanical characterizations for solar grade silicon wafers

The rigidity and the strength of the centerpiece-embedded silicon plates, are of great importance from an economical point of view. Their reliability impacts the overall cost based on production, transportation and in-service use. The aim of this chapter is to propose a method for the Young's modulus assessment and to analyze the fracture behavior of silicon plates at room temperature. The Si plates are laser cut from two different manufacturing processes of silicon wafers, MCSi and RST. 4-point bending tests have been performed. The beam hypothesis has been used to analyze bending tests for determining the Young's modulus. A correction strategy has then been proposed with a numerical model in order to determine with a higher accuracy the mechanical data and the measurement uncertainty. For fracture investigation, high speed imaging technique and fractography have been used to identify the failure mode as well as the crack origin. The Young's modulus is found to be 166 ± 5 GPa for MCSi wafers. The anisotropic stiffness of RST plates correlates well with the micro-structural texture. Both kinds of plates fracture from the edges where some defects are located due to laser cutting.

Contents

1	Introduction	21
2	Material presentation	23
2.1	Manufacturing processes	23
2.2	Grain orientation distribution	26
2.3	Thickness variation and surface roughness	29
3	Experimental and numerical methods for determination of elastic stiffness	30
3.1	Experimental set up	30
3.2	Finite element modeling	32
3.3	Characterization of Young's modulus with relative error correction	37
4	Investigation on crack propagation mode and fracture origin	38
4.1	Crack propagation mode analysis	38
4.2	Identification of fracture origin	41
4.3	Weibull distribution	46
5	Discussion	48
5.1	Identification of the Young's modulus	48
5.2	Fracture investigation	49
6	Conclusion and remarks	50
7	Outlook	51

1 Introduction

In photovoltaic (PV) domain, innovative technologies were developed or are still under development to produce thinner or more robust silicon wafers. The characterization of the mechanical properties are of great practical interest, as the material rigidity and fracture strength are highly influenced by the crystallinity and defects induced by the manufacturing process [POP 11].

Many investigations have been carried out to characterize the stiffness of single crystalline silicon which has the diamond lattice structure. Due to the cubic symmetry of the atom arrangements of the crystal structure, the material owns only three independent parameters C_{11} , C_{12} , and C_{44} in the crystallographic coordinate system of principal axes $\langle 100 \rangle$, $\langle 010 \rangle$, and $\langle 001 \rangle$. At room temperature (298 K) and ambient pressure (1 bar), the measurements that are considered as the most accurate in the literature were reported by [HAL 67] thanks to sound-velocity measurements, as recalled below :

$$\underline{\underline{C}} = \begin{pmatrix} 165.7 & 63.9 & 63.9 & & & \\ 63.9 & 165.7 & 63.9 & & & \\ 63.9 & 63.94 & 165.7 & & & \\ & & & 79.6 & & \\ & & & & 79.6 & \\ & & & & & 79.6 \end{pmatrix} (GPa)$$

It can be deduced that the smallest value of Young's modulus is 130 GPa (along a $[100]$ direction) and the greatest is 188 GPa (along a $[111]$ direction).

For silicon wafer owning three axes in $\langle 110 \rangle$, $\langle -110 \rangle$, and $\langle 001 \rangle$ directions¹, the expression of the elastic constants can easily be inferred by a rotation of 45° around the $\langle 001 \rangle$ axis, as presented in the below elasticity matrix. Along a $[110]$ direction, the rigidity is 169 GPa. It should be noted that doping quantitatively modifies elastic constants by 1 to 3% [GAN 15].

$$\underline{\underline{C}} = \begin{pmatrix} 194.5 & 35.7 & 64.1 & & & \\ 35.7 & 194.5 & 64.1 & & & \\ 64.1 & 64.1 & 165.7 & & & \\ & & & 79.51 & & \\ & & & & 79.51 & \\ & & & & & 50.9 \end{pmatrix} (GPa)$$

As an aggregate of multiple silicon single crystals separated by grain boundaries, the multi-crystalline silicon owns theoretically an intermediate value of Young's modulus between 130 GPa and 188 GPa. The rigidity depends mainly on the distribution of crystallographic orientations of the grains, but it can also be influenced by the density and

1. The orientation of the single crystalline silicon plate used for finite element model validation, see section 3.2.1

the cohesion of the grain boundaries. If the average grain size is negligible compared to the dimensions of the studied structure, the multi-crystal without texture can be homogenized into an isotropic material with only two parameters, the Young's modulus and the Poisson's ratio. The homogenization can be well applied for poly-crystalline silicon used for MEMS systems because of the nanometric to micrometric grain size, the appropriate properties were given by [Sha 01b] ($E=160$ GPa; $\nu=0.2$). For PV grade multi-crystalline silicon, characterization works were not affluent in the literature. An analytical calculation was performed over a representative volume element and gave $E=162.5$ GPa; $\nu=0.223$ [FUN 04]. However, these results are considered unreliable for our studied wafers, since the typical grain size of the latter has almost the same order of magnitude as the specimen's dimension. Furthermore, when a specific texture exists, the characterization should account for the loading direction (bending axis here).

Generally, failure initiates mostly from defects such as impurities and pre-existing cracks that act as local stress risers. For solar grade silicon, the strength should be free of size effect², as the grains are in centimeter range which exceeds the size effect threshold of $30\ \mu\text{m}$ reported by [BRO 03]. It has been shown in the literature that the strength of defect-free single crystalline silicon ranges between 5 and 7 GPa [KOZ 07, KOZ 10], which is much higher than that of MCSi wafers, which is generally below 1 GPa [FUN 04]. The commonly recognized fracture causes in silicon wafer are subsurface micro-cracks generated by wire sawing, as discussed by [MÖL 05, WU 13] (see FIG. 2.1) and spotted in [KLU 14]. The grain boundaries have particularly been put into question in [POP 13, POP 11], since the authors highlighted some cracks propagating along the grain boundaries and they supposed that the latter reduce the overall fracture strength³. Inclusions can also be critical fracture origins, as Si-C particles are frequently found in silicon ingots. These particles have sharp edges, and may be very large – up to $50\ \mu\text{m}$ or even more [SØI 04] (see FIG. 2.1(b)). Moreover, other defects induced by alternative cutting processes, such as the laser cutting, are less studied. Sudani et al. [SUD 09] investigated the strength of silicon dice with respect to different cutting parameters like repetition rate and pulsewidth, they found that the material resistance increases with increase of repetition rate while decrease of pulsewidth.

In this chapter, we are focusing on the mechanical strength of Si plates stemming from two different silicon wafer manufacturing processes, *i.e.* classical sawing of multi-crystalline silicon produced by the ingot cast process (called MCSi) and Ribbon on Sacrificial Template process (called RST [De 12] (see section 2.1). The objective is to characterize the stiffness and to analyze the fracture behavior of these two kinds of plates at room temperature. 4-point bending tests were used for the overall study. Concerning the rigidity, we applied the beam theory to calculate the Young's modulus. A Finite Element (FE) model was used in order to better analyze experimental data - with a correction procedure - and assess the overall rigidity with numerical simulations. Regarding the fracture behavior, high speed imaging technique and fractography were combined to explore the

2. Size effect here means the dependence of the mechanical strength on the grain size

3. We discuss the results of [POP 13, POP 11] more in detail in chapter 4, where it will be shown that these works lack fairness

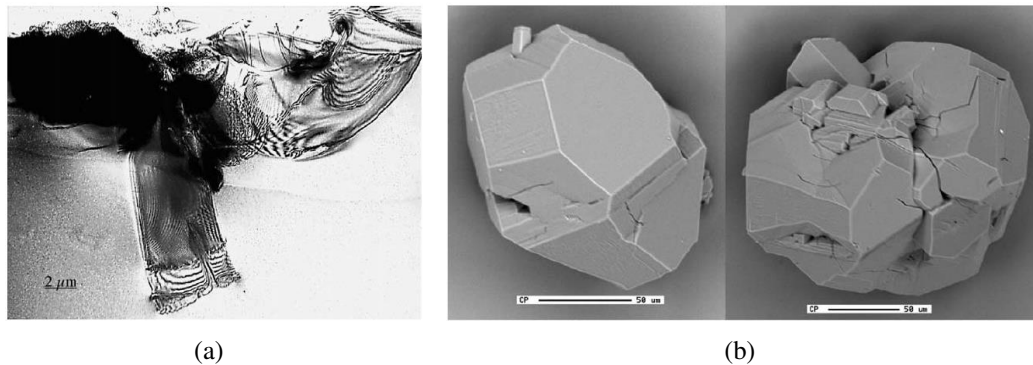


FIGURE 2.1: Commonly recognized fracture causes in silicon wafer. The wire sawing induced micro-cracks as revealed by [MÖL 05] (a), and the inclusion cluster as shown in [SØI 04] (b).

fracture modes and sources.

The second section of the chapter describes in details the materials, their fabrication and the induced micro-structures. A third section is dedicated to the experimental and numerical methods for the characterization of the elastic stiffness. In the fourth section, the investigations on the crack propagation mode as well as the fracture origin are addressed. The fifth part presents a discussion on the results, followed by the conclusions and outlook.

2 Material presentation

As mentioned in the introduction, the specimens come from two different manufacturing processes, MCSi and RST. Both types of plates are laser cut from silicon wafers to obtain a square shape of size $50 \times 50 \text{ mm}^2$. The RST plates are thinner (90 μm thick) than the MCSi plates (170 μm thick). The following paragraphs describe the two different manufacturing processes and the corresponding micro-structures. Moreover, single crystalline silicon was used as reference in the investigation, the manufacturing process is also presented in section 2.1.

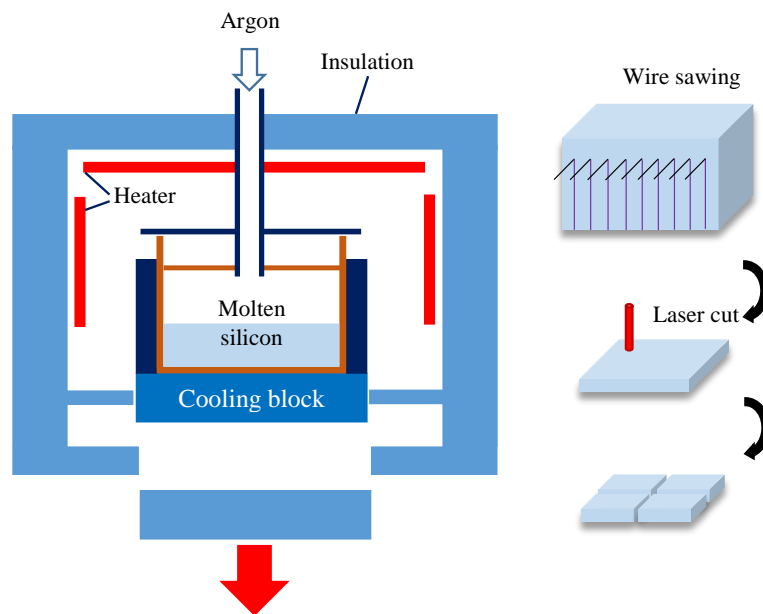
2.1 Manufacturing processes

- MCSi ingot cast

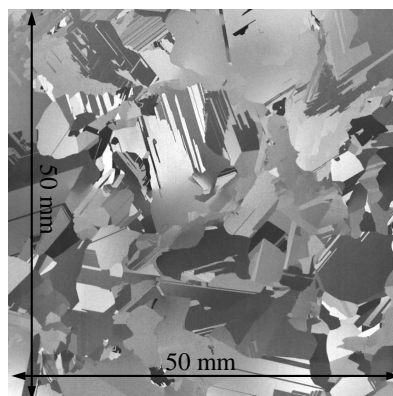
The MCSi manufacturing process is based on the solidification of molten silicon into ingot cast. As presented in FIG. 2.2(a), the crystal growth is controlled in a heated furnace where inert gas (argon) is injected in the crucible to guarantee an oxygen-free environment. After solidification, the ingot can be removed out of the furnace through the bottom opening. The ingot is then sawed into circular slices over the desired thickness. Wire sawing ensures good flatness (see FIG. 2.7) to the

2. Mechanical characterizations for solar grade silicon wafers

wafer, while the material loss is important due to the wire width. The latter is finally laser cut to get the final plate shape and size. The characteristic grain shapes are presented in FIG. 2.2(b). Most grains are centimeter wide, which can be compared to the plate thickness ($170\mu\text{m}$ for MCSi specimens). The grain boundaries are visible to naked eye. It reveals that the grain shape is mostly polygonal with a random distribution. In addition, twins can be distinguished by light reflection contrast in many grains. They are parallel to one another within a grain but their orientation differs from grain to grain, which is a characteristic feature of grain disorientation.



(a)

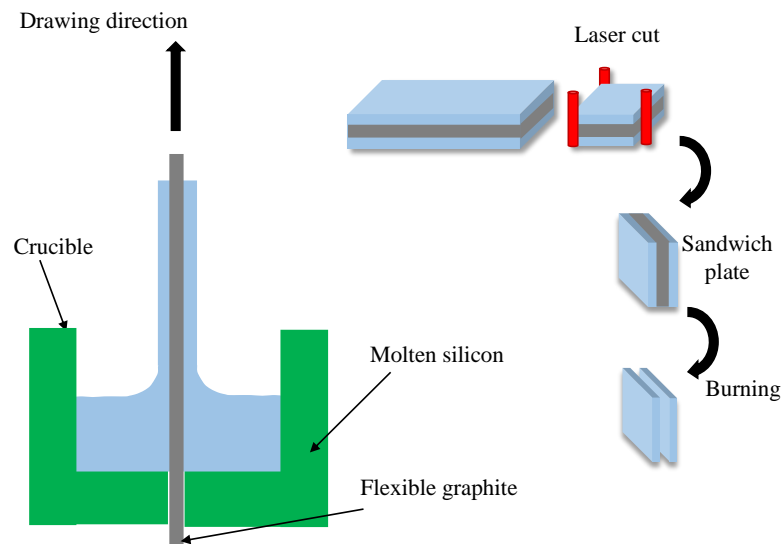


(b)

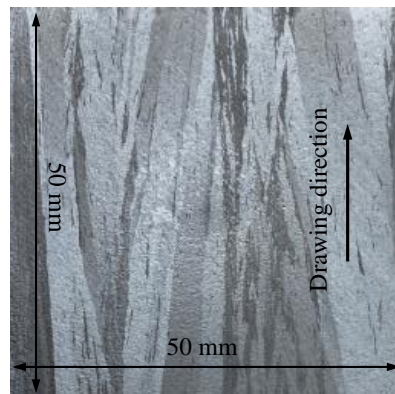
FIGURE 2.2: MCSi specimens manufacturing process (a) and a look at the representative grain shapes (specimen size : $50 \times 50 \times 0.17 \text{ mm}^3$) (b).

- RST crystal growth

RST manufacturing process aims at producing thinner silicon wafers in order to reduce the global cost of PV modules. Even if the process principle was proposed a few decades ago, the process has been mainly developed in recent years by the french company SOLARFORCE [De 12].



(a)



(b)

FIGURE 2.3: RST specimens manufacturing process (a) and a look at the representative grain shapes (specimen size : $50 \times 50 \times 0.09 \text{ mm}^3$) (b).

As shown in FIG. 2.3(a), this kind of wafers are obtained by drawing a graphite ribbon through a crucible of molten silicon. The latter continuously solidifies on the two sides of the ribbon when it comes out of the crucible. A thin layer of pyrocarbon prevents the formation of Si-C precipitates during solidification at the interface with the ribbon. Thus, a kind of "sandwich" ribbon composed of silicon-carbon-silicon is formed. The layered ribbon is then laser cut, simultaneously on the two faces to

obtain the desired dimensions. In the following step, the carbon substrate is removed by heating the tri-plate to around 1000 °C in an oxygen environment. The obtained silicon layer is finally scoured to get the RST plate as shown in FIG. 2.3(b).

Due to the drawing effect, the grains have a predominant dimension in the drawing direction (with a length larger than 50mm, and a width lower than 6mm, see FIG. 2.3(b)). Even if the sample surface has the appearance of orange peel, one can easily observe that some grains have numerous twins, covering the entire surface of the grain.

- Single crystalline silicon wafer

We precisely know the material stiffness and the crack path, so the single crystal can be used to validate the experimental set up and numerical modeling. The used wafers come from the Czochralski (Cz) [CZO 18] process. As shown in the left part of FIG. 2.4(a), the Cz process consists in withdrawing a crystal seed (monocrystalline silicon) that was inserted in the melton silicon. The solidification in contact with the seed leads to the same crystallographic orientation of the silicon cylinder with the seed. The solid cylinder is then sliced into thin silicon wafers with the wire sawing technique. The thickness is around 190 μm . The surface dimension, 50×50 mm² silicon plates is ensured by (110) cleavage (no laser cutting is involved). The sample and the crystal orientation is shown in FIG. 2.4(b), we have two [110] in plane directions and a [001] normal direction.

2.2 Grain orientation distribution

- MCSi orientation distribution

Laue X-ray diffraction was carried out on a MCSi standard wafer (156×156 mm²). The color coded map is presented in FIG. 2.5(a). Correspondingly, the {110} and {111} pole figures are plotted with respect to the specimen's coordinate system, *i.e.* normal direction (ND), rolling direction (RD) and transverse direction (TD) (see FIG. 2.5(b) and FIG. 2.5(c)). 60 grains have been considered in the pole figures, their projection points indicate that the grain orientation distribution is random.

- RST orientation distribution

From the elongated grain shape, one can assume an inherent texture due to the drawing effect. Thus, EBSD (Electron backscatter diffraction) measurements were performed to investigate the crystallographic orientations of the RST grains. The analyzed area was the central part of the plate surface that measures 5×1mm². An example of the EBSD color coded map and corresponding inverse pole figure (see Appendix C for (inverse) pole figure definition) are shown in FIG. 2.6. The color coded point clusters shown in the triangle next to the map represent the drawing direction (Y direction in the map) drawn in the crystallographic axis pole figures of all the studied grains. Thus, by looking at a green grain, it means that the drawing

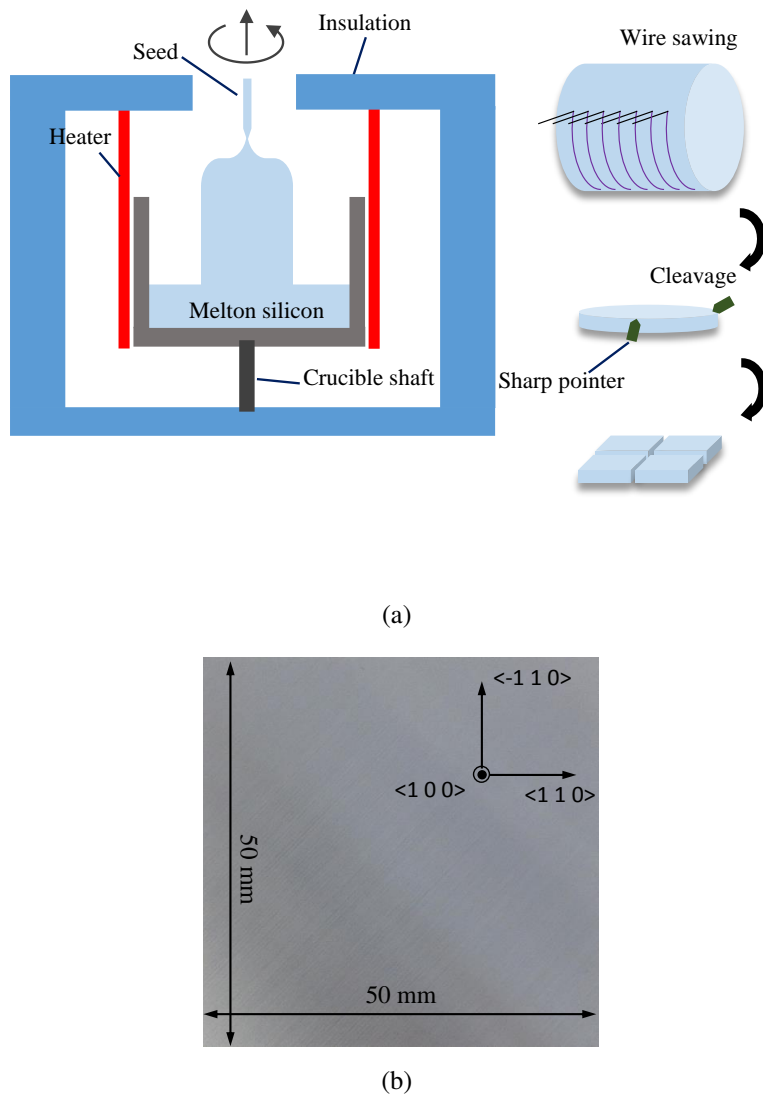


FIGURE 2.4: Single crystalline specimens manufacturing process (a) and a look at the representative specimen (specimen size : $50 \times 50 \times 0.19 \text{ mm}^3$) (b).

direction aligns with a $[110]$ crystallographic direction of the grain, since the green points are close to the $[101]$ pole (see the inverse pole figure in FIG. 2.6). Interestingly, the green grains are quite dominant in the map (around 70%), which highlights a crystallographic texture such that the $[110]$ directions of the grains of a RST plate is primarily parallel to the drawing direction.

The presence of the texture necessitates a directional characterization of the mechanical properties. The global homogenization should not be applied. Moreover, along the drawing direction, the Young's modulus is expected to be around 169 GPa (the value in $[110]$ direction, as mentioned in the introduction of this chapter). Ex-

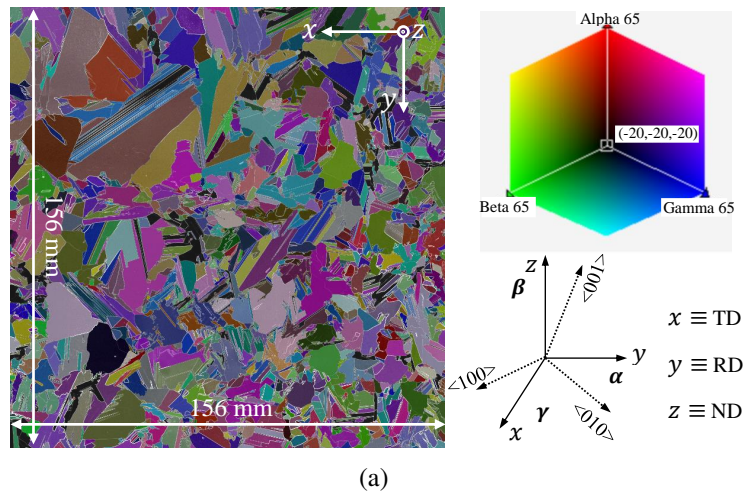


FIGURE 2.5: MCSi grain orientation distribution. Color coded map of the grain orientations measured by the Laue X-ray diffraction on a standard wafer (a) and pole figures over one part of the wafer (containing 60 grains) for 011 directions (b) and 111 directions (c).

perimentally, two test configurations will be investigated, the first one with then bending axis parallel to the grain orientation and the second perpendicular.

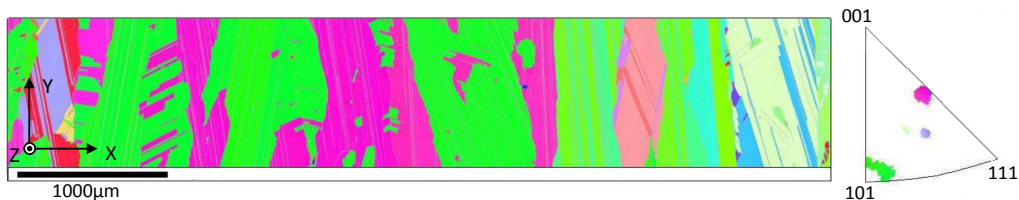


FIGURE 2.6: RST grain orientation distribution. Color coded map (left) where Y corresponds to the drawing direction. Inverse pole figure (right),

2.3 Thickness variation and surface roughness

The thickness variation was investigated thanks to a con-focal optical microscope (Keyence VHX-2000). The thickness measurements were conducted every 0.5 mm along the plate edge for MCSi and RST specimens. Conversely, for mono-crystalline silicon plate, the resolution is 2 mm since the thickness profile is very uniform (see FIG. 2.7). The surface roughness assessment was carried out with a 3D micro coordinate measurement machine Alicona InfiniteFocus (IFM G4 3.5) and the results are presented in FIG. 2.8.

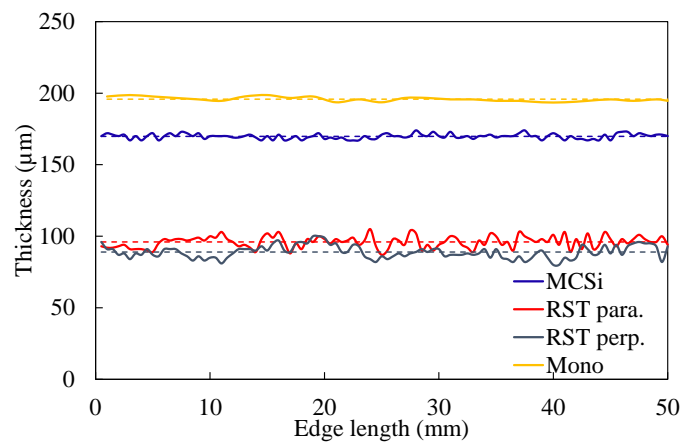


FIGURE 2.7: Thickness variation of the studied silicon plates investigated by optical microscopy. Para. signifies the direction parallel to the drawing direction, perp. stands for the direction perpendicular to the drawing direction, mono represents mono-crystalline silicon.

Generally, silicon wafers used for PV modules have small thickness, to lower the cost. In this work, the studied RST plates are almost 2 times thinner than MCSi plates and Mono-crystalline silicon plates. Meanwhile, the RST manufacturing process leads to more significant thickness variation (see FIG. 2.7) and surface roughness (see FIG. 2.8) compared to the wire sawing process. The relatively large thickness variation and the surface roughness of RST plates are probably due to the poor surface state of the graphite ribbons.

Since the thickness variation is not monotonously increasing nor decreasing along the plate length and width, the characterization method—based on 4 point-point bending tests and beam theory is applicable in this work (see section 3).

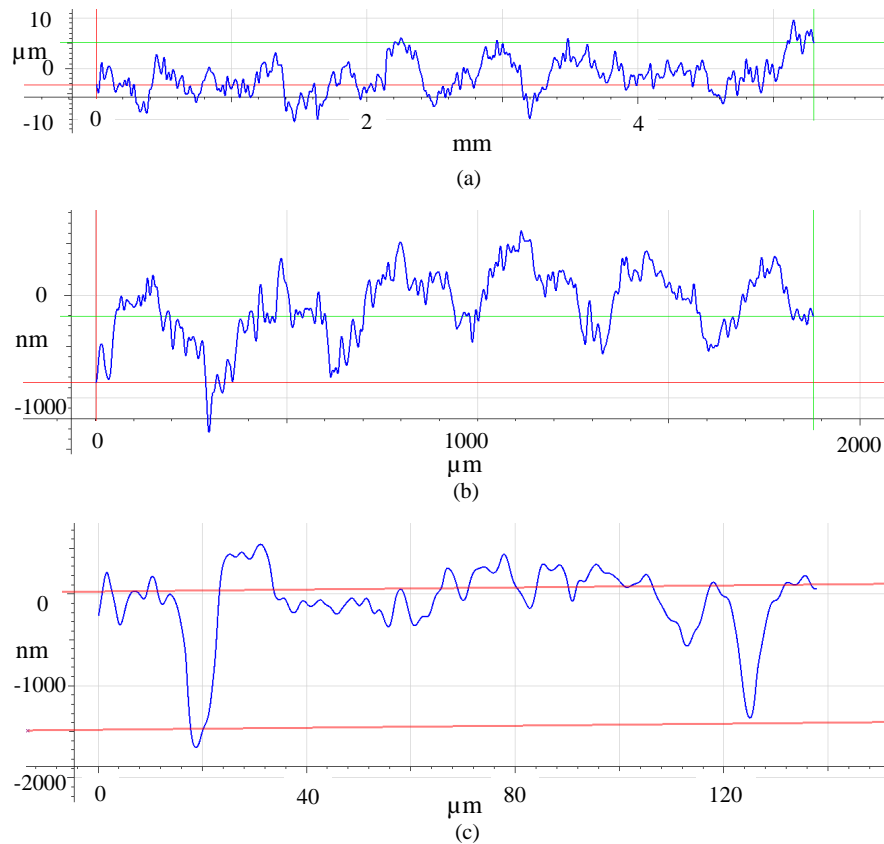


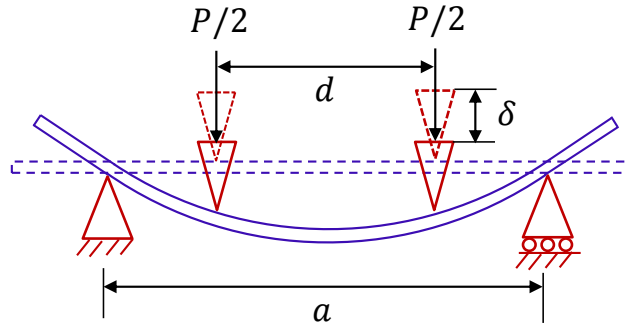
FIGURE 2.8: Surface roughness of the three kinds of silicon plates. RST plates (a), MCSi plates (b) and single crystalline silicon plates (c).

3 Experimental and numerical methods for determination of elastic stiffness

3.1 Experimental set up

Since the studied material is brittle at room temperature and the thickness of the specimen is small, tensile tests are very difficult to perform. Conversely, bending tests are very appropriate for thin and brittle specimens and therefore have been often used in the literature for thin silicon specimens [POP 11, KLU 14]. Moreover, Young's modulus and fracture stress can be easily calculated from the force-deflection relationship by beam theory.

In this study, a 4-point bending test bench – as shown schematically in FIG. 2.9 – has been preferred to 3-point bending configuration in order to have a large area of uniform mechanical state, which is in accordance with the recommendation of [AST]. In FIG. 2.9, P represents the punch load force, a and d indicate the inner and outer spans, δ stands for the load cell displacement, which is also the plate deflection under the punch rollers. The


FIGURE 2.9: 4-point bending test

parameters of our experimental set up are given in TAB. 2.1. The outer and inner spans correlate well with the recommendations of [AST], while the suggestion for the punch roller radius (approximately 1.5 times the specimen thickness) is not practical in our case. The punch and support rollers are in steel, and of low roughness to avoid local stress concentration at the contact interfaces.

The tests were performed at constant punch velocity with a LLOYD-Ametek LFPLUS electro-mechanical machine. The cross-head moving down rate was 0.2mm/min, it means a strain rate in the order of $10^{-6}s^{-1}$ and thus a quasi-static loading. An integrated displacement sensor provided in real time the punch displacement, and an external force sensor with a capacity of 10N measured the reaction force on the punch. Thus, a force-deflection ($P; \delta$) curve could be drawn after each test.

TABLE 2.1: Parameters of experimental set up (mm)

Outer span	Inner span	Punch roller radius
$a=40$	$d=21$	$r=3$

The expressions for the maximum tensile strain and stress as a function of the load force, the deflection, the plate dimensions and contact spans were given by [BRU 62] as listed below :

$$\epsilon_{max} = \frac{6h\delta}{(a-d)(a+2d)} \quad (2.1)$$

$$\sigma_{max} = \frac{3P(a-d)}{2bh^2} \quad (2.2)$$

where b denotes the width of the specimen along the transverse direction and h the thickness.

It yields, for the Young's modulus,

$$E = \frac{P(a-d)^2(a+2d)}{4bh^3\delta} \quad (2.3)$$

Our characterization work was based on EQ. 2.3. It should be noted that the beam theory is simplistic. It relies on the assumption that the material is homogeneous and isotropic and not subjected to geometric non-linearity. The Poisson's effect is not taken into account. Moreover, the contact is assumed to be perfect and invariant. Thus, the results obtained with EQ. 2.3 should be used with caution. To ensure the validity of our measurements and correct them if necessary, a finite element (FE) model was elaborated and parametric simulations were performed, which will be addressed in Section 3.2.

According to the material presentation section (Section 2), the grain shape of a MCSi plate is quite random (see FIG. 2.2(b)), the grain orientations manifest in addition a random distribution (see FIG. 2.5). Due to the manufacturing process, the RST plates have elongated grains along the drawing direction (see FIG. 2.3(b)), and preliminary EBSD measurements revealed a texture (see FIG. 2.6). Thus, directional characterization was taken into account by considering the Young's modulus along the drawing direction different from the one along the perpendicular direction.

3.2 Finite element modeling

A parametric finite element model was elaborated using the commercial FE package Abaqus V6.13 in order to reproduce more faithfully the bending tests. To have a parametric numerical set up and automatic silicon plate modeling, a Matlab code was developed and coupled to an Abaqus script (see FIG. 2.10), so that the plate thickness, the grain shape and orientation could be considered in different ways and easily modified. Three configurations were considered, one for MCSi and two for RST depending on the grain orientations that could be either longitudinal or transverse, as shown in FIG. 2.11. The microstructure of the material could be taken into account. The grain boundaries are assumed as perfect interfaces and the twins are not considered in this study. For the MCSi micro-structure, the grain boundaries were generated with 2D Voronoi tessellation assuming that the modeled grains in the MCSi plates have random polygonal shapes and that they have more or less the same characteristic size (see FIG. 2.11(a) and 2.11(b)). The grain determination is performed as following : firstly, a set of points were obtained at the centers of the squares that equally partitioned the plate surface, then a moderate random deviation (between 0 and 40% of the square length) was applied to each point to get the Voronoi seeds, finally the plate surface was partitioned into the Voronoi cells with these seeds. For the RST plates, the grains were modeled by an assembly of adjacent rectangles of same width, which were representative for the real grain shapes (see FIG. 2.3(b)). In terms of Voronoi modeling, it consists in providing one row of equidistant control points. Based on parametric studies, many numerical simulations were carried out to evaluate the influence of each parameter.

Triangular continuum shell elements with 6 nodes (SC6R) have been used to mesh the plate. This family of elements was considered suitable for our application since the

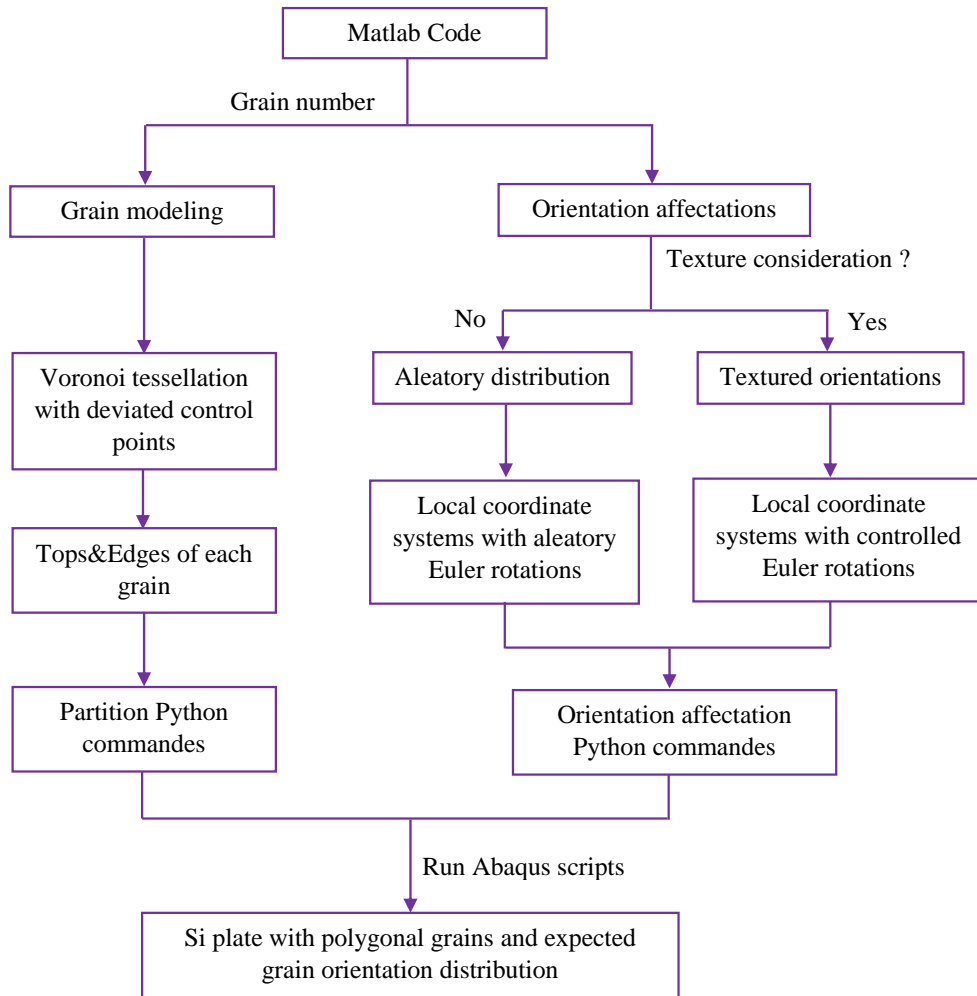


FIGURE 2.10: Parametric modeling assisted by Matlab code

continuum shell wedge performs very well in bending and permits to ensure a uniform mesh for any grain with a random shape. The element size was such that the plate edge was covered by about 150 elements with 4 layers of elements in the thickness. The material orientations associated to these elements, which are also the crystallographic orientations, could be chosen in a random manner or associated with a micro-structural texture (see FIG. 2.10).

In this numerical study, no locking pathology has been encountered, mostly due to the fact that a well refined mesh has been used, as well as 4 layers of elements in the thickness, and a moderate flexural deflection applied in the simulations. Nevertheless it could become a non-negligible issue when modeling solar cell plates embedded in multi-layered polymeric structures. A relevant strategy is the use of solid shell finite elements with enhanced assumed strain (EAS) and assumed natural strain (ANS) techniques [CAR 08].

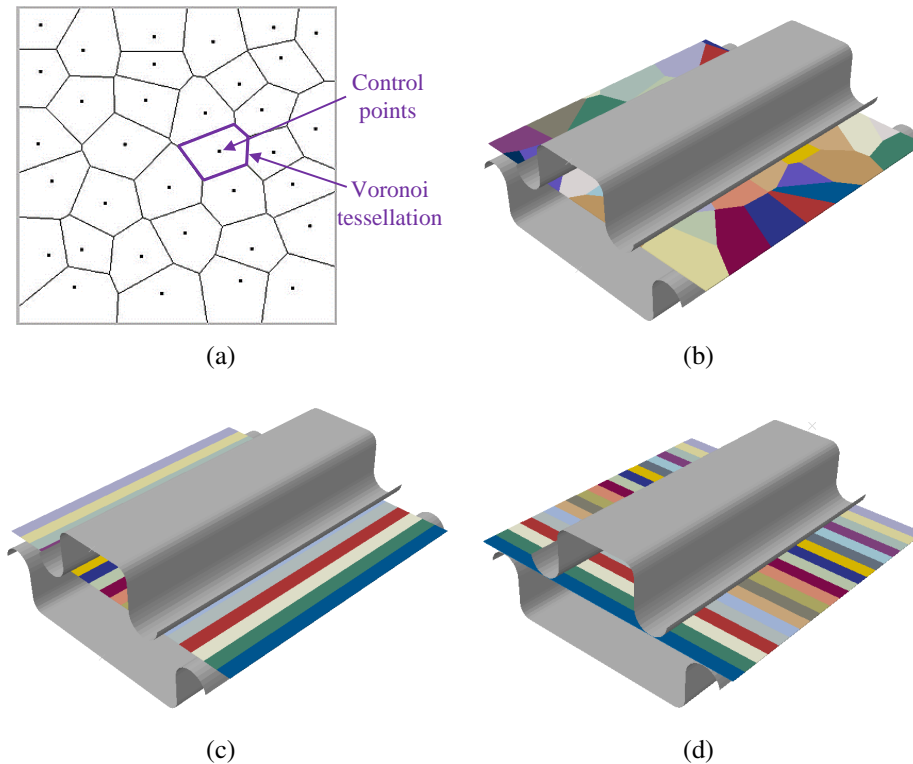


FIGURE 2.11: The modeling of MCsi and RST plates in FE analysis. Voronoi tessellation method (a), MCSi modeling with Voronoi tessellation (b) and RST modeling with long strips for the two loading configurations, longitudinal (c) and transverse (d).

They are indeed required to model the solar cell plate embedded in PV modules [PAG 16] or for solar cells bonded to substrates for flexible electronics [REI 16]. In those applications, large displacements occur due to the much higher flexibility of the system caused by the surrounding polymer.

The simulations were conducted by a static analysis (Abaqus standard) with finite deformation. Particularly, the normal contact between the Si plate and the bending set up was established using penalty algorithm. The loading was quite similar to the experimental solicitation, that is the support being blocked, the punch, having only up down moving mobility, descended and pressed the modeled silicon plate.

3.2.1 Model validation with mono-crystalline wafer

As a first step, a plate cut from the standard single crystal PV wafer along the cleavage planes (110) was considered. The crystallographic directions with respect to the plate structure are shown in FIG. 2.4(b). This plate was tested experimentally and simulated thanks to the FE model. For the simulations, the elastic properties of the plate corresponded to the second elastic stiffness tensor presented in the introduction of this chapter (Section 1). A friction coefficient of 0.15 was used at the interfaces between the

plate and the rollers, which represents well the frictional contact between steel and silicon [YAN 08]. FIG. 2.12 shows the force-deflection curves for a $193\mu\text{m}$ thick plate obtained by FE simulation (red plain line) and experiment (blue dotted line). The excellent agreement found here for the single crystal Si specimen permits to validate both the model and the experimental procedure (for experimental framework, the force and displacement given by the corresponding sensors are correct).

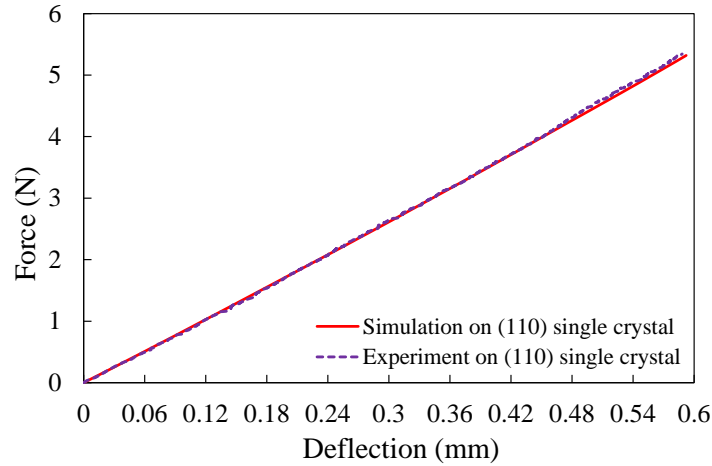


FIGURE 2.12: Comparison of numerical and experimental force-deflection curves on a $193\mu\text{m}$ thick single crystalline wafer under 4-point bending

3.2.2 Correction of the analytical solution based on the beam theory

In a second step, some preliminary calculations were performed in order to assess the relative error due to the identification of the Young's modulus using the beam theory *i.e.* when neglecting the Poisson's effect and the contact interactions. A bending simulation for a homogeneous isotropic plate with a Young's modulus of 160 GPa and a Poisson's ratio of 0.2 was performed. The plate thickness was chosen as equal to $175\mu\text{m}$. The numerical force-deflection curve in the range $[0.1 - 0.3]$ mm was extracted to assess the Young's modulus with EQ. 2.3. The calculated value is 174.4 GPa, which points out an overestimation of 9% in the experimental characterization when the analytical calculation is performed.

The advantage for extracting a deflection interval instead of a force one is that the relative error remains almost the same for a large range of plate thickness, as presented in FIG. 2.13(a). This is of great practical interest in this study since the RST plates are much thinner than the MCSi plates and for both kinds, the thicknesses of the plates differs from one another. When this correction strategy was applied on the experimental curve in FIG. 2.12, the deduced Young's modulus was 170 GPa, which was extremely close to the theoretical value of 169 GPa. It should be noted that, for any other displacement range such as $[0.4 - 0.6]$ mm, the resulted relative error will be a little more important (16% v.s.

9%), but the correlation conducts to the same results finally since EQ. 2.3 gives bigger value before correction.

The friction coefficient initially used was 0.15. In order to assess the influence of the friction coefficient on the simulation results, we varied this parameter from 0.1 to 0.3 with an increment of 0.025. The range [0.1 – 0.3] (here for friction coefficient, to be differentiated from the deflection range) was also used in the simulations of [FUN 04]. The thickness and the material properties of the plate were the same as in the previous paragraph. From FIG. 2.13(b), it can be noticed that the friction coefficient has a weak effect on the relative error, with a value ranging from 8.5 to 10%. Therefore, the relative error of 9% will be used later for correcting the experimental characterization.

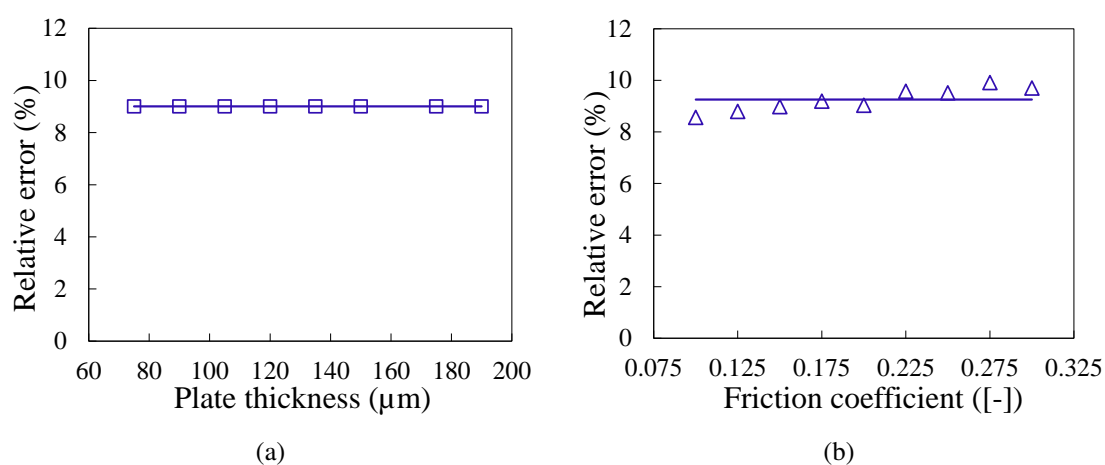


FIGURE 2.13: Relative error determination based on [0.1 – 0.3] mm deflection interval for stiffness calculation. Influence of the plate thicknesses (a) and influence of the friction coefficient (b). The straight lines denote the average of the assessed relative errors.

3.2.3 Numerical characterization of Young’s modulus

Finally, several parametric studies were carried out for heterogeneous Si plates in order to assess the equivalent Young’s modulus from a numerical point of view. In the simulations, each grain was assigned a local coordinate system (the grain orientation), and in such local coordinate system, the cubic crystal elasticity was applied. For MCSi kind, the plate contained 49 grains (see FIG. 2.11(b)), which is representative of a real plate (see FIG. 2.2(b)), when the twins are not considered. For RST kind, the plate contained 20 rectangular grains (see FIG. 2.11(c)), which also corresponded to the typical specimen (see FIG. 2.3(b)). The simulations were performed with the same grain geometry and distribution but with different grain orientations. Regarding the orientations, random distribution was selected for MCSi kind. Conversely, artificial texture compatible with the EBSD measurements was considered for RST kind (see Section 2). As one can notice in FIG. 2.6, about 70% of the grains have [110] directions parallel to the drawing direction.

This particular orientation distribution for FE model was achieved with a Matlab code. It firstly consisted in finding out all the possible Euler angles triplets that allowed the parallelism (by 5°) between the $[110]$ direction and the drawing direction : three loops were launched to cover the three Euler angles every 1° from 0 to 360° , if the parallelism was verified with one triplet, the latter would be saved. Upon defining the orientation for a grain, a random selection among the obtained triplets was carried out if the grain was associated with the texture. Otherwise, a random orientation was affected to the 30% of the grains that remain. A representative orientation distribution for numerical RST plate is highlighted in FIG. 2.14. The green and blue axes denote the drawing direction and the perpendicular direction, respectively. The RD inverse pole figure gives insight to the texture with the stereographic projections localized by the $[110]$ top. However, the TD inverse pole figure reveals a scattered projection pattern, which means that there is no privileged crystallographic axis in the perpendicular direction.

For uniformity, the numerical assessment of the global Young's modulus was also carried out with the beam theory applied to the numerical force-deflection curve. All the obtained results were then corrected with the determined relative error.

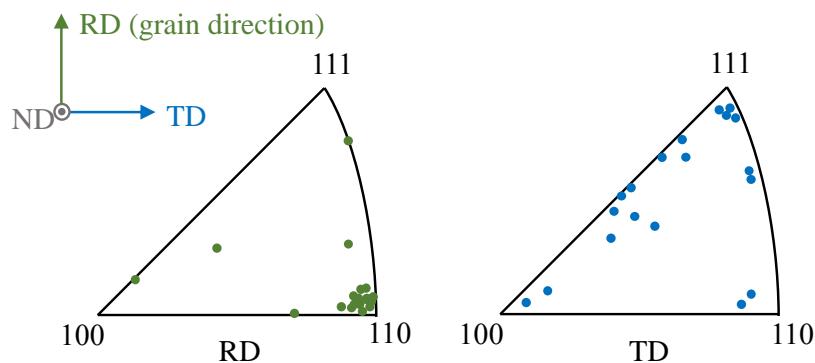


FIGURE 2.14: Artificial texture of RST plates for the stiffness characterization using the FE model : inverse pole figure for the grain direction (RD) and inverse pole figure for the perpendicular direction (TD)

3.3 Characterization of Young's modulus with relative error correction

Three representative experimental stress-strain curves for the lower surface (in tension) in the inner span region are displayed and compared with three numerical ones in FIG. 2.15. The experimental and numerical results match well till the fracture. The sharp drop is characteristic of the brittle nature of the material. It can be noted that the two curves for the MCSi plate and the RST plate with grains parallel to the punch rollers manifest very close slopes, *i.e.* similar Young's modulus. However, the slope of the curve

for the RST plate in the other loading direction is more important, which reveals a higher stiffness.

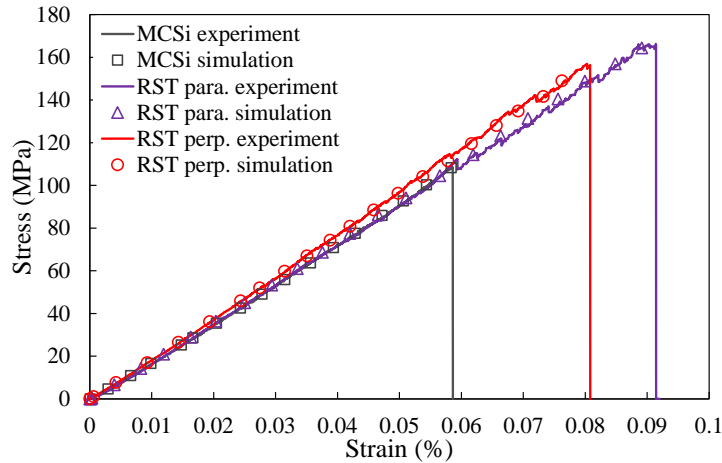


FIGURE 2.15: Representative experimental and numerical stress-strain curves for MCSi and RST plates

- Elasticity of MCSi plates

From the experimental characterization combined with the correction based on the preliminary FE analysis, the equivalent Young's modulus of the MCSi silicon wafer when averaged as homogeneous and isotropic material is 166 ± 5 GPa. Full FE simulations result in an equivalent Young's modulus of 163 ± 2 GPa, which is in good agreement with the experimental determination.

- Elasticity of RST plates

The experimental characterization leads to an equivalent Young's modulus of 172 ± 4 GPa along the drawing direction and 163 ± 6 GPa in perpendicular direction. The corresponding simulations result in an equivalent Young's modulus of 171 ± 3 GPa and 164 ± 3 GPa in the two directions, which match well the experimental results. The difference between the two directions in both experimental and numerical assessments reveal an anisotropy of the RST plates, which correlates with the preliminary EBSD measurements.

4 Investigation on crack propagation mode and fracture origin

4.1 Crack propagation mode analysis

The crack propagation velocity in a silicon single crystal can be higher than 3000 m/s. In literature, we can find 2300 ± 300 m/s and 3300 m/s by [HAU 99] and [SHE 03a],

respectively. For solar grade silicon plates, as the grains are visible to the naked eye, it is possible to determine the propagation mode of the crack in the experiments, as long as the crack pattern can be captured by an imaging device. Otherwise, fractography would be conducted for a definitive determination.

In our 4-point bending framework, a high speed imaging device was used in order to track the cracking process. Since it was impossible to set up the high speed camera below the plate, a tilted mirror (with 45 deg inclination from the plate surface) was put between the two outer supports (cylinders). The camera used in this study is a Phantom V710 one, which is adjustable in frequency and resolution, with one feature waxes when the other one waxes. The maximum frequency at which the resolution allowed to clearly cover the mirror surface was 33000Hz. In the present application, the frequency of the camera was fixed at 13000Hz to obtain images of good quality for further digital treatment which consisted of subtraction of two consecutive images. Note that the high speed camera was manually triggered to record the 2s preceding the cracking, once the first noise was heard by the operator. The camera view is presented in FIG. 2.16, it can be noticed that the area of interest, *i.e.* the zone in uniform tension between the two punch rollers, is clearly observed. Thus, the crack path will be easily imaged to investigate the propagation mode.

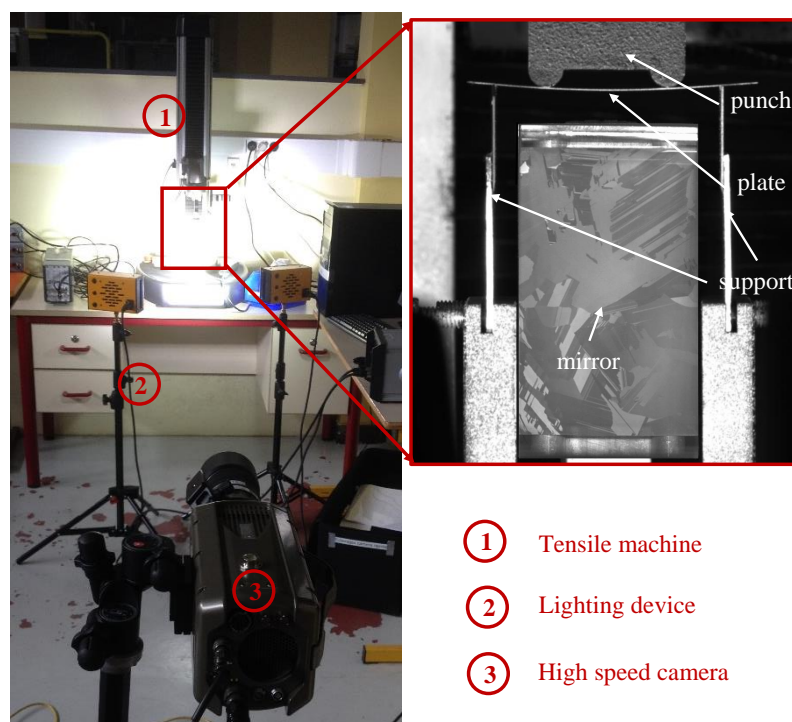


FIGURE 2.16: 4-point bending with mirror.

- MCSi crack path

FIG. 2.17 presents two successive images of the fracture of a MCSi plate, the third one being a copy of the second one which underlines the longest crack pass. Note

that, conversely to FIG. 2.16, the central rollers are located at the left and right sides of each photo (*i.e.* vertical), which is also the bending axis. Thus the tensile direction on the observed side is horizontal. The cracks are easily observed thanks to the apparition of gray broken lines. It can be seen (in FIG. 2.17) that the cracks remain straight in each grain but the propagation direction changes when they enter into another grain. In the largest grain (top) many parallel cracks are observed. No crack is observed at the grain boundaries. This crack pattern indicates a trans-granular fracture, which takes place on some specific planes rather than the plane perpendicular to the maximum tensile stress.

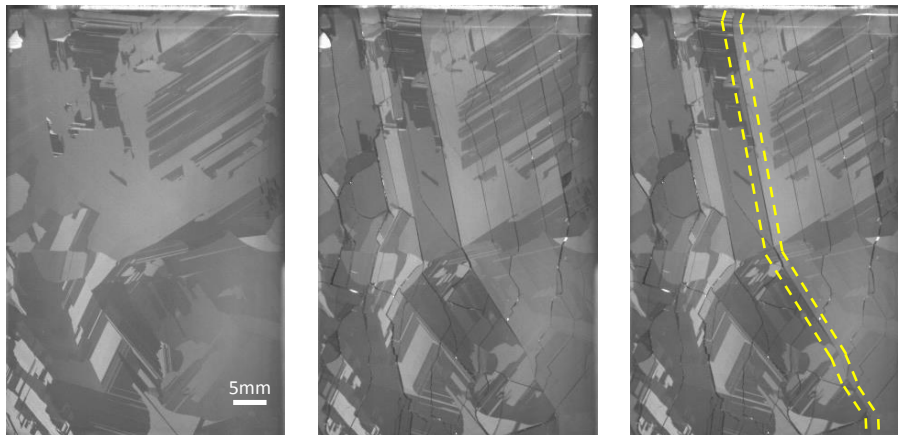


FIGURE 2.17: MCSi plate before (left) and after (right) cracking.

- RST crack path

In the case where the grains are perpendicular to the tension direction, the cracks are quite straight and likely cross through the whole plate without remarkable direction change, as shown in FIG. 2.18. The conclusion for the fracture mode is not straightforward to the naked eye since the roughness and the multitude of twins prevent from properly identifying the grain boundaries.

Under microscope, the grain boundaries are easy to distinguish. From the upper image in FIG. 2.19, we can see that the grain boundary generally manifests a curved shape, *i.e.* the crack surface would be very rough in case of inter-granular fracture. However, by fractography, the representative crack surface is revealed very plate and smooth as shown in lower image of FIG. 2.19. Accordingly, it is believed that the fracture takes place on a cleavage plane rather than along a grain boundary.

Concerning the load case where the elongated grains are parallel to the tension direction, one can observe in FIG. 2.20 that each crack passes through the plate with multiple direction changes. Moreover, all the crack paths seem to be aligned with one another. The fracture mode is certainly trans-granular and likely based on cleavage planes.

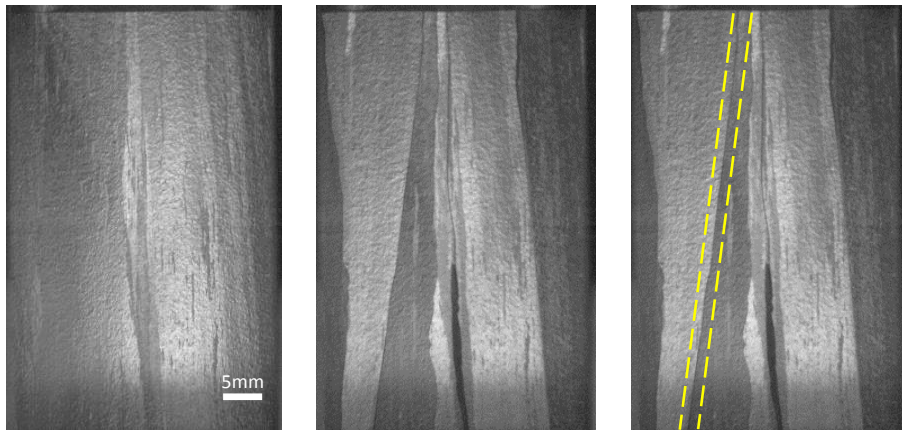


FIGURE 2.18: RST plate before (left) and after (right) cracking with grains perpendicular to the tension direction.

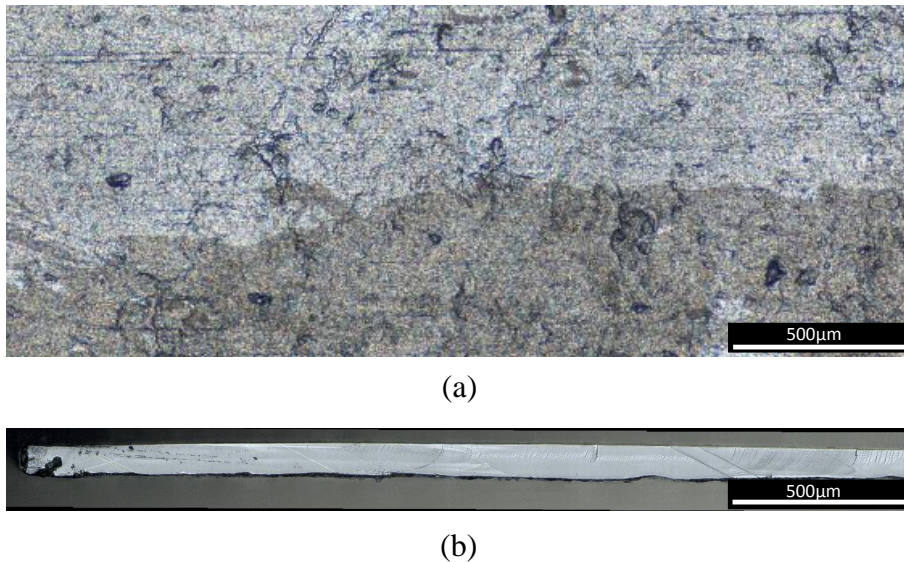


FIGURE 2.19: The grain boundary shape on the upper surface (a) and fracture surface of RST plate crack with grains perpendicular to the tension direction (b).

4.2 Identification of fracture origin

With respect to the manufacturing processes of our silicon wafers, the potential defects that lead to failure are the micro-cracks located at the near surface due to wire-sawing (for MCSi plates), the inclusions generated in the bulk during the solidification (for both kinds), and the laser cutting induced defects at the edges (for both kinds). In addition, it should be noted that the RST plates locally undergo important variations of thickness, that may also induce local over-stress during loading.

Considering the reported crack propagation velocity, during the time increment between two successive images, a crack could travel about 75mm over the maximum fre-

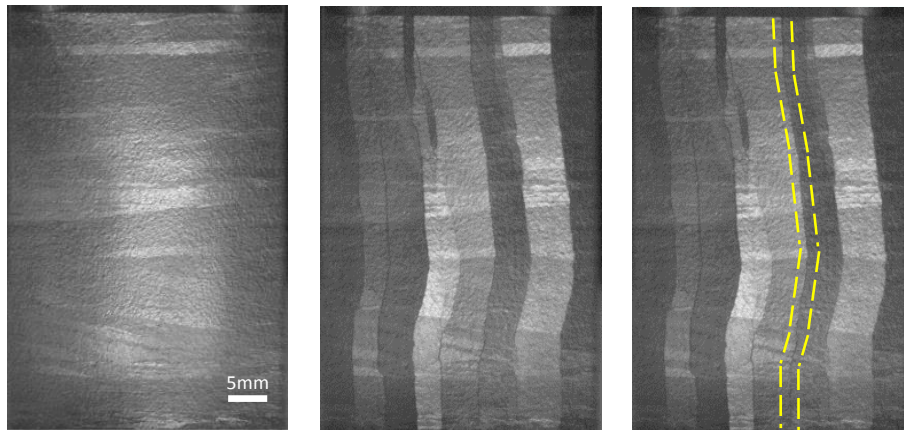


FIGURE 2.20: RST plate before (left) and after (right) cracking with grains parallel to the tension direction.

quency *i.e.* 33000Hz, yet the plate length is only 50mm. It means that the high speed camera used here has little chance to capture the initiation of the crack. However, this high speed imaging set-up used here was able to identify the first cracks. Knowing that the fracture origin is usually surrounded by some special surface marks, a fractographic analysis was then carried out only for the first crack(s) in order to find out the defect that initiated the cracking. In this work, a Keyence confocal microscope (VHX-2000) was used to draw the crack surface micrographs.

Under bending solicitation, the crack profile presents a quarter of an ellipse followed by a straight line representing the crack front in the thickness of the plate [FRÉ 90a, SHE 03a]. This feature is shown schematically in FIG. 2.21, inspired from the works of [FRÉ 90a] and [SHE 03a]. When the crack front encounters severe surface defects, some elastic waves are released. The latter interact with the advancing crack front and then generate the so called Wallner lines [WAL 39] (FIG. 2.21). The Wallner lines manifest a shape close to the one of the crack front and can thus be used to identify locally the crack propagation direction. Particularly, in [SHE 08] the authors reported specific surface perturbations (instabilities) on $\{111\}$ cleavage planes due to crack velocity gradient in thickness under bending. These surface instabilities have also been found in our preliminary tests on single crystalline silicon plates, as shown in FIG. 2.22. This $(11\bar{1})$ fracture surface exhibits corrugated instabilities near the compression side (top), the form of terrace-like kink instabilities near the tensile side as well as the imaginary crack front profile. The above described Wallner lines and specific surface perturbations allow to elucidate the crack propagation direction and were used in this study to localize the fracture origin where one could observe two opposite propagation directions. In addition, the specific surface instabilities allow to identify the crack plane nature as $\{111\}$ planes.

- MCSi failure source

As illustrated in FIG. 2.23, the analysis of consecutive images enables the identifi-

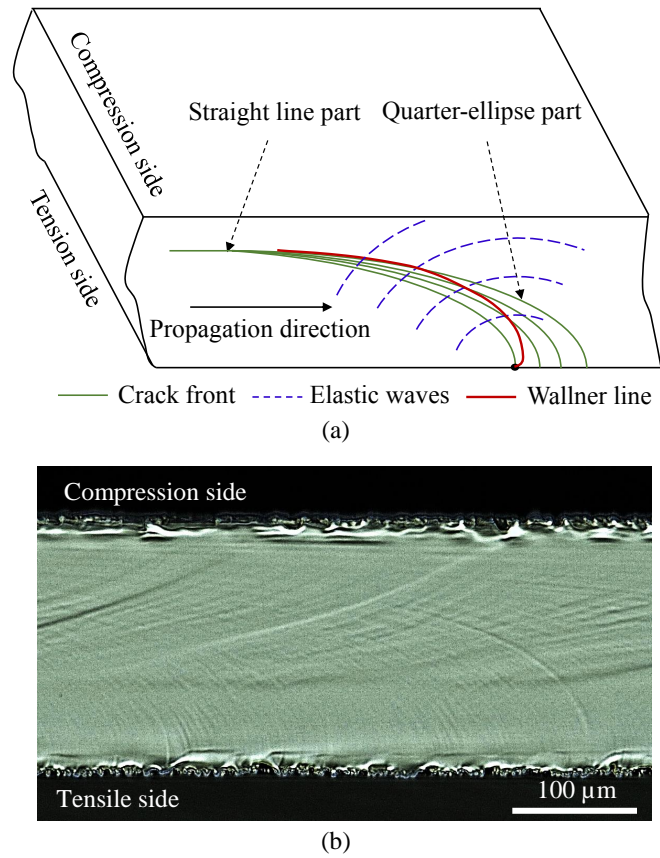


FIGURE 2.21: Wallner lines shape under bending. The schematic showing the generation of Wallner lines (a), and the observation of the Wallner lines on the fracture surface (b).

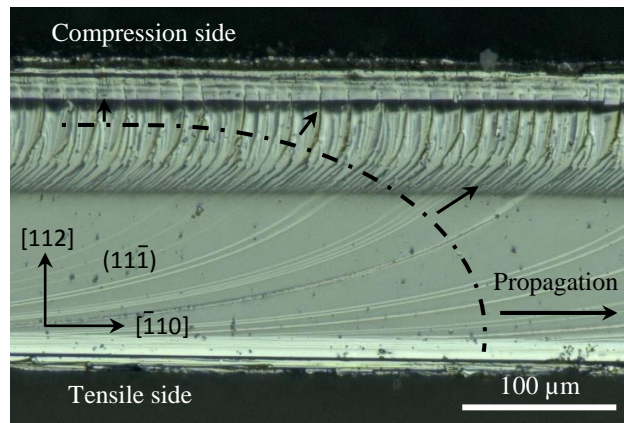


FIGURE 2.22: Optical image of the $(11\bar{1})$ fracture surface of single crystalline silicon under 4 point bending. The dotted line represents approximately the crack front shape.

cation of the first cracks that is framed in the right image. This image comes from the subtraction of the two left photos that correspond to the last image before and

the first image after the cracking.

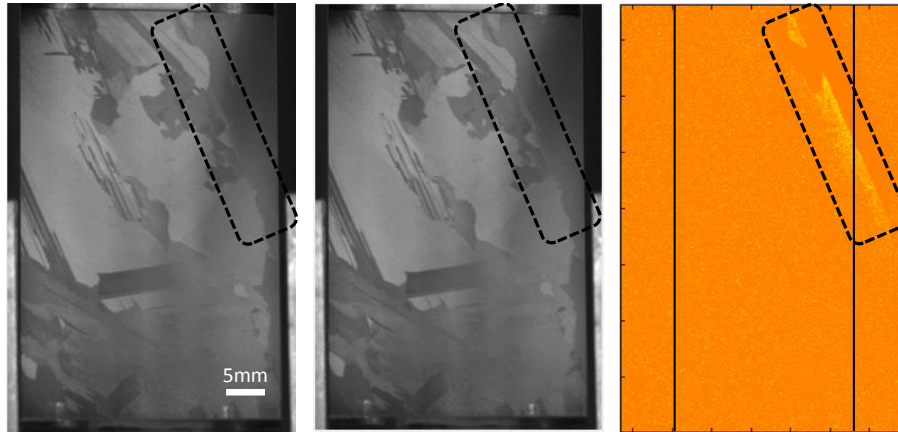


FIGURE 2.23: First cracks marked in two consecutive images for MCSi plate with (left) the last image before cracking and (center) the first image after cracking. Why these are the first cracks is coming from analysis by image subtraction (right). The two black vertical lines in the right image reveal the punch rollers' positions.

The fractography brings us to the fracture origin located surface shown in FIG. 2.24(b). The Wallner lines are not noticeable. Meanwhile, the surface instabilities help to identify the tensile and compression sides as well as the crack propagation direction, which ultimately enables us to locate the fracture origin, as pointed out by the arrow. To enhance the readability, FIG. 2.24(a) shows the further propagation direction at the end of the same crack as in FIG. 2.24(b). In this specific example, the initiation point is located at the edge. Basically it has been found that most crack initiation sites are located at the edge or at a point less than $200\mu\text{m}$ from the edge. It can be concluded that, for MCSi plates, fracture mainly initiates on the edges of the wafer on defects assumed to be caused by laser cutting.

- RST failure source

The same process is used to identify the first crack created during the bending tests with RST plates. An example is given in FIG. 2.25, where the first crack is framed in the right image. Here the punch rollers are parallel to the drawing direction *i.e.* parallel to the grains (vertical).

One fractography showing the corresponding fracture surface is presented in FIG. 2.26(a). Once again, the tensile and compression sides of the wafer and the propagation directions are determined thanks to the presence of (111) surface instabilities (the propagation directions are indicated by the black arrows). The crack origin is easily identified and spotted by the black arrow. FIG. 2.26(b) addresses further propagation direction on the same crack as in FIG. 2.26(a) for a better substantiation. In this test, the fracture initiated on a large defect, $250\mu\text{m}$ far from the edge of the plate.

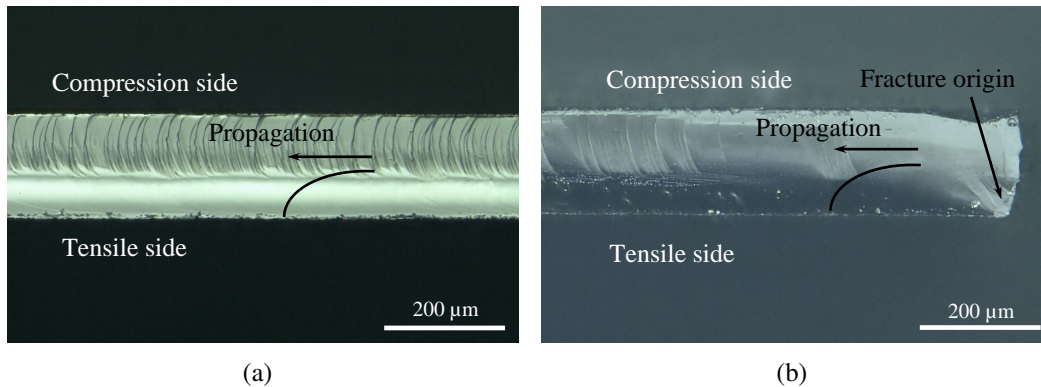


FIGURE 2.24: MCSi fracture source identification. Crack surface pointing out the initiation locality (b), and fracture surface on the same crack as in (b) pointing out further propagation direction (a).

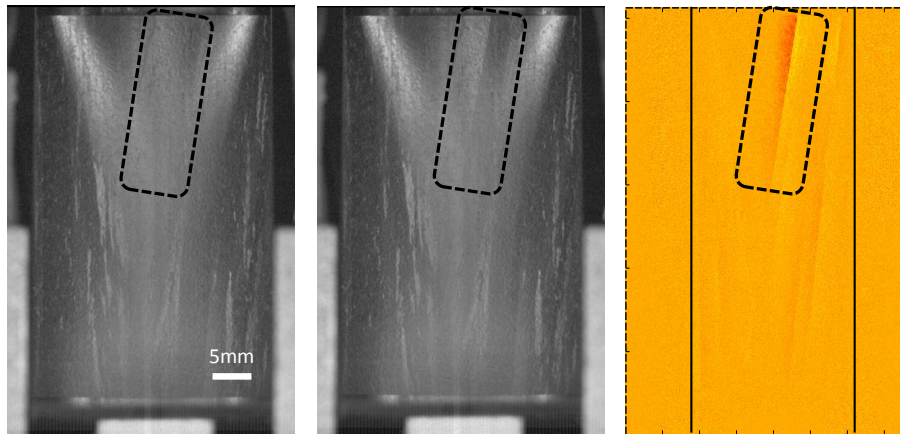


FIGURE 2.25: First crack marked in two consecutive images for RST plate with (left) the last image before cracking and (center and right) the first image after cracking. The two black vertical lines in the right image reveal the punch rollers' positions.

Several other RST bending tests have been analyzed this way and none of the observed fractures seems to have been initiated from a thickness reduction, even if the local variation may reach 20%, as shown in FIG. 2.27(a). No precipitate or inclusion has been identified as crack source, neither. The passage through some inclusion like defects is observed and presented in FIG. 2.27(b). To conclude for RST plates, the fracture is believed to initiate almost always from defects close to the edges, probably induced by the laser cutting, as for MCSi ones.

For RST plates in which the drawing direction is perpendicular to the punch rollers, the fracture surface is much more complicated. An example of fractography is presented in FIG. 2.28, where the crack surface highlights repeated changes of the cleavage planes. The latter are of very small widths, typically in the order of a

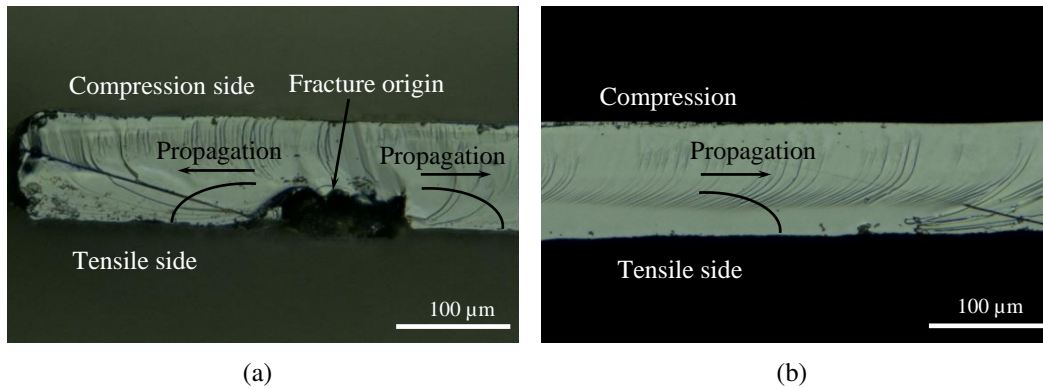


FIGURE 2.26: RST fracture source identification with grains parallel to the punch rollers. Crack surface pointing out the initiation locality (a), and fracture surface on the same crack as in (a) pointing out further propagation direction (b).

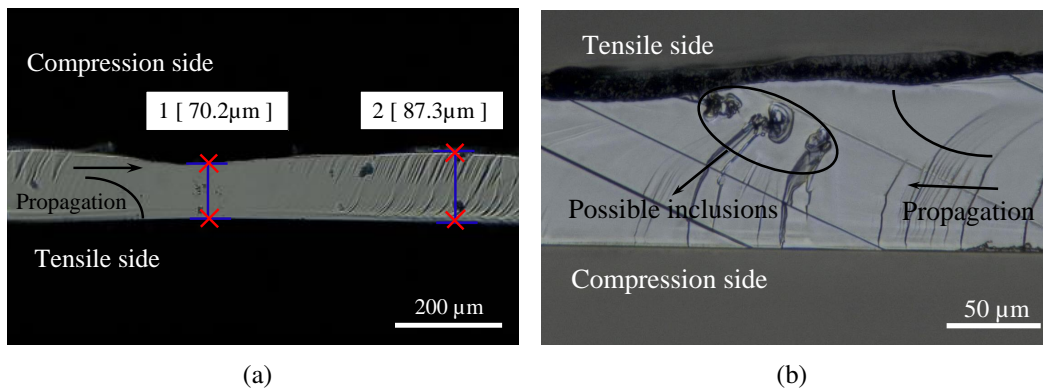


FIGURE 2.27: Elimination of possible fracture roots thanks to determined crack propagation directions. Important local thickness variation (a) possible inclusions (b). The horizontal arrows indicate the crack propagation directions.

few tens of μm . Therefore, no straight conclusion can be made here regarding the initiation point. These so frequent changes in cleavage planes are likely to indicate that there are intensive twinning in this kind of silicon wafers.

4.3 Weibull distribution

Weibull distribution [WEI 51] is widely used in fracture strength characterization for brittle materials, as recommended in [AST]. The distribution (see EQ. 2.4) involves two parameters *i.e.* the characteristic fracture stress σ_θ and the slope or modulus m that highlight the characteristic size of defects at the origin of failure and the scatter of the defect sizes due to the manufacturing process. Mathematically, σ_θ stands for the stress at which the fracture probability is 63%. Regarding m , a more important value represents a weaker

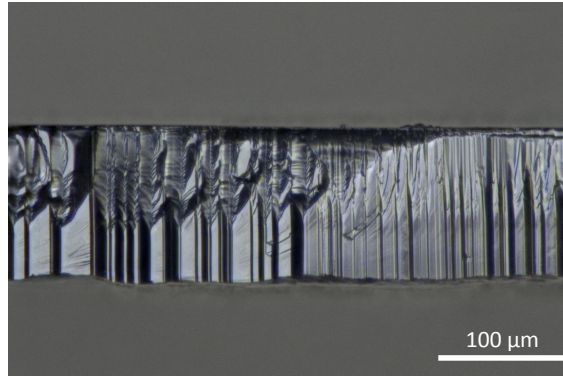


FIGURE 2.28: Crack surface of a RST plate with grains elongated along the direction perpendicular to the punch rollers

scatter thus a better reproducibility of the defect introduction. A Weibull analysis was performed here in order to better understand the correlation between the mechanical strength and the identified fracture origin. The fracture stresses were calculated with EQ. 2.2 for MCSi plates and RST plates (in the two loading configurations for the later).

$$P = 1 - \exp\left[-\left(\frac{\sigma}{\sigma_0}\right)^m\right] \quad (2.4)$$

The Weibull distributions plotted from our tested samples are shown in FIG. 2.29. The corresponding parameters are listed in TAB. 2.2. RST perp. and RST para. denote the tensile stress direction perpendicular and parallel to the RST grains, respectively. It has been noticed that the fracture initiates from the laser cut edge for MCSi plates and RST plates with grains parallel to the punch rollers. Thus, the Weibull distribution evaluates particularly the laser cutting induced defects.

TABLE 2.2: Weibull parameters with 90% confidence intervals for MCSi and RST plates

Specimen	Test quantity	Char. Fracture stress σ_0 [MPa]	Weibull Modulus m [-]
MCSi	21	106 (100...113)	6.3 (4.9...8.7)
RST perp.	30	152 (144...161)	5.8 (4.6...7.4)
RST para.	30	159 (148...166)	6.1 (5.1...9.6)

From the Weibull parameters, one can see that the strength of the MCSi plates is lower than that of the RST plates. The latter possess almost the same fracture stress in the two considered directions. Concerning the Weibull moduli (slopes), the three cases hold all a value of about 6. This reveals that the fracture may have the same origin for the studied plates : defects due to manufacturing process especially edge laser cutting.

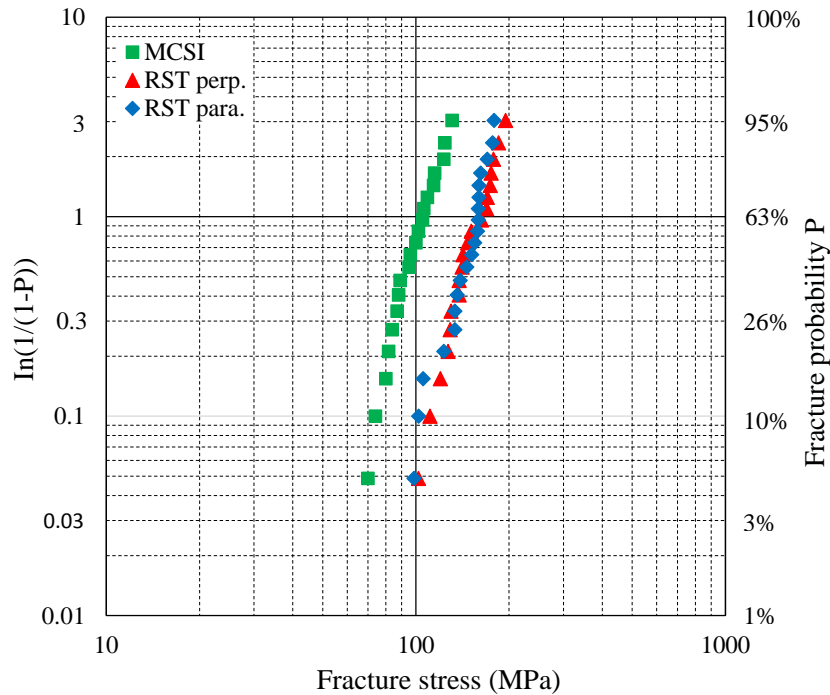


FIGURE 2.29: Weibull distributions of both MCSi plates and RST plates in the two loading configurations

5 Discussion

5.1 Identification of the Young's modulus

For a thin brittle material, the 4-point bending test is a very appropriate characterization method. Yet, for high accuracy assessment, the beam theory owns some limitations due to strong hypotheses such as homogeneity, isotropy, linear elasticity, perfect contact condition, and no Poisson ratio effect.

In our study, the two kinds of silicon plates possess different micro-structures, with RST kind manifesting a specific texture due to the manufacturing process. The recall of existing works and the elasticity of single crystalline silicon allowed to highlight a reasonable range for the stiffness of multi-crystalline silicon. The FE analysis helps to improve the accuracy and to enhance the reliability of the characterization.

With the correction procedure used to analyze the experimental data we have found that the Young's modulus of MCSi plates is close to 165 GPa, which is not far away from the literature (160 GPa [Sha 01b] and 162.5 GPa [FUN 04]). In the other hand simulations performed with a stochastic distribution of grain orientation have been also found in very good agreement with measurements (see FIG. 2.15). The numerical characterization results in a very similar value (163 GPa), which justifies the random grain orientations, as mentioned in Section 3.1. Regarding RST plates, the preliminary EBSD measurements show a specific micro-structural texture such that the [110] axes are essentially aligned

along the drawing direction. The variation of loading direction with respect to the elongated grains leads to two different equivalent rigidities. The corresponding numerical assessment matches very well the experimental characterization when the texture effect is taken into account (see FIG. 3.1). It is quite remarkable to see that the characterized Young's modulus in the drawing direction, 172 GPa and 171 GPa from the experimental and numerical assessments, is comparable to that in the $[110]$ axis, 169 GPa.

5.2 Fracture investigation

The crack propagation mode for crystalline silicon is an interesting issue. The specific cleavage planes for a single crystal are well-known. For multi-crystalline silicon, transgranular, inter-granular modes were both addressed in the literature [POP 11, INF 14, MUL 15]. Meanwhile, it should be recalled that the works based on the inter-granular fracture have no reliable experimental support.

Concerning the silicon plates studied in this work, the crack path was investigated by high speed imaging technique and fractography when necessary. For MCSi plates, it is found that the cracks never overlap the grain boundaries, conversely they follow probably some cleavage planes as in a single crystal of silicon. Further works should be performed to properly identify the cleavage planes (Refer to Chapter 4). On the surface involving the fracture initiation spots, one can observe the specific surface instabilities (see FIG. 2.24(b) and 2.24(a)). These instabilities have only been reported to be present on the $\{111\}$ crack surface, as presented in [SHE 08] and revealed in our study on a single crystal silicon plate (see FIG. 2.22). This finding indicates that the crack initiates on one of the $\{111\}$ planes. Regarding the RST plates, when the tensile stress direction is perpendicular to the grains, it is not obvious a priori to state if the cracks follow the grain boundaries or a cleavage plane within a silicon crystal. However based on a fractography analysis, it has been observed that the grain boundaries are mostly curved while the cracks follow a plane path (see FIG. 2.19). Consequently it can be concluded that the plates crack along some cleavage planes. Moreover, the fractography on the first crack reveals also the presence of instabilities as expected on the $\{111\}$ surface (see FIG. 2.26(a) and 2.26(b)). These instabilities highlight that the crack initiates on one of the $\{111\}$ planes as for MCSi specimens. For RST plates in the other configuration, *i.e.* when the grain boundaries are almost parallel to the tensile stress, the cracks propagate perpendicular to the grains. Therefore it is clear here that the crack path does not follow grain boundaries. It has been also observed that each crack deviates when entering into a new grain. In addition many parallel cracks can be seen in each grain, again following a certain cleavage plane. One may so conclude that the crack propagation mode in solar grade silicon, for single crystal or MCSi or RST, is transgranular (this point will be further discussed in chapter 4) and that the crack path may follow one of the cleavage planes as $\{111\}$ or $\{110\}$.

As mentioned in the introduction, the identification of the fracture origin in silicon PV plates has been investigated by [KLU 14]. These authors relied only on fractography to find out the fracture cause of silicon wafer, and the observations incriminated wire sawing induced micro-cracks. However, this study was limited to single crystalline silicon

wafers in the framework of 3-point bending tests. It has been concluded that the cracks follow one of the cleavage planes. In addition it is worthy to mention that the fracture of a rectangular plate made in a single crystal of Si under 3-point bending test leads to a few large fragments whereas many small fragments are produced when a MCSi or a RST plate fractures with 4-point bending (see FIG. 2.17). It means a lot of work to perform the fractography analysis in order to identify the potential initiation site. This difficulty has been overcome by the use of a high speed imaging technique to detect and locate the first crack, limiting the fractography analysis to this first crack. With these two correlated methods, it is found that the fracture initiates from the plate edges on laser cutting induced defects for MCSi plates and the RST ones when the tensile stress is perpendicular to the grains (see FIG. 2.24 and 2.26). Although it is difficult to determine the fracture origin in RST plates undergoing the tensile stress in the grain direction, the Weibull distributions indicate that the fracture origin should be of the same nature as in the other loading configuration.

Finally the Weibull distribution analysis has shown that a lower fracture stress is found for MCSi plates compared to the RST ones, *i.e.* 106 MPa against 152 – 159 MPa. It should be noticed that the flexural strength of a brittle material is dependent on both the fracture toughness and the defect size [AST]. For crystalline silicon, the toughness slightly varies from one cleavage plane to the other since $K_{IC(110)}/K_{IC(111)} = 1.1$ as reported by [LI 05]. Thus, the key factor for the failure strength is the severity of the defects. Since MCSi plates are thicker than the RST ones, they need more laser energy to be cut which indeed produces more and more severe defects. This explains the lower strength found for MCSi plates than for RST plates. The Weibull slope is close to 6 for the three sets of tested Si plates. To compare with the wire sawing induced fracture root, 9 has been obtained in [POP 11] and 11.3 in [FUN 04] for multi-crystalline silicon wafers, while a much higher value of 26 has been reported in [KLU 14] for single crystalline silicon wafers. The single crystal undergoes the defects with less scattered sizes since it is free of the influence of grain orientation, which should affect the interaction between the cutting particles and the crystal from one grain to another due to the anisotropic fracture behavior. Concerning the silicon multi-crystal, the laser cutting results in a slightly larger but comparable dispersion of the strength with respect to that induced by the wire sawing. This is probably due to the fact that the laser defect is affected by many factors in the cutting process such as the laser energy, the cutting velocity and the thickness of the plate.

6 Conclusion and remarks

The objectives of this study were to characterize the mechanical properties of brittle PV silicon plate, *i.e.* the rigidity and the fracture behavior. The studied specimens possess two different micro-structures corresponding to two different manufacturing processes. For MCSi specimens, the grain orientation was considered as random, while for RST ones, a specific texture was revealed by EBSD measurements which showed that the [110] direction of the grains was mainly parallel to the drawing direction. Regarding the stiff-

ness characterization from 4 point-bending tests, the beam theory was applied based on the force-deflection curve. Meanwhile a FE model was elaborated to quantify the relative error inherent to the beam theory when applied to the bending of a thin plate and characterize the Young's modulus from a numerical point of view. For fracture investigation, a high speed imaging technique and fractography were carried out to identify the fracture mode and its origin. A Weibull analysis has then be performed and both the mean stress and the Weibull slope have been identified. The main conclusions are the following :

(i) The MCSi plates possess a mean Young's modulus of 165 GPa. This value is comparable with data for poly-crystalline silicon when it contains micro range grains (160 GPa) and the numerical assessment that considers similar grain size but random grain orientation (163 GPa).

(ii) The RST plates own two different Young's moduli depending on the bending direction relative to the grain elongated orientation. In the grain direction, the characterization gives 172 GPa which is similar to the rigidity in the [110] crystallographic axis (169 GPa) ; in the perpendicular direction, the assessment results in 163 GPa which is close to the Young's modulus of poly-crystalline silicon. For FE results, the consideration of the texture allows to match the experimental assessment with comparable rigidities 171 GPa in the grain direction and 164 GPa in the perpendicular direction .

(iii) Both kinds of plates fracture in trans-granular mode. The first crack surface is revealed to be one of the {111} planes. The crack path deviates at the grain boundary when it skips from one grain to the next one. Straight cracks have been also observed in RST plates when the bending direction is parallel to the direction the grains are elongated (*i.e.* when the tensile stress is perpendicular to the grains).

(iv) The pre-existing defects on the plate edges due to the laser cutting have been identified as the fracture origin for both kinds of plates. These defects lead to a lower mechanical strength for MCSi plates (106 MPa) compared to the one for RST plates (152 – 159 MPa). It should be also emphasized that these fracture stresses are at least one order of magnitude lower than the one observed for a defect-free single crystal of Si (5 to 7 GPa). The Weibull modulus of 6 obtained here experimentally tends to show a limited scatter in the distribution of laser induced defects.

7 Outlook

- With the fracture origin identification method, the single crystalline silicon wafers have also be studied. The crack initiates mostly from a subsurface micro-crack that nucleates in wire sawing process. The initiation spot is far away from the free edge of the plate but very close to the punch rollers, as shown in FIG. 2.30(a). The fractographic analysis lies sometimes on the Wallner lines sometimes on surface instabilities, it depends on the cleavage plane upon crack initiation. As expected, we identify two opposite propagation directions which bring us to the fracture origin, as can be noticed in FIG. 2.30(b).

Massive fractographic analysis conduct to some derived observations (single crys-

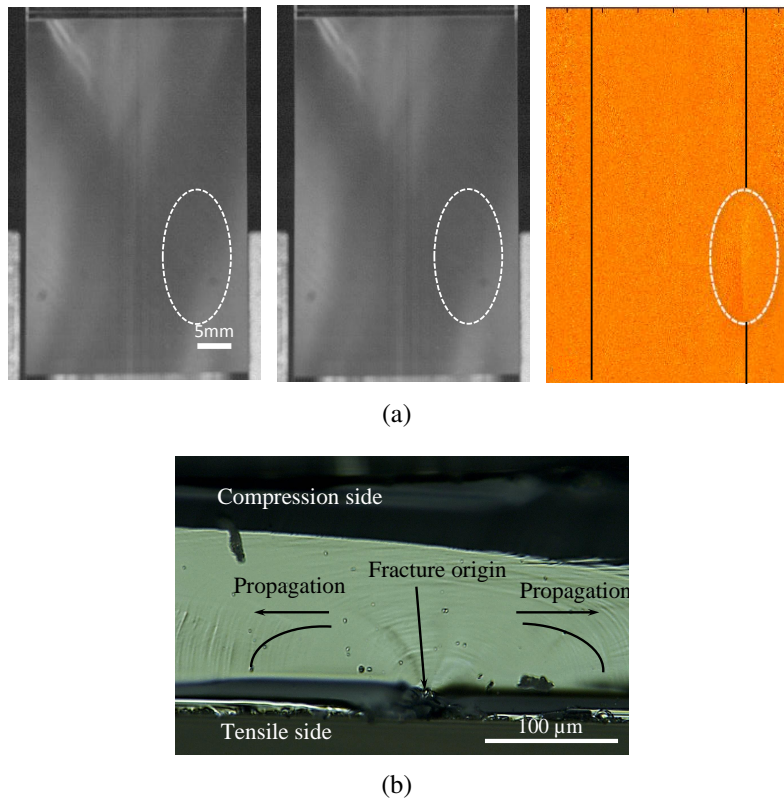


FIGURE 2.30: Fracture cause identification for single crystalline silicon wafer. The high speed camera points out the first crack (a) and the fractography highlights the initiation point (b). The two black lines denote the punch rollers in (a).

talline silicon concerned) which have never been reported in literature. These complementary points will be addressed with the following example. FIG. 2.31 reveals different spots on the same crack surface including the initiation point. This crack is right under the punch roller.

It is found that the crack initiates on a (111) plane. However, it deflects progressively onto a (110) plane, and in transition region, the (111) part resides on the lower portion of the crack surface. This finding is contradictory against some previous literature works, which highlighted a cleavage plane deflection from (110) to (111) [SHE 03b, SHE 04b]. The authors related this (110)–(111) deflection to the crack propagation velocity, since they observed the deflection once the crack velocity reaches 1560 m/s and the deflection takes place from the lower portion of the crack surface. Moreover, on the (110) plane (the most left subfigure in FIG. 2.31), it can be noticed that the Wallner shapes are also very different from that presented in [SHE 08] (see FIG. 2.32).

The (110) cleavage is the main fracture path in mono-crystalline silicon wafers inside the solar panels, it will thus be important to elucidate this fracture behavior. In

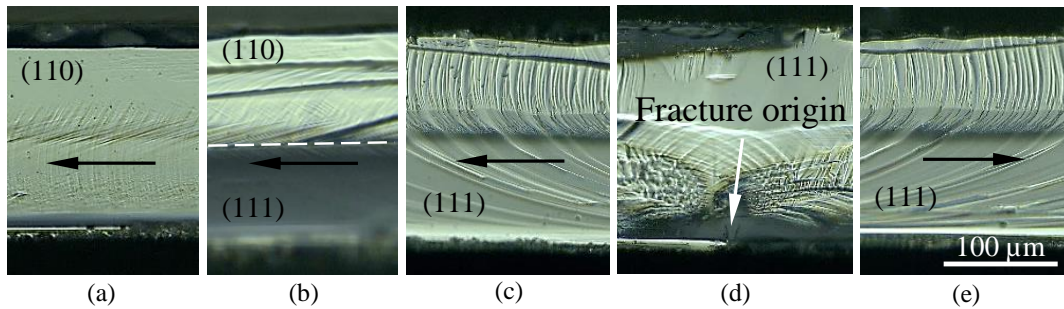


FIGURE 2.31: New insights on crack surface in single crystalline silicon. (111)–(110) deflection revealed in (a)-(d) and the special shape of Wallner lines in (a). The horizontal arrows indicate the crack propagation directions at different spots on the same crack surface including the initiation point.

order that the crack propagates in the contact free region with 4-point bending test, pre-cracks will be introduced and well controlled to obtain different crack velocities. Then, we should correlate properly the cleavage plane as well as the fracture surface morphology with the crack propagation velocity.

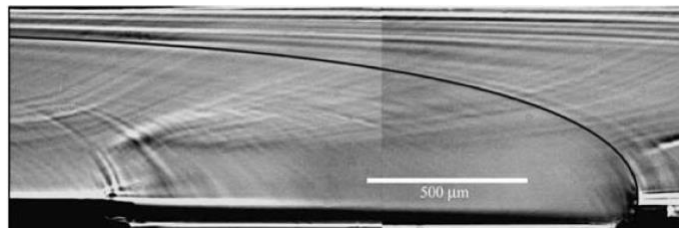


FIGURE 2.32: The Wallner lines shape found in literature [SHE 04b].

- The investigation on the multi-crystalline silicon deserves further studies. Along the crack propagation path, no overlapping on the grain boundaries has been revealed. While in literature, some researchers still consider inter-granular fracture in silicon. Indeed, [POP 11] stated that the crack in the solar grade MCSi can go through the grain boundaries, but no evidence has been made. Special attention should be drawn on the confounding between the grain boundaries and the twin boundaries. A sophisticated study should not rely on only surface observation, fractography is more convincing to verify the boundary overlapping.

As presented in Section 5.2, the crack initiates and propagate very firstly on a (111) plane. What is the crack path (cleavage planes) in multi-crystalline silicon? Can it be reproducible? What is the role of the grain boundaries in the fracture process?

With these questions to be clarified, more detailed studies with both silicon single crystals and multi-crystals will be carried out to explore the fracture behavior.

Chapter 3

Fracture in single crystalline silicon

In this chapter, we investigate the fracture initiation and crack propagation of single crystalline silicon. 4 point bending tests have been performed to produce (110) cleavage, which is the main cracking path in mono-crystalline silicon wafers embedded in PV modules. We show that the crack velocity can reach 3700 m/s without cleavage plane deflection neither crack branching. The static energy release rate exceeds systematically the material toughness upon crack initiation, which conducts to an important initial crack velocity. The crack front shape reveals strong velocity dependence and presents curvature jump for high speed propagation. We also highlight, as the first experimental observations, special surface marks that arise only on the rapid crack surface, and we propose that they are front wave traces resulting from toughness induced local velocity fluctuation. This finding gives insight to the waving crack front in absence of material heterogeneity.

Contents

1	Introduction	57
2	Experimental procedure	62
3	Crack velocity	63
3.1	Steady state velocity	65
3.2	Initial velocity	66
3.3	Global crack stability	70
3.4	Summary on the crack velocity	71
4	Crack front determination	73
4.1	Wallner lines shapes	73
4.2	Crack front evolution	75
5	High velocity surface marks	77
5.1	Special surface marks characteristics	78
5.2	Velocity correlation	80
5.3	Special surface marks origin	80
6	Discussion	85
6.1	Stability of (110) cleavage	86
6.2	Crack initiation behavior	86
6.3	Crack velocity correlated crack front shape	87
6.4	Presence of front waves for high speed crack	88
7	Conclusion	88
8	Outlook	88

1 Introduction

The fracture of silicon has received a lot of investigations due to special manifesting phenomena (which will be detailed in following paragraphs) that challenge our understanding of fracture mechanics [COX 05, BIT 15]. Among the investigations, (110) cleavage stands out and has drawn much attention because of the anisotropic in-plane fracture behavior. In practice, the (110) cleavage plane is the main fracture path in mono-crystalline silicon solar wafers and thus should be studied carefully. Yet previous investigations have built several theoretical interpretations for the fracture of this cleavage plane, we will show here, based on our observation and analysis, a couple of results that either arbitrate previously published conclusions or give new insights on the Si brittle fracture behavior.

The single crystalline silicon is highly anisotropic in the fracture process. The crack propagates preferentially on crystallographic planes as (111) and (110) due to the energetic consideration [GEO 93, LI 05, PÉR 00a, HOL 98, OHR 92]. The brittle characteristic makes the fracture a rapid dynamic process with a propagation velocity comparable to the surface waves [CRA 97, HAU 99, SHE 04b]. For dynamic fracture behavior investigation, the crack propagation velocity is crucial since many material properties and special phenomena in silicon are related to the velocity such as the dynamic toughness [CRA 00] and crack surface instabilities [SHE 08, KER 08]. The classical continuum fracture theories fail to predict the crack propagation in silicon, since a velocity threshold has been experimentally revealed. Indeed, experimental investigations [HOL 98, CRA 97, HAU 99] showed that slow crack velocity ($\ll 2000$ m/s) is never observed. Buehler et al. [BUE 07] explained this velocity threshold by highlighting localized phase transformation of silicon lattice from 6-membered rings to 5-7 double ring which blunts the crack tip. On the other hand, Cramer et al. [CRA 00] indicated that the silicon fracture presents a terminal velocity of 3800 m/s (*i.e.* 0.85 Rayleigh velocity C_R).

In order to monitor the crack velocity, the most widely used one is the 'potential drop' method [STA 83]. Concretely, it consists in pasting an ultra thin conductive film on the specimen's surface and correlating the resistance variation with the crack length. In most of the published experimental results using this method, one can notice a moderate acceleration phase. This phase begins from a very slow initial crack velocity and terminates after about a propagation of 5 to 10 mm before the crack reaches the steady state [HAU 99, SHE 04b, CRA 00] (see FIG. 3.1(a) and 3.1(b)). In the numerical investigation mentioned above addressing the crack threshold [BUE 07], the crack instantaneously jumps to a rapid propagating state upon initiation, as noticed in FIG. 3.1(c). However, this incoherence has never been addressed properly in the experimental framework since most of the studies addressed only the steady state fracture response to highlight the velocity correlated properties or phenomena. Hence, it will be interesting to deepen the experimental research on the crack velocity to clarify the very beginning propagation state.

The fracture path in silicon is affected by deflection mechanism. Cracking along the [100] direction on a (110) plane cannot be achieved. The experimental observations have revealed a systematical deflection towards a (111) plane [EBR 99], as schematized

3. Fracture in single crystalline silicon

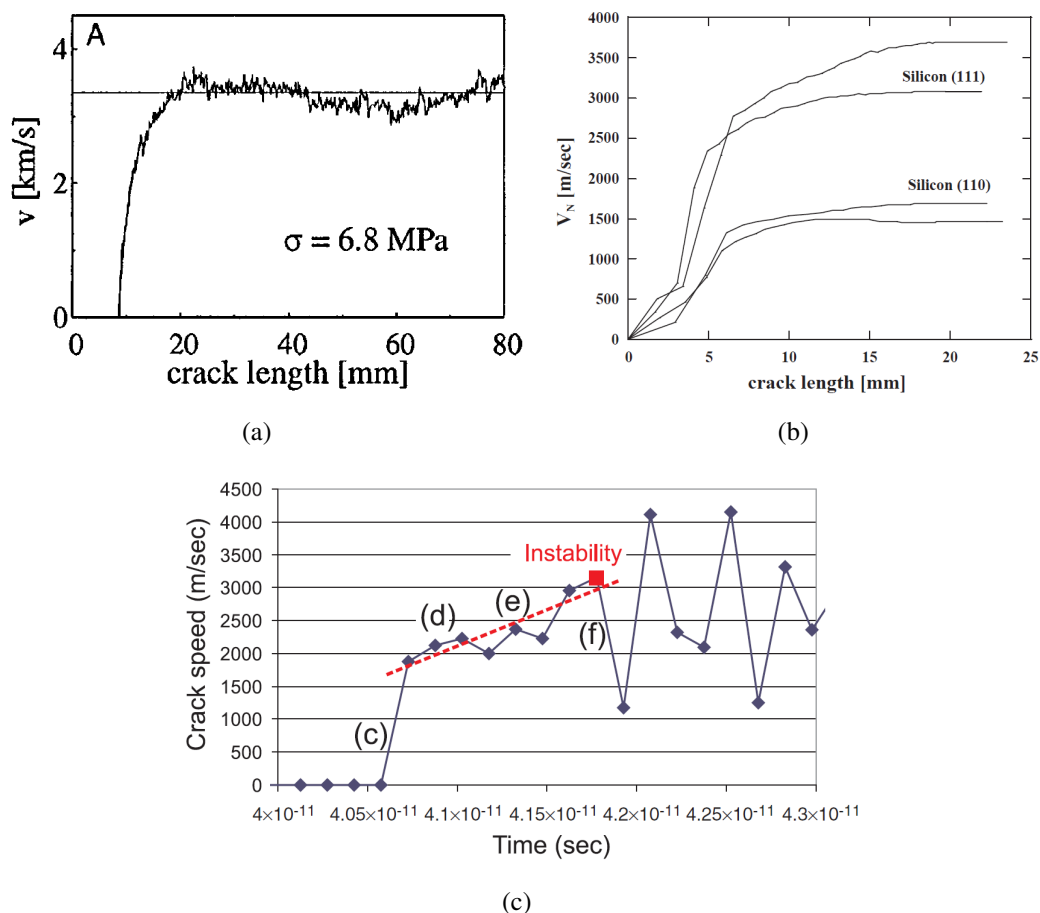


FIGURE 3.1: The crack velocity profile after initiation. (110) cleavage conducted by uniaxial tensile tests using 'potential drop' method [CRA 00] (a), and fracture investigations performed with 3 point bending tests using 'potential drop' method [SHE 04b] (b), (111) cleavage simulated with molecular dynamic model [BUE 07] (c).

in FIG. 3.2. Elucidation for this phenomenon has been provided thanks to quantum mechanical calculations [PÉR 00b], the authors highlighted that the bond breaking process is discontinuous and can cause a large lattice trapping [THO 71] if crack is forced to go along [100] direction on the (110) plane. The concept of lattice trapping can be readily expanded to include fracture in environments where the atoms are not arranged on a regular lattice [BIT 15]. Moreover, Sherman and Be'ery [SHE 03b, SHE 04b] have reported that a global deflection from (110) [110] to the (111) plane arise when the crack propagation velocity is greater than 1560 m/s under 3 point bending condition (see Figure 3.3). Based on their observation, a series of publications came out throughout the years [ATR 11a, ATR 11b, ATR 12], which correlated the deflection with the phonon emission mechanism. Cramer et al. [CRA 00] also highlighted this kind of deflection in tensile configuration, but it takes place only locally in the hackle zone for a high speed crack (when faster than 3000 m/s, see FIG. 3.4). Regarding the explanation of this deflec-

tion mechanism, Kermode et al. [KER 08] indicated with quantum-mechanical hybrid, multi-scale modeling, that the deflection is due to slight disturbance which can be a small shear stress. Thus, the conclusions in [SHE 03b, SHE 04b] should be considered with caution since the contact pressure and tangential friction can affect the crack path. In the other hand, the fracture tests should be carried out where the crack propagates in a contact free region.

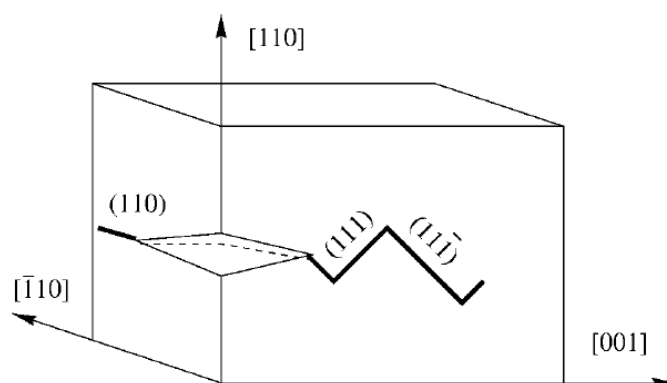


FIGURE 3.2: Cleavage plane deflection from (110) to [100] [PÉR 00a].

In fracture investigation, surface marks have been widely studied since they help to monitor the fracture behavior, for example the in thickness crack front shape and the crack propagation direction. In Chapter 2, we have identified the fracture origin thanks to the fractographic analysis. In brittle fracture, the most studied marks stem from the interaction between surface waves and propagating crack front, the so called Wallner lines [WAL 39, BON 03]. Another important class of surface marks, called front waves (FW), are some special waves that are generated by front-asperity interaction and propagate along the crack front at approximately the Rayleigh wave speed (C_R) [MOR 98, MOR 00]. These waves had been numerically predicted and depicted as propagating velocity fluctuation confined to the fracture plane [RAM 97, WIL 95, WIL 97]. In experimental framework, Sharon et al. [SHA 01a, SHA 02] have firstly observed the FW tracks in brittle soda-lime glass plates. However, arguments arised on the origin of the observed marks in Sharon's works. Bonamy and Ravi-Chandar [BON 03] proposed that these marks were in fact Wallner lines. Sharon et al. [SHA 04] latter justified their finding in comparing the fundamental difference between the FW traces and the Wallner lines, as mentioned below :

For FW traces :

- i) Initial exponential decay followed by persistent propagation with negligible decay over large distances.
- ii) A non-linear character; exhibiting either self-focusing for strong perturbations or dispersion for "weak" ones.
- iii) Strong correlation of the surface marks with large local velocity fluctuations.

While concerning the Wallner lines :

3. Fracture in single crystalline silicon

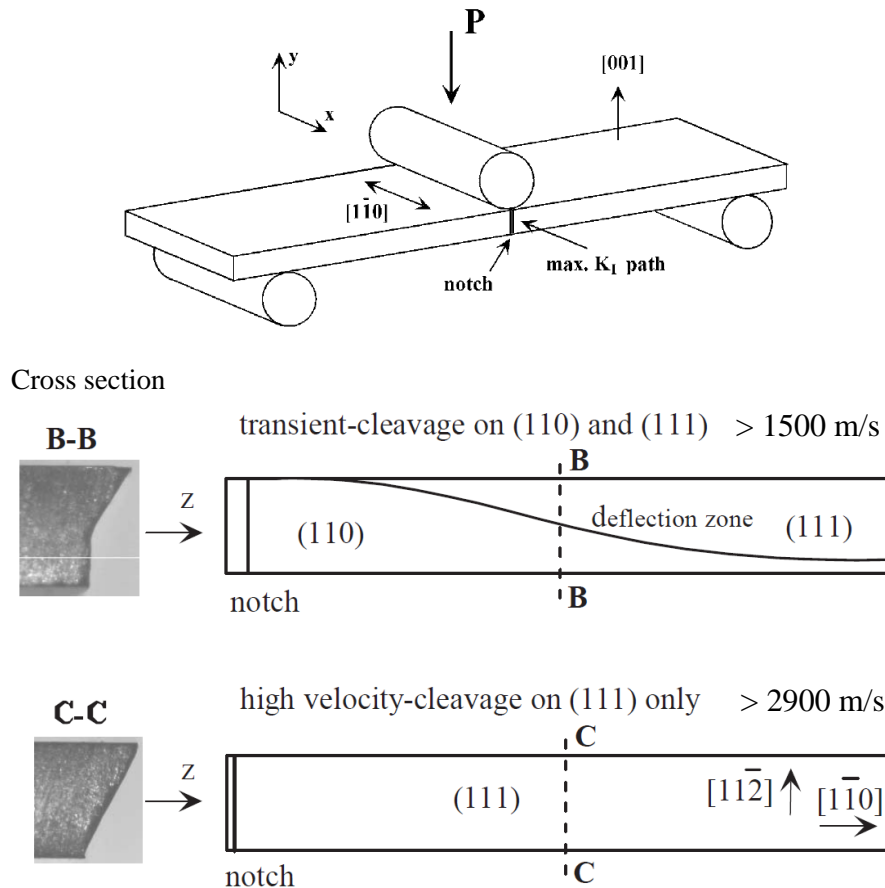


FIGURE 3.3: The (110)-(111) deflection observed in [SHE 03b]. The 3-point bending set up is presented on the top, and the deflection results are presented at the bottom of the figure (the sub-figures are extracted from [SHE 03b]).

i) The surface marks created by waves propagating normal to the fracture plane do not persist beyond the traveling time of the wave front.

ii) The decay of the amplitude of the surface marks generated by the traveling of shear waves across the fracture surface echoed the decay amplitude of the waves themselves.

In fact, when the crack front is straight (in tensile configuration), these two different surface marks have very similar shapes because of the similar velocity of the two conducting waves [SHA 01a]. In fracture investigation on crystalline silicon, no reports have highlighted FW traces neither in tensile tests nor in bending experiments.

In order to investigate the local crack behavior (local velocity for example) which can differ from that of the global propagation, it is necessary to determine the crack front shape. Indeed, when the solid fractures under bending, the crack front is curved due to the stress gradient in thickness, the local crack velocity (the velocity along the atomic debonding direction, see FIG. 3.5) is thus smaller than the global velocity (the velocity revealed on the specimen's surface). For single crystalline silicon under bending, the frontal part

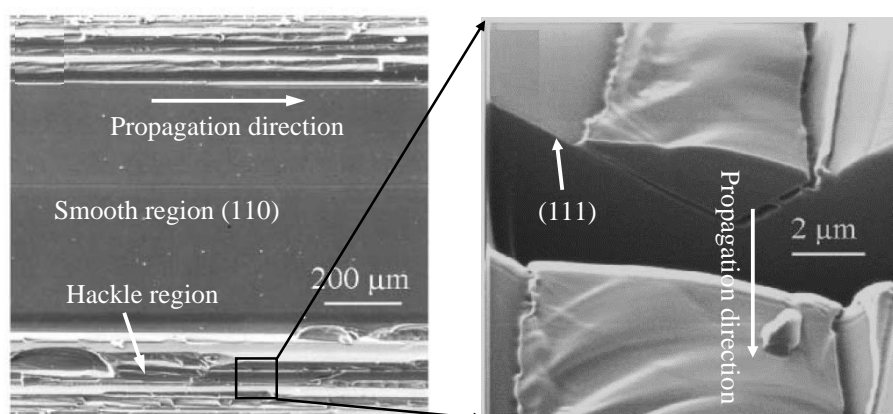


FIGURE 3.4: The (110)-(111) deflection observed in [CRA 00] for a crack velocity higher than 3000 m/s. The central (major) part of the crack is (110) plane while local (111) planes can be observed in the hackle region (the sub-figures are extracted from [CRA 00]).

has been depicted independently of the crack velocity, with a quarter ellipse whose minor axis is $0.8h$ and major axis $3h$, where h is the specimen's thickness [SHE 03a, SHE 04b] (see FIG. 3.5). This shape has been deduced for propagation velocity below 1560 m/s. The authors did not address the crack front shape for higher crack speed since their fracture experiments turned out a deflection from (110) to (111) plane, where the surface instabilities [SHE 08] obscured Wallner lines. Thus, our goal is to investigate the crack front shape at high crack propagation velocity, *i.e.* > 1560 m/s.

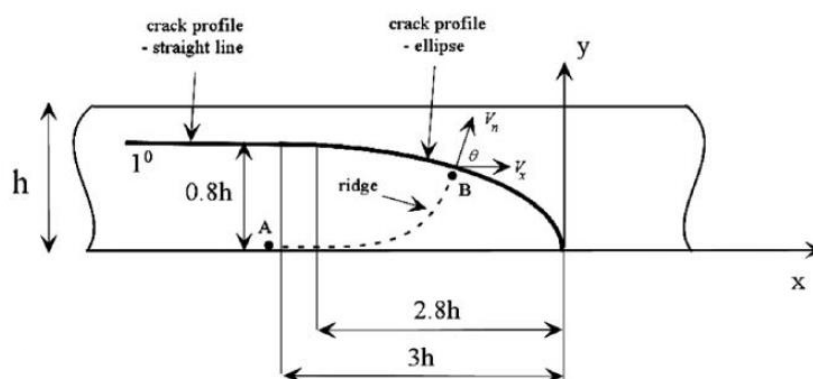


FIGURE 3.5: The crack front shape under bending, the dotted line denotes the atomic debonding path [SHE 04b].

This chapter focuses on the crack behavior along (110) plane of silicon single crystal under 4 point bending. The high speed camera was used to assess the crack propagation velocity. Finite element model was elaborated for static energy release rate. Fracture surface observations were conducted by diverse microscopic tools such as confocal optical microscope (COM), scanning electron microscope (SEM) as well as atomic force micro-

scope (AFM). The AFM topographies were analyzed with WSxM software [HOR 07].

2 Experimental procedure

The specimens are $50 \times 50 \text{ mm}^2$ single crystalline silicon plates, as presented in chapter 2. As previously mentioned, they were obtained from silicon cylinder with diamond wire sawing and (110) cleavage. The latter results in a thickness around $200 \mu\text{m}$. A scouring is carried out to eliminate a small layer of the damaged surface, while the saw traces (see FIG. 3.6) are intentionally kept in order to generate the surface marks. A pre-crack is introduced with a Vickers indent at one edge center of each specimen. In order to have variant crack velocities, two strategies (see FIG. 3.7) are used to control the pre-crack's dimension. The first one is to indent the specimen on a rigid plat support so that a sharp notch can be obtained, the second one is to indent the specimen edge into a shallow hollow valley so that a longer pre-crack is generated.

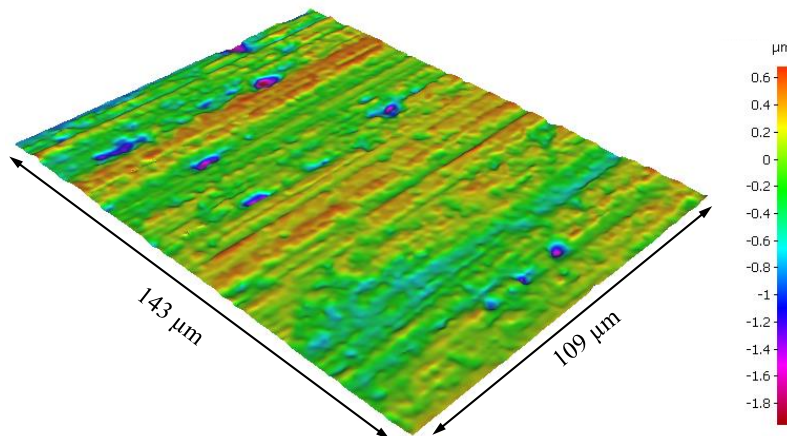


FIGURE 3.6: Surface roughness measurement conducted with a profilometer. The wire sawing traces can be revealed on the mono-crystalline silicon wafer.

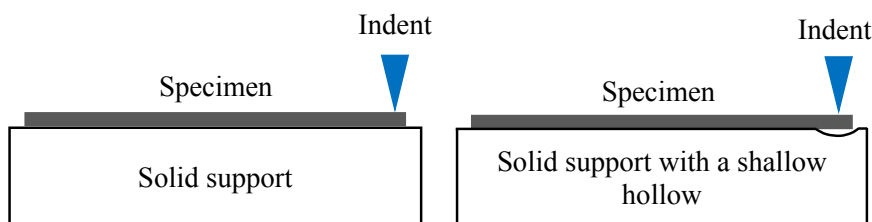


FIGURE 3.7: Two strategies for pre-crack introduction.

4-point bending was chosen to perform the fracture tests. This kind of loading allows to get rid of contact influence on the crack path. The inner and outer spans are 21 mm and

40 mm for the used bending set-up. The specimens are loaded quasi-statically (10^{-6} /s) with a LLOYD-Ametek LFPLUS electro-mechanical machine. The crack velocity was measured using a high speed camera (Phantom V710) and a 45° tilted mirror. The experimental set up is schematized in FIG. 4.7 for a better readability. Since the crack path is straight, the observation zone can be reduced to 512×64 pixels. Thus, the image acquisition frequency is set to 180kHz to track more quickly the fracture process. The crack length was estimated with image post processing, thanks to the light refraction variation with the crack propagation (see FIG. 3.10). It consists in performing subtraction between the images after the crack initiation and a reference image before the cracking. Then, contrast reinforcement as well as denoising (Matlab Wavelet algorithm) were performed to highlight the crack tip position. This high speed imaging analysis allows to address a large crack velocity range, from about 1000 m/s to 3700 m/s. With a crack position uncertainty of approximately 5 pixels, the velocity uncertainty is 100 m/s.

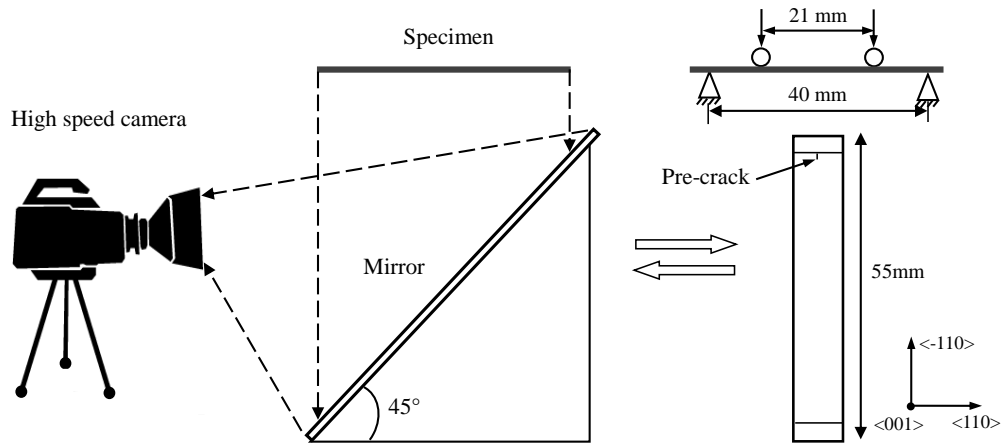


FIGURE 3.8: Experimental set up of 4 point bending tests equipped with a tilted mirror and a high speed camera.

3 Crack velocity

90 tests have been carried out, for each of them we have measured the crack propagation velocity and observed the fracture surface under the COM. Depending on the pre-crack's size, varying fracture stresses and propagation velocities were obtained and plotted in FIG. 3.9. The stress is estimated with beam theory. The velocity varies from 1000 m/s to 3700 m/s, *i.e.* $0.22C_R$ to $0.83C_R$ ¹. It can be seen that the crack velocities that are measured tend towards the terminal velocity (3800 m/s) highlighted in [CRA 00], which means that our results in bending configuration is in good agreement with that in tensile tests. This terminal velocity, as presented by the red line, is about 700 m/s lower than the Rayleigh velocity as presented by the blue line in FIG. 3.9. This velocity

1. C_R denotes Rayleigh velocity, in [110] direction on (110) plane, C_R is 4460 m/s [COU 94]

gap has been interpreted as a result of energy dissipation conducted by phonon emission [CRA 00].

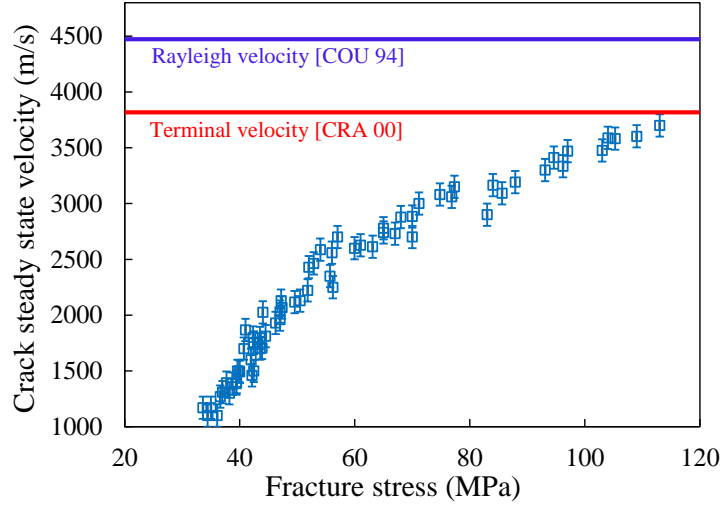


FIGURE 3.9: The measured crack propagating velocities with respect to the fracture stress, each point corresponds to one test.

In fracture mechanics, the crack initiation and propagation in brittle materials obey widely the Griffith criterion [GRI 21] and the Freund condition [FRE 90b], under condition that the crack tip is sharp. For the initiation :

$$G_s = \Gamma_0 = 2\gamma \quad (3.1)$$

G_s is the static energy release rate (SERR), Γ_0 stands for the material toughness which equals to 2 times the surface energy of the fracture plane γ .

During steady state propagation, Freund condition states that the SERR, *i.e.* the propagation driving force, should be associated with the dynamic toughness Γ_D , the crack velocity v as well as the Rayleigh velocity C_R :

$$G_s \left(1 - \frac{v}{C_R}\right) = \Gamma_D \quad (3.2)$$

Indeed, if the Griffith criterion is met at initiation, the initial crack velocity would be zero and the crack will progressively accelerate to steady state. However, if the crack tip is blunted by phase transformation as the loading increases, how will the crack behave when the global stationary state is broken?

In this section, the presentation of the main results begins with the steady state velocity, which is the major concern in dynamic fracture. A particular study is then dedicated to fracture initiation behavior, that is the initial crack velocity. Moreover, with the known crack velocity, we will be able to verify whether the crack path deflection from (110) to (111) takes place at velocity higher than 1560 m/s (which is the conclusion in [SHE 03b, SHE 04b]).

3.1 Steady state velocity

As mentioned in Section 2, a massive experimental test program has been conducted within a large crack velocity range. Some representative fracture processes are illustrated in FIG. 3.10. The faster the crack, the fewer images the high speed camera can capture. When the velocity is larger than 3000 m/s, only one or two crack length increments can be precisely captured (see FIG. 3.10(d)-3.10(f)). However, since the crack has already propagated over several millimeters, the steady state is assumed to be reached. Even a few images are sufficient.

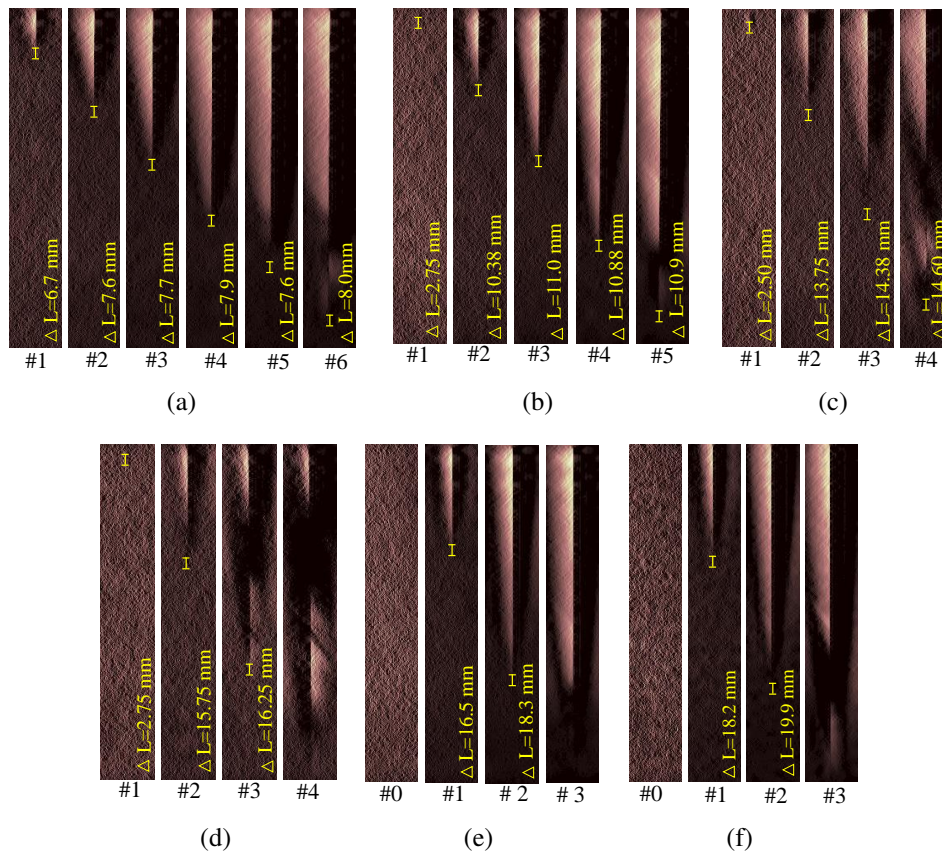


FIGURE 3.10: Crack propagation tracked by high speed camera and highlighted thanks to wavelet denoising. Cases for crack steady state velocities of 1400 m/s, 2000 m/s, 2600 m/s, 3000 m/s, 3300 m/s, 3600 m/s (a)-(f). The yellow bar stands for the uncertainty of the crack tip position. Number 1 denotes the first image revealing the crack propagation and number 0 is the image just before.

From the fracture processes presented above, the crack velocity profiles were addressed (see FIG. 3.11), accounting for sometimes the image #0, *i.e.* the image before the first image (#1) that shows a visible crack length. With each length increment highlighted in FIG. 3.10, an average crack velocity was calculated, considering a fixed time lap of 5.56 μ s. In FIG. 3.11, for the plots that start exactly from 0 (crack length), the image #0

gets involved, the related average velocity could be higher since the time gap should have been smaller than $5.56 \mu\text{s}$. It can be noticed that each crack goes into a steady state propagation. This observation is in good agreement with previous works based on either tensile tests [CRA 00] or bending tests [SHE 03a]. Since the specimen is under a quasi-static loading which results in an uniform stress field along the crack path, the crack propagation is then feeded by the release of the elastic energy ahead the crack front. As the stress drops while the crack length increases during the propagation, the static energy release rate (G_s or SERR) reaches a constant value and thus leads to a steady state propagation.

Besides the steady state propagation, what draws our particular attention in FIG. 3.10 is that, for all cases, the average velocity even in the early stages of the process is comparable to the steady state velocity. In order to further clarify the determination of the initial crack velocity, a dedicated investigation is carried out and presented in the next section. Particularly, the steady state velocities measured by the high speed camera are used to build a correlation between the crack velocity and the fracture surface morphology (see next section, FIG. 3.18). Then the latter can be referred to monitor the local crack velocity, such as in the early stage of propagation.

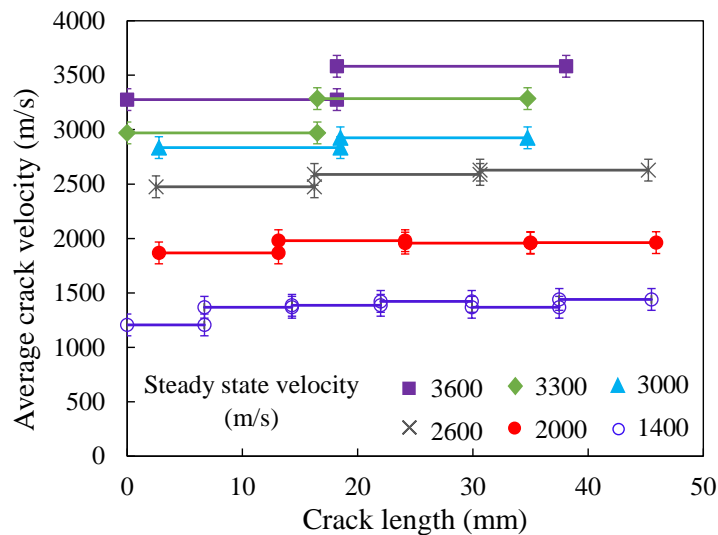


FIGURE 3.11: Crack velocity profiles measured as a function of the crack length.

3.2 Initial velocity

It has been revealed in the previous section that the crack velocity in the early stage of the propagation is close to the steady state velocity (see FIG. 3.11). This observation is contradictory with the measurement obtained with the "potential drop" method in the literature, which provides a long acceleration phase from very a low crack velocity to the steady state velocity (see FIG. 3.1(a) and 3.1(b)). This method measures in fact the crack length in a second body (thin film in copper or chrome) which is ductile. Thus hysteresis

can be problematic which can invalidate the crack tracking in the early crack propagation in silicon. In order to more precisely determine the crack initial velocity, two approaches were used : the first one is to calculate the SERR at crack initiation and then use the Freund condition to predict the initial velocity; the second one is to analyze the crack surface morphology at the crack initiation spot and to determine the velocity using the velocity-fracture surface correlation.

3.2.1 SERR at crack initiation

SERR at cracking initiation can be assessed thanks to the recorded fracture stress and the well controlled pre-crack shape. The latter can be distinguished on the fractography. We notice in FIG. 3.12 that the pre-crack front presents either elliptical shape or as a tilted straight line with respect to the two indentation supports (see FIG. 3.7). Concerning the elliptical shape, the long and short axes (a and b) are around 0.8 and 2.8 times the specimen thickness (h). The front part behind the $2.8h$ is like a straight tail. This shape is very close to that reported in [SHE 03a, SHE 08] (see FIG. 3.5).



FIGURE 3.12: Two different precrack front shapes in accordance with the two precracking strategies. Crack propagation $< 2900\text{m/s}$ initiates from long elliptical precrack (a) and crack propagation $> 2900\text{m/s}$ starts from short straight precrack (b). The dimension can be referred to the specimen's thickness *i.e.* $190\ \mu\text{m}$

The SERR was estimated by a finite element simulation with the commercial FE software Abaqus 6.13-4. In order to limit simulation time, only a square part of $5 \times 5 \times 0.195\ \text{mm}^3$ of the specimen is considered. In order to reproduce the pure bending loading of the experiment on the reduced part, a pure bending moment is applied at the edges (see FIG. 3.13(a)). The pre-crack modeling is shown in FIG. 3.13(b) and 3.13(c), which takes into account the real pre-crack shape. The whole model is meshed with quadratic brick elements with reduced integration (3D 20-node C3D20R elements with Abaqus) for higher accuracy. Particularly, the elements surrounding the crack front are degenerated to wedge elements in order to well represent the sharpness. The element quantity varies from 20000 to 30000 with respect to the shape as well as the dimension of the pre-crack. 15 simulations with varying pre-crack geometry have been carried out. For each analysis, the SERR (Gs) is computed with the J-integral ([PAR 77, SHI 86]) around the crack tip at the tensile face of the bent specimen when the applied stress in the far-field reaches the experimentally deduced fracture stress. The estimated SERR at initiation are presented as a function of the crack velocities in FIG. 3.14. For comparison,

3. Fracture in single crystalline silicon

the SERR for crack steady state propagation [CRA 00] is added in the same figure. Two main observations can be noted, followed by a deduction on crack initial velocity :

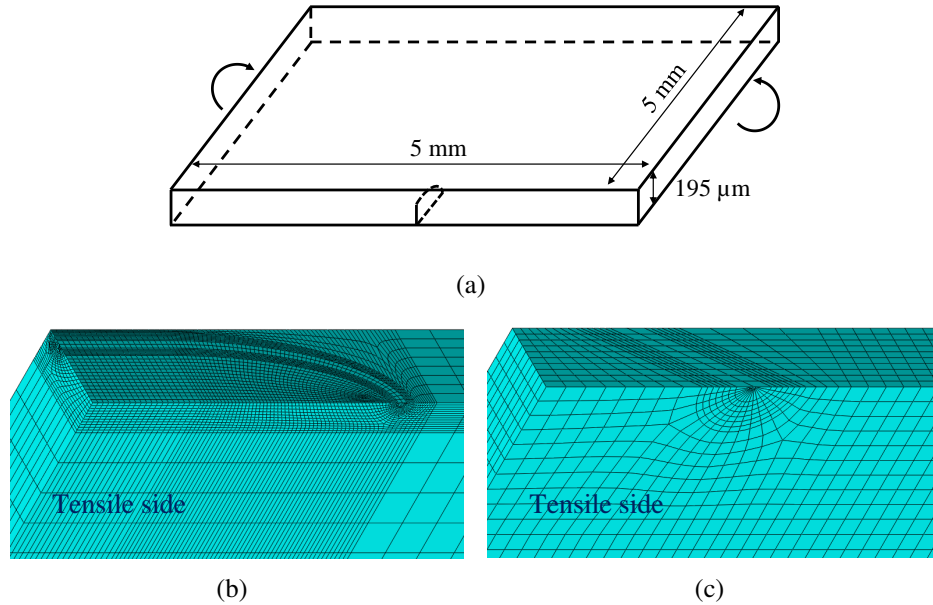


FIGURE 3.13: Finite element analysis of SERR at crack initiation. Geometry of the analyzed structure loaded by pure bending (a), snapshots on the modeled pre-crack with elliptical front shape (b) and pre-crack with tilted straight front shape (c) corresponding to the experimental pre-cracks as presented in FIG. 3.12(a) and FIG. 3.12(b).

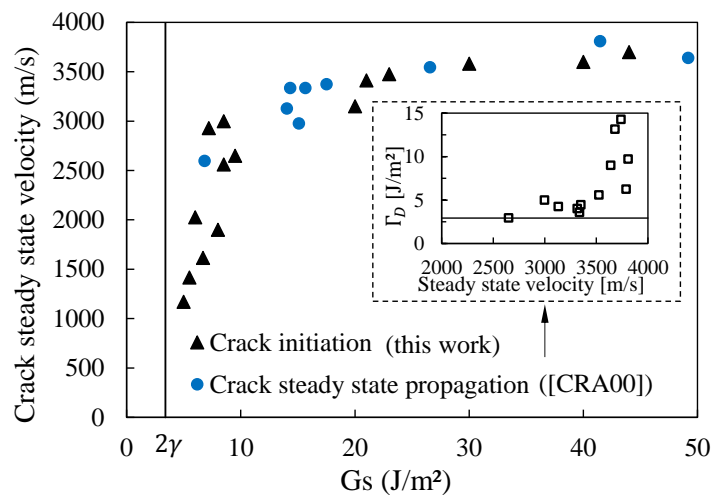


FIGURE 3.14: Energy release rate at crack initiation (assessed in this study) and propagation (reported in [CRA 00]) with respect to different steady state velocities.

i) at crack initiation, the SERR is always bigger than the static material toughness (the vertical line), and it evolves as the steady state velocity varies from one case to another.

ii) the SERR at initiation and during propagation have comparable dependence on the crack propagation velocity. In other words, the SERR at initiation can "predict" the further crack steady state velocity v .

According to EQ. 3.2, the crack initiation is directly associated with a non negligible initial velocity v_0 .

$$v_0 = C_R \left(1 - \frac{\Gamma_D}{G_s}\right) \quad (3.3)$$

G_s is obtained with the finite element analysis (SERR at initiation), the dynamic toughness Γ_D can be extracted in experimental results of [CRA 00], as shown in the center figure in FIG. 3.14. EQ. 3.3 is theoretically valid for a steady state propagation, however, it is used here to assess the order of the magnitude of the crack initial velocity. The results are plotted in FIG. 3.15. The straight line represents the diagonal of the plane composed by the two axes. So when a point is above the line, it means that the steady state velocity is larger than the initial velocity. We note that the two velocities are comparable for each case, the steady state velocity is generally a little larger. The similarity points out that the crack initiation state is very close to the steady state. In other words, the crack very quickly jumps to a very high velocity when the stationary state of the material is broken. This conclusion is in good agreement with [BUE 07] (see FIG. 3.1(c)). Indeed, the silicon requires higher energy flux than toughness to break the atom bonds affected by the local phase transformation in order to initiate the cracking. Thus, upon initiation, the extra energy would be dissipated instantaneously, the structure should undergo rapid new surface creation, *i.e.* a large crack initial velocity.

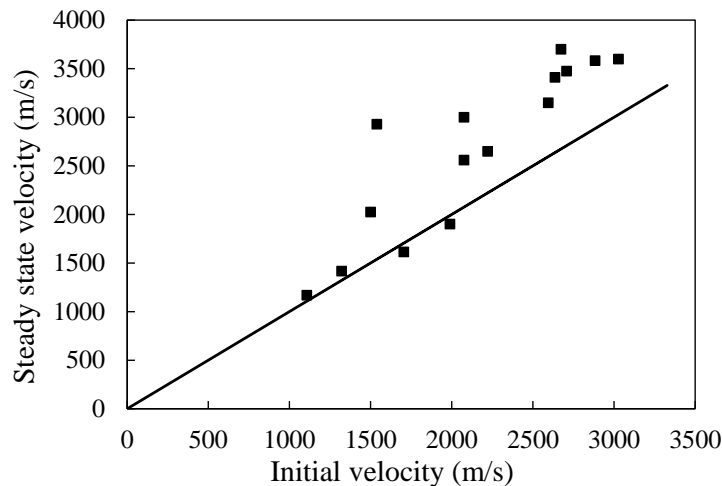


FIGURE 3.15: Initiation velocity versus propagation velocity. The straight line represents the assumed case such that the propagation velocity is equal to the initiation velocity.

3.2.2 Fractographic monitoring

The previous calculations are based on experimental data which are only available at the instantaneous crack initiation. A fractography analysis was carried out in order to clarify the crack propagation in the early stage and how fast it reaches the steady state. The analysis was based on the crack surface marks whose shape show strong velocity dependence (the surface marks and the velocity correlation will be analyzed more in detail in Section 4.2). Thanks to massive fracture surface observations, we have built a correlation between the surface marks and the steady state velocity, as mentioned in section 3.2.1 and figured out in FIG. 3.16(a). When looking at the fracture surface (FIG. 3.16(b)) with steady state velocity of 3600 m/s, we can notice that the crack velocity exceeds 2800 m/s at a crack length of 100 μm and reaches mostly the steady state starting from a crack length of 300 μm . This revealed crack initial state is in quantitative agreement with the estimated initial velocity (2900 m/s) from SERR at crack initiation (see FIG. 3.14).

According to the crack velocity measured using the high speed camera, the crack initial velocity predicted with the Freund condition based on the SERR, as well as the fractographic analysis at the crack initiation spot, we can conclude that the cracking process in silicon has an initial velocity comparable with the steady state velocity. This conclusion can be an experimental evidence of the phase transformation at the crack tip [BUE 07].

3.3 Global crack stability

In the literature, Sherman and Be'ery [SHE 03b, SHE 04b] have stated, using 3-point bending tests, that the crack would deflect from the initial (110) plane onto the (111) plane when the crack velocity reaches 1560 m/s. Nonetheless, in their 3-point bending set up, the crack propagates right under the punch roller and thus can be disturbed by the contact conditions. Hence, their conclusion should be considered with caution. It should be noted that in the tensile configuration for the same cleavage tests, only very tiny surface deflection can be observed in local hackle regions for a extremely rapid (3800 m/s) crack, as shown in [CRA 00].

With our fracture tests for which the crack velocities are known, and the 4-point bending ensures a disturbance free loading, the crack stability has been examined. According to the crack surface observations under confocal optical microscope (Keyence VHX-2000), all the primary cracks initiating from the pre-cracks reside on (110) plane as can be noted for example in the fractographic images in FIG. 3.17(a). No evident deflection onto (111) plane has been revealed, even for the extremely high velocity of 3700 m/s. This finding contradicts the crack plane deflection reported in [SHE 03b, SHE 04b]. We suppose that the observation in our work is more reliable since the primary crack undergoes a contact free stress field in 4-point bending, while the deflection observed in [SHE 03b, SHE 04b] should be due to the contact which induces a complex stress field with non uniform contact pressure and perhaps lateral friction. Indeed, it has already been demonstrated that the deflection from (110) [110] to (111) plane can be conducted by stress disturbance such as a shear component [KER 08]. This supposition has been ve-

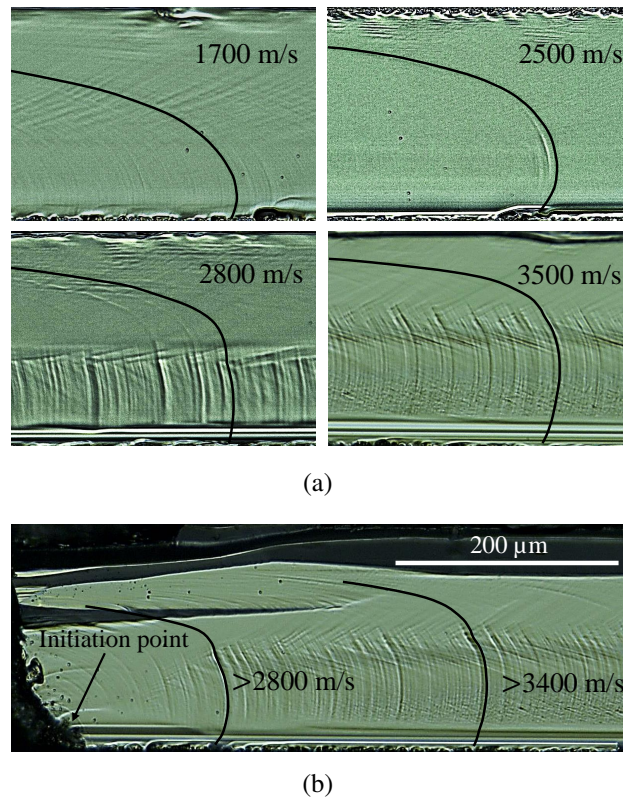


FIGURE 3.16: Fractographic determination of crack initiation state. Snapshot of correlation between the surface marks and the steady state velocity with massive studies (a), the fractography at initiation spot for the crack with steady state velocity of 3600 m/s (b).

rified in our work, for a crack propagating faster than 3600 m/s, secondary cracks arised underneath the punch rollers, these cracks propagated locally or totally on (111) plane, as shown in FIG. 3.17(b). The tilt angle is about 33° , which is close to angle between (110) and (111) plane, *i.e.* 35.2° . The topographies in FIG. 3.17 are obtained with the confocal optical microscope. The reconstruction begins from the lowest position and ends at the highest position² with the microscope's head moving up every μm .

The deflection free propagation points out that the (110) cleavage is quite stable when no significant perturbation impacts the stress field at the crack front.

3.4 Summary on the crack velocity

Well-controlled experimental set-up allowed the measurement of very fast crack propagation velocity within a single crystal of silicon (*i.e.* from 1000 to 3700 m/s for steady state propagation, see FIG. 3.11), thanks to high speed image analysis (180 kHz). It has been revealed with the high speed imaging that crack initial velocity of the fracture pro-

2. The lowest position and the highest position are defined such that the lowest region and the highest region of the crack surface are the clearest to the naked eye through the microscope.

3. Fracture in single crystalline silicon

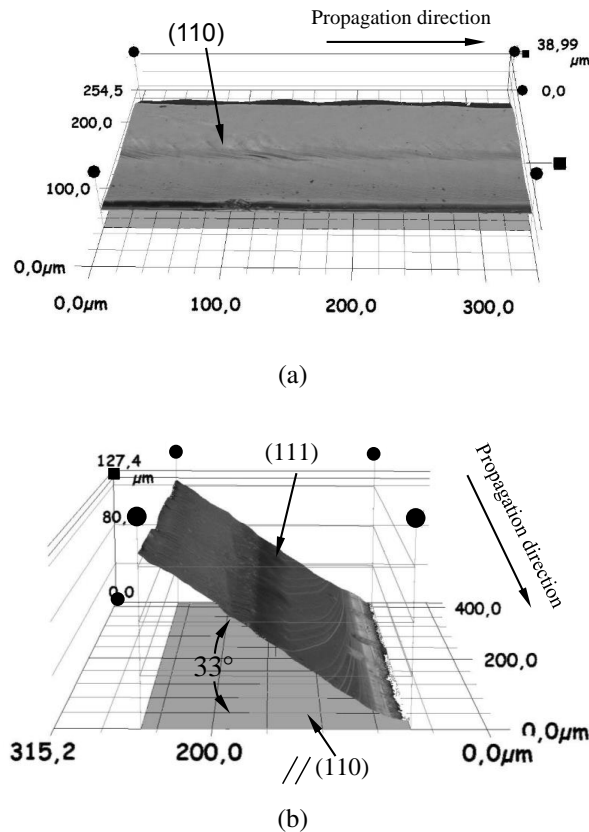


FIGURE 3.17: Crack surface topographies for the rapid propagation case of 3600 m/s. (a), topographic surface of the primary crack that initiates from the pre-crack. (b), topographic surface of the secondary crack that initiates underneath the punch roller.

cess is very high (see FIG. 3.11). This revelation has then been confirmed by two evidences : the first one is the static energy release rate upon the crack initiation which is higher than the material toughness ; the second one is the estimation of the velocity thanks to the crack velocity-crack surface morphology correlation. Both indicate that the crack initial velocity is nearly comparable with the steady state velocity. The fracture surface of each of the 90 samples has been carefully observed. Conversely to some works recently published [SHE 03b, SHE 04b], we show that there is no (110) to (111) cleavage plane deflection neither crack branching, for well-controlled pure bending loading, even when the crack is propagating at speed up to 3700 m/s. On the other hand, our experiments confirm the occurrence of the (110)-(111) deflection phenomena, but only in the volume where the stress is multi-axial *i.e.* nearby the contact with the punch rollers. We conclude that the crack velocity will not affect the crack propagation path in the silicon single crystal, at least for the (110) cleavage. Since the crack surface is free of deflection, then it is possible to investigate the crack front shape for velocities higher than 1560 m/s.

4 Crack front determination

In bending condition, the crack front is curved due to the in-thickness stress gradient. As a result, the local crack velocity through out the thickness is not constant : it is the largest at the lower surface of the specimen and corresponds to the global velocity that we measure with the high speed camera ; then, it decreases from the lower surface to the upper surface of the specimen. The crack front shape allows to address the local velocity at any spot along the crack front which is eventually needed to interpret some local crack behaviors. For example, Sherman et al. [SHE 04b] relied on the local velocity to elucidate the onset position of surface instabilities on (111) cleavage plane.

As mentioned in the introduction, under bending condition, the crack front shape on (110) plane has been investigated only for velocities below 1560 m/s because of the cleavage plane deflection at higher velocity [SHE 03a, SHE 04b]. However, the result has then been used for higher crack velocity cases [SHE 04b] without verifying whether the front shape evolves with the crack velocity or not. In the previous section, we have shown that the deflection has not been encountered even at 3700 m/s, thus the crack front shape can be investigated for a large velocity range. Knowing that there is no technique which is capable to capture in-situ a rapid crack front shape in an opaque material, the determination will be addressed with fractographic analysis. In this work, we rely on the Wallner lines.

4.1 Wallner lines shapes

It has been shown in section 3.2 that the crack surface is covered by surface marks whose shape depends on the crack propagation velocity. In fact, these marks are generated due to the presence of the wire sawing traces on the specimen's surface. All the specimens have been observed under the optical microscope, the representative morphologies relative to the crack velocities are presented in FIG. 3.18. The surface marks are highlighted with the black solid lines for better readability and to be distinguished with the special surface marks as can be noticed in FIG. 3.18(d) (see also section 5). These black solid lines are then superimposed in FIG. 3.18(e) for comparison. The dotted lines represent the atom debonding path, which is also the local crack velocity direction along the crack front. The determination of the local velocities based on the debonding orientation will be addressed in section 5.3.1.

As mentioned in the introduction section, two kinds of surface marks can be encountered, the Wallner lines and the Front Waves (FW) traces. The observed marks are less remarkable at the lower part than at central and upper part (see FIG. 3.18(b) and FIG. 3.18(d)), if they were FW traces, they would be the most outstanding (according to the FW properties as presented in section 1.) since the crack front-asperity interaction takes place at the lower surface of the specimen. Hence, we consider that these marks are Wallner lines³.

3. These hollow like surface marks are widely recognized as Wallner lines in bending loading [FRÉ 90a, SHE 04b], the justification is addressed here just to distinguish the Wallner lines with the Front Waves traces

3. Fracture in single crystalline silicon

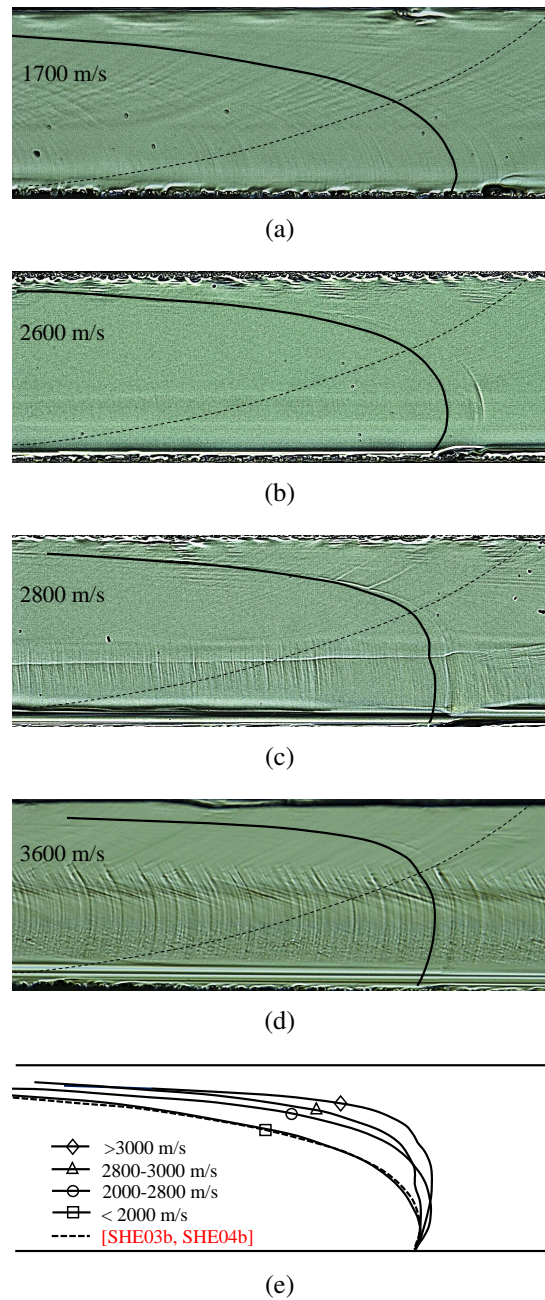


FIGURE 3.18: Crack surface for different propagating velocities. Representative for velocity below 2000 m/s (a), representative for velocity between 2000-2800 m/s (b), representative for velocity between 2800-3000 m/s (c), representative for velocity beyond 3000 m/s (d), comparison of the former 4 shapes as well as the shape in [SHE 03a, SHE 04b] with <1700 m/s (e). Solid lines denote the Wallner lines and the thin dotted lines stand for the atomic debonding path. The dimension can be referred to the specimen's thickness *i.e.* 190 μm

The nucleation of the Wallner lines is due to the intersection of the moving crack front and the surface waves on the cleavage plane, as schematized in FIG. 3.20(a). The surface waves arise when the lower crack front encounters a surface defect (roughness), which is symbolized by the full circle at lower surface in the schematic drawing. In FIG. 3.18(a), the Wallner lines are representative for crack velocities below 2000 m/s, they look like ellipses. This shape is very close to that reported in [SHE 03a, SHE 04b], as figured out in FIG. 3.18(e). However, in the range of 2000 m/s to 2800 m/s and above 3000 m/s presented in FIG. 3.18(b), the Wallner lines present a hook shape. Particularly, in a narrow velocity range 2800 m/s to 3000 m/s, as we can see in FIG. 3.18(c), the Wallner lines change roughly the shape curvature at a certain height. This curvature jump can also be found on crack surface of larger velocity (>3000 m/s), but at higher position on the fracture surface, as revealed in FIG. 3.18(d). It should be noted that Wallner lines shape in silicon under bending for velocity faster than 1560 m/s has not been seen in the literature, especially the "discontinuous" shape has never been reported.

According to the generation scenario (FIG. 3.20(a)), the Wallner lines shape depends on the crack propagation velocity, the Rayleigh waves shape as well as the crack front shape. Since the Rayleigh velocity can be obtained in the literature [COU 94], the crack velocity has been measured and the Wallner lines are observed, the crack front shape can thus be determined, as will be presented in the next section.

4.2 Crack front evolution

Rayleigh waves depend only on the elastic properties of the material and thus their velocities are constant. Using the measurement in [COU 94], we can construct the wave shape during the wave dilatation. With the measured crack velocity, Wallner lines can be artificially reconstructed following the generation steps shown in FIG. 3.20(a). Supposing that the reported front shape, *i.e.* elliptical shape with $a = 3h$ and $b = 0.8h$ [SHE 03a, SHE 04b], remains consistent for any crack velocity, two cases with distinguished velocities of 1700 m/s and 3600 m/s are considered. The results are compared with experimentally observed Wallner lines in FIG. 3.19. Obviously, the assumption of the crack front shape consistency is wrong since the induced and observed Wallner lines' shapes are remote one from another, for the 3600 m/s case.

To determine the crack front shape, the following steps are performed, as illustrated in FIG. 3.20(b). This method is based on the idea that each point of a Wallner line belongs to the crack front at different moments, as the latter advances :

- i) choose a representative Wallner line, then discretize it from the lower part to the upper part with a couple of (n) surface waves using a fixed time increment Δt ;
- ii) conduct horizontal translations from the last discretized point and go down with distances $0, \Delta t.v, 2\Delta t.v, \dots, n\Delta t.v$ until the first discretized point, *i.e.* the lowest point on the Wallner line. v is the measured crack propagation velocity ;
- iii) after accomplishing the second step, n new points are obtained, the highest point being the last discretized point of the Wallner line. It consists thus in connecting these new points to get the crack front shape.

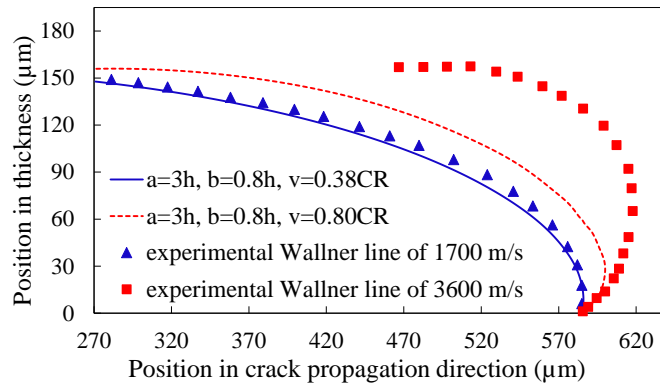


FIGURE 3.19: Comparison between the experimentally observed Wallner lines and composed ones following FIG. 3.20(a).

Thanks to this method, the crack front shapes corresponding to the cases presented in FIG. 3.18 are determined and shown in FIG. 3.20(c). Distinguished front shapes can be noticed for different crack velocities. The only common feature is that all the crack front shapes present an asymptotic part in the top part, the local velocity of this asymptotic part tends to zero (as will be addressed in section 5.3.1, FIG. 3.24(b)). For crack velocities below 2000 m/s, the crack front shape can be approximately described by the ellipse that highlighted in [SHE 03a, SHE 04b]. However, for velocity larger than 2000 m/s, the crack front shape can no more be associated with elliptical function. Beyond 2800 m/s, a curvature jump is observed and the onset height (the position of the curvature jump on the fracture surface) moves up as the crack velocity increases.

The evolution of the crack front shape can be explained by the following analysis : the velocity gradient in thickness impacts the energy release rate distribution, so that the crack front shape adjusts to accommodate the necessary energy flux. For example, when the crack propagates at 1700 m/s, the necessary static energy release rate (SERR) at the lowest point is 5.6 J/m^2 using the Freund condition (EQ. 3.2) and the material toughness in [PÉR 00b], *i.e.* $2\gamma_{(110)}=3.46 \text{ J/m}^2$. The local velocity decreases at the upper portion of the crack front and decreased down to zero at the asymptotic point (beginning point of the straight tail) where the needed SERR is equal to 3.46 J/m^2 . However, for the crack running at 3600 m/s, the SERRs at the two points are about 30 J/m^2 ([CRA 00]) and 3.46 J/m^2 , respectively, with the same calculation basis. Therefore, when the macroscopic crack velocity, *i.e.* the velocity of the lowest point changes, while the local velocity at the asymptotic point remains almost the same (null), the distribution of the necessary crack driving force (SERR) along the crack front varies. The variation then drives the evolution of the crack front shape. The curvature jump, never addressed in the literature, is visible in all of our fracture tests whose crack velocity is higher than 2800 m/s. It promotes a further detailed analysis in the next section which deals with the special surface marks.

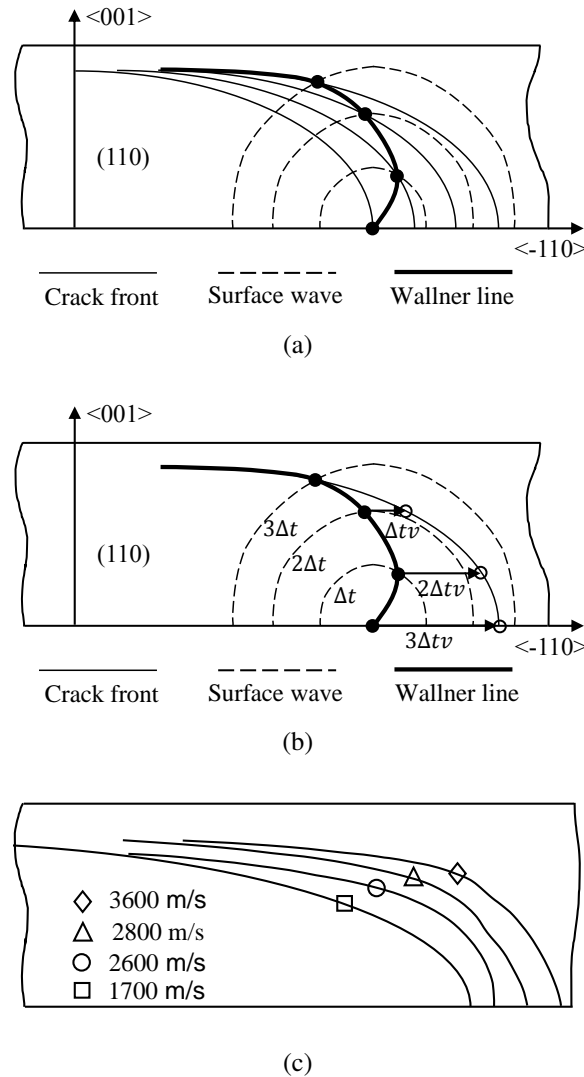


FIGURE 3.20: Crack front determination : method and results. The generation of Wallner lines from surface defects (a), method for recovering the crack front shape from Wallner lines and the surface waves (b), the real crack front shapes for different crack propagation velocities (c). The front for rapid crack presents curvature jump while that for slow crack is smooth.

5 High velocity surface marks

When a crack propagates faster than 2800 m/s, besides the Wallner lines, there present some special surface marks (SSM) and eventually some local instabilities at still higher velocity (above 3600 m/s). The SSM appear together with the onset of the curvature jump along the crack front. This section is dedicated to a description of the characteristics of these marks, to show the velocity correlated appearance and to propose a generation mechanism (front waves). It should be noted that the SSM have been encountered in 22 tests

and they are well reproducible at similar crack velocities.

5.1 Special surface marks characteristics

The SSM are periodic and cover the whole crack length (see central traces in FIG. 3.18(d)) from the crack initiation. A representative region of a crack whose steady state velocity is 3600 m/s is illustrated in FIG. 3.21(a) with an optical image, and then detailed with SEM observations in the following subfigures and AFM topographies in FIG. 3.22. Concretely, AFM topographies in FIG. 3.22(b)-3.22(d) address the central SSM, tiny instabilities and the lower SSM corresponding to FIG. 3.21(b)-3.21(d), respectively. FIG. 3.22(a) presents the micro-geometry along the black dotted lines shown in FIG. 3.22(b)-3.22(d). These lines are perpendicular to each kind of marks : central SSM, Wallner lines and lower SSM. The characteristics of the SSM are illustrated by the following observations :

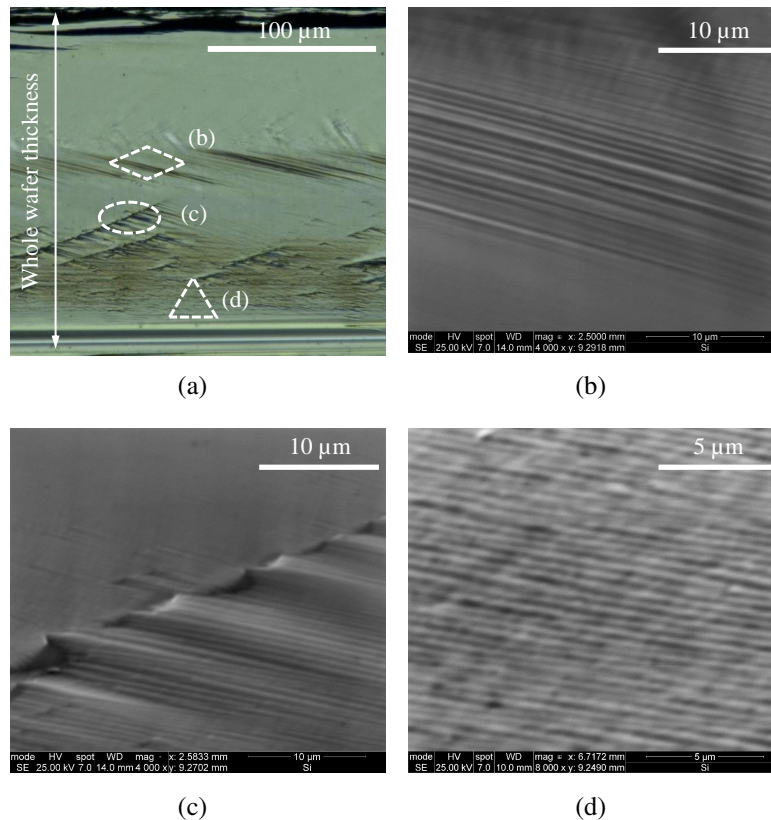


FIGURE 3.21: Special surface marks on (110) plane for a rapid propagation (3600 m/s). Optical images showing different marks at different loci (a). Local details obtained with SEM are illustrated in (b)-(d), which correspond to the framed regions in parallelogram, ellipse and triangle, respectively. The crack propagation direction is from the left to the right.

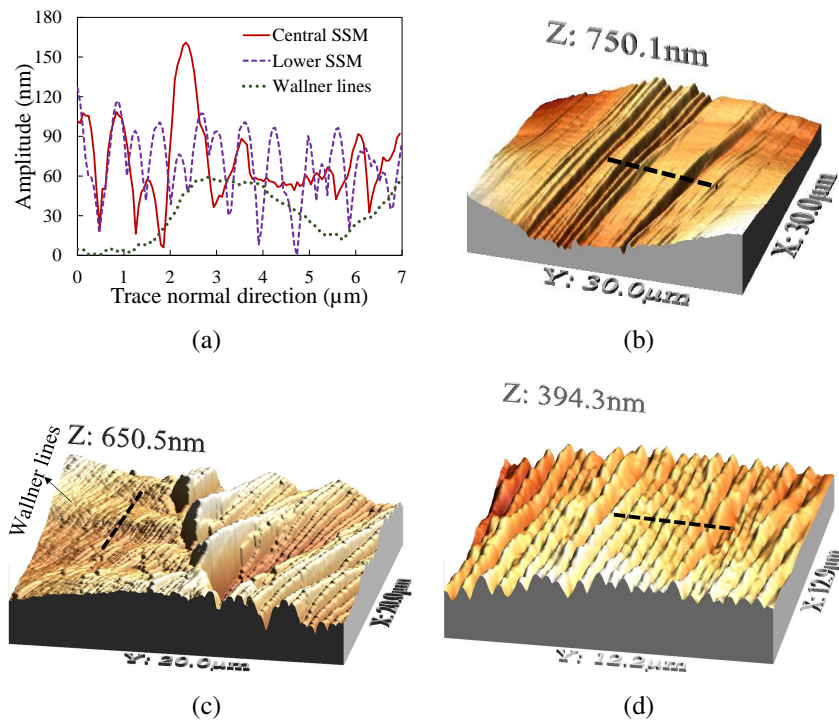


FIGURE 3.22: SSM characteristics imaged with AFM measurements. Spacing and amplitude of the SSM and the Waller lines along the straight dotted lines in the three following subfigures (a), central surface traces in the same region of FIG. 3.21(b) (b), surface instabilities & SSM in the same region of FIG. 3.21(c) (c), lower surface traces in the same region of FIG. 3.21(d) (d).

i) As shown in FIG. 3.21(a), the SSM are only present from a certain height (called onset height) to the lower portion of the fracture surface. The SSM onset height will be shown dependent on the crack propagation velocity in the next section. The displayed traces in FIG. 3.21(b) are almost straight and tilted by 15° from the horizontal line, *i.e.* the crack propagation direction (from the left to the right in FIG. 3.21). The SSM in the lower part present a similar tilt angle (see FIG. 3.21(d)). This similar angle seems to be characteristic and will be further investigated in the next section, in particular its link with the crack propagation velocity.

ii) According to the AFM topographies FIG. 3.22, one can see that the SSM consist of surface undulations more than local crack surface deflection onto (111) plane that was highlighted in [CRA 00] (see FIG. 3.4). The reported surface deflection is parallel to the crack propagation direction while the SSM are tilted by 15° . In addition, the deflection is not periodic, which is contradictory to the observed SSM in this study. The periodicity of the SSM indicates that they might be the traces of one kind of waves. This will be discussed in section 5.2.

iii) Local instabilities arise as revealed in FIG. 3.21(c) that generate more readable SSM. It can be noticed from FIG. 3.22(c) that the instabilities seem to nucleate upon in-

tersections between the atomic debonding and important undulations along Wallner lines. The local SSM amplitude sharply increases, followed by rapid decay.

vi) The micro-geometry variations along the black dotted lines of FIG. 3.22(b)-3.22(d) are plotted in FIG. 3.22(a), one can notice that the central SSM present similar spacing as the lower ones (in both cases the traces are distant of about $0.5 \mu\text{m}$). Concerning the amplitude, center SSM exhibit local peaks of about 150 nm and smaller heights between $50\text{-}90 \text{ nm}$. The lower SSM do not exhibit important peaks, the amplitudes are more constant, varying between $60\text{-}90 \text{ nm}$. These similarities conduct us to suppose that the SSM at the central and lower part are of same nature. However, Wallner lines manifest much larger spacing which is about $5 \mu\text{m}$. Thus, it can be concluded that the SSM are not generated by Rayleigh waves as the Wallner lines are. The SSM nucleate from a certain height and extend to the lower part with a slight decay.

5.2 Velocity correlation

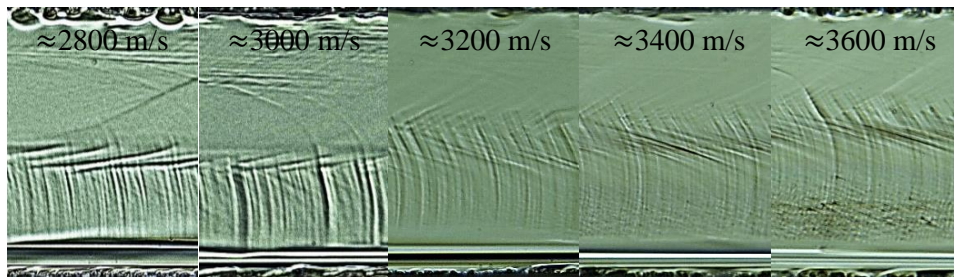
As shown in FIG. 3.23(a), a fracture surface velocity dependence can be observed for different steady state velocities. 5 cases are considered, with crack velocities increasing from 2800 m/s to 3600 m/s . It can be seen that as the velocity increases, the onset height rises (see FIG. 3.23(c)), while the tilt angle decreases (see FIG. 3.23(d)). Moreover, the SSM evolution can also be revealed when observing the fracture surface of a single crack that has a steady state velocity of 3600 m/s , around the initiation point, where the crack is slightly accelerating, as shown in FIG. 3.23(b). In this case, the SSM appear after a propagation length of $200 \mu\text{m}$ where the crack velocity reaches 2800 m/s . The onset height is about $0.33h$ (h stands for the specimen's thickness) and the tilt angle is about 28° . This corresponds well to the evolution tendency plotted in FIG. 3.23(c) and 3.23(d). Then the onset height increases and the tilt angle decreases, as the crack accelerates to the steady state. After a propagation length of about $800 \mu\text{m}$, the onset height is about $0.58h$ and the tilt angle is about 14° . Both are in good agreement with the curves in FIG. 3.23(c) and 3.23(d), they remain constant thereafter. Hence, it can be concluded that the SSM are dependent on the crack velocity in terms of the onset height and the tilt angle.

From the fractography (see FIG. 3.23(a) and 3.23(b)), it can further be observed that the SSM amplitude depends on the crack velocity : faster the crack is, more remarkable the SSM are. Meanwhile, the SSM spacing seems not influenced by the crack velocity. More characterization work should be performed with AFM topographies to confirm this optical observation.

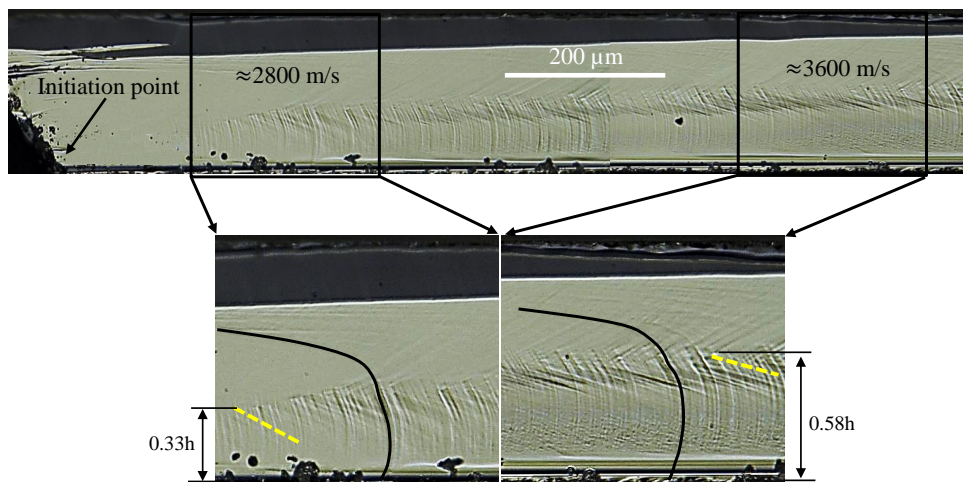
5.3 Special surface marks origin

5.3.1 Front wave hypothesis

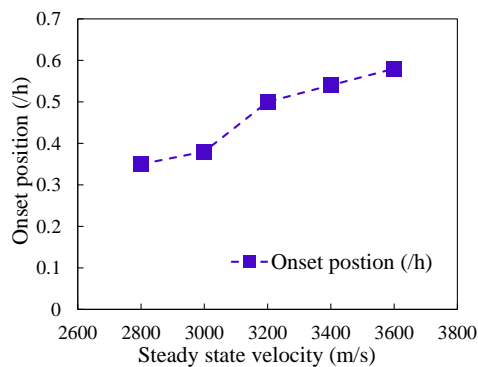
The former analysis eliminates the possibility of the SSM nucleation by surface waves (see section 5.1). Meanwhile, the characteristics of the SSM (Section 5.1), particularly the waving surface undulation morphology, are quite consistent with the specific aspects of



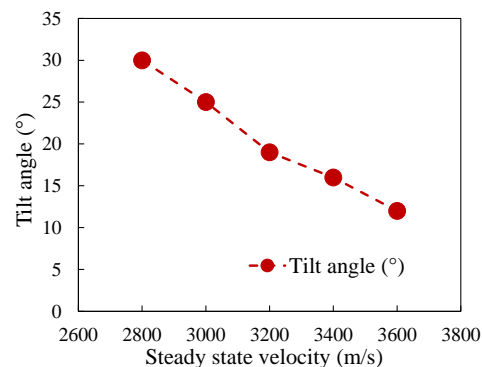
(a)



(b)



(c)



(d)

FIGURE 3.23: The SSM with respect to the crack velocity. The correlation with different steady state velocities (a), the SSM evolution in the transitory phase of a rapid crack (3600 m/s) (b), the onset position established with (a) (c), and the the tilt angle of the SSM established with (a) (d). For figures without scale bar, the dimension can be referred to the specimen's thickness *i.e.* 190 μm .

the Front Waves (FW) traces [SHA 01a]. As mentioned in introduction of this chapter, the crack FW are generally nucleated due to the presence of material heterogeneity (asperity, defect) [SHA 01a]. However, in this work, the used specimens are of high purity (99.99999% for general solar grade silicon [MOR 03]), there is little chance that the material defects (inclusions, precipitates) are present everywhere and regularly spaced. Even if we postulate well distributed defects, there would be no reason that the generated FW manifest crack velocity dependence. Thus, the material defects can be ruled out in the analysis of the FW source. Physically, the FW represent the consequence of important velocity fluctuations conducted by a strong gradient of the static energy release rate (SERR) along the crack front [MOR 98]. The local in-plane fluctuation will then render the other crack front loci waving to generate the so called front waves. The nucleated FW have not only in-plane component but also out-of-plane motion which leaves traces on the fracture surface. It should be noted that the SSM appear at a crack velocity beyond 2800 m/s, which is also the onset velocity of the curvature jump along the crack front. In addition, the SSM and the curvature jump raise at approximately the same in-thickness height and this onset height evolves in the same way with respect to the crack velocity. Therefore, we suppose that the curvature jump can be the underlying origin of the SSM. In order to interpret the curvature jump, we assess the local velocity along the crack front with the following equation, according to the velocity relationship revealed in FIG. 3.24(a) :

$$v_l = \frac{\sin(\alpha)}{\sin(\alpha + \beta)} \cdot v \quad (3.4)$$

v_l is defined as the crack local velocity along the atomic debonding path (revealed in FIG. 3.18). The curvature jump impacts on α which represents the front shape tangential slope, thus on v_l . Indeed, for any global crack velocity greater than 2800 m/s, the deduced local velocity curve presents a fluctuation, as shown in FIG. 3.24(b). The fluctuation happens at approximately the same height as the curvature jump along the crack front, and presents a strong crack velocity dependence (see FIG. 3.24(b)). Interestingly, when looking at the local velocity from the lower part to the upper part, the fluctuation occurs roughly after about the same velocity value, *i.e.* 2500 m/s, for any global crack velocity. This finding figures out that the SSM and the curvature jump might be jiggered due to the crack velocity gradient crossing 2500 m/s along the crack front.

In order to validate the FW assumption, a test has been carried out to examine the special surface marks (SSM). Taking into account the front shape and the FW nucleation spot, the FW traces can be artificially produced as the FW propagate to lower part at Rayleigh velocity. Two cases, 2800 m/s and 3600 m/s, are concerned for the reproduction of the FW traces which are then compared with the experimentally observed ones. The corresponding onset heights are $0.35h$ and $0.57h$ for the two cases. The results are shown in FIG. 3.25. Two distinguished FW traces are obtained, while each is in very good agreement in terms of tilt angles with the observed SSM. Thus, the assumption of FW traces can be adopted. In the next section, analysis will be conducted in order to elucidate the nucleation mechanism for the FW, which appear in most of the cases when material heterogeneity is present.

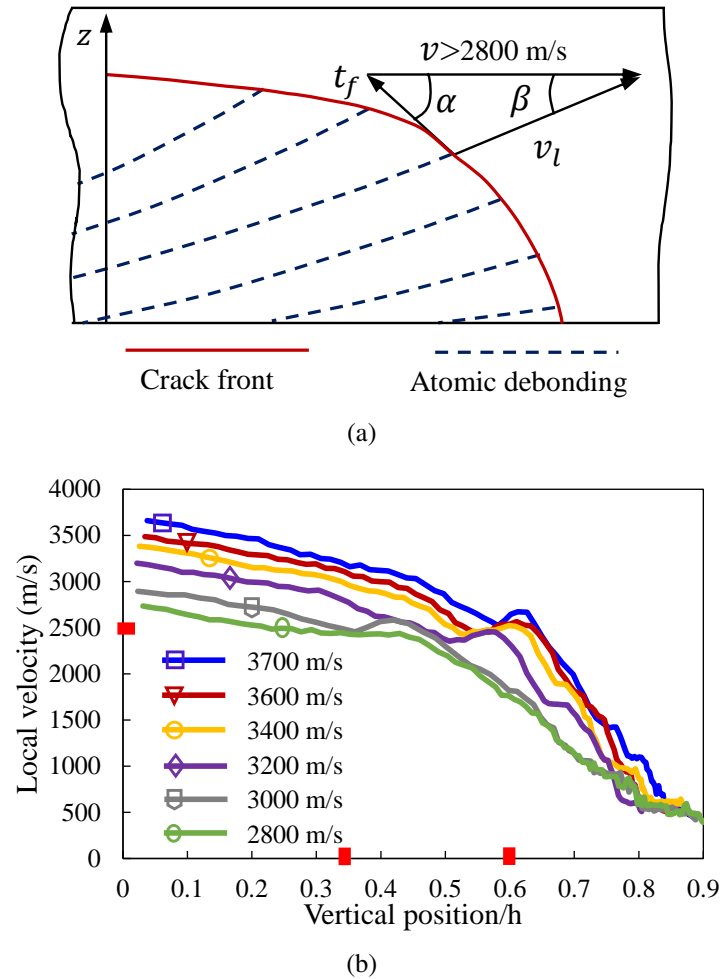


FIGURE 3.24: Analysis of the FW origin and generation process. The relationship between the local velocity v_l and the macroscopic propagation velocity v , t_f is the local tangent of the crack front (a), the local velocity plots for several propagation velocities (b), the red mark on the vertical axis indicates that the velocity fluctuation appears at approximately 2500 m/s for all cases, while the two red marks on the horizontal axis show that the fluctuation onset height varies between 0.34h to 0.6h.

5.3.2 Front waves generation mechanism

In former works, either in experimental framework [SHA 01a, SHA 02] or based on theoretical predictions [RAM 97, WIL 95, WIL 97], the FW are generated due to the presence of an asperity that changes locally the material toughness. Thus, upon the crack front encounters this impurity, the formerly established energy flux distribution can no more correspond to the need where the impurity is located. Consequently, the crack accelerates if the asperity reduces the material toughness or decelerates if the asperity enhances the material toughness. In any case, a crack velocity fluctuation will be initiated at the asperity location. This fluctuation propagates along the crack front and thus generates

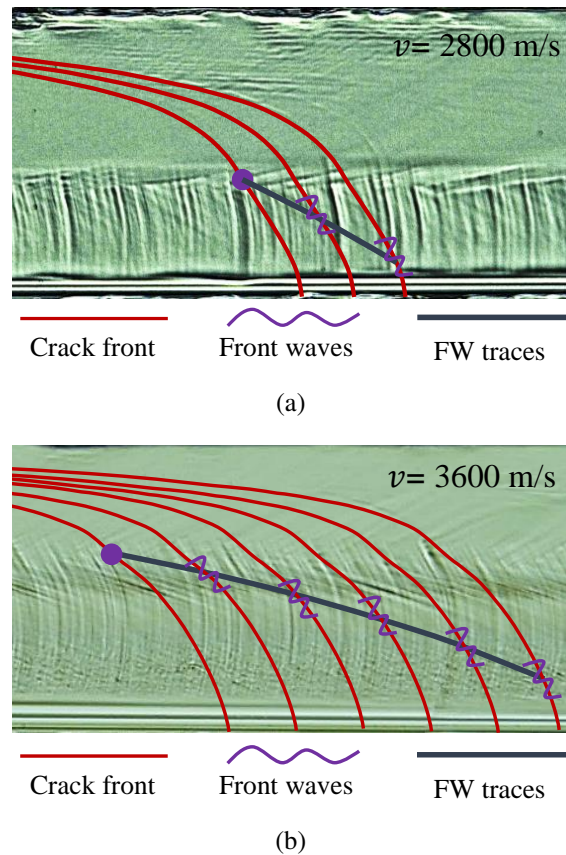


FIGURE 3.25: Real scale schema on the FW generation and propagation, the trace is compared with the experimentally observed SSM. Case for 2800 m/s (a), and case for 3600 m/s (b).

the front waves.

In our specimens, impurities should not be considered since the silicon is of high purity. Moreover, the overall presence and the periodicity of the SSM indicate that the FW are "intrinsically" generated. One should also keep in mind that the SSM have not been observed in tensile configuration, where the local crack velocity approximates to the global propagation velocity and the SERR is almost constant along the crack front. However, in bending condition, a crack velocity gradient appears and induces a gradient of SERR distribution along the crack front. Particularly, the dynamic material toughness (Γ_D) on silicon (110) plane is quite nonlinear. As shown in FIG. 3.26(a), Γ_D is equal to 2γ (the surface energy) for a crack velocity below 2700 m/s (we call transition velocity v_T), then it increases with the velocity. If we linearize this Γ_D evolution until 3600 m/s using EQ. 3.5 (see the blue dotted line in FIG. 3.26(a)), we will obtain, with EQ. 3.6, a SERR distribution profile along a 3600 m/s crack from the lowest point to the asymptotic point, as presented in FIG. 3.26(b). In FIG. 3.26(b), the dotted line represents the SERR distribution if the linear Γ_D evolution is retained for velocities lower than v_T , while in reality, Γ_D is equal to 2γ and remains constant below v_T . It can be noticed (solid line

in FIG. 3.26(b)) that the SERR distribution presents a gradient, but this gradient is not strong enough (we suppose) to nucleate the FW in the range of velocity greater than v_T as well as in the range smaller than v_T . However, at v_T , a SERR gradient jump appears due to the Γ_D evolution regime switch (from linear evolution to constant value). This jump can be more clearly revealed in FIG. 3.26(c). We propose that this SERR distribution jump has the same effect as the presence of an asperity, it conducts to a crack velocity fluctuation which renders the crack front shape to change locally (curvature jump) and nucleates the FW.

$$\Gamma_D = 2\gamma + (3600 - v_l) \frac{6 - 2\gamma}{3600 - 2700} = 3.4 + 0.002889(3600 - v_l) \quad (3.5)$$

where $\frac{6-2\gamma}{3600-2700}$ is the slope of the linearized evolution curve (dotted line in FIG. 3.26(a)).

$$G_s = \Gamma_D \left(\frac{C_R}{C_R - v_l} \right) \quad (3.6)$$

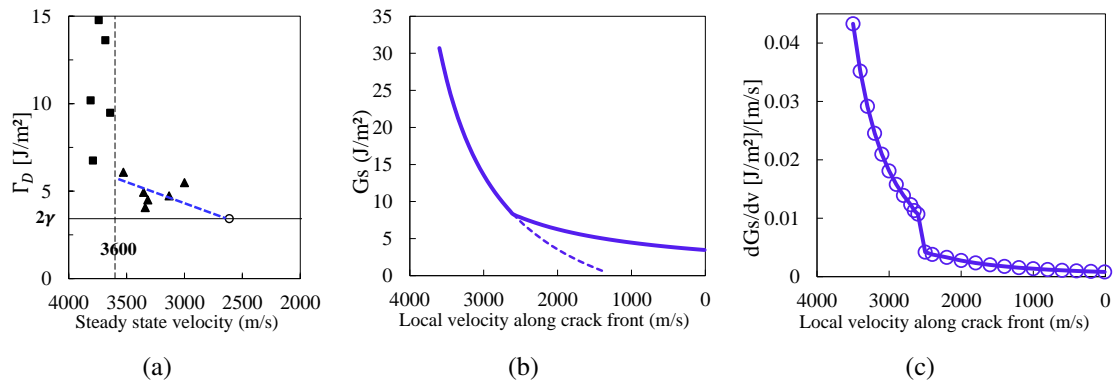


FIGURE 3.26: SERR and SERR gradient distribution along the crack front. Dynamic toughness extracted from [CRA 00] 3.26(a), the SERR distribution from the lowest point to the asymptotic point along the crack front (b) and the corresponding SERR gradient distribution with respect to the local crack velocity along the same path (c). The dimension can be referred to the specimen's thickness *i.e.* 190 μm .

6 Discussion

In this chapter, (110) cleavage has been addressed based on 4-point bending tests. The fracture behavior of 90 samples has been studied in order to propose reliable analysis and conclusions. The well controlled pre-cracks allow to obtain a large range of crack propagation velocities, from 1000 m/s to 3700 m/s. The crack velocities have been measured with high speed camera. The analysis of the cleavage plane has been performed thanks to several experimental methods : (confocal) optical microscope, SEM and AFM. Four

significant results have been presented, which are all crack velocity correlated : the deflection free cracking, the high initial crack velocity, the crack front shape evolution and the supposed FW nucleation, as will be discussed below.

6.1 Stability of (110) cleavage

In tensile configuration for (110) cleavage, even at a velocity as high as 3000 m/s, most of the crack surface are mirror like belonging to (110) plane (see FIG. 3.4 [CRA 00]). The present work deals with 4-point bending loading, here no evident (111) crack surface has been observed in the contact free region (inner span of the 4-point bending set up) even for a extremely great velocity of 3700 m/s. Thus, the strong stability of (110) cleavage can be concluded. In the other hand, the deflection revealed in 3-point bending framework [SHE 03b, SHE 04b] deserves more investigations. It is highly probable that the real deflection force is the contact perturbation or concentrated stress field rather than the crack velocity correlated fracture criterion.

When highlighting the outlook in chapter 2, it has been mentioned that, the crack initiated eventually on (111) due to the contact force, can deflect back to the right cleavage path, *i.e.* (110) plane. Another example is given below in FIG. 3.27. The crack initiates on a (110) plane and propagates to the two sides. For the left side, the crack resides on (110) plane. For the right side, the crack deflects onto (111) plane shortly when propagating under the contact force perturbation, but then comes back to the initial (110) plane. The (111) part covers a crack length of about 5 mm. From the fractography, the Wallner lines shape and the SSM indicate that the crack should have a velocity higher than 3500 m/s.

6.2 Crack initiation behavior

The estimated SERR by finite element analysis is shown systematically more important than the material toughness. The Griffith condition fails to predict the crack initiation probably since the phase change induces a crack tip blunting thus increases locally the material toughness [BUE 07]. When the crack driving force breaks down the atomic bonding reinforced by the the 5-7 double ring, the material undergoes then normal new cleavage surface creation.

Non negligible initial crack velocity can be predicted with Freund condition, due to the extra energy flux upon initiation. High speed imaging technique highlights a "quasi-steady state" upon the crack initiation. High initial velocity is theoretically possible since the crack front is massless so that the inertial effect is not relevant. Precise fractographic analysis gives insight to an important crack velocity near the initiation spot, which can be as fast as 3000 m/s when the energy flux ahead the pre-crack is much higher than the material toughness. A second proof should be highlighted for the elevated initial velocity. It concerns the special surface marks that arise only when the crack moves faster than 2800 m/s. In FIG. 3.23(b), it can be noticed that the special surface marks appear when the crack is 150 μm far away from the initiation point. It means that at this tiny crack length, the crack velocity reaches already at least 2800 m/s.

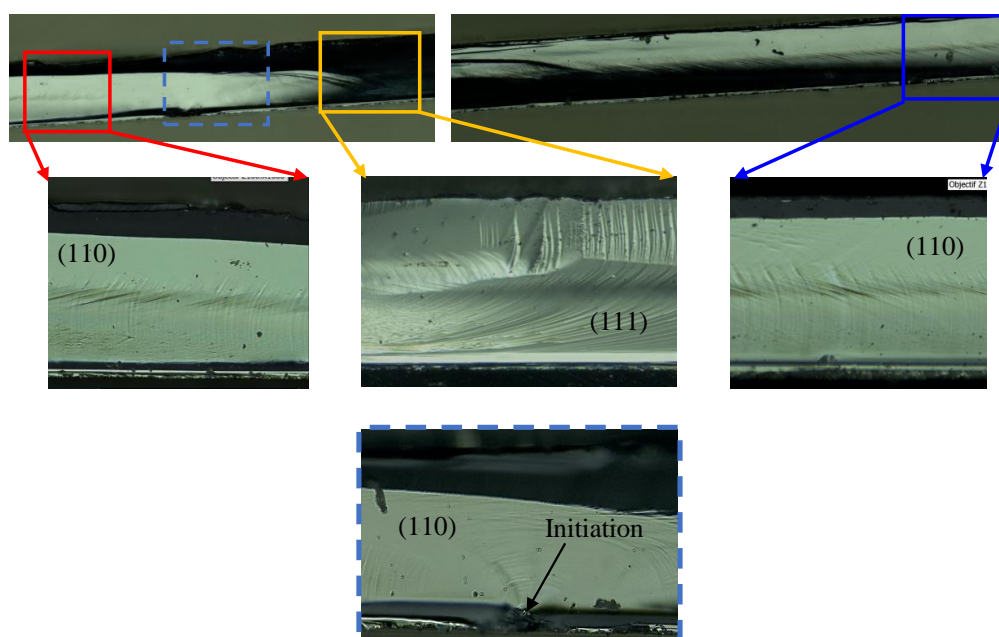


FIGURE 3.27: A case without pre-crack showing deflection from (111) to (110) plane under contact force perturbation. The dimension can be referred to the specimen's thickness *i.e.* 190 μm .

The present findings suggest that the 'potential drop' method (see introduction) has some limitations for capturing the beginning of crack length increase when the crack jumps from the stationary state to a high speed propagating state. This can be due to the material ductility of the coating layer which induces an hysteresis effect, or due to imperfect adherence or delamination of the coating layer at the edge of the specimen.

6.3 Crack velocity correlated crack front shape

Crack front shape variation is rarely reported in fracture investigation, especially when simple load (pure tensile) is applied and simple fracture mode (pure mode I) is concerned. Because of the uniform solicitation, the crack behavior is consistent along the crack front and all local velocities are aligned and equal to the macroscopic fracture velocity.

However, for bending condition, stress gradient arises in thickness which leads to a curved crack front. Each point along the crack front has its own local velocity that differs from one to another. From tensile side to compression side, the local velocity decreases from the macroscopic crack velocity at the lowest point until zero at the asymptotic point, *i.e.* after which the crack front is like a straight tail. Due to the velocity gradient along the crack front, the energy flux varies as well, so the crack front converges to an optimal shape to accommodate the needed crack driving force. The determination of the crack front shape allows to address the local crack velocity which then can eventually be used to elucidate special crack behavior or surface marks—in this work the generation of the

front waves.

6.4 Presence of front waves for high speed crack

This fourth achievement enriches well the former investigations for the fracture mechanism in the single crystalline silicon. We propose that crack front waves traces have been observed on the crack surface, which are related to a threshold velocity of 2800 m/s. According to our analysis (see section 5.3), the front waves are nucleated due to in-plane velocity fluctuation as well as surface waves' perturbation, both are in good agreement with the numerical prediction [WIL 97, MOR 98]. We propose that the velocity fluctuation is caused by special dynamic toughness-velocity correlation (presence of transition velocity v_T) rather than the material inhomogeneity. The v_T is equal to 2800 m/s in [110] direction on (110) cleavage plane [CRA 00]. We suppose a such transition velocity in other directions between [110] and [111] on (110) is slightly different from 2800 m/s. Here, we have obtained a velocity around 2500 m/s (see Fig. 3.24(b)).

7 Conclusion

With the high speed camera and the crack surface observation, this work has investigated the crack propagation velocity and the induced crack surface morphology on (110) plane of single crystalline silicon under pure bending. Following significant conclusions can be drawn :

(i) The (110) cleavage is stable, the crack path can be impacted by external perturbation but then rectifies when the perturbation diminishes or vanishes.

(ii) The crack initiation needs more energy flux than 2γ , thus the crack tends to propagate abruptly from a stationary state with high speed. The initial velocity is lower than but comparable to the steady state velocity.

(iii) The crack front shape has been demonstrated to evolve in function of propagation velocity.

(vi) Under bending, the crack front undergoes a local velocity fluctuation when the macroscopic velocity reaches 2800 m/s. The fluctuation turns to generate crack front waves. Consequently, the front waves give rise to marks on the crack surface that can be used as "post-mortem" determination of the crack velocity.

8 Outlook

Single crystalline silicon contains few lattice defects such as dislocations and grain or twin boundaries. It has been shown that the cleavage path is barely controlled by the surface energy when external perturbations are not involved. Conversely, the multi-crystalline silicon contains massive grain boundaries and sub-grain accommodated by dislocation coalescence. The crack path has not been properly investigated in the literature, and some vagueness rest to be figured out, such as what is the crack propagation

mode (trans-granular or inter-granular), what is the cleavage plane nature and how does the grain boundary affect the crack path? Therefore, the next chapter will be dedicated to investigate in-depth the fracture behavior of solar grade multi-crystalline silicon wafers.

Chapter 4

Fracture in multi-crystalline silicon

This chapter focuses on the fracture behavior of multi-crystalline silicon under 4-point bending configuration. The aim is to investigate the crack path as well as the grain boundary effect on the crack propagation. Twin specimens that contain the same grains have been tested under identical loading in order to assess the consistency of the fracture process. The fracture paths have been compared at the level of intersection trace on surface by macroscopic images as well as at the level the crack surface by microscopic fractography. The latter is also used to identify the cleavage plane thanks to special surface instabilities and to reveal the grain boundary crossing. Laue X-ray diffraction has been carried out to measure the grain orientations and further identify the cleavage planes without instabilities. It is observed that the fracture of multi-crystalline silicon is transgranular and can be totally reproducible. The crack takes place mainly on the crystallographic plane (111) and eventually on (110) one. The grain boundary can slow down or stop shortly the crack propagation. In order to reproduce the specific cleavage mode, a fracture initiation model has been elaborated in extended finite element framework which provides comparable results with the experiments.

Contents

1	Introduction	93
2	Materials and experimental methods	97
2.1	Multi-crystalline silicon plates	97
2.2	Bending tests with high speed imaging technique	98
3	Intergranular or transgranular fracture	100
3.1	Crack overlapping twin boundary	100
3.2	Zigzag crack path along grain boundary	101
4	Fracture path reproducibility	103
4.1	Inconsistent path	103
4.2	Consistent path	108
5	Crack velocity in multi-crystal	110
5.1	Fracture stress	111
5.2	Crack propagation velocity	111
6	Cleavage plane investigation	114
6.1	Fractography analysis	114
6.2	Cleavage plane identification with grain orientation	115
6.3	Fracture energy assessment	121
7	Grain and twin boundaries crossing	124
7.1	Misorientation characterization	124
7.2	Grain boundaries crossing	126
7.3	Twin boundaries crossing	130
8	Fracture modeling	133
8.1	Cohesive-XFEM method	133
8.2	Damage initiation model	134
8.3	Simulation	137
9	Discussion	140
9.1	Transgranular crack	140
9.2	Reproducibility of the fracture	141
9.3	Fracture path	142
9.4	Crack velocity and grain boundary effect	142
10	Conclusion	143

1 Introduction

As previously mentioned in chapter 3, single crystalline silicon (SCSi) predominantly fractures along either (111) or (110) cleavage plane. In chapter 3, (110) fracture surfaces have been investigated, Wallner lines and front waves traces have been highlighted.

Concerning other surface roughness risers on (110) fracture surface, local perturbations emerge (see FIG. 4.1) when the crack front encounters stationary dislocations [SHI 02, SHE 04a]. It can be noticed in FIG. 4.1(c) that even a single dislocation can induce a local cleavage plane deflection. The deflection region becomes larger and the deflection amplitude becomes higher when the dislocation number increases, as can be seen in FIG. 4.1(d). This indicates that the local disarranged atoms of the lattice make the crack path unstable. Regarding (111) fracture surface, Wallner lines are barely visible due to the presence of specific surface instabilities, as highlighted by Sherman and Be'ery [SHE 03a] in bending loading. This phenomenon has been recently demonstrated to be initiated at dopants [KER 13, BER 14], which locally deflect the crack when the propagation velocity is low [KER 08].

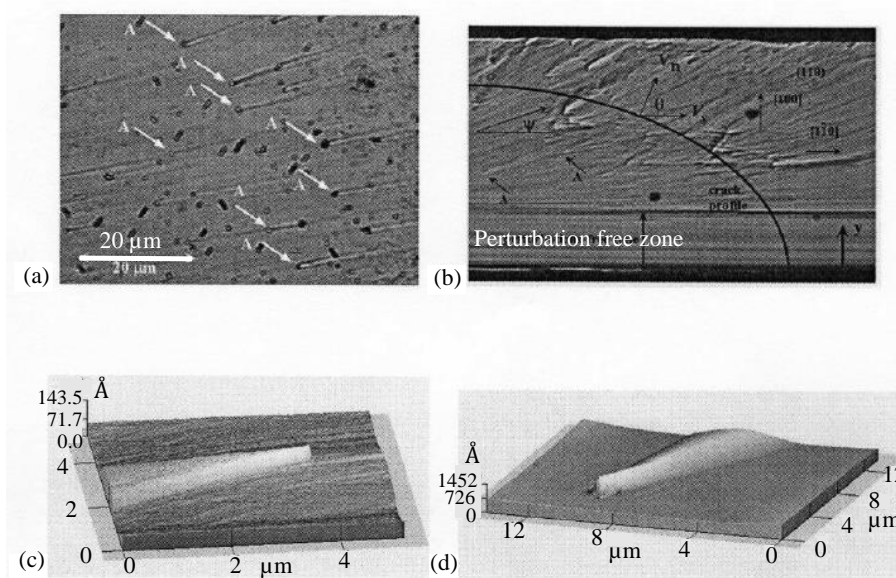


FIGURE 4.1: Ridge nucleated from the dislocation perturbation on the crack front. Optical microscope micrograph of a slightly etched (110) fracture surface (a), optical photograph of the (110) surface, with the quarter-elliptical crack front (note the large perturbations-free zone) (b), AFM micrograph of a small perturbation resulting from interaction with a single perturbation (velocity vector from right to left) (c), and large perturbation resulting from interaction with several adjacent dislocations (velocity vector from left to right)(d) [BER 14].

Considered as crystal surface defects, the grain boundaries are very complicated structures that are usually related to a misorientation [LEJ 10]. The atomic arrangement in these regions is highly disturbed by the presence of geometrically necessary dislocations

(GNDs) [ASH 70] and stacking faults. With the presence of these crystal defects, it could be expected that the crack would take place more easily along the grain boundaries than on the transgranular cleavage planes. Indeed, some authors have supposed that the fracture of multi-crystalline silicon can be intergranular. Paggi et al. [PAG 13] and Infuso et al. [INF 14] have performed some numerical studies with cohesive zone model (CZM) to investigate fracture of silicon solar cells. They inserted cohesive elements inside the grains as well as at the grain boundaries, and they studied the crack propagation with different postulated toughness ratios between the crystal plane and the grain boundary. Coffman and James [COF 08] have carried out molecular dynamic simulations to assess the surface energy of the grain boundaries in function of the misorientation. However, the real fracture toughness by experimental measurements is rare in the literature. Sato et al. [SAT 90] obtained artificial silicon bicrystals by press-joining at high temperature and then tested the strength of the artificial $\langle 111 \rangle$ twist boundaries. However, the intergranular fracture of natural (as grown) multi-crystalline silicon has not been experimentally revealed in a proper way. Some researchers tended to include the grain boundaries in fracture path based on relatively superficial observations [POP 13], as presented in FIG. 4.2. However, in this chapter, we will show that the crack-overlapped-boundary highlighted in the dotted rectangle in FIG. 4.2 would be rather a twin boundary than a general grain boundary, as will be presented in section 3.1.

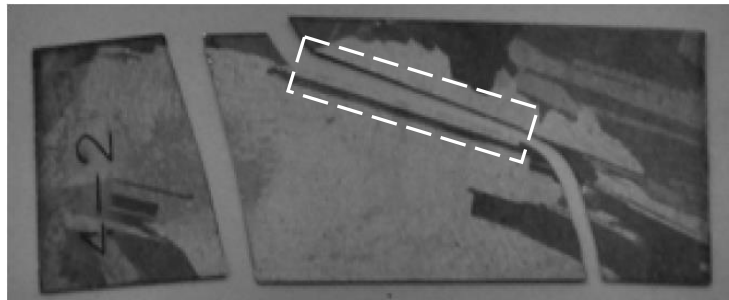


FIGURE 4.2: Reported crack along the grain boundary rather expected as a twin boundary [POP 13].

Whereas the intergranular fracture is deficient in convincing proofs, there are much more evidences that support the transgranular crack propagation mode. Mulay et al. [MUL 15] have performed both fracture experiments and CZM simulations on polysilicon (PolySi) in which the grains are in micro-metric scale, and they came out with the conclusion that the fracture is only transgranular. In our own work presented in chapter 2, only transgranular cracks have been observed during numerous 4-point bending tests performed on MCSi wafers. Recently, it has been highlighted, thanks to molecular static simulations [MÖL 14], that the brittle fracture can encounter what is called bond trapping effect when the crack tends to propagate along the grain boundary. The authors performed a $(112) [11 - 1]$ cleavage fracture in a single tungsten crystal (see FIG. 4.3(a)) as well as a intergranular cracking along a common (112) bicrystal boundary (see FIG. 4.3(b)). As presented in FIG. 4.3, the bond trapping finally leads the crack to deflect onto a cleavage

plane whose toughness is higher than that of the grain boundary. The concept of bond trapping is more general than lattice trapping, it takes into account irregular lattice structures not only inside a homogeneous matrix but also heterogeneous interfaces such as grain boundaries [BIT 15]. Another recent interesting work [VAY 16] showed that in nanoscale, the crack propagation mode switches from transgranular to intergranular when the specimen's thickness is below 100 nm. The authors performed tensile tests on polycrystalline silicon obtained by Low Pressure Chemical Vapor Deposition (LPCVD) process. This transition is promoted by the significant stress concentration at grain boundaries due to the presence of so called "grain boundary grooves" (related to the manufacturing process).

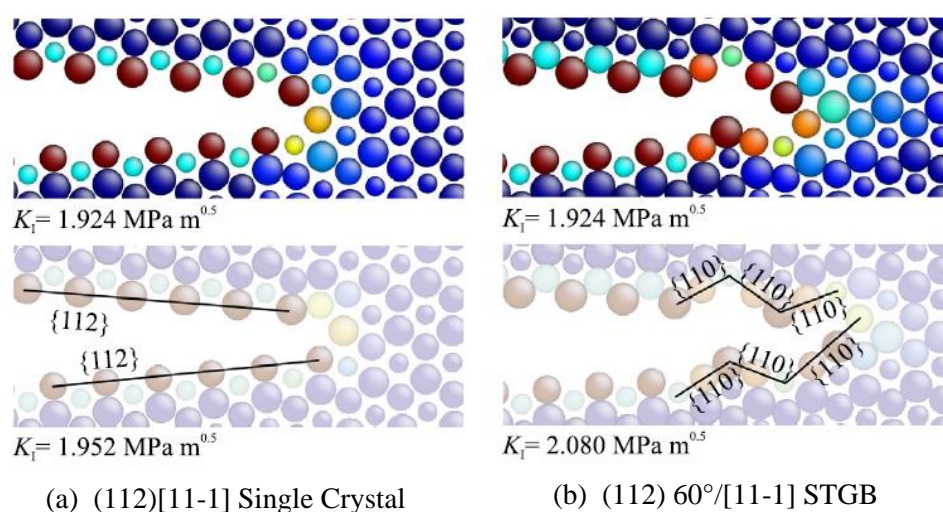


FIGURE 4.3: Bond trapping effect numerically revealed in intergranular crack [MÖL 14]. (112) plane cleavage in a single crystal and the crack path is smooth (a), fracture along (112) symmetrical tilt grain boundary (STGB) but the crack penetrates in the crystals and propagates on (111) planes with higher material toughness.

Assuming a transgranular crack in MCSi, will it propagate on the same cleavage planes as the silicon single crystal and how will it choose among the numerous crystallographic planes, *i.e.* at least 4 (111) and 6 (110) planes? This question has never been properly answered. Brodie and Bahr [BRO 03] have shown wild fracture surface roughness for PolySi at room temperature, while the cleavage plane characteristic has not been addressed. Mulay et al. [MUL 15] has concluded that the PolySi fracture surface follows approximately the (111) plane according to the grain orientation texture, yet further verification has not been conducted.

It has been experimentally observed in chapter 2 that the cracks are likely to initiate on the (111) plane in MCSi. However, upon crossing the grain boundary, will the crack be perturbed by the latter on the crack plane choice? Indeed, several studies have highlighted the obstacle effect of the grain boundary on the crack propagation in brittle polycrystalline materials. Gerberich et al. [GER 90] have revealed the grain-boundary-

4. Fracture in multi-crystalline silicon

affected-zone in which the crack-tip stress field is distorted. Persistent effect of the silicon grain boundary has been shown, which increases locally the fracture toughness via misorientation [QIA 07, CHE 07a, CHE 07b]. Under uniaxial tensile condition, the crack disengage the grain boundary either by one unique breakthrough point or by multiple, followed by the total crossing, as shown in FIG. 4.4. Particularly, over a relatively high twist misorientation at the grain boundary, the crack could be arrested [PIN 16], applied stress should increase in order to unpin the crack front.

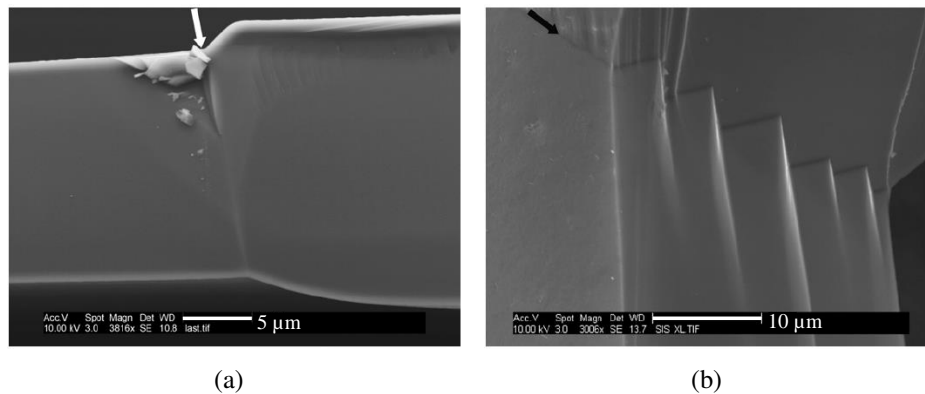


FIGURE 4.4: Grain boundary crossing behaviors in tensile configuration [CHE 07b]. The crossing takes place with one breakthrough point (a), and the crack overcomes the grain boundary with multiple breakthrough points (b). The propagation directions are from the left to the right in (a) and from the top to the bottom in (b).

To conclude, according to the review of the previous works in the literature, i) the crack propagation mode has not been properly determined, ii) the grain orientation affects the fracture path in each grain due to the anisotropy of the crystal, but the nature of the cleavage plane has not been precisely figured out, iii) the grain boundary has a barrier effect on the crack propagation, while its influence on the crack path has not been investigated, v) can the fracture process be experimentally reproducible and numerically modeled in MCSi? This point has never been addressed before.

In order to address the above questions, we investigated more in detail the fracture behavior of photovoltaic grade multi-crystalline silicon plates. Particularly, twin specimens were used, *i.e.* pairs of two different plates that are composed of the same grains in terms of grain shapes and orientations. Therefore, it is interesting to compare the fracture behaviors of the two naturally equivalent specimens under the same experimental conditions. The major concerns of this chapter focus on the reproducibility of the dynamic fracture, the crack path (including elucidation of inter- or transgranular mode), the grain and twin boundaries' effects on the crack propagation. Finally, we try to elaborate a crack plane choice criterion in order to predict the MCSi failure.

2 Materials and experimental methods

2.1 Multi-crystalline silicon plates

The specimens are square plates ($50 \times 50 \text{ mm}^2$) laser cut from solar grade multi-crystalline silicon wafers. The thickness of the latter is around $170 \text{ }\mu\text{m}$. It should also be recalled that for the solar grade silicon, the grains are generally millimeter to centimeter large, with the grain boundaries visible to naked eye. Due to the small thickness of the silicon wafers, we can get a sort of twin wafers (surface dimension of $156 \times 156 \text{ mm}^2$) *i.e.* wafers cut consecutively from a vertically grown silicon ingot. By precise laser cutting, twin plates can be obtained : two different plates involving the same grain shapes and orientations, as presented in FIG. 4.10-4.15.

Inside the grains, one can observe frequently a couple of long strip like twins. As a symmetric plane of a crystal lattice, the twin boundary of a long strip like twin is demonstrated to belong to $\{111\}$ family in this study¹. The determination is illustrated below in FIG. 4.5 presenting preliminary Electron BackScatter Diffraction (EBSD) measurements on one random specimen. The conclusion is consistent with that in [QUE 63, STO 15]. From the color codes maps associated with the inverse pole figure, one can find clearly that the twin changes locally the crystallographic orientation. In all the three corresponding pole figures (refer to section 4.25 for detailed definition), a symmetric crystalline structure can be easily revealed (a twin boundary is a symmetric plane within a crystal lattice). The red straight line denotes the approximate twin boundary that is supposed perpendicular to the specimen's surface, while the blue curved line represents the symmetric plane and therefore the real twin boundary. From FIG. 4.5(b), it can be noticed in (110) pole figure that the twin boundary contains three $\langle 110 \rangle$ directions. In the (111) pole figure, one can observe that one (111) direction is almost perpendicular to the twin boundary. With the above analysis, it can be confirmed that the twin boundary belongs to $\{111\}$ family.

Besides the twins, sub-grains can eventually be observed inside the grains, as revealed in FIG. 4.6(a) where the two grains containing sub-grains are highlighted. In fact, a sub-grain boundary is a small angle grain boundary [JOU 12] which is accommodated by the dislocations, as illustrated in FIG. 4.6(b). The dislocations are generally generated during the crystal solidification due to thermo-mechanical stress [LEE 84]. The small degree of incompatibility on the crystallographic orientation inside and outside the sub-grain makes the sub-grain boundary less remarkable than a general grain boundary.

In order to avoid multi-cracks or the crack bifurcation that we have encountered in the former studies in chapter 2, a pre-crack has been introduced with a Vickers indenter at the edge center of each specimen. The pre-crack dimension results in a varying fracture stress generally below 50 MPa.

1. In fact, a (111) twin boundary is a coherent twin boundary, while in silicon, there exists also incoherent twin boundary which corresponds to (112) plane [STO 15] and higher order twin boundary, these incoherent twin boundaries are not considered here

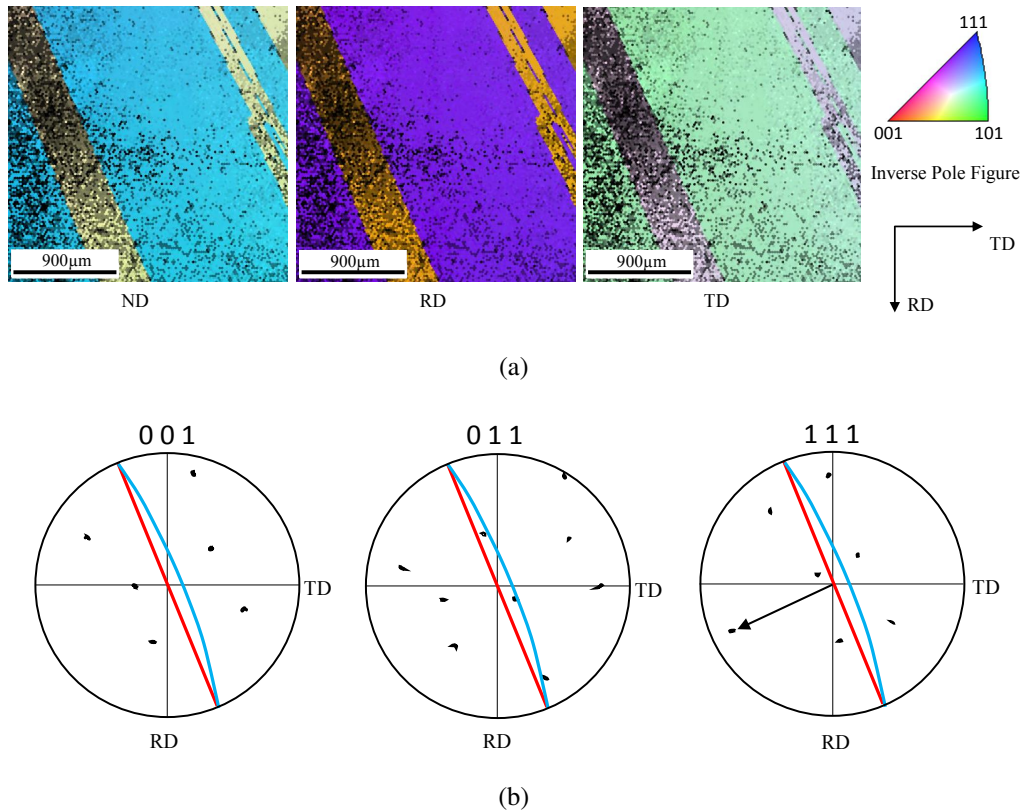


FIGURE 4.5: Twin boundary characteristic. The color coded map (a) and the corresponding pole figures (b). The red straight line denotes the twin boundary supposed perpendicular to the specimen's surface as presented in the color code map, the blue curved line represents the the projection of the real twin boundary obtained with the symmetry of the poles.

2.2 Bending tests with high speed imaging technique

4-point bending tests were performed. On the one hand, classical tensile tests are difficult to perform on the studied thin (thickness around 170 µm) and brittle silicon plates, due to gripping and alignment issues. On the other hand, the fracture surface contains more useful information under bending compared to that under tensile, such as the typical (111) surface instabilities as mentioned in the introduction [SHE 04b]. The same bending set up was used as presented in chapters 2 and 3 (the inner and outer spans of 21 mm and 40 mm). The tests were performed at constant punch velocity with a LLOYD-Ametek LF-PLUS electro-mechanical machine. The cross-head displacement rate was 0.2 mm/min. This implies a strain rate on the order of 10^{-6}s^{-1} and thus a quasi-static loading. An integrated displacement sensor provides in real time the punch displacement, and an external force sensor with a capacity of 10 N measures the reaction force on the punch.

The high speed imaging technique was to track the fracture process. The used high speed camera (Phantom V710) was set with a frequency of 49000 Hz and a resolution of

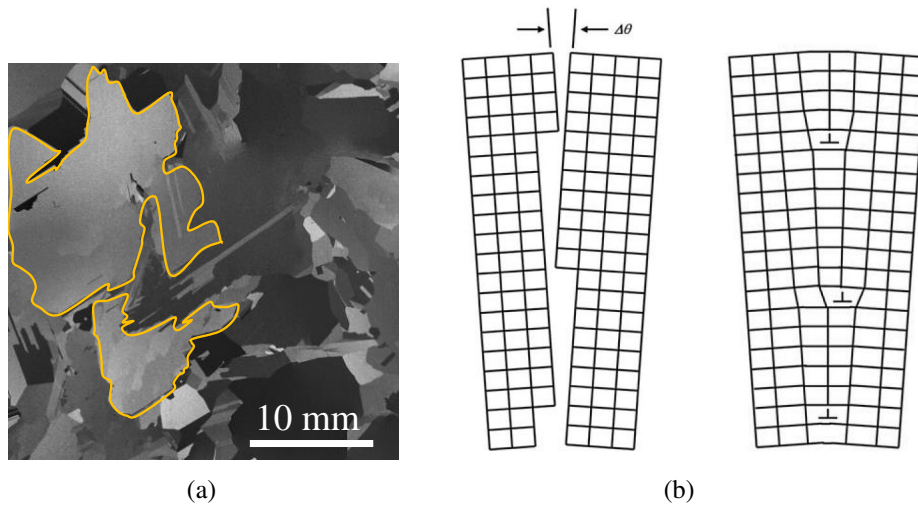


FIGURE 4.6: Sub-grains in multi-crystalline silicon. The sub-grains optically revealed in the studied specimens (a), sub-grain boundary accommodated by dislocations [NAK 09] (b).

256×512 pixels for all the tests. A manual trigger allowed to save the last 2 seconds so that the fracture can be entirely captured. A tilted mirror was set up under the specimen which allowed the camera to image the tensile surface of the specimen. FIG. 4.7 provides a comprehensive schematic of the test configuration. It should be noticed that the observation region is reduced (50 mm to 25.6 mm) but the pure bending area is still fully encompassed.

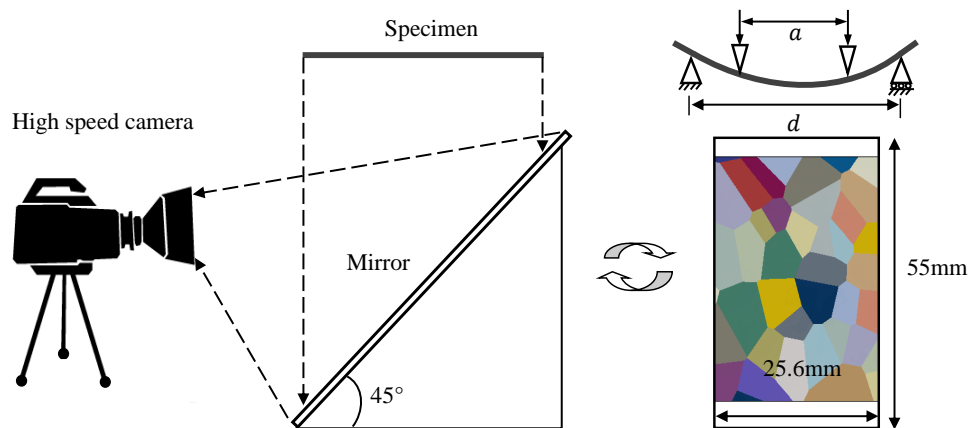


FIGURE 4.7: Schema of the experimental set up : a tilted mirror is put under the specimen to allow the camera to view the tensile surface. The grain boundaries can be distinguished in the mirror thanks to the different light reflections with respect to different grain orientations.

3 Intergranular or transgranular fracture

It is important to determine first the crack propagation mode, since it is part of exploring the fundamental fracture mechanism for materials. In addition, the crack propagation mode guides the fracture modeling in numerical framework : cohesive zone model (CZM) is very appropriate for intergranular fracture, while it has limitations in transgranular fracture since the crack path is influenced by the mesh. Conversely, extended finite element method (XFEM) handles well transgranular fracture, while it is not very suitable for intergranular fracture when the grain boundaries are explicitly modeled.

As mentioned in the introduction, how the solar grade multi-crystalline silicon cracks remains unanswered in the literature. Some researchers rely on intergranular or mixed propagation mode [PAG 13, INF 14] to model the fracture within solar cells. However, the investigations lack reliable experimental support. Indeed, Popovich et al. [POP 11, POP 13] showed a case where the crack overlaps on a sort of boundary, as illustrated in FIG. 4.2. However, more precise analysis has not been performed to determine the nature of the overlapped boundary. In this section, based on experimental observations we argue that intergranular crack propagation is unfavorable in silicon. The "prohibition" of intergranular mode can be explained by bond trapping or the deflection conducted by dislocations. Conversely, twin boundary can be part of crack path since it represents exactly a (111) crystal plane.

3.1 Crack overlapping twin boundary

In most of the cases, the fracture mode of solar grade multi-crystalline silicon can be distinguished by naked eye, since the grain boundaries are detectable without auxiliary processing. However, particular attention should be drawn to avoid the confusion between a general grain boundary and a twin boundary. As shown above in section 2.1, the boundary of a long strip like twin corresponds to a common (111) plane of two mirror crystal lattices, which are both free of atomic disarrangement at the interface. Meanwhile, a general grain boundary contains crystal defects (like dislocations) which accommodate the lattice mismatch at the grain boundary.

Among several fracture tests a particular case stands out, showing that the crack overlaps on a boundary, as can be noticed in FIG. 4.8(a). This crack path is highly similar with that (see FIG. 4.2) reported in [POP 13], where the authors concluded that the fracture mode was intergranular. However, the nature of this boundary (both in FIG. 4.2 and FIG. 4.8(a)) is not straightforward to determine. It looks like rather a twin boundary than a general grain boundary, note that it belongs to a long straight strip which is the characteristic shape of a twin (see FIG. 4.8). In order to draw a more definitive conclusion, a characterization should be performed. Before measuring the grain orientation, fractography is proposed to determine quickly whether the fracture surface corresponds to a (111) plane. The crack surface is observed under the optical microscope (Keyence VHX2000) and shown in FIG. 4.8(b). On the upper part of the fracture surface, it can be noticed that surface instabilities that typically arise on (111) plane under bending condition are

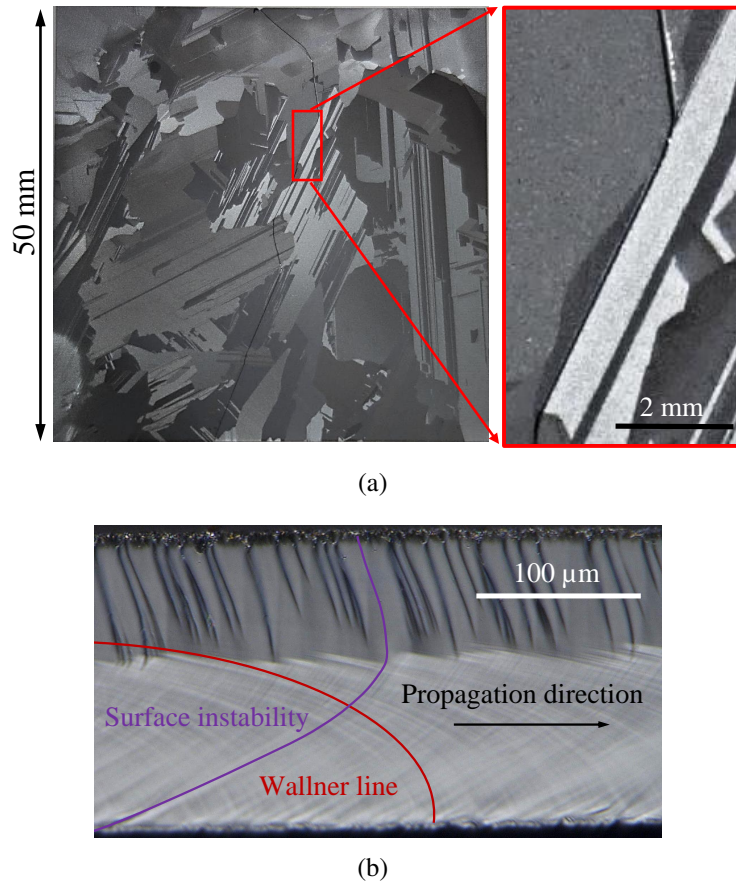


FIGURE 4.8: A particular case showing an overlap of the crack on a twin boundary. The crack path revealed by a macroscopic image with a zoom exhibiting the overlap on a boundary (a) and the corresponding fractography on the crack-boundary overlap portion (b). The red and pink lines highlight the Wallner lines and the surface instabilities in (b).

present. This indicates that the crack surface is a (111) plane, and the encountered boundary is in fact a twin boundary instead of a general grain boundary. We suppose this conclusion can be extended to the observation in [POP 13]. In this particular case, the overlapping on the twin boundary is just like a cleavage on a (111) crystal plane.

3.2 Zigzag crack path along grain boundary

In thermodynamic framework, grain boundaries are commonly viewed as weak interfaces in brittle materials, thus there would be tendency for cracks to propagate around instead of through the grains [LAW 93]. In this sense, some researchers suppose that the crack can be intergranular in multi-crystalline silicon.

At the macroscopic scale, the crack dissipates the stored energy to create a new surface for propagation. Yet at the microscopic (atomic) level, the crack moving is physically

based on the local force that breaks the atomic bonds. The crack will thus be sensitive to lattice distortion or defects : i) It has been numerically indicated [MÖL 14] that the microstructure of grain boundary can induce a bond trapping effect, leading to a significantly larger toughness at local spots of the grain boundary than the cleavage plane of the same orientation inside a single crystal. Therefore, the crack imposed to propagation along the grain boundary switches into cleavage planes inside the grains and manifests a tortuous path (see Figure 4.3). ii) In experimental framework, a local deflection of the crack front induced by a static dislocation line has been revealed [BER 14], as mentioned in the introduction of this chapter (see FIG.4.1). In this case, the crack front kinks out of the initial cleavage plane when it encounters a single or several dislocations. Resuming from the two above points, one can imagine that the crack front would get trapped in grain boundary, which renders the propagation unfavorable along this particular interface.

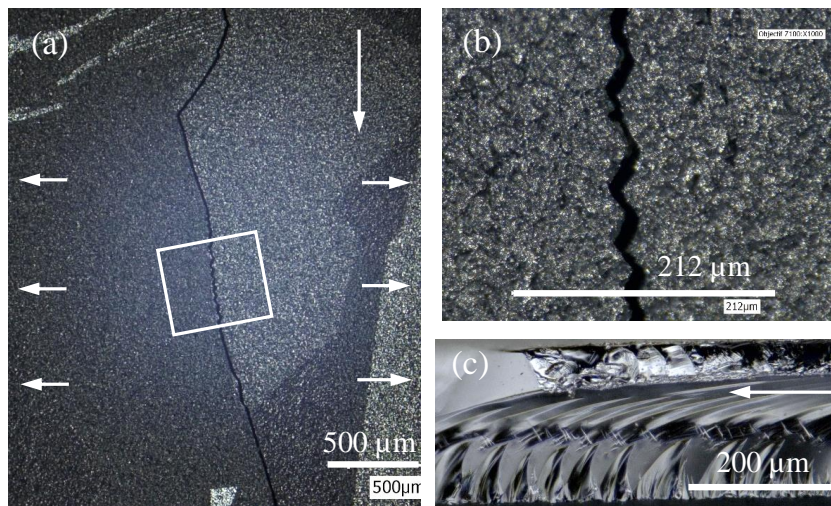


FIGURE 4.9: False grain boundary overlap. The observation of the crack path at a relatively large scale reveals a grain boundary overlap (a), while a zigzag crack path can be seen at a smaller scale indicating that the crack does not really superimpose the grain boundary (b), the crack surface morphology under optical microscope (c). The horizontal arrows in (a) indicate the tensile direction, the others point out the crack propagation direction.

In our fracture tests, there is one case that justifies the postulated trapping scenario on the crack. The appearance is illustrated in FIG. 4.9. In macroscopic observation, it seems that the crack propagates along the grain boundary as revealed in FIG. 4.9(a). However, when zooming the crack path, it can be clearly noticed that the crack follows a zigzag trajectory instead of exactly overlapping the grain boundary (see FIG. 4.9(b)). The fracture surface morphology confirms this unceasing crack plane changes, as can be noticed in FIG. 4.9(c). This particular fracture path is very similar to that numerically predicted in [MÖL 14], as presented in FIG. 4.3. With this case, we propose that the investigation of the crack propagation mode in MCSi should be carried out with caution and observation on the specimen surface is not sound enough to draw the conclusion.

According to the zigzag crack path shown in FIG. 4.9, together with the bond trapping effect revealed by static molecular simulations [MÖL 14], we conclude that the intergranular crack mode is unfavorable in multi-crystalline silicon.

4 Fracture path reproducibility

Single crystalline silicon cracks in the most energetically favorable cleavage plane which can be (110) and (111). However, in multi-crystalline silicon, the crystallographic orientation differs from one grain to another and grain boundary has barrier effect on crack propagation. In this case, the fracture issue is more complex, given that inside each individual grain the fracture behavior is anisotropic and follows low energy cleavage planes, while between adjacent grains the misorientation would lead to a crack path deflection when crossing a grain boundary. Moreover, knowing that the cleavage plane can be randomly oriented, the crack is in fact subject to a mix mode of fracture, in other words, the combination of modes I, II and III (see Appendix D for the fracture mode definition).

Concerning the investigation on crack path, twin specimens provide an underlying support to analyze the key factors that impact the crack propagation directions. In other words, it will be possible to assess the reproducibility of the fracture process in MCSi and figure out the cause for deviation. Within this section, we present 3 representative cases where inconsistent paths appear and 2 other representative cases where consistent fracture processes are obtained, as listed in TAB. 4.1.

TABLE 4.1: MCSi twin plates for fracture reproducibility investigation

Specimen label	Consistent path	Deviation root
Twin plate 1-1&1-2	No	Pre-crack orientation
Twin plate 2-1&2-2	No	Pre-crack position
Twin plate 3-1&3-2	No	sub-grains
Twin plate 4-1&4-2	Yes	None
Twin plate 5-1&5-2	Yes	None

4.1 Inconsistent path

Introduction of a pre-crack is carried out in all of the twin specimens. The artificial pre-crack, acting as a local stress riser and the cracking initiator, can be of course extended to any sort of fracture origin such as micro-cracks, inclusions, residual stresses etc. In the following paragraphs, the crack path deviation due to the pre-crack state will be discussed. In addition, the significant influence of sub-grains on the crack direction will be highlighted.

4. Fracture in multi-crystalline silicon

- Pre-crack orientation

When indenting the edge of a MCSi specimen with a Vickers pointer, there may be several equivalent cleavage planes that undergo a similar sollicitation. Therefore, a tiny discrepancy of indentation angle could lead to differently oriented pre-cracks which then result in different crack directions in the first grains of the twin plates.

In the twin specimens shown in FIG. 4.10, inconsistent pre-crack orientations can be observed. Consequently, the crack directions are different in the first grains. When entering the second grain, the difference of the crack path remains. It can be revealed that each crack chooses a cleavage plane such that the propagation direction undergoes a relatively small rotation angle. In this sense, the surface energy of the cleavage plane plays a secondary role while the crack path depends more on the rotation angle. As the crack propagates and steps inside the third grain, the crack directions are aligned in the two plates. The alignment means that the same cleavage planes are selected and it is the surface energy that dominates the crack path in the third grains.

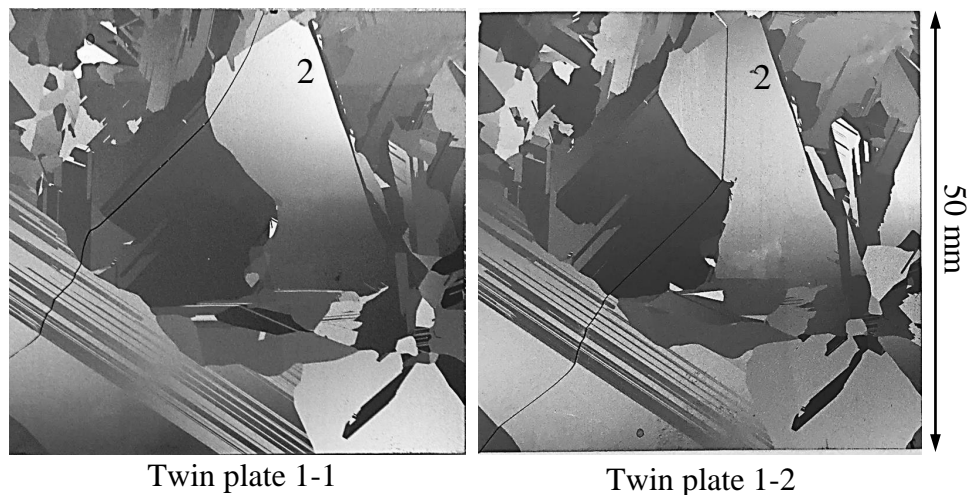


FIGURE 4.10: Crack paths of twin plates 1-1 and 1-2. The fracture paths differ from the beginning but share consistency in several grains. The specimen's dimension is $50 \times 50 \text{ mm}^2$, the crack propagates in up-down direction.

With this representative example, it can be concluded that the crack path in MCSi can be influenced by the orientation of the fracture origin. In this case, the crack path is not repeatable since the cleavage plane choice can be strongly affected by the crack direction in the previous grain.

- Pre-crack position

In every single grain the fracture behavior is anisotropic, penetration in different grains can thus easily lead to different fracture paths. This kind of crack incoherence

in twin specimens is frequently encountered since it is delicate to get the pre-cracks at exactly the same place in twin plates.

A representative case is exhibited in FIG. 4.11. According to the overall observation, the two fracture paths differ strongly from one to another. When looking for the difference initiation with local observations, it is found that the cracks share the same propagation direction from the beginning until entering the third grains. However, there exists a slight mismatch in terms of crack position in the first two grains, even though the two cracks are well aligned. The underlying cause of this mismatch is that the pre-crack in twin plate 2-1 is about 0.6 mm closer to the left edge with respect to the pre-crack position in twin plate 2-2. The offset on the pre-crack position and the early crack path leads the two cracks to propagate into different grains after the third grains (see the two framed grains in the zooms in FIG. 4.11). Then, the two cracks shift completely as they cross continuously different grains thereafter.

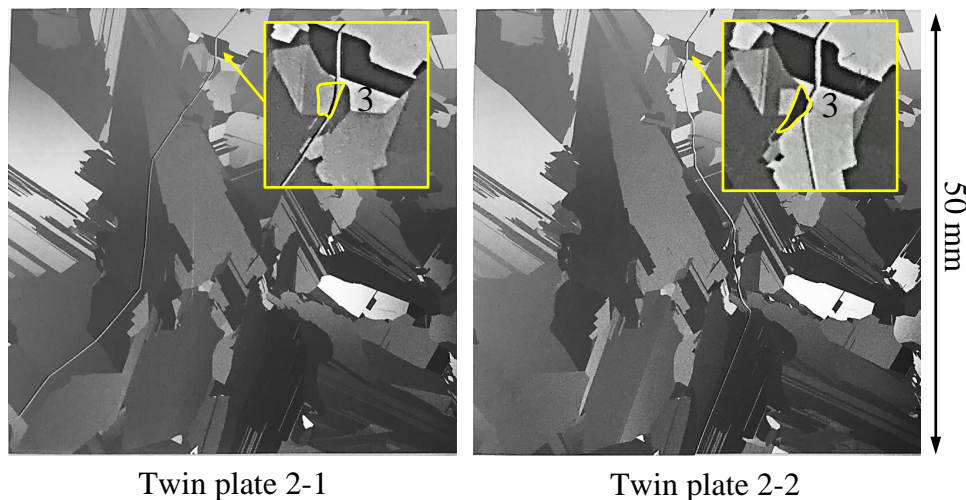


FIGURE 4.11: Crack paths of twin plates 2-1 and 2-2. The discrepancy in the fourth grain lead to totally different crack paths thereafter. The specimen's dimension is $50 \times 50 \text{ mm}^2$, the crack propagates in up-down direction.

To conclude, in order to obtain consistent crack paths in twin specimens, the pre-crack introduction is crucial : the position as well as the orientation should be highly consistent.

- Sub-grains

Sub-grains are grain level crystal defects. They are commonly recognized as dislocation cascades [NAK 09, WIT 08, STO 09]. The misorientation across a sub-grain boundary is usually small [NAK 09]. The latter is thus also called small angle grain boundary. According to EBSD measurement performed in [JOU 12], a sub-grain boundary is misoriented by 4° to 6° relative to the matrix (container grain) in solar

4. Fracture in multi-crystalline silicon

grade silicon crystal. Whereas this kind of crystal defects has been shown to be deleterious for electrical performance [JOU 12], their impact on the fracture process is unknown.

Here we show, with a representative example, that sub-grains can divide the crack path. As presented in FIG. 4.12, the crack directions are almost the same in the first two grains in twin plates 3-1 and 3-2. However, when the cracks run into the same sub-grain regions (in the third grains), different propagation directions develop. Even though the crack paths are again aligned in the next 2 grains, there is a gap in terms of crack positions, and this gap leads the two cracks to cross different grains from the middle of the specimen.

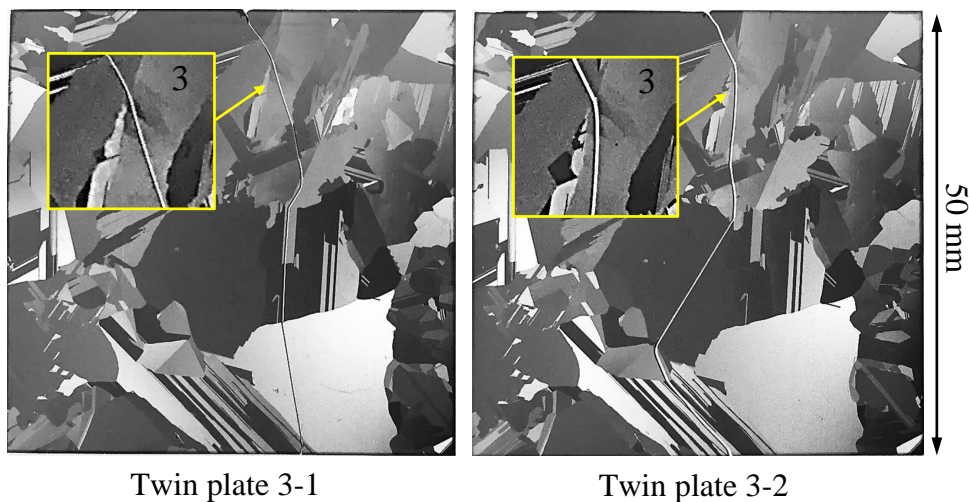


FIGURE 4.12: Crack paths of twin plates 3-1 and 3-2. The inconsistency occurs at the third grain, with totally different crack directions. The crack propagates in up-down direction.

In order to figure out the effect of the sub-grains on the fracture behavior, the first step is to identify the nature of the cleavage planes. The two crack paths inside the grain number 3 (see FIG. 4.12) of twin plates 3-1 and 3-2 are schematically reconstructed and compared, as shown in FIG. 4.13(a). The angle between the two cleavage planes is determined with two elementary angles, the angle formed by the two intersection lines on the specimen's surface (23° , see FIG. 4.13(a)) as well as the tilt angle of each cleavage plane with respect to the specimen's surface, as revealed in FIG. 4.13(b). Concretely, the tilt angle is measured thanks to a 3D reconstruction under the confocal optical microscope (Keyence VHX 2000). For fast cleavage plane identification, the crack surface morphologies of the two divided paths are revealed, as presented in FIG. 4.13(c) and 4.13(d), respectively. The nature of the two cleavage planes is thus analyzed with following points :

i) the intersections of the two cleavage planes with the surface of the specimen form an angle of 23° (see FIG. 4.13(a)). The cleavage plane of path ① is nearly perpen-

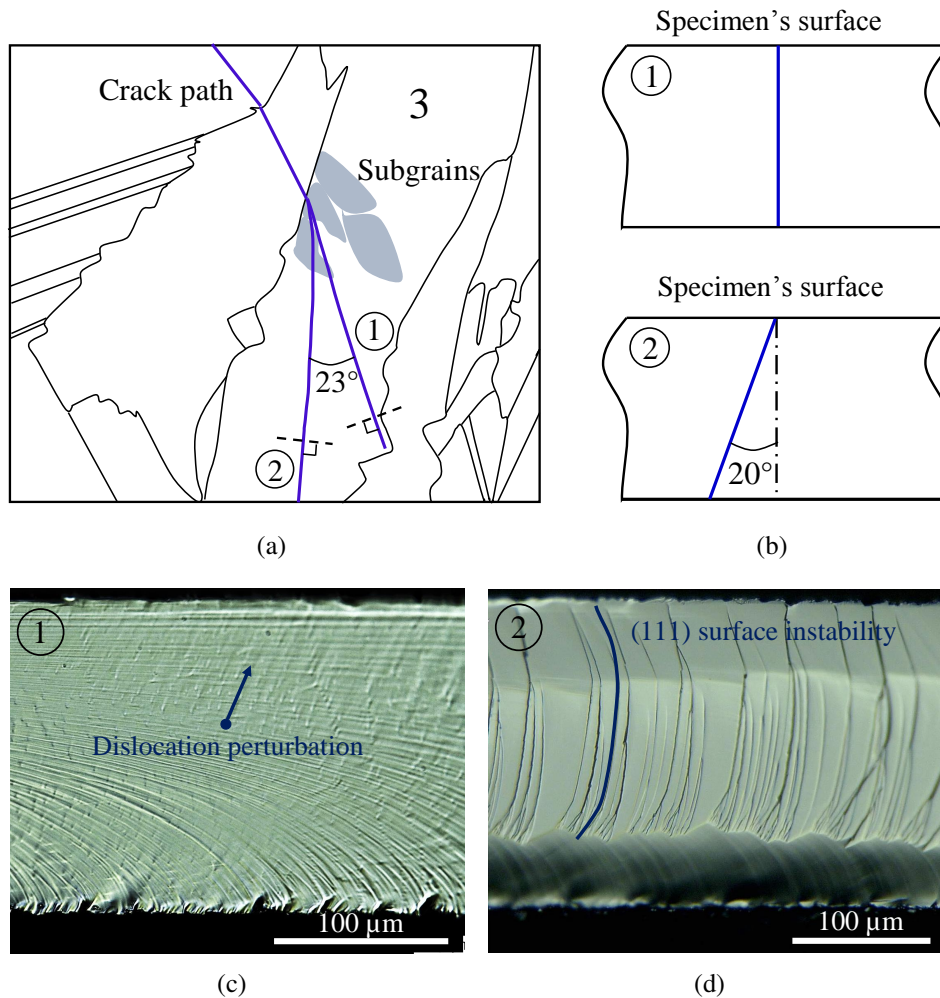


FIGURE 4.13: Crack paths and fracture surface morphologies in grain 3 of twin plates 3-1 and 3-2. Reconstruction of the two different paths (indicated as ① and ②) in grain number 3 containing sub-grains (a), the two paths form an angle of 23° on the surface of the specimen. Tilt angles of the cleavage planes ① and ② related to the specimen's surface (b), the two cross sections follow the dotted lines in (a). Crack surface morphology (indicated as path ①) in twin plate 3-1 where dislocation induced marks are likely to exist (c), crack surface morphology (indicated as path ②) in twin plate 3-2 (d), the surface instabilities indicate that the cleavage plane of path ② is (111). The propagation direction is from left to right in (c) and (d).

dicular to the specimen's surface while that of path ② is tilted by approximately 20° from the perpendicular position (see FIG. 4.13(b)). The tilt angle between each cleavage plane is thus calculated and it equals to 30° .

ii) according to the crack surface morphology, it can be stated that the cleavage plane of path ② is a (111) plane thanks to the presence of the typical (111) instabi-

lities (see 4.13(d)). Regarding the crack surface of path ①, a relative smooth surface can be revealed (see FIG. 4.13(c)). Particularly, the arrow in FIG. 4.13(c) highlights a kind of surface roughness which is very similar to dislocation induced perturbation, as has been reported in the literature [SHI 02] (see FIG. 4.1). However, the nature of the cleavage plane ① is not straightforward to determine.

From the two previous points, it is known that the cleavage plane ② is a (111) plane, and the angle formed by the two planes is about 30°. Beforehand, the angles between the low energy planes {110}, {111} and {112} can be determined, as listed in TAB. 4.2. It should be noted that there are 6 equivalent (110) planes, 4 equivalent (111) planes and 12 equivalent (112) planes, so they may exist several angles between two plane families. One can easily notice that a (110) plane is tilted by 35.3° from a (111) plane, which is the closest angle to 30°— the formed angle between the two investigated crack planes. Therefore, it can be concluded that the cleavage plane ② is a (110) plane.

TABLE 4.2: Angles between low energy cleavage planes in silicon.

Plane	{110}	{111}	{112}
{110}	60°, 90°	35.3°, 90°	30°, 54.7°, 73.2°, 90°
{111}	35.3°, 90°	70.5°	19.5°, 61.9°, 90°
{112}	30°, 54.7°, 73.2°, 90°	19.5°, 61.9°, 90°	33.6°, 48.2°, 60°, 70.5°, 80.4°

Note :

{110} : (110) (-110) (101) (-101) (011) (0-11)

{111} : (111) (-111) (1-11) (11-1)

{112} : (112) (-112) (1-12) (11-2) (121) (-121)

(1-21) (12-1) (211) (-211) (2-11) (21-1)

To summarize, sub-grains can divide the crack path. From the (110) crack surface morphology in sub-grain regions (see FIG. 4.13(c)), dislocation perturbations are likely present, which is in good agreement with the fact that the sub-grain boundaries are accommodated by dislocation cascades. The misorientation across a sub-grain boundary is small, while the localization of dislocations can distort the crystal lattice and induce residual stresses in the sub-grain regions. These local defects are unlikely to be highly identical in microscopic scale in twin plates and thus might trap the crack front in different ways. This can be seen as the reason why different fracture paths turn out when the cracks cross the same sub-grain regions in twin plates at macroscopic level.

4.2 Consistent path

When consistent pre-crack's orientation and position are well conducted, and when the crack does not get trapped by the sub-grains, the fracture path is highly reproducible

in twin specimens. Here two cases are chosen for illustration. The observation addresses the crack path manifestation on the specimen's surface. In section 6.1, the crack surface morphology will be furthermore revealed to compare the in-thickness crack path in fractured twin plates.

- The first example exhibits the fracture paths in the twin plates 4-1 and 4-2, as shown in FIG. 4.14. These two plates contain nearly no twins, except the central grain which possesses a close-horizontal and a close-vertical twins. When looking at a single crack path in either twin plate 4-1 or twin plate 4-2, it can be noticed that the crack only propagates inside the grains. The propagation direction is straight in every grain and then changes upon crossing a grain boundary. In the particular central grain, the crack is aligned with the close-vertical twin.

For the fracture paths comparison, it can be seen that the two cracks cross exactly the same grains from the edge containing the pre-crack to the opposite edge. Within each couple of twin grains, the crack directions are parallel. The overall alignment of the two fracture paths indicates that they are identical in the twin plates 4-1 and 4-2.

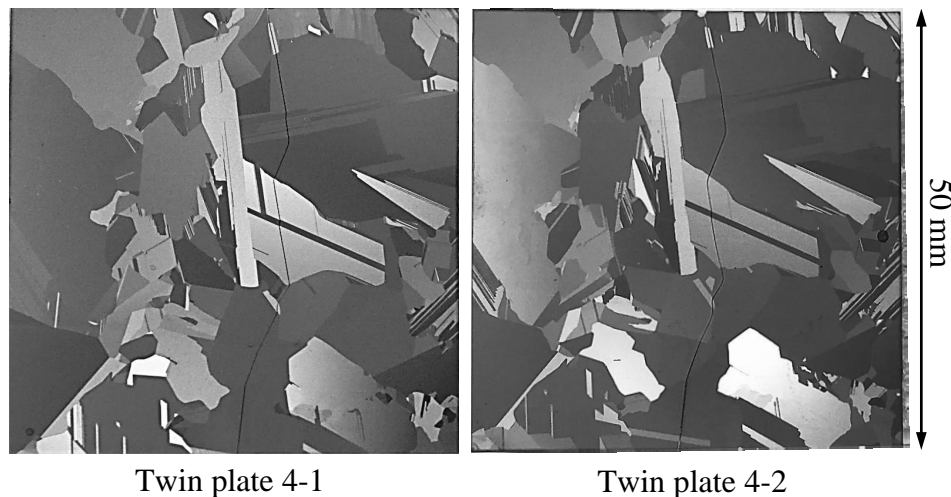


FIGURE 4.14: Crack paths of twin plates 4-1 and 4-2. The fracture paths are nearly the same. The specimen's dimension is $50 \times 50 \text{ mm}^2$, the crack propagates in up-down direction.

- The second example shows well consistent crack paths within the twin plates numbered as 5-1 and 5-2. The results are illustrated in FIG. 4.15. The cracks pass through both large and small grains. Particularly, a couple of twinned regions are present in the left bottom region of the specimen. It can be noticed that the crack switches between two directions as it crosses these unceasing twin boundaries.

To conclude, the observations of fractured twin plates show that the crack follows transgranular propagation on cleavage planes in a highly repeatable way. Nonetheless, it

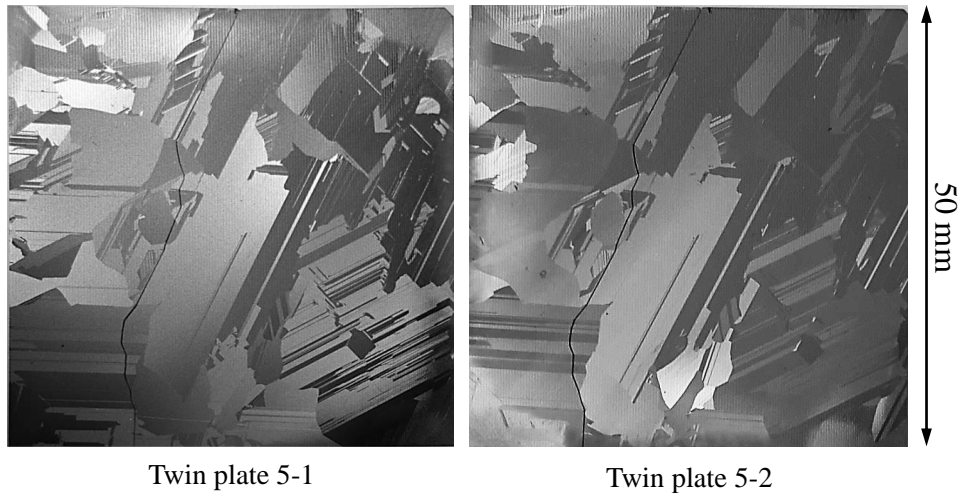


FIGURE 4.15: Crack paths of twin plates 5-1 and 5-2. The crack paths are perfectly the same according to optical observation on surface. The specimen's dimension is $50 \times 50 \text{ mm}^2$, the crack propagates in up-down direction.

should be noted that the path is strongly influenced by the crack direction in the former grain (twin plates 1-1 and 1-2) and can be sometimes modified within a grain, by crossing a sub-grain region (twin plates 3-1 and 3-2). On the other hand, the good repeatability between plates presenting the same grains and pre-cracks (twin plates 4-1 and 4-2 as well as 5-1 and 5-2) indicates that the crack path is likely to follow low energy crystal planes. Thus, the crack propagation, or the entire fracture process which is fully deterministic regardless of material defect, could be modeled in order to predict PV wafer fracture (This work will be presented in section 8).

The fracture path has been shown reproducible within multi-crystalline silicon, the next step is to focus on the fracture process to assess the crack velocity, the nature of cleavage planes, the influence of grain boundaries. Twin plates 5-1 and 5-2 are retained for further investigations, as will be developed in the following sections.

5 Crack velocity in multi-crystal

In chapter 3, the crack velocity has been assessed in mono-crystalline silicon crystal, and it has been shown that the crack velocity reaches quickly a steady state. Moreover, a correlation between the fracture stress and the crack steady state velocity has been established. Thus, the fracture stress allows to indicate approximately the crack velocity when no grain boundaries are present.

In this section, investigation on the crack velocity in silicon multi-crystal is carried out. The assessment is based on the fracture of twin plates 5-1 and 5-2 which will also be used to analyze the influence of grain boundaries (as will be detailed in section 7). Thus the crack velocity can be related to the grain boundary crossing behavior. As a first step,

the fracture stress is addressed, and an expected crack velocity can be given supposing that the fracture process is free of barrier. Then, the real crack velocity will be assessed thanks to the high speed imaging technique and compared to the expected value.

5.1 Fracture stress

The corresponding force-deflection curves for the twin plates 5-1 and 5-2 are presented in FIG. 4.16. The strain and stress are estimated from the recorded displacement and force using the beam theory.

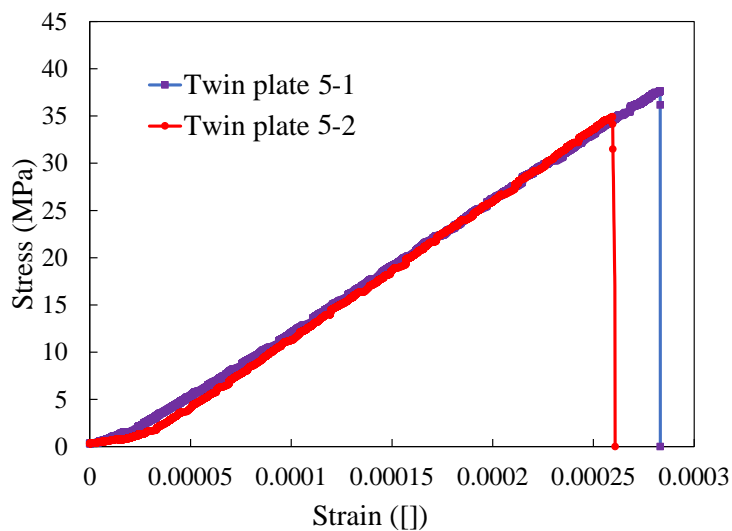


FIGURE 4.16: The stress-strain curves of the two twin specimens : twin plates 5-1 and 5-2

The fracture stresses are very close for the two specimens, 35MPa and 38MPa. At this stress state upon the crack initiation, the steady state velocity of the crack would be around 1200 m/s in silicon single crystal, according to the fracture studies in chapter 3 (section 3, FIG. 3.9). This estimated value will be compared with the measured crack propagation velocity using the high speed camera monitoring, as will be presented in the next subsection.

5.2 Crack propagation velocity

Thanks to high speed imaging, the subtraction between every two consecutive images highlights the crack propagation. To properly detect the crack tip, the contrast is reinforced with a wavelet denoising. Even if this method presents uncertainties (1 mm over crack length and 50 m/s over crack velocity when 5 pixels of uncertainty are taken to determine the crack tip position), it gives a relevant estimation of the crack growth rate during the cracking process. The main limitation is linked to the relatively low acquisition frequency

(here about $20\mu\text{s}$ between two consecutive images), knowing that the estimated velocity is an average during the lap between two consecutive images. However, in this study, this technique enables us to correlate the crack velocity and the crack path, especially the large velocity variation associated with the grain boundary crossings.

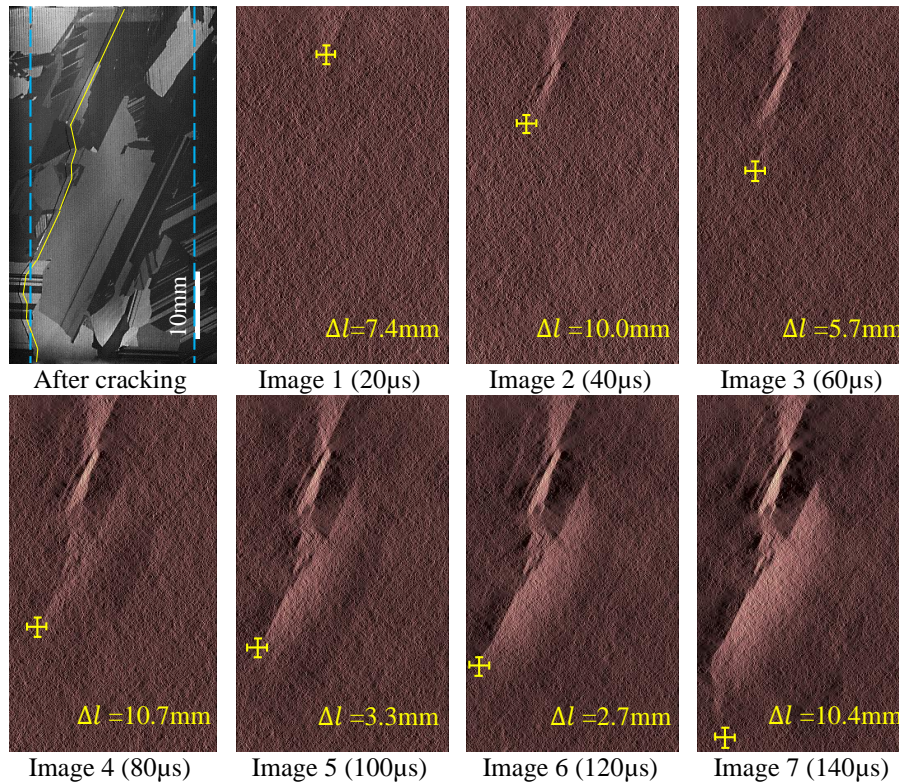


FIGURE 4.17: Cracking process of twin plate 5-1. The first image presents the completely fractured plate, the yellow line highlights the entire fracture path and the dashed blue lines indicate the punch roller positions. The second image corresponds to the subtraction between the first photo after cracking and the last photo before cracking, thus the first observation of the crack. The rest images are the following subtraction results. The yellow marks spot the crack tip positions in sequential subtractions.

The fracture process in the twin plate 5-1 is presented in FIG. 4.17. The reference image is one on the completely cracked specimen which helps to figure out the entire propagation path on surface, image 1 is then the subtraction in which the crack can be firstly revealed, and the other images correspond to the following subtractions until the crack crosses the specimen. In each subtraction result, an instantaneous crack length can be measured then a crack advancing can be deduced from two successive subtraction results. According to the applied frequency of 49000 Hz *i.e.* $20\mu\text{s}$ between two successive images, the average crack propagation velocity has been addressed and presented in FIG. 4.18.

The propagation in MCSi is relatively slow (400 m/s on average on the entire path)

compared to the expected steady state velocity which is about 1200 m/s in SCSi. Besides, it can be noticed that the velocity has never reached a steady state value, conversely to the crack process in a single crystal reported in [HOL 98, SHE 04b] as well as revealed in our work in chapter 3, section 3.1. The averaged velocities significantly vary in different grain regions and are sometimes extremely low. Interestingly, the extremely low velocities can be related to the presence of grain boundaries, as can be noticed in FIG. 4.18. This indicates that the crack has been slowed down or shortly stopped by the grain boundaries. The indication is in good agreement with the findings of [QIA 07, QIA 08] on the fact that grain boundary increases the material toughness. According to the dynamic propagation criterion of [FRE 90b], the propagation velocity v has an inverse relationship with the dynamic energy release rate G_D , *i.e.* the dynamic crack propagation force. Thus, in order to overcome the grain boundary obstacle which increases the material toughness Γ_D , the crack slows down to have more important driving force, as illustrated in EQ. 4.1. On the other hand, after crossing the grain boundary, the crack continues to propagate on a crystal plane that has lower toughness, the crack velocity will increase again. This is why the crack velocity varies in MCSi.

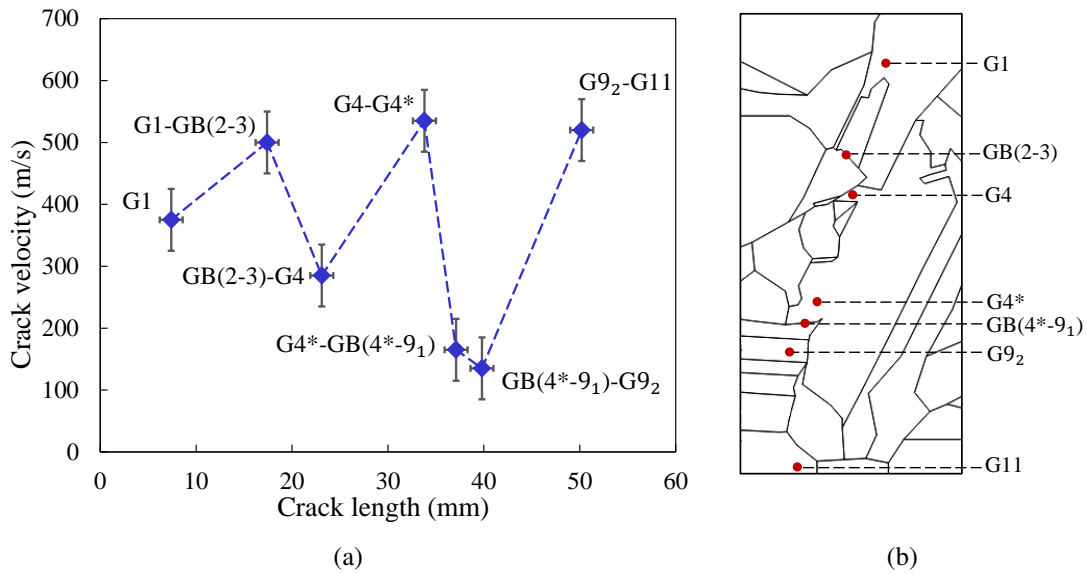


FIGURE 4.18: Crack propagation velocity associated to the grains in twin plate 5-1. Mean crack propagation velocity measured with high speed camera images (a), and indication of the crack tip positions (b). G denotes grain and GB the grain boundary. Refer to FIG. 4.19 for the grain numbering.

$$G_D \uparrow = G \left(1 - \frac{v \downarrow}{C_R}\right) = \Gamma_D \uparrow \quad (4.1)$$

It can thus be concluded that the crack propagation does not reach a steady state in MCSi due to the presence of grain boundaries. Yet the latter slows down the crack, while

their influence differs from one to another. The deceleration efficiency of the grain boundaries can be associated with the misorientation, as will be elucidated in section 7.

6 Cleavage plane investigation

According to the discussion in section 3, the intergranular crack propagation mode is unfavorable in multi-crystalline silicon. Whereas the crack paths are highly identical between the twin plates 4-1 and 4-2 (see FIG. 4.15) as well as between the twin plates 5-1 and 5-2 (see FIG. 4.15), the nature of the cleavage planes rests unknown.

In this section, two methods are proposed to identify the crystallographic plane overlapped by the crack. The first method is fractographic analysis and the second one is based on measurement of crystallographic orientation. The fracture paths in the twin plates 5-1 and 5-2 are investigated.

6.1 Fractography analysis

As mentioned in chapter 3, the fracture surface provides a lot of information about the fracture process, such as the crack propagation direction, the crack front shape. Particularly, the presence of the typical (111) surface instabilities [SHE 08, BER 14] allows the determination, without any prior knowledge of the crystal orientation, of whether the crack propagates on a (111) plane or not. This aspect has already been treated in section 3.1 and 4.1.

For fracture surface investigation, the confocal microscope VHX-2000F was used. The investigation addresses the grains that are crossed by the crack in the twin plates 5-1 and 5-2. The observations are presented in FIG. 4.19 and FIG. 4.20, in which an overall reconstitution is shown. The concerned grains are numbered in the order of the crossing sequence. One can notice that the grain 9 contains a couple of twins and, it is divided into 5 parts with respect to the crack directions (the twin boundaries are more noticeable in FIG. 4.33(a)).

From the two overall fractography displays, two main observations can be highlighted :

i) Regarding the comparison between the two twin plates, one can notice that fracture surface morphologies are highly identical for all the grains cut by the crack. This consistency demonstrates a second time but more clearly the repeatability of the fracture behavior in multi-crystalline silicon : the crack propagates on the same cleavage plane within the same grain.

ii) Focusing on one of two overall displays, it is found that the typical (111) surface instabilities clearly appear in grains 1, 2, 4, 5, 6, 9₃, 9₅, 10. This indicates that the crack propagates on (111) planes in the above grains. For the crack surface in grains 3 and 7, the instabilities are present but not outstanding, while these cannot be observed for the other grains. The cleavage planes that cannot be identified with fractography should be analyzed with the second method, as will be presented in the following section.

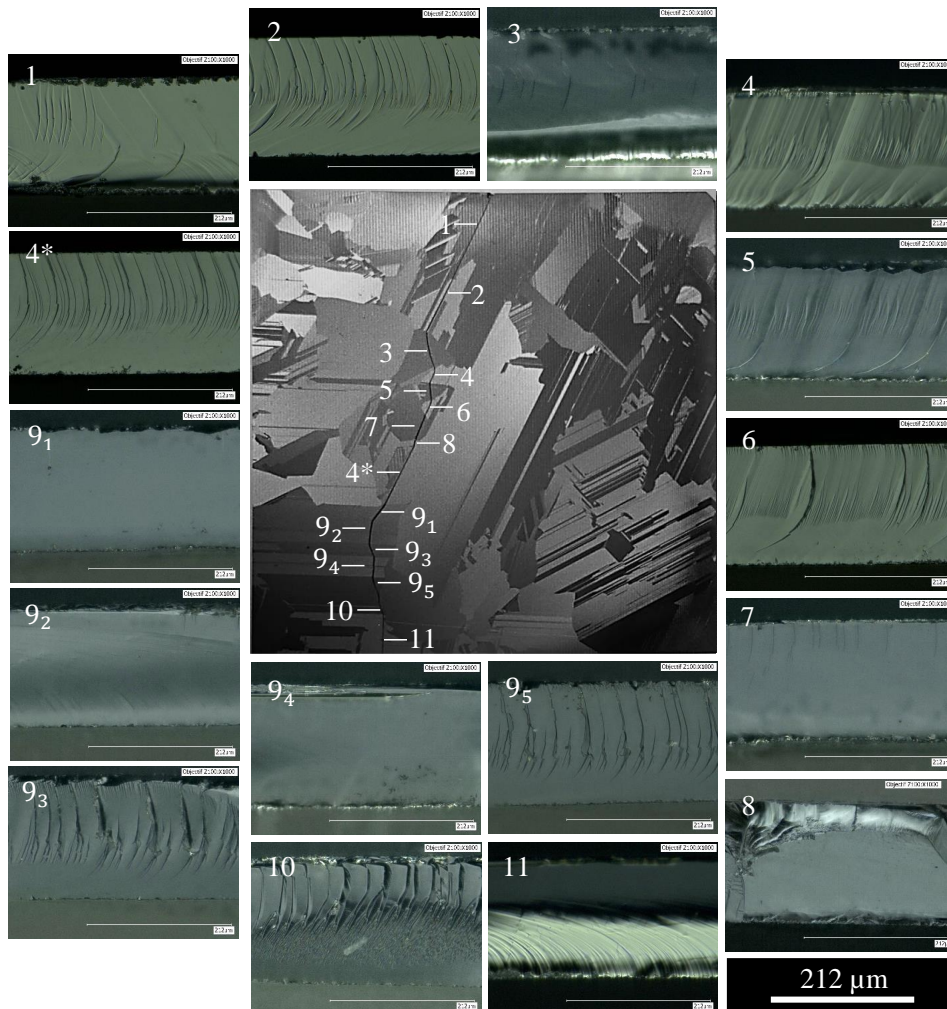


FIGURE 4.19: Fractographies on all the fracture involved grains for twin plate 5-1. The numbers represent the crossing order of the crack through the grains from the beginning to the end, the grain 9 owns many twins.

6.2 Cleavage plane identification with grain orientation

In order to further identify the cleavage planes in the twin plate 5-1, the orientations of the grains along the crack trajectory should be determined. Basically, the grain orientation allow accessing the normal direction of any crystallographic plane with respect to the specimen's geometry, the cleavage plane crossing the grain can thus be identified. This section is divided into two parts, firstly, the Laue X-ray measurement will be presented, followed by the interpretation of the measurement in terms of grain orientation. Then, pole figure analysis will be addressed to identify the nature of the cleavage planes in grains 3, 7, 8, 9₁, 9₂, 9₄, 11 of the twin plate 5-1.

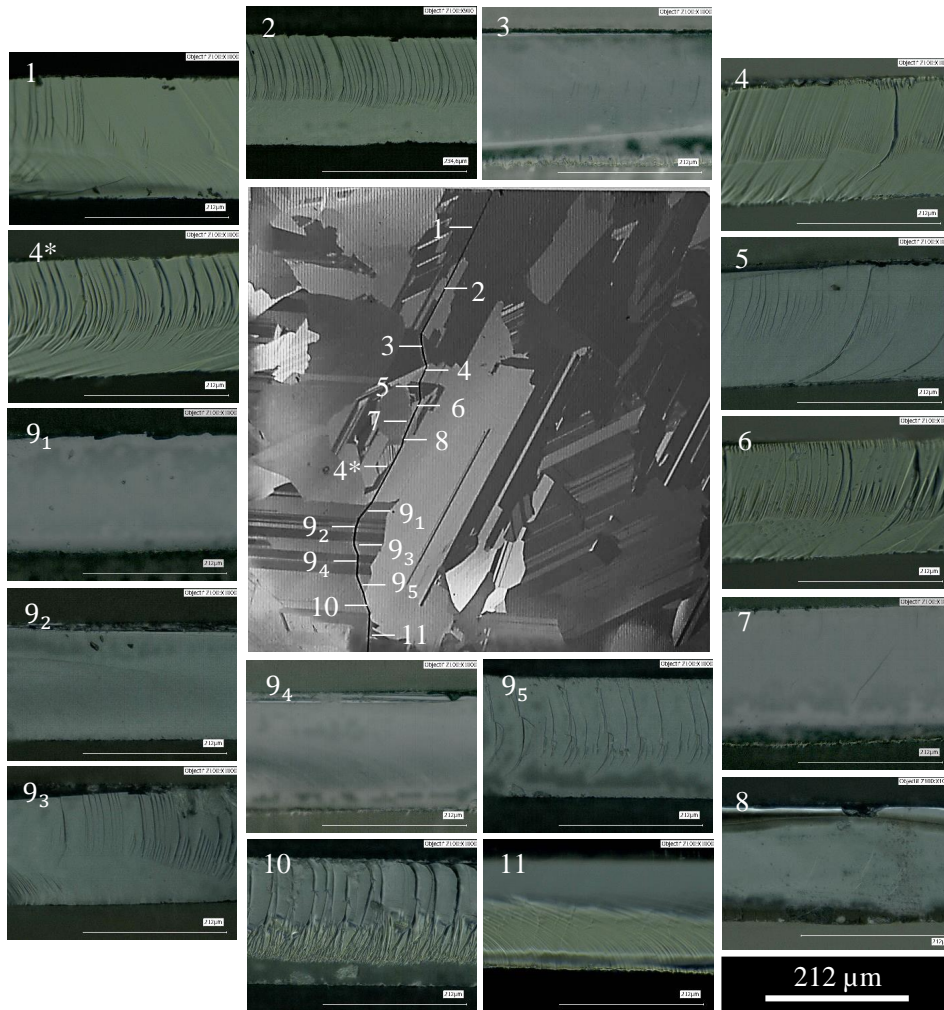


FIGURE 4.20: Fractographies on all the fracture involved grains for twin plate 5-2. The numbers represent the crossing order of the crack through the grains from the beginning to the end, the grain 9 owns many twins.

6.2.1 Grain orientation determination by X-ray analysis

Compared to the EBSD, the Laue X-ray diffraction covers relatively larger specimens. Moreover, mirror polishing is not necessary for this technique, conversely to the EBSD. It should be noted that mirror polishing on a thin silicon plate of $50 \times 50 \times 0.17 \text{ mm}^3$ is very delicate². Considering the feasibility, X-ray diffraction is more appropriate in our case.

The measurement has been carried out at the CEA-INES. The procedure is that, in each grain a single measurement is performed at the centroid of the grain. Thus the grain contour needs to be defined beforehand. Thanks to the different light reflections with

2. Meanwhile, mirror polishing on a standard solar wafer ($156 \times 156 \times 0.17 \text{ mm}^3$) is feasible with some dedicated devices

respect to the different orientations of the grains, the grain boundaries are visible to the naked eye. Therefore, the grain contours have been drawn in the software ImageJ based on a photo of the twin plate 5-1 and then fed for orientation measurements. For simplification, the grains crossed by the crack have been figured precisely while the grains elsewhere have been drawn approximately.

The angular color map is presented in FIG. 4.21. The measurements initially resulted in three angles γ , β , α that denote the rotation angles around x , z and y axes, sequentially. These angles have then been used to define the Euler angles. In the Euler angles convention, the rotations are based on updated axes (z , x' , z') and the global rotation matrix is easier to establish (see Appendix B). The initial rotation angles α , β , γ and the corresponding Euler angles are presented in TAB. 4.3. The orientation information will be used to plot pole figures in order to identify the cleavage planes in the next subsection.

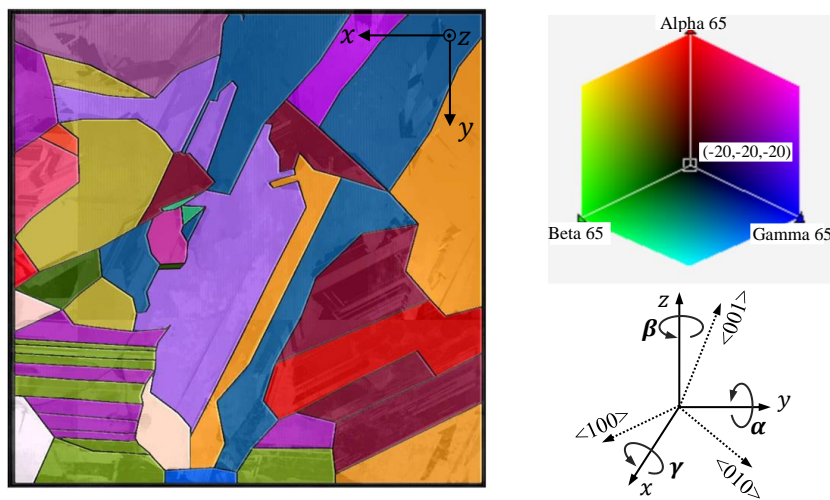


FIGURE 4.21: Angular color map of grain orientation distribution measured with Laue X-ray diffraction. The three angles γ , β , α denote the rotations around the axes x , z , y , sequentially.

6.2.2 Cleavage plane identification with pole figures

A pole figure is based on the stereographic projection which represents a spatial direction on a 2D plane (see Appendix C). Through this kind of projection, a direction is turned to a point, a plane is turned to a line. Conventional pole figure takes the specimen's coordinate system as the stereographic projection basis. As presented previously in FIG. 4.5 in section 2.1, to identify a plane (for example a cleavage plane) using the conventional projection basis, one should firstly draw the plane and a couple of crystallographic directions such as $[100]$, $[110]$, $[111]$ in a same pole figure. Then, one should determine which directions are in the studied plane and which are perpendicular to that plane. This analysis procedure is complicated and cumbersome. However, if the cleavage plane is chosen as the stereoprojection plane, the projection point of any in-plane direction will be located

TABLE 4.3: Orientations of the grains crossed by the crack in the twin plate 5-1.

Grain	Laue system α, β, γ ($^{\circ}$)	Euler triplet around z, x', z' ($^{\circ}$)
1	-15.6, 10.4, 32.4	-14.3, 32.9, 29.1
2	33.5, 11.3, 59.4	26.5, 70.6, -35.0
3	25.9, -14.9, -3.0	96.4, 26.8, 249.4
4	34.0, 11.2, 59.3	26.7, 70.7, -35.5
5	-3.2, 47.4, 26.0	42.6, 23.7, 5.3
6	-15.2, 10.6, 32.3	-13.5, 32.7, 28.4
7	50.1, -4.4, 36.3	45.0, 56.5, -66.5
8	12.6, 20.0, 6.7	66.9, 16.1, -47.6
4*	34.0, 11.2, 59.3	26.7, 70.7, -35.5
9 ₁	35.2, -12.7, 40.7	26.6, 45.4, -52.1
9 ₂	22.9, 34.8, -10.4	117.2, 18.9, -80.7
9 ₃	35.5, -11.3, 39.7	28.9, 45.6, -52.8
9 ₄	23.6, 34.6, -10.5	116.6, 19.5, -80.2
9 ₅	34.6, -12.6, 40.6	26.3, 45.1, -51.4
10	96.6, 51.2, 43.5	56.8, 128.1, -52.2
11	22.4, 35.2, -10.5	118.4, 18.3, -81.5

on the figure outline and the projection point of a perpendicular direction will be right at the figure center³, as can be noticed in FIG. 4.22. In this way, the pole figure will be a very direct expression of a cleavage plane.

The cleavage plane in MCSi is most probably one of the low energy planes $\{110\}$, $\{111\}$ and $\{112\}$. To fix a crystal plane, the normal direction is the main indicator, but the in-plane directions are also important. The spatial relationship between the low energy planes as well as the dense directions in silicon can be addressed within a regular tetrahedron comprised of the 4 (111) planes, as shown in the schematic drawing in FIG. 4.23. For a (110) plane, it contains one [110], two [111] and two [112] directions, see FIG. 4.23(a). Regarding a (111) plane, there are three [110] and three [112] in-plane directions, see FIG. 4.23(b). A (112) plane includes one [110] and one [111] direction, see FIG. 4.23(c). In summary, the cleavage plane identification consists in analyzing the projection points of the dense crystallographic directions on a pole figure based on the cleavage plane.

In order to draw the pole figure based on a cleavage plane, the normal direction of the studied cleavage plane should be determined in the specimen's coordinate system (see FIG. 4.21). Generally, a plane can be defined with two angles in a orthogonal coordinate system. In our case, the first angle ϕ_1 is a tilt angle between the crack direction

3. In this case, the rolling direction (RD) and the transverse direction (TD) are of no importance, they only influence the location of the projection point of an in-plane direction on the figure outline but will not bring it into the figure.

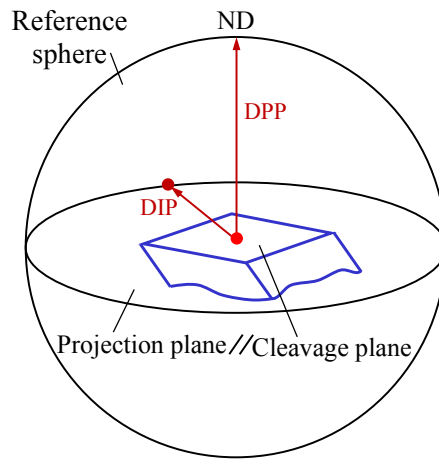


FIGURE 4.22: Pole figure taking a crack plane as the stereographic projection plane. DPP denotes a perpendicular direction to the cleavage plane, DIP (any) direction in the cleavage plane.

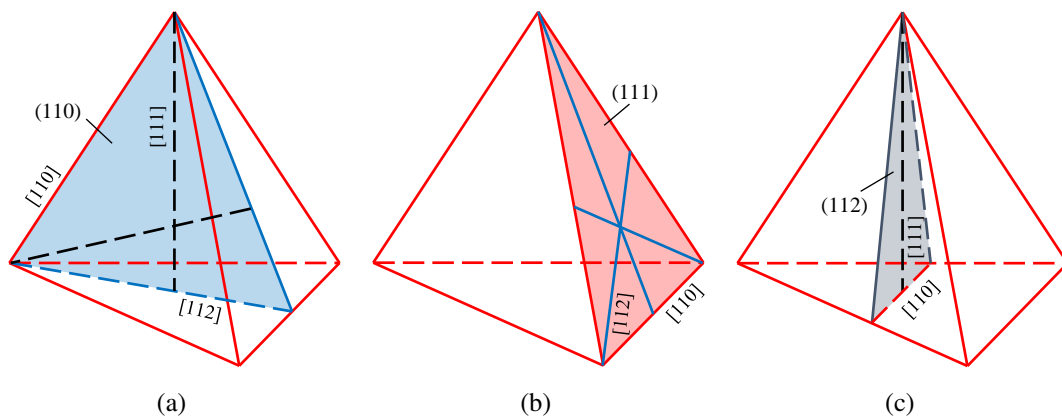


FIGURE 4.23: Low energy cleavage planes in silicon, the four (111) planes constitute a tetrahedron. A (110) plane contains one [110], two [111] and two [112] directions (a), a (111) plane contains three [110] and three [112] directions (b), a (112) plane contains one [110] and one [111] direction (c).

and the y axis of the specimen's coordinate system, as can be seen in FIG. 4.24. This angle can be directly measured on the specimen's surface. The second angle ϕ_2 is the tilt angle of the studied cleavage plane with respect to a reference plane that is normal to the specimen's surface and contains the crack direction manifested on the specimen's surface (see FIG. 4.24). This tilt angle is determined thanks to the confocal optical microscope. The results concerning ϕ_1 and ϕ_2 are presented in TAB. 4.4

With the grain orientations and the cleavage planes' tilt angles, the pole figures have been drawn for the grains 3, 7, 8, 9₁, 9₂ and 11 in the twin plate 5-1, as presented in

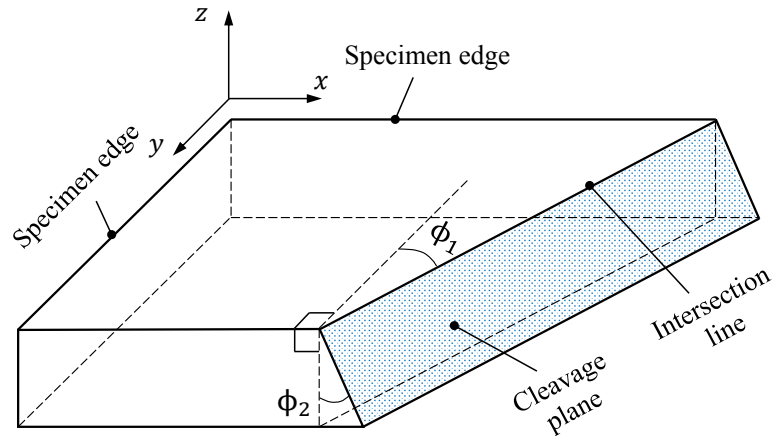


FIGURE 4.24: Cleavage plane orientation in sample's coordinate system.

TABLE 4.4: Cleavage plane orientation expressed with ϕ_1 and ϕ_2 in the twin plate 5-1

Grain	Cleavage plane orientation ϕ_1, ϕ_2 ($^\circ$)	Grain	Cleavage plane orientation ϕ_1, ϕ_2 ($^\circ$)
1	-26, 0	4*	-26, 0
2	-26, 0	9 ₁	-39, -28
3	12, 40	9 ₂	-6, -12
4	-26, 0	9 ₃	22, 9
5	4, -14	9 ₄	-6, -12
6	-26, 0	9 ₅	22, 9
7	-23, -40	10	5, 10
8	-14, -25	11	-2, -10

FIG. 4.25. The pole figure for grain 9₄ is highly identical to that for grain 9₂ and thus is not displayed. Each pole figure contains the normal directions of {110}, {111} and {112} plane families which are denoted by blue circles, red squares and green triangles, respectively.

For the four pole figures (a), (b), (c), (d), one can see that there is one [111] direction located near the center, while one or two [112] directions can also be noticed in the center region. This is due to the fact that the smallest angle between [111] and [112] directions is 19° (see TAB. 4.2), then the two corresponding projection points are very close. However, the (112) plane should be eliminated from the identification, since one can find three [112] directions near the figure contour line, knowing that a (112) plane does not contain such directions but a (111) does. Besides, the three [110] projections located near the figure contour line confirm that these four cleavage planes belong to the {111} family. Regarding the two rest figures FIG. 4.25(e) and 4.25(f), it can be clearly observed that one [110] is close to the figure center on the one hand, and two [111] as well as two [112]

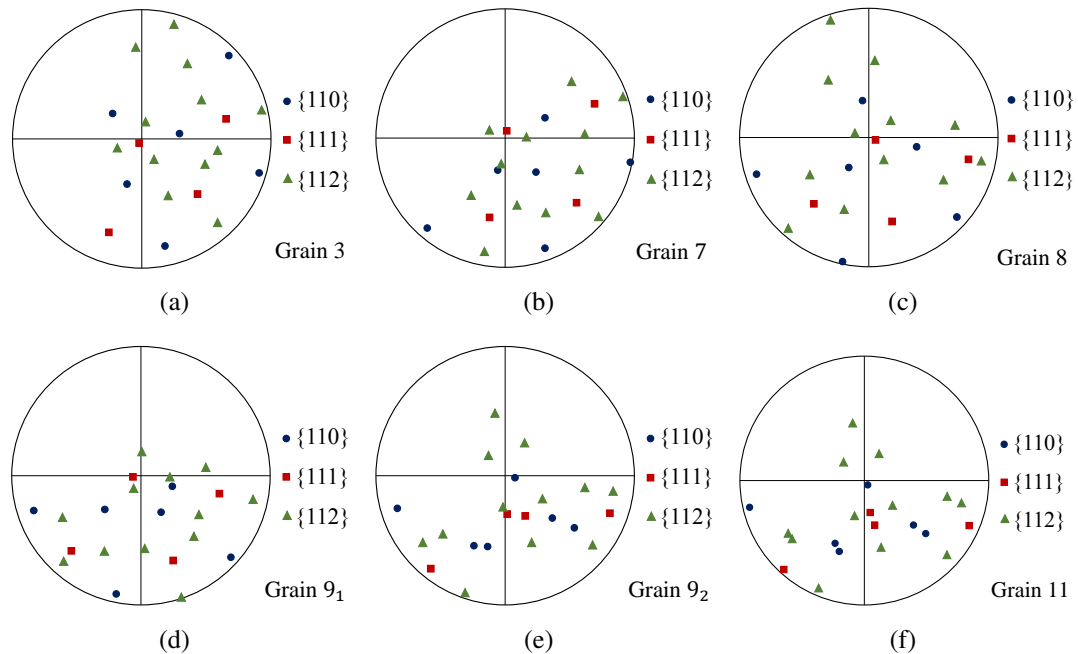


FIGURE 4.25: Cleavage plane investigation with pole figures ($\{110\}$ -blue circles, $\{111\}$ -red squares and $\{112\}$ -green triangles families) taking the cleavage plane as the projection plane. The pole figures (a), (b), (c), (d), (e), (f) are based on the cleavages planes of grains 3, 7, 8, 9₁, 9₂, 11 (see FIG. 4.20), respectively.

directions are very close to the figure contour line on the other hand. Thus, the cleavage planes belong to the $\{110\}$ family.

Based on the above analysis, it can be concluded that the fracture in grains 3, 7, 8 and 9₁ occurs on (111) cleavage planes while in the grains 9₂, 9₄, and 11 on (110) cleavage planes. Within the grain 9, where a couple of twins are present, the crack changes the propagation direction upon crossing every twin boundary and the cleavage plane alternates between (111) and (110) planes.

6.3 Fracture energy assessment

The nature of the cleavage planes in twin plate 5-1 has been well determined with the analysis carried out in section 6.1 and section 6.2. It has been shown that the crack crosses the grains by low energy planes (111) and (110) families. Whereas the equivalent crystal planes have the same fracture toughness, their effective energy dissipation considering the cleavage plane's orientation can differ from one to the others. Hence, this section is dedicated to assess the fracture energy relative to the cleavage plane in each grain of the twin plate 5-1. The aim is to compare the effective energy dissipation of the experimentally obtained cleavage plane with the theoretically lowest energy plane, as will be discussed below.

6.3.1 Effective energy dissipation

As can be noticed in FIG. 4.24 and TAB. 4.4, the cleavage planes have different surface areas due to their distinguished orientations. In order to assess the fracture path in the point of view of the fracture energy, the surface area should be unified, *i.e.* converted to that of the cross-section parallel with the specimen edge (plane yz in FIG. 4.24). Consequently, the effective energy dissipation (can also be termed effective fracture energy) of each cleavage plane will be higher than its original fracture toughness. The effective fracture energy can be calculated by EQ. 4.2.

$$E_{hkl}^{fracture} = \frac{\Gamma_{hkl}}{\cos(\phi_1)\cos(\phi_2)} \quad (4.2)$$

where Γ_{hkl} denotes the fracture toughness of a cleavage plane defined by Miller Index $\{hkl\}$, ϕ_1 and ϕ_2 represent the tilt angles of the cleavage plane, as can be noticed in FIG. 4.24.

The fracture toughness of the low index (also low energy) planes in silicon can be found in the literature, see TAB. 4.5. In Jaccodine [JAC 63], the estimation was carried out using direct cleavage tests—the material toughness is calculated with the fracture force and the geometry of the pre-crack. In Hesketh et al. [HES 93], the surface free energy was calculated based upon the number of bonds on the target surface exposed by etching process. The values that are the most widely used in fracture investigations were obtained by fully-density functional molecular dynamic simulations [PÉR 00a, PÉR 00b].

TABLE 4.5: Fracture toughness of low energy crystal planes in silicon.

Plane family	Fracture toughness (J/m ²)		
	[JAC 63]	[HES 93]	[PÉR 00a, PÉR 00b]
{111}	2.46	2.30	2.88
{110}	3.02	2.82	3.46
{112}	–	3.26	–

6.3.2 Fracture energy review

In sections 6.1 and 6.2, only the cleavage plane nature has been indicated, yet the exact plane index can be determined with pole figures. It consists in drawing a pole figure for every equivalent plane within the known plane family and finding out whose project point is located at the center of the pole figure. With the orientation of each cleavage plane, as presented in TAB. 4.4, the effective fracture energy can thus be determined using EQ. 4.2.

Since the grain orientation has been measured, the orientation of any crystal plane can be obtained (the normal direction of a low energy plane can be calculated with transformation matrix, as will be detailed in section 8.2). Therefore, the effective energy dissipation

can be calculated for all potential low energy crystal planes, and then the lowest energy plane as well as the plane index can be theoretically determined. The comparison between the experimental cleavage planes and the theoretical lowest energy planes are exhibited in TAB. 4.6.

TABLE 4.6: Energy review on the fracture planes in the twin plate 5-1.

Grain	Cleavage plane		Lowest energy plane	
	Effective energy dissipation (J/m ²)	Nature	Effective energy dissipation (J/m ²)	Nature
1	3.20	(11-1)	3.28	(11-1)
2	3.20	(11-1)	3.28	(11-1)
3	3.84	(-111)	3.92	(-111)
4	3.20	(11-1)	3.28	(11-1)
5	2.98	(11-1)	2.94	(11-1)
6	3.20	(11-1)	3.28	(11-1)
7	4.08	(11-1)	3.40	(1-11)
8	3.28	(11-1)	3.34	(11-1)
4*	3.20	(11-1)	3.28	(11-1)
9 ₁	4.20	(11-1)	3.13	(1-11)
9 ₂	3.55	(110)	3.27	(111)
9 ₃	3.15	(1-11)	3.20	(1-11)
9 ₄	3.55	(110)	3.27	(111)
9 ₅	3.15	(1-11)	3.13	(1-11)
10	2.94	(11-1)	2.96	(11-1)
11	3.52	(110)	3.26	(111)

Note : The calculation is based on $\Gamma_{111}=2.88 \text{ J/m}^2$ and $\Gamma_{110}=3.46 \text{ J/m}^2$ [PÉR 00a, PÉR 00b].

It can be noticed that the majority of the cleavage planes are coherent with the lowest energy planes. Unexpectedly, in grains 7, 9₁, 9₂, 9₄ and 11, the crack has chosen a crystal plane that has a higher energy dissipation. This means that besides the effective fracture energy, the crack is influenced by other factors. It should be noted that there are no sub-grains within these grains, so in-grain crystal defects can be ruled out. This inconsistency could be conducted mainly by three mechanisms : the first is the crack propagation velocity, the second is the cleavage plane level misorientation (CLMIS) *i.e.* the orientation difference between the two cleavage planes by the two sides of the grain boundary, and the third is the applied stress field.

i) For the first possibility, as reported in [SHE 03b, SHE 04b, CRA 00], the crack will choose the a higher energy plane (3.52 J/m²) rather than a lower energy one (3.46 J/m²) when the propagation velocity exceeds 3000 m/s. However, in this work, we have already proven in chapter 3 that the conclusion in the literature should be considered with cau-

tion. The reported cleavage plane deflection is due to rather stress perturbation than crack propagation velocity. Thus, the velocity related cleavage plane choice can be disregarded.

ii) The second is the CLMIS effect. If the planes with theoretical lowest energies were chosen, the CLMISs would eventually be very important, in our case 55° , 48° , 39° , 39° , 17° for 6-7, 4*-9₁, 9₁-9₂, 9₃-9₄, 10-11 grain boundary crossings, respectively, while these angles are 40° , 30° , 35° , 35° , 21° , with respect to the experimental cleavage planes. When penalizing the effective energy dissipation with $1/\cos(\text{CLMIS})$ (here the tilt part $\Delta\phi_1$ and the twist part $\Delta\phi_2$ are not considered separately), as done in [QIA 07], the values for the experimental cleavage planes and the theoretical lowest energy planes become 5.32 J/m^2 versus 5.93 J/m^2 in grain 7, 4.85 J/m^2 versus 4.68 J/m^2 in grain 9₁, 4.27 J/m^2 versus 4.20 J/m^2 in both grain 9₂ and 9₄, and 3.77 J/m^2 versus 3.41 J/m^2 in grain 11. We notice that the consideration of the CLMIS only helps to explain the incoherence in the grain 7. Regarding the rest cleavage planes, the third mechanism is taken into account.

iii) As can be seen in FIG. 4.17, the crack finally runs out of the inner contact span, and the grains 9₁, 9₂, 9₄, 11 are in fact subjected to a disturbed stress field in vicinity of the punch roller. The fracture path is likely affected by the contact perturbation, since inside the above grains, the energy dissipation of the cleavage planes is very close to that of the lowest energy planes, as analyzed in the second mechanism.

Through the cleavage plane identification by fractographic analysis and pole figure monitoring, as well as the energetic review inside all the fractured grains in the twin plate 5-1, it can be concluded that the crack follows a low energy plane but not always the lowest energy plane. The grain boundary plays an important role over the fracture path by toughening the cleavage plane with CLMIS.

7 Grain and twin boundaries crossing

In section 5.2, it has been shown that the velocity did not reach a steady state, unlike the crack propagation in silicon single crystal. The crack velocity variation is due to the effect of the grain boundaries. Moreover, the fracture path investigation has already revealed the crack surface morphology in the grains, but little is known about that in the grain boundary and twin boundary regions. In this section, the misorientations of the adjacent grains will be considered, and the grain boundary and twin boundary crossings will be investigated.

7.1 Misorientation characterization

A grain boundary can be unambiguously described by five macroscopic degrees of freedom [LEJ 10] : a common crystallographic axis (see Appendix E for explanation) of the two separated grains l (two DOFs), the grain level misorientation (GLMIS) angle θ that allows to bring both grains in perfect matching (one DOF), and then the boundary plane normal direction n (two DOFs), as schematized in FIG. 4.26. Two particular cases can be encountered : when l is perpendicular with n , the grain boundary misorientation

can be described by a pure tilt angle; when l is parallel to n , the misorientation can be characterized by a pure twist angle. Generally, a grain boundary owns a mixed character. In practice, the grain level misorientation can be calculated from a rotation matrix \underline{H} represented by Euler angle triplet in reference of one grain crystallographic coordinate system. \underline{H} can be computed with the Euler rotation matrix of both grains in the reference coordinate system of the specimen (the global system) as indicated in EQ. 4.3.

$$\underline{H} = \underline{R}_{g2} \cdot \underline{R}_{g1}^T \quad (4.3)$$

with \underline{R}_{g1} and \underline{R}_{g2} the rotation matrix from the global system to the local crystalline systems of the two involved grains.

The misorientation is then obtained with the expression reported in [MAI 93] and presented in EQ. 4.4 :

$$\theta = \text{Arcos}((H_{11} + H_{22} + H_{33} - 1)/2) \quad (4.4)$$

Due to the symmetry of cubic structure, the rotation matrix has 24 equivalent rotations which ensure the same crystalline structure (see Appendix B). Thus, the calculations with EQ. 4.4 turn out 24 misorientations based on the 24 equivalent rotations, but only the smallest value makes sense.

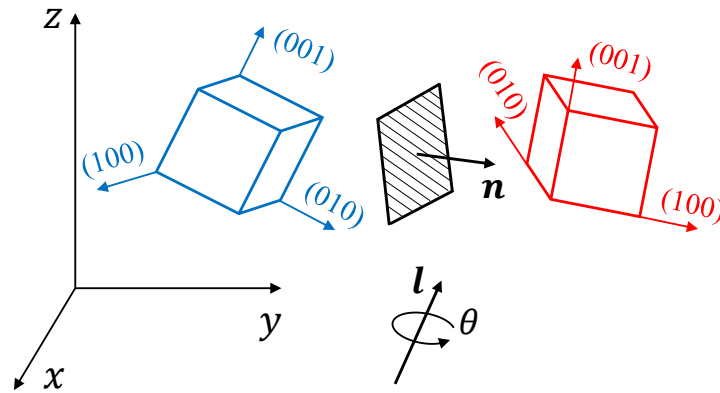


FIGURE 4.26: Schematic drawing for grain boundary misorientation : the hatched plane denotes the grain boundary; l and n represent the common crystallographic axis of both grains and the normal vector to the boundary plane, respectively; θ represents the misorientation.

With the orientations measured by the Laue X-ray diffraction, the common axes, the GLMISs as well as the angles between the common axes and the grain boundary normal have been determined and presented in Table 4.7. The latter have been addressed in order to assess the weights of the twist and tilt angles for each GLMIS. When the angle formed by the common axis and the grain boundary plane ξ is between 0° and 45° , the twist part is more important. Otherwise, the tilt angle occupies a greater part when ξ is between

45° and 90°. The grain boundary's normal is determined thanks to the fractography on the grain boundary crossing that will be detailed in the next part. It can be noticed that twins are associated with a common axis of [111] family and a GLMIS of 60°. The grains 1 and 2 have a twin relationship, but their common mirror (symmetrical) plane is also the cleavage plane, this is why the crack does not change the direction across the their grain boundary (see FIG. 4.20 and FIG. 4.27). Besides the twin regions, across each two successive grains crossed by the crack, the GLMISs are generally important, with mainly a mixed character.

TABLE 4.7: Grain boundary misorientations based on the Laue X-ray diffraction measurements

Grain passage	Common axis (°)	GLMIS θ (°)	Common axis/GB ξ (°)
1-2	$\langle 1, 1, -1 \rangle$	60	82
2-3	$\langle -1, 1, 0 \rangle$	39	85
3-4	$\langle 1, 0, -1 \rangle$	39	67
4-5	$\langle 1, 1, 1 \rangle$	59	3
5-6	$\langle 0, 1, 1 \rangle$	38	61
6-7	$\langle 5, 4, 5 \rangle$	58	64
7-8	$\langle 5, 4, -5 \rangle$	56	88
8-4*	$\langle 1, 0, 1 \rangle$	38	17
4*-9 ₁	$\langle 6, 6, 5 \rangle$	30	2
9 ₁ -9 ₂	$\langle 1, 1, 1 \rangle$	60	2
9 ₂ -9 ₃	$\langle 1, -1, 1 \rangle$	60	2
9 ₃ -9 ₄	$\langle 1, 1, 1 \rangle$	60	2
9 ₄ -9 ₅	$\langle 1, -1, 1 \rangle$	60	1
9 ₅ -10	$\langle -5, 2, 5 \rangle$	22	62
10-11	$\langle 1, 2, -2 \rangle$	57	80

7.2 Grain boundaries crossing

Two cleavage planes separated by a grain boundary are mostly discontinuous due to the GLMIS, which results in a CLMIS (cleavage plane level misorientation). Thus, when a crack arrives at a grain boundary, it should break through the barrier and then propagate on the chosen cleavage plane in the grain ahead of the grain boundary. Because of the discontinuity, the fracture path can be affected heavily by the CLMIS, as shown in section 6.3.2. Here, the authors differentiate the GLMIS from the CLMIS since they are different in most cases. Generally, CLMIS is smaller than GLMIS since the grain contains more cleavage planes (6 (110) and 4 (111)) than crystalline coordinate system directions

(3 (100) plane normal). In a fracture process, CLMIS should be taken into account in grain boundary resistance analysis rather than GLMIS, as done in [QIA 07, CHE 07b].

The resistance effect of silicon grain boundaries on the crack has been investigated in tensile configuration [QIA 08]. It has been highlighted that the crack front will go across the grain boundary at several breakthrough points and the persistent grain boundary islands between these points will release the rest part of the crack front till a critical penetration. In our case, the loading configuration is the 4-point bending, which induces a very different cracking process compared to the tensile configuration. As depicted in [SHE 04b], the crack front covers first completely the lower (tensile) part of the specimen's section and then advances toward the compression part. In bending condition, the maximal tensile stress resides on the lower skin of the specimen, the first breakthrough points would therefore be near to the specimen's lower surface and the breakthrough points would initiate progressively toward the specimen's top surface.

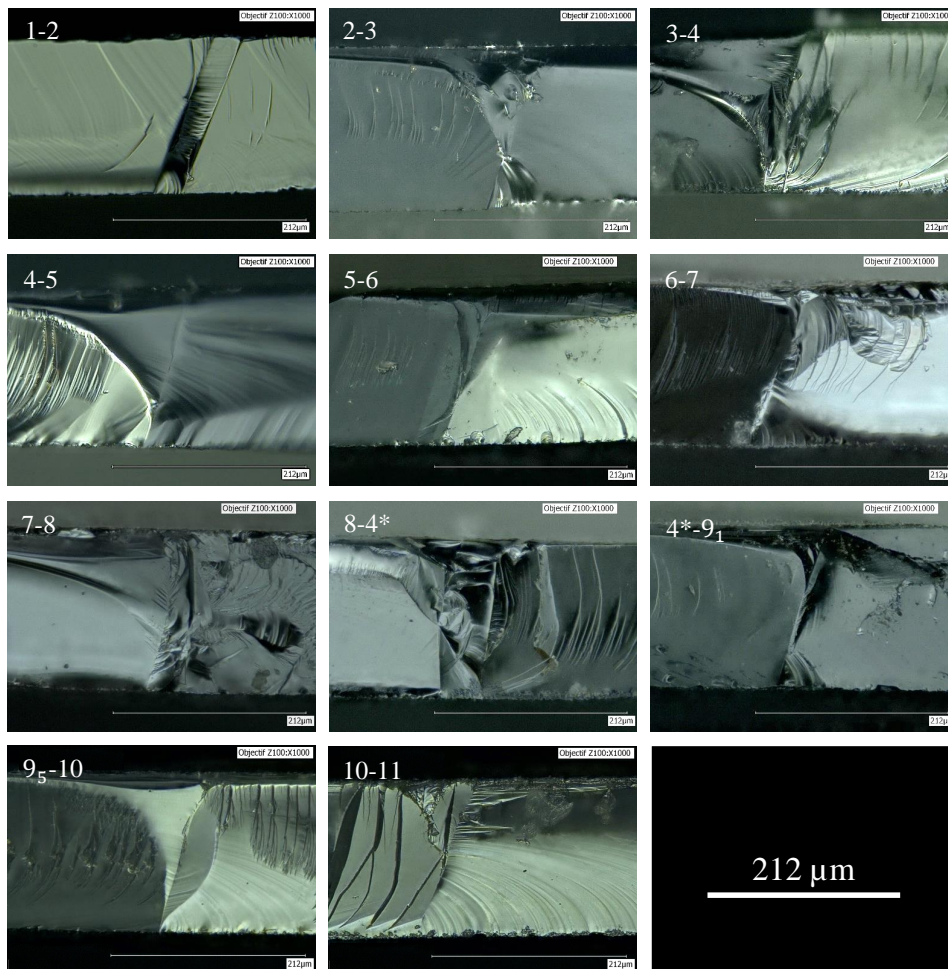


FIGURE 4.27: Fractography on the grain boundaries crossing (crack runs from the left to the right)

4. Fracture in multi-crystalline silicon

In order to study the fracture behavior at the grain boundaries, the micrographies of the fracture surface in the vicinity of the grain boundaries have been taken on one of the twin plates (twin plate 5-1). The results are displayed in FIG. 4.27, all the crossing spots have been considered. Except the crossing at the boundary 1-2 for which the two separated crystals have twin properties, two kinds of passing behaviors can be distinguished. For the boundaries 3-4, 4-5, 5-6, 7-8, 9₅-10, 10-11, one can observe that the crack front deflects almost from the lowest point into a non-planar area before arriving at the grain boundary. Besides, this area covers the grain boundary and looks like a "V" shape. For the other crossing micrographs, the transition region can be depicted as a "X" shape, where the deflection begins from a middle point that is about 1/3 the thickness away from the lower surface. From the Scanning Electron Microscope (SEM) images presented in FIG. 4.28, we can observe the Wallner lines at the lower part ahead the grain boundary for the two cases. The shape of Wallner lines means that the crack front is elliptical at this place thus the break points are always located at the lower surface (according to the crack front advancing in [SHE 04b]), event though the second crossing case results in the deflection at a middle point. The deflection can be explained such that the CLMIS between grains leads to a disturbance of the stress field near the grain boundary, as discussed in [GER 90]. When the crack runs close to the latter, the crack front would be strongly trapped. This trapping effect is maintained until the crack continues on the proper cleavage plane after crossing the grain boundary.

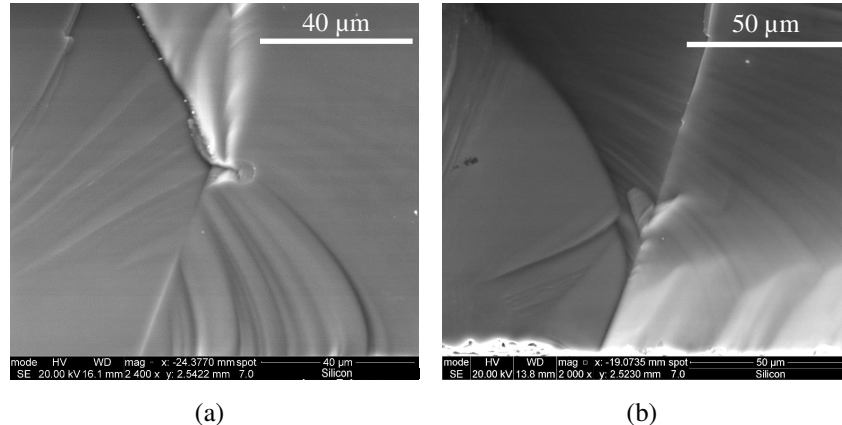


FIGURE 4.28: SEM images for grain crossing details. The crossing locality from the grain 2 to 3 (a) and the crossing locality from the grain 4 to 5 (b).

The difference between the two kinds of crossing behaviors is likely related to the CLMIS across the grain boundary. The CLMIS can be assessed, given that the cleavage plane orientations have been determined and presented in TAB. 4.4. The tilt part of the CLMIS is $\Delta\phi_1$ and the twist part is $\Delta\phi_2$ (Δ denotes the difference). When reporting the CLMIS (tilt and twist parts) and the crossing shape at each grain boundary in a single figure, as shown in FIG. 4.29, it can be noticed that the "X" shape corresponds mainly to a high twist angle—in this case a value greater than 25° , while the tilt part has no signifi-

cant effect. An exception can be seen—the crossing should be of a "X" shape at the grain boundary G3-G4, since the latter has the same and high twist angle as the grain boundary G2-G3—while a "V" crossing shape has been observed, see FIG. 4.27. This might be explained by the fact that the crack has encountered a tiny twin when entering the grain 4, as can be noticed in FIG. 4.27. Thus, the local CLMIS would be smaller than that presented in FIG. 4.29.

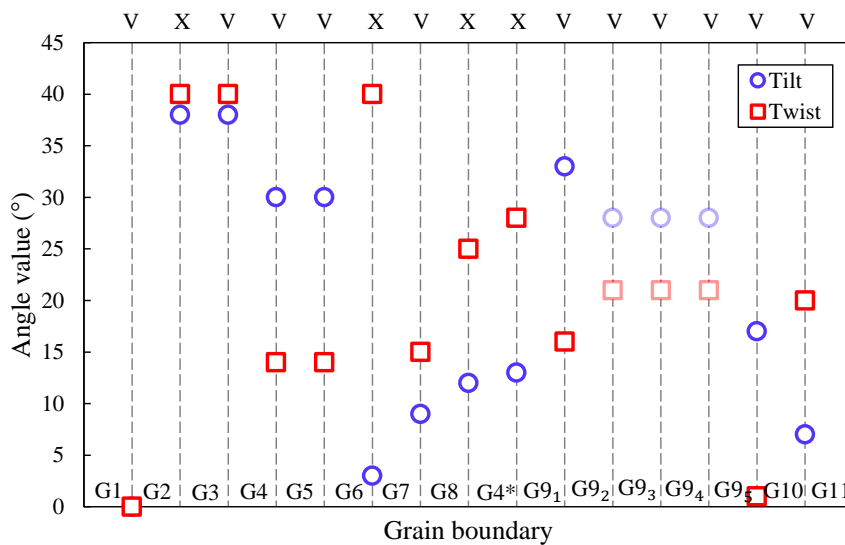


FIGURE 4.29: Correlation between the CLMIS and the crossing shape. The light color points correspond to the twin boundaries that will be detailed in section 7.3.

It has been indicated in [QIA 08] that the twist angle leads to a more resistant grain boundary than an equivalent tilt angle. Thus, for the "X" crossing case, one can imagine that the crack is stopped shortly at the lower front part so that the corresponding elliptical front is pinned at the straight grain boundary. As the crack velocity is heavily reduced, the crack propagation force raises and releases the crack front from the lower surface to the upper surface. The pinning-unpinning process is schematized in FIG. 4.31. However, for the "V" crossing case, as the resistant effect of the grain boundary is not very important, the crack front passes the grain boundary without sudden stop, as schematized in FIG. 4.30.

The grain boundary crossing behaviors can be well correlated to the monitored fracture process by the high speed camera. As presented in FIG. 4.18 in section 5, the average velocity is very low in the vicinity of the grain boundaries 2-3 and 4*-9₁. This indicates that the crack is slowed down or stopped for a short while over there. Correspondingly, the crossing morphology is exactly of a "X" shape at these two grain boundaries.

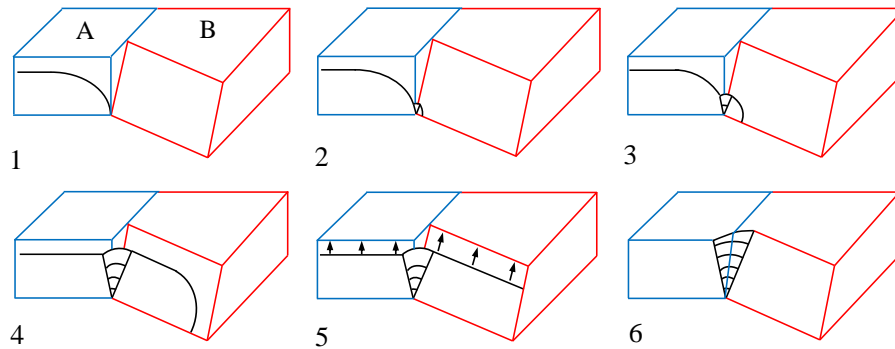


FIGURE 4.30: Schematized process on the "V" crossing mechanism at a grain boundary, grain A and grain B are the two adjacent grains, the numbers address the successive advancing. This crossing behavior correlates a low twist angle between the two cleavage planes.

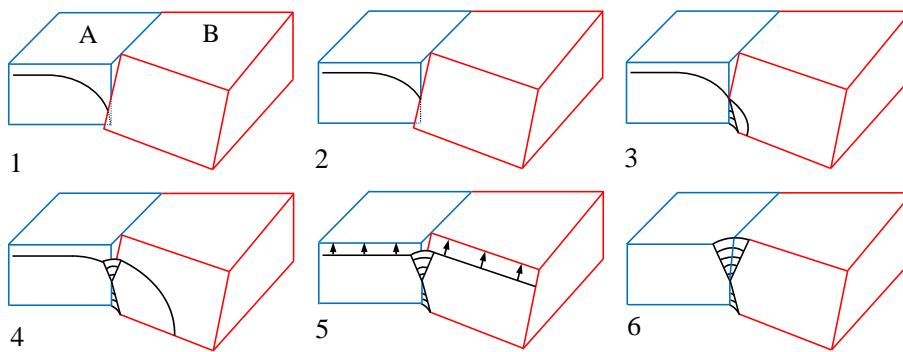


FIGURE 4.31: Schematized process on the "X" crossing mechanism at a grain boundary crossing, grain A and grain B are the two adjacent grains, the numbers address the successive advancing. This crossing behavior correlates a high twist angle between the two cleavage planes.

7.3 Twin boundaries crossing

A long strip like twin boundary corresponds to a (111) plane in a grain. For this special boundary, it is easy to identify 4 dense common axes, *i.e.* three [110] axes associated with a same pure tilt angle and one [111] axis associated with a pure twist angle. Using EQ. 4.4, the tilt and twist angles are 70.5° (coherent with the measurement in [STO 15]) and 60° (coherent with the analysis presented in TAB. 4.7), respectively.

The twin boundary crossing can be theoretically analyzed since the angular relationship between the low energy planes is well established, as presented in FIG. 4.32. When the cleavage plane behind the twin boundary is (111), the most favorable plane ahead the twin boundary is either a (111) plane or a (110) plane (FIG. 4.32a), as the corresponding CLMIS is relatively small – 38.9° if the (111) is chosen (FIG. 4.32b) and 35.3° if the

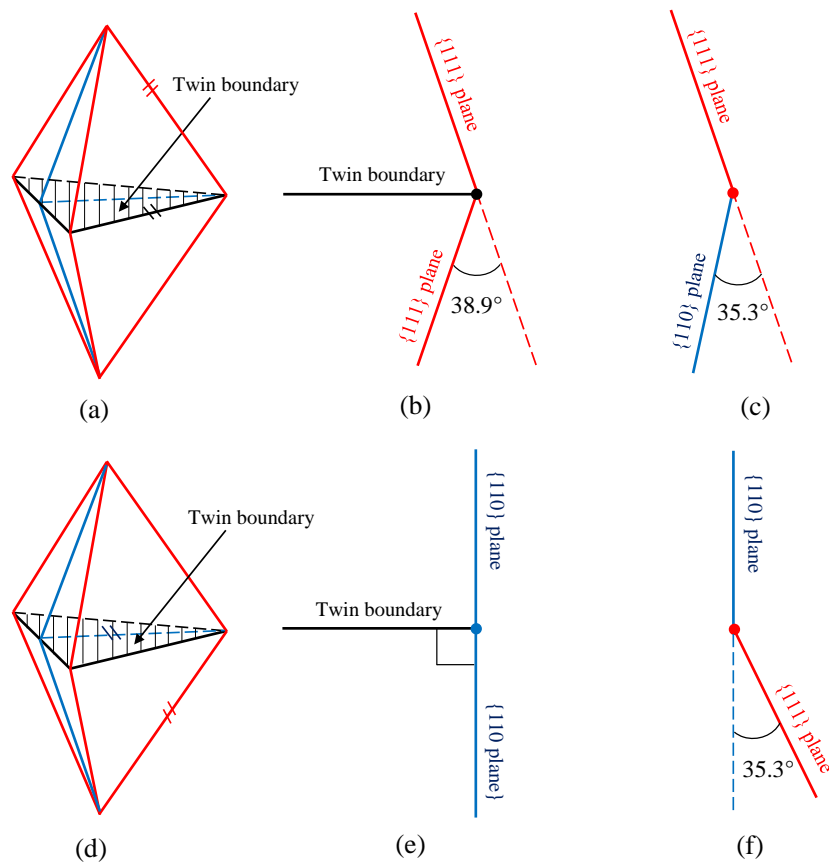
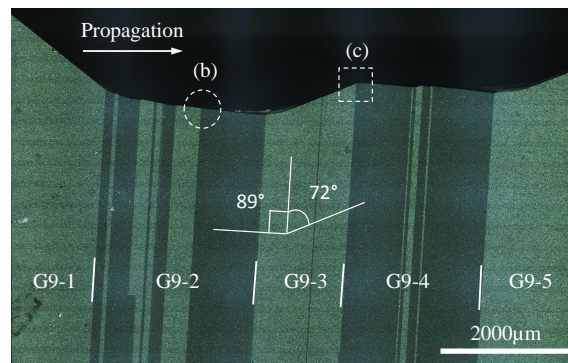


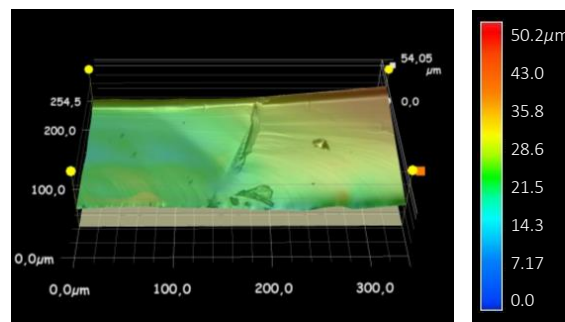
FIGURE 4.32: Theoretical twin boundary crossing from the up to down. Two tetrahedrons with a common face of a $\{111\}$ plane, the initial cleavage plane is $\{111\}$ (a), the preferential plane ahead of the twin boundary is either the $\{111\}$ plane (b), or the $\{110\}$ (c), two tetrahedrons with a common face of $\{111\}$ plane, the initial cleavage plane is $\{110\}$ (d), the preferential plane ahead the twin boundary is either the $\{110\}$ (e) or the $\{111\}$ plane (f). The two short parallel lines in (a) and (d) indicate the intersection between the two cleavage planes with a color correspondence in (a)-(c) and another in (d)-(e).

$\{110\}$ plane is selected (FIG. 4.32c). When the cleavage plane behind the twin boundary is a $\{110\}$ plane (FIG. 4.32d), the crossing will most probably result in a direct connection to a $\{110\}$ plane (FIG. 4.32e) or a deflection onto a $\{111\}$ plane (FIG. 4.32f) just like in opposite direction of FIG. 4.32c.

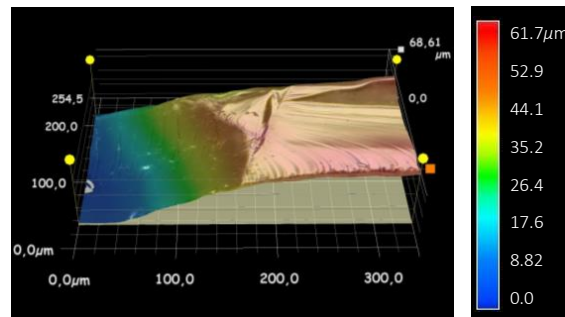
In section 6.1 and 6.2, the cleavage planes have already been experimentally identified as $\{111\}$, $\{110\}$, $\{111\}$, $\{110\}$, $\{111\}$ in twins 9_1 , 9_2 , 9_3 , 9_4 , 9_5 , respectively. The crack path and representative crack surface topography are illustrated in FIG. 4.33. The 3D morphology has been obtained under the confocal microscopic (Keyence VHX 2000) with a vertical moving up down every micrometer. One can see in FIG. 4.33(a) that the crack on $\{110\}$ planes is almost perpendicular to the twin boundaries, while the $\{111\}$ cleavage planes form an angle of 72° with the twin boundaries. Both are coherent with



(a)



(b)



(c)

FIGURE 4.33: Twin boundary crossing. Surface observation of the twins (a), topographies on the twin boundary crossings in ϑ_2 (b) and from ϑ_3 to ϑ_4 (c), as spotted by the dashed circle and the dashed square in (a). The measured CLMISs are 2° and 33° for (b) and (c), respectively.

the theoretical angles *i.e.* 90° between a (110) plane and a (111) plane and 70.5° between two (111) planes, see TAB. 4.2. The topography illustrated in FIG. 4.33(b) addresses the passage from one (110) to another one without remarkable deflection as the two planes are continuous. This corresponds well to the predicted case shown in FIG. 4.32(e). Regarding the connection from a (111) plane to a (110) plane, as revealed in FIG. 4.33(c), we have

measured a CLMIS of 33° thanks to the angle measurement tool in the Keyence system. This is coherent with the predicted case in FIG. 4.32c in which the theoretical CLMIS is 35.3° . The tilt part ($\Delta\phi_1$) of this CLMIS can be measured in FIG. 4.33(a), the value is about 28° . Thus, the twist part $\Delta\phi_2 = \arccos(\cos(\text{CLMIS})/\cos(\Delta\phi_1)) = 21^\circ$. Corresponding to this twist angle, the twin boundary crossing manifests a "V" shape, which follows the CLMIS–crossing shape correlation established at grain boundaries (see FIG. 4.29).

8 Fracture modeling

Most works dealing with silicon fracture were based on experimental testing, with sometimes dynamic molecular or quantum mechanical simulations explaining specific phenomena. Indeed, the fully anisotropic fracture characteristics can hardly be dealt with linear elastic fracture mechanics. Cohesive zone model can be used to simulate fracture propagation comparable to atomic debonding process, while a very small scale should be considered in order to have smaller mesh size with respect to the characteristic cohesive length [DRU 01]. Thus, the modeling and simulation on a structure of $50 \times 50 \times 0.17 \text{ mm}^3$ would be very computationally expensive. In this work, we find the Extended Finite Element Method (XFEM) based on the cohesive section a very good alternative to give insight to the overall macroscopic fracture simulation, given that in MCSi the fracture is transgranular, and the crack follows cleavage planes. The modeling will be presented in the following sections.

8.1 Cohesive-XFEM method

Conventional XFEM method, which was first introduced by [BEL 99], consists in enriching the shape function with a Heaviside function and eventually some asymptotic functions to introduce the discontinuity in the displacement field and to well represent the singular stress field around the crack tip, respectively, as can be seen in EQ. 4.5 :

$$u = \sum_{I=1}^N N_I(x) [u_I + H(x)a_I + \sum_{\alpha=1}^4 F_\alpha(x)b_I^\alpha] \quad (4.5)$$

where u_I is the usual nodal displacement vector associated with the continuous part of the finite element solution; $N_I(x)$ are the usual nodal shape functions; the product of $H(x)$ and a_I introduces the discontinuous jump across the crack surfaces, thus the crack can cross the elements; the product of $F_\alpha(x)$ and b_I^α handles the elastic asymptotic crack-tip field. Thanks to this asymptotic term, the crack can stop inside the elements.

Concerning the XFEM method implemented in the Abaqus software [ABA 13], the discontinuity is introduced in the way that a cohesive surface is inserted in the element via phantom nodes when the damage initiation criterion is reached upon the integration point [SON 06]. As illustrated in FIG. 4.34, phantom nodes, which are superposed on the original real nodes, are introduced to represent the discontinuity of the cracked elements. First of all, the element is intact, each phantom node is completely constrained to its

corresponding real node. When the element is cut through by a crack, phantom node and its corresponding real node are no longer tied together and can move apart. The magnitude of the separation is governed by the cohesive law until the cohesive strength of the cracked element is zero, after which the phantom and the real nodes move independently.

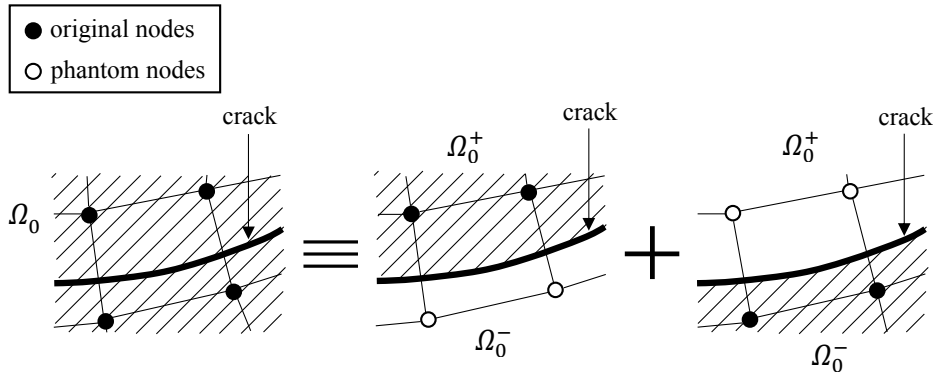


FIGURE 4.34: The principle of the XFEM with phantom nodes [ABA 13].

Using this method, the crack front cannot stop in the elements, and the singular stress field can not be taken into account since the jump in the displacement field is realized only by introducing a single cohesive interface inside the enriched element. This XFEM method is more appropriate than the classical cohesive zone model, as used in [INF 14], in which the fracture path is very dependent on the mesh, given that the crack can only take place along the element boundaries. In addition, Abaqus offers the user the possibility to define the crack initiation criterion, which suits well the modeling of anisotropic fracture behavior.

Whereas the Abaqus-XFEM is appropriate for fracture modeling of multi-crystalline silicon, there exist some limitations. The explicit integration scheme is not available for XFEM [ABA 13] – at least till version 6.13-4, and also no crack branching can be reproduced. Moreover, shell elements and solid shell elements are not enriched so that bending simulation is difficult to perform. Therefore, in this work, only one crack propagating from a pre-crack will be simulated in tensile loading, with an implicit integration scheme *i.e.* without inertial or speed effect.

8.2 Damage initiation model

A damage initiation model was elaborated in Abaqus 6.13-4 User Subroutine UDMGINI in the framework of XFEM. The initiation criterion is based on combination of the normal stress σ_n and two tangential stresses σ_{t2} and σ_{t3} of each potential cleavage plane in each grain. σ_{t2} and σ_{t3} correspond to the shear stresses that conduct the fracture modes II and III, respectively. The considered potential cleavage planes are the 4 (111) planes and the 6 (110) planes (note that no (112) planes have been experimentally identified). The stress based criterion is defined in Eq. (4.6) :

$$\delta_1 \cdot \delta_2 \cdot [\langle \sigma_n \rangle^2 + (\delta_3 \cdot \sigma_{t2})^2 + (\delta_4 \cdot \sigma_{t3})^2] = \sigma_c^2 \quad (4.6)$$

$\langle \rangle$ denotes Macaulay brackets⁴. They are used here to signify that a pure compressive stress state does not initiate damage. $\delta_1, \delta_2, \delta_3, \delta_4$ are weight coefficients, their values will be justified in following discussion.

It should be noted that the tangential components should be rigorously taken into account in the fracture behavior, with the weight coefficients δ_3 and δ_4 greater than 1. As indicated in [KOZ 07, KOZ 10], the shear stress can be more important than the tensile stress in cleavage initiation of crystalline silicon. Quantitatively, *ab initio* calculations [ROU 01] have resulted in ideal tensile stress of 22 GPa and ideal shear strength of 6.8 GPa for a (111) plane. Indeed, in our experimental work, it has been observed that the crack path is mostly far away from the maximal stress plane, implicating that the plate undergoes a mixed mode fracture where the in-plane shear stress plays an important role. Thus, δ_3 and δ_4 are set to 3 in the criterion according to the *ab initio* calculations. In order to have a stress criterion assimilated to the energy one (effective energy dissipation, see section 6.3.1), the cleavage surface inclination is taken into account in the parameter δ_1 :

$$\delta_1 = \cos(\phi_1) \cdot \cos(\phi_2) \quad (4.7)$$

with ϕ_1, ϕ_2 the tilt angles describing the cleavage plane in the global coordinate system (see FIG. 4.24).

δ_2 is another penalty factor that is used across the grain boundary. It allows to consider the CLMIS and thus set as :

$$\delta_2 = (\underline{v}_n^i)^T \cdot \underline{v}_n^{i-1} \quad (4.8)$$

\underline{v}_n^i denotes the normal direction of the potential cleavage plane in the current grain i , \underline{v}_n^{i-1} stands for the normal direction of the determined cleavage plane in the last grain $i-1$, the expression of v_n will be addressed in EQ. 4.10.

(110) and (111) cleavage planes present different fracture toughness [PÉR 00a, PÉR 00b] : $3.46 J/m^2$ for the (110) planes and $2.88 J/m^2$ for the (111) planes. This should be taken into account in the criterion by differentiating the two thresholds $\sigma_c^{(110)}$ and $\sigma_c^{(111)}$. Based on the relationship between stress and energy release rate : $G \approx \sigma^2 l / E'$ (l standing for the crack length and E' the rigidity), the thresholds ratio is deduced as $\sigma_c^{(110)} \approx 1.1 \sigma_c^{(111)}$.

When the cleavage plane is determined, the surface normal direction should be fed back to Abaqus solver to deduce the propagation direction. Since the Crystal Coordinate System (CCS) is different from the Global Coordinate System (GCS), to each grain a Local Coordinate System (LCS) which is equivalent to the CCS was established according to the orientation measurements (see FIG. 4.35). Besides, identical orthotropic rigidity matrix can be attributed to all the grains. The elastic constants used in the simulation are obtained in [HAL 67], as recalled below in CCS with $\langle 100 \rangle, \langle 010 \rangle, \langle 001 \rangle$ axes :

4. Only a positive value is retained through Macaulay brackets, otherwise, the value is rendered null

$$\underline{\underline{C}} = \begin{pmatrix} 165.7 & 63.9 & 63.9 & & & \\ 63.9 & 165.7 & 63.9 & & & \\ 63.9 & 63.94 & 165.7 & & & \\ & & & 79.6 & & \\ & & & & 79.6 & \\ & & & & & 79.6 \end{pmatrix} (10^9 Pa)$$

In order to obtain the stress components associated with the potential cleavage planes, the stress field, initially constructed in the LCS within the Abaqus solver, is transformed to a Deviated Crystal Coordinate System (DCCS). The DCCS is defined with two axes in the potential cleavage planes and the third perpendicular to this plane (see FIG. 4.35). $\underline{\underline{\sigma}}$, containing σ_n , σ_{t2} , σ_{t3} can be easily calculated as following :

$$\underline{\underline{\sigma}} = \underline{\underline{Q}}^T \cdot \underline{\underline{\sigma}}_{LCS} \cdot \underline{\underline{Q}} \quad (4.9)$$

where $\underline{\underline{Q}}$ is the transformation matrix for rotating (001) of the CCS to the DCCS. Then, the shear stresses in mode II and mode III are calculated such that σ_{t2} aligns with the intersection line between the cleavage plane and the specimen's surface and σ_{t3} in the direction perpendicular to the intersection line (see FIG. 4.35). However, the crack must be visualized in GCS, the normal direction of the crack plane in the CCS should be expressed in GCS. To do this transformation, the following formula was applied to obtain the normal direction of the crack plane :

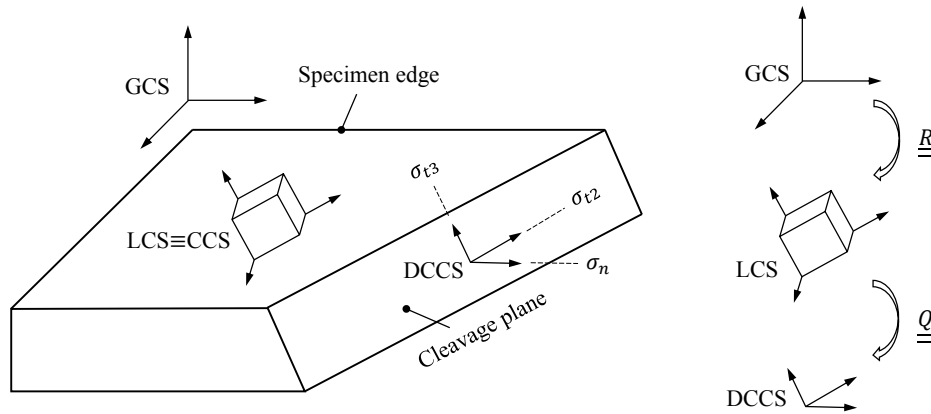


FIGURE 4.35: Different coordinate systems involved in the fracture modeling. GCS denotes global coordinate system, LCS (equivalent to CCS) stands for local coordinate system and DCCS denotes deviated crystal coordinate system.

$$\underline{\underline{v}}_n = (\underline{\underline{R}} \cdot \underline{\underline{Q}})^T \cdot \underline{\underline{v}}_n^{(111)/(110)} \quad (4.10)$$

where $\underline{\underline{R}}$ represents the transformation matrix from the GCS to the LCS, $\underline{v}_n^{(111)/(110)}$ denotes the normal direction to the chosen (111) or (110) plane.

As mentioned above, the element that undergoes damage involves a cohesive interface. The damage initiation criterion deals with the selection of the cleavage plane. A damage evolution law is then necessary in order to obtain a real crack *i.e.* introduction of geometrical discontinuity in the structure. In this study, the energy-based damage evolution was applied over a classic linear traction-separation law, as presented in FIG. 4.36. Specifically, the normal and tangential stiffness on the cohesive interface is calculated based on the elastic properties of the enriched element [ABA 13]. The area under the cohesive response curve corresponds to the dissipated fracture energy G_c , which is equal to the intrinsic fracture energy of silicon given by [PÉR 00a, PÉR 00b] ($3.46 J/m^2$ for the (110) planes and $2.88 J/m^2$ for the (111) planes). The linear damage evolution accounts for the mode mixity. So the real fracture (when the cohesive interface is totally debonded) takes place upon the following energy relationship is reached :

$$G_n + G_s + G_t = G_c \quad (4.11)$$

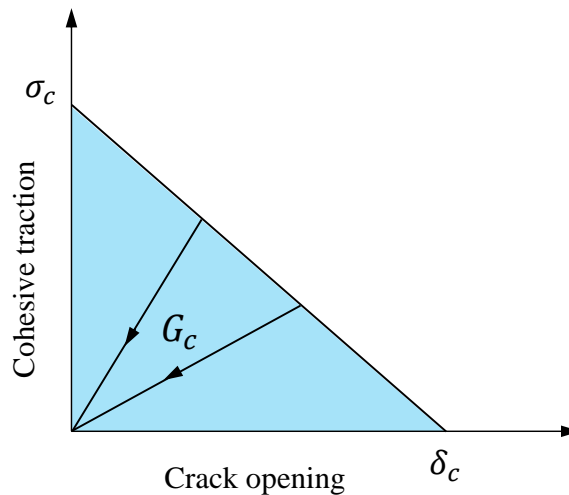


FIGURE 4.36: Typical linear traction-separation response.

8.3 Simulation

Regarding the modeling of the geometry of a multi-crystalline silicon plate, one can choose the Voronoi tessellation to generate random grain shapes, as performed in chapter 2. In this study, modeling of the real grains with respect to the specimen was carried out in order to compare with the experience (twin plate 5-1). It consisted in generating the grain shapes in Abaqus model from the grain contours obtained in ImageJ, as presented in FIG. 4.37(a). Concretely, the grain contours' coordinates are imported into the finite element model through a Matlab code, then the grain boundaries are generated with the

partition tool of Abaqus⁵. The grain orientations (LCS, also CCS) are assigned to the grains thanks to the Laue X-ray diffraction measurements that have been presented in section 6.2.1.

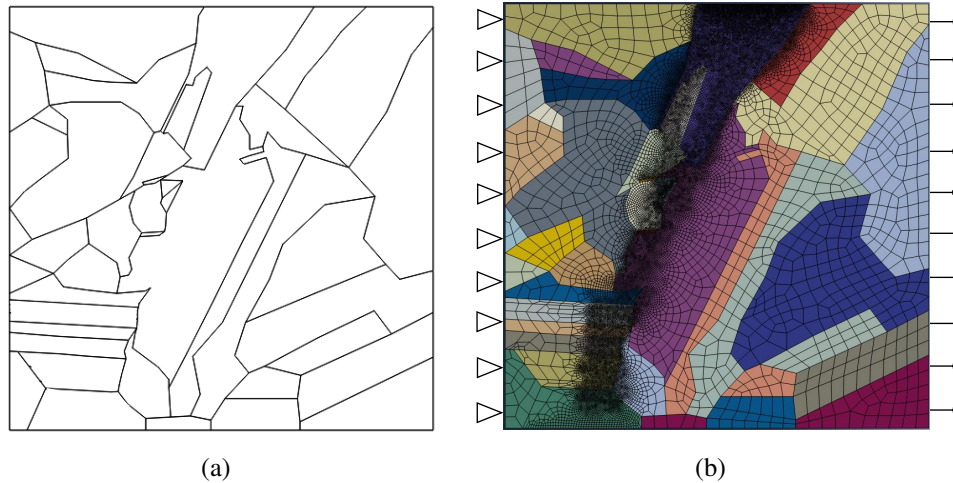


FIGURE 4.37: Grain modeling of the twin plate 5-1 (a), boundary conditions and mesh on the modeled specimen (b).

A tensile loading condition is considered for the simulation, given that in bending the lower surface undergoes pure tensile loading where the crack initiates and propagates to the upper surface. The meshed plate as well as the boundary conditions are presented below (see FIG. 4.37(b)). The mesh contains 31287 linear brick solid elements with reduced integration (referred C3D8R with 1 integration point [ABA 13]). The grains along the crack are meshed with 0.1 mm element size while the other grains are assigned a global mesh size of 1 mm. Only one layer of elements is present in the thickness since the tensile loading does not induce stress gradient in thickness direction. The whole in-thickness cross section of the left edge is blocked while a displacement is applied at the right side. A pre-crack is introduced at the same location as in the real specimen. The simulation results are presented and compared with the experiments in FIG. 4.38 and in Table 4.8. In addition, the lowest energy planes are also highlighted in Table 4.8, which give insight to the expected cleavage planes in the energetic point of view.

From FIG. 4.38, it can be noticed that the numerical model results in a globally consistent crack path with respect to the experimental one. While discrepancy arises, particularly for cleavage planes of grains 9_1 , 9_2 , 9_4 and 11. The same conclusion can be drawn when comparing the exact cleavage planes both in experiment and simulation, as illustrated in Table 4.8. It has been discussed in section 6.3.1 that there exist inconsistency between the experimental crack path and the lowest energy planes in grains 7, 9_1 , 9_2 , 9_4 and 11. The main reason for the difference in grain 7 results from neglecting CLMIS in theoretical expectation. The local inconsistency in grains 9_1 , 9_2 , 9_4 and 11 is likely related

5. In this way, the grain boundaries are perfect interfaces

to the disturbed stress field due to the contact stress and the stress gradient out of the inner span. When comparing the simulation results with the experimentally identified cleavage planes as well as the lowest energy planes, it can be noticed that the consideration of CLMIS allows to numerically predict the experimental crack path in grain 7, while the tensile loading of the simulation results in a coherent path with the lowest energy planes (thus incoherent path compared to the experimental results) in grains 9_1 , 9_2 , 9_4 and 11, both do not take into account the stress perturbation in the contact region.

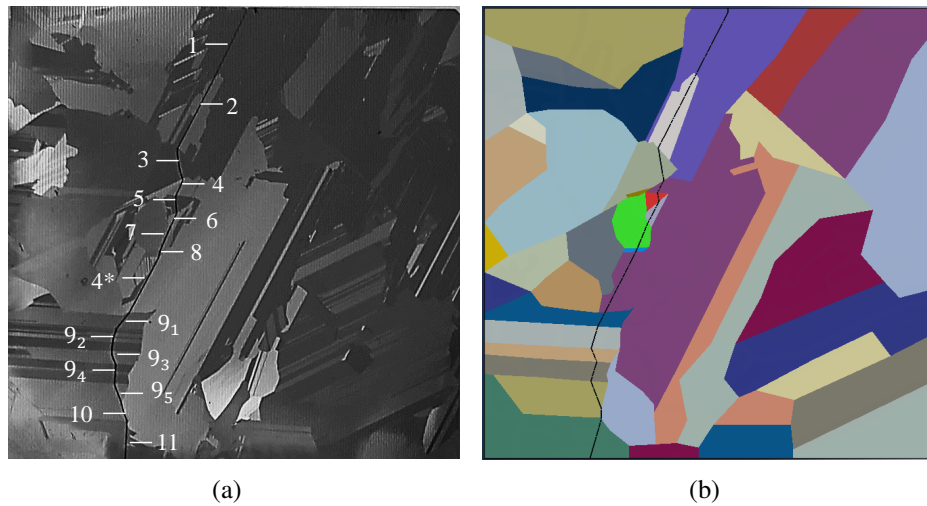


FIGURE 4.38: Comparison of the crack path between the experiment (a) and the simulation (b). The experiment was conducted in bending condition and the simulation was performed in tensile condition.

In a nutshell, this cohesive-XFEM modeling has given encouraging results on the prediction of fracture path in silicon multi-crystal. In a future work, it would be interesting to extend the model in the dynamic explicit framework and account for in-thickness stress gradient using enriched solid shell elements.

TABLE 4.8: Comparison of the cleavage planes between the experiment and the simulation

Grain	Experiment	Simulation	Lowest energy plane
1	(11-1)	(11-1)	(11-1)
2	(11-1)	(11-1)	(11-1)
3	(-111)	(-111)	(-111)
4	(11-1)	(11-1)	(11-1)
5	(11-1)	(11-1)	(11-1)
6	(11-1)	(11-1)	(11-1)
7	(11-1)	(11-1)	(1-11)
8	(11-1)	(11-1)	(11-1)
4*	(11-1)	(11-1)	(11-1)
9 ₁	(11-1)	(1-11)	(1-11)
9 ₂	(110)	(111)	(111)
9 ₃	(1-11)	(1-11)	(1-11)
9 ₄	(110)	(111)	(111)
9 ₅	(1-11)	(1-11)	(1-11)
10	(11-1)	(11-1)	(11-1)
11	(110)	(111)	(111)

9 Discussion

In this chapter, the fracture in multi-crystalline silicon has been investigated using twin plates. Thanks to high speed imaging technique, confocal microscopy, Laue X-ray measurement, as well as finite element modeling, the crack propagation mode, the fracture reproducibility, the fracture path, and the grain boundary crossing behavior have been assessed. The principal results are discussed below.

9.1 Transgranular crack

Despite of the disunified conclusions on whether crack follows grain boundaries in the multi-crystalline silicon, the discussion from different points of view promotes more fundamental researches that advance our understanding of fracture behavior in materials.

As crystal defects, grain boundaries are indeed main fracture path in many metals such as steel [KOY 12], aluminum [YAM 06] and nickel [FAR 02]. In these ductile materials, the fracture proceeds by the coalescence of microvoids formed due to plastic flow accumulation or impurity segregation at the grain boundaries. However, in MCSi, the material deforms elastically before breaking up, and the fracture proceeds by the consecutive atomic debonding. In this case, the crack front is sensitive to crystal lattice disarrangement and can be deflected by crossing a single dislocation, as experimentally observed

in [SHE 04a]. Moreover, according to a numerical prediction [MÖL 14], bond trapping can be encountered as the crack propagates along an incoherent twin boundary. This indicates that the grain boundary is unfavorable for the debonding process in brittle fracture.

Based on our experimental observations, most of the cracks show clearly transgranular fracture path, they propagate straightly in each grain and then change the direction upon crossing a grain boundary. There exist also experimental evidence that a crack overlaps perfectly a (111) twin boundary, as presented in FIG. 4.8. In fact, a (111) twin boundary has no difference with a (111) crystal plane, the propagation along this kind of boundary is equivalent to the transgranular cleavage. The most interesting finding in our work, as presented in FIG. 4.6, is that a crack proceeds actually a zigzag path (unceasing deflections around the grain boundary) when it tends to propagate along a well oriented (with respect to the loading) grain boundary. This zigzag crack path can be seen as the first experimental proof of the numerically predicted bond trapping that the crack front undergoes at a grain boundary. In addition, the unceasing deflections should also be promoted by the dislocation perturbation. Considering the widely observed in-grain cleavage and the occasionally revealed detour at grain boundary, the crack propagation mode in MCSi is transgranular.

9.2 Reproducibility of the fracture

The reproducibility is always a very important issue for a convincing research work, especially when a complex problem is concerned. In main of the literature works, the fracture of silicon has been limited to single crystal case where one unique crack path is somehow predefined due to the anisotropic fracture characteristic. To the best of our knowledge, this is the first work that investigates the fracture reproducibility of the silicon multi-crystal.

The prior condition is to get twin specimens. The pre-crack introduction and the loading should be consistent. In this work, we successfully obtained multi-crystalline silicon twin plates from consecutively sliced silicon ingot. Yet there exist sometimes discrepancies on the pre-crack position and orientation, which lead to different fracture paths, as presented in FIG. 4.10, 4.11 and 4.12. When highly consistent pre-cracks have been obtained, fracture repeatability has been verified with the twin plates 4-1, 4-2 (see FIG. 4.14) and 5-1, 5-2 (see FIG. 4.15). The presented results in FIG. 4.15, FIG. 4.19 and 4.20 show in different scales the consistency of the fracture on twin specimens. The same crack trace on the specimen's surface reveals the same cleavage planes, while the similarity of the surface marks indicate that the two crack fronts have experienced the same atomic debonding.

The most important attention should be paid on the sub-grains, which manifest a great influence on the cleavage plane selection. Even if the misorientation is small, the atomic disarrangement should be significant in sub-grain regions due to the presence of dislocations. The authors suppose that the crack front would be trapped by crossing a relatively large disordered lattice, and the perturbation on the crack propagation is likely unpredictable.

9.3 Fracture path

The fracture of single crystal of silicon takes place preferentially on low energy crystallographic planes as (111) and (110). In silicon multi-crystal, the fracture is transgranular and the crack propagates on cleavage planes, as discussed in above section 9.1.

Thanks to the fractographic analysis and the grain orientation measurement, the nature of cleavage planes have been identified in one of tested specimens, named twin plate 5-1. The typical (111) surface instabilities rapid identification. In absence of instabilities, cleavage plane-based pole figure allows to indicate fairly the plane index of the crack surface. In summary, the majority of the cleavage planes in twin plate 5-1 belong to {111} family, the (110) cleavage planes have been found in twin regions. When assessing the effective energy dissipation of the cleavage planes, it is found that the cleavage plane level misorientation plays a role on the crack plane selection across the grain boundary, thus the crack does not completely follow the lowest energy planes (see TAB. 4.8). With the elaborated cohesive-XFEM model, the experimental fracture path can be well reproduced for the grains in the inner span region with the tensile simulation. The consideration of the CLMIS in the damage criterion allows the prediction of the (experimental) cleavage plane in the grain where the experimental fracture path deviates from the expectation, as exhibited in TAB. 4.8.

9.4 Crack velocity and grain boundary effect

As displayed in FIG. 4.18, the average crack velocity varies, conversely to the steady state of crack propagation in silicon single crystal that has been shown in chapter 3. This variation is due to the resistant effect of the grain boundaries, where the crack is slowed down or shortly stopped in function of the misorientation.

Two crossing behaviors can be distinguished, named "V" shape and "X" shape, which are likely related to the twist angle between the two consecutive cleavage planes (see FIG. 4.29). When the twist angle is important, the deflection tends to initiate from a middle thickness point ("X" shape). In this case, the crack front can not penetrate the grain boundary region immediately and thus is pinned on the grain boundary. When relating the crack velocity to the grain boundary crossing behavior, it can be noticed that the mean velocity is small when the crack crosses particularly the grain boundaries 1-2 and 4*-9₁ (see FIG. 4.18) where "X" shape deflection zones are remarkable (see FIG. 4.27).

The switch of cleavage planes concerns mainly the {111} and {110} families across a twin boundary, as analyzed in FIG. 4.32. The tilt part of the cleavage plane level misorientation is relatively small, and the crossing morphology manifests a "V" shape (see FIG. 4.33). There is no evidence that crack is significantly slowed down even it crosses unceasing twin regions.

10 Conclusion

In this chapter, the crack propagation of solar grade multicrystalline twins samples has been investigated thanks to image analysis, fractography and microscopy. Since the grains' orientations were determined with Laue X-ray diffraction, the anisotropic fracture of multicrystalline is presented by taking into account the specific orientation of each grain crossed by the crack front. A physical based XFEM modeling has been proposed in order to successfully predict the crack path produced during these experiments. The main conclusion of this work are :

(i) Under well controlled 4 points bending solicitation it is possible, for twin specimens, to reproduce exactly the same crack path since the grain shapes as well as their crystallographic orientations are well consistent in the two specimens.

(ii) The crack propagation is transgranular in multi-crystalline silicon. The cleavage planes inside the grains are the $\{111\}$ and $\{110\}$ families as in single silicon crystal. The crack front switches from one plan to another at the grain boundary by selecting the most favorable one (most of the time (111)) in term of not only the surface energy but also the CLMIS across the grain boundary. These results can be then well reproduced by XFEM simulations.

(iii) The grain boundaries have an important impact of fracture propagation since the various kinds of misorientations (twist and tilt angles) produce two different crossing mechanism. These latter namely "X" or "V" shape grain boundary crossing affect the crack velocity and therefore inhibits the crack velocity close to an average value of 400 m/s, compared with 1200 m/s of single crystal at a similar fracture stress.

General conclusions and prospects

Conclusions

In this thesis, we have investigated the elastic properties as well as the fracture behavior of silicon wafers. The main body of the work is based on experimental studies, auxiliary numerical modeling and simulations have also been performed. A special attention has been paid on the fracture behavior of silicon wafers in correlation with not only their microstructure (grain boundary, twins, sub-grains) but also with the mechanical solicitation and the crack propagation velocity. The major achievements are highlighted below, followed with some prospects for future investigations.

- I- With respect to silicon wafers stemming from novel manufacturing process, it is necessary to assess the material rigidity and strength, as well as to figure out the root which reduces the material strength. In this work, an experimental-numerical method is proposed to characterize accurately the material stiffness. The coupling between the high speed imaging technique and the fractographic analysis allows to identify more precisely the fracture origin.

- II- A large number of experiments (90) are carried out to investigate the silicon (110) cleavage. It is found that, for this cleavage plane in silicon single crystal, the fracture path is free of macroscopic deflection, contradictory to what has been shown previously in the literature. Thanks to velocity measurements, fractography, it is revealed that the initial crack velocity is close to the steady state velocity. This crack initiation behavior can be elucidated by the high energy release rate upon the crack initiation. Moreover, we highlight the crack front evolution in function of the crack propagation velocity. Particularly, when crack velocity exceeds 2800 m/s, special surface traces are observed at the fracture surface whose origin is proposed to be crack front waves. These fundamental investigations are of great interest for the scientific community in order to understand more in depth the fracture of this widely used material.

- III- Twin specimens provide us a interesting vision to investigate the cracking behavior of multi-crystalline silicon. At the very beginning, we rule out the of inter-granular

fracture mode which has been considered in the literature. With twin plates, it is highlighted that the sub-grains have a huge influence on the crack path. Through a couple of tests, a nearly perfect cracking reproducibility is demonstrated at both macro and micro scales. Most cleavage planes are identified as (111) crystal plane thanks to surface instabilities as well as non-conventional pole figures. Crack velocity is measured with the high speed imaging technique and manifests the slow-down feature close to the grain boundaries. The deceleration level can be correlated with the grain boundary crossing behavior (V shape or X shape) with respect to the cleavage plane level misorientation. A fracture modeling is carried out, thanks to an UDMGINI subroutine in Abaqus XFEM framework. It chooses the most favorable crystallographic plane and a particular attention is paid on the misorientation upon crossing the grain boundaries. This original modeling allow us to predict crack path in multi-crystals when sub-grain boundaries are rare.

Prospects

- I- Based on the observed surface traces, the highlighted velocity fluctuation as well as the good agreement between artificial front waves traces and the observed ones, we can nearly confirm the existence of front waves. Nevertheless, it would be very interesting to theoretically demonstrate the relation between these fluctuations and the generation of such solitary waves in silicon fracture.
- II- We have shown that with the high speed camera, we are limited to average velocity assessment. In the future work, it is interesting to elaborate a novel method of measuring the crack velocity with a finer resolution. This will help to correlate more precisely the deceleration effect of grain boundaries with the grain boundary misorientation.
- III- Although a sub-grain boundary represents a small misorientation, it is revealed in this work that an important deviation of the crack path can be turned out. Therefore, a more profound study should be conducted to understand the impact of sub-grains on the crack direction. A characterization of the sub-grain by EBSD is necessary. This work is in progress.
- IV- With the obtained knowledge on the fracture behavior of silicon wafers, particularly at the material level, the fracture investigation can be extended in solar cells with or without encapsulates. In this composite structure made of (EVA,) silicon wafer, metalization layer and electric connections i.e. busbars and print-fingers, the mechanical strength and the crack path of embedded silicon wafer would be impacted by residual stresses from lamination/welding points and the interaction between the layers. It will be interesting to perform tensile or bending tests with thermomechanical loading to simulate the severe solicitation that the solar cell would undergo in the service environment.

Appendices

Appendix A

Silicon plasticity

1 Introduction

The first studies of the yield behavior of silicon dated to the 1960s. Pearson et al. [PEA 57] found that silicon whiskers could yield above 600 °C when carrying out creep tests at different temperatures. Then, Patel and Chaudhuri [PAT 63] reported the macroscopic yield drop—the stress decreases after reaching the yield point rather than increasing as in metals (hardening stage)—for dislocation free semiconductor crystals like germanium during experimental straining. This phenomena encouraged other researchers to grasp this specific yield behavior which had never been observed in metals. The pioneer modelers were [ALE 69], they constructed a crystal viscoplastic model for diamond crystal materials. This model used the Orowan's equation that links the microscopic dislocation movements with the macroscopic plastic deformation. A particular dislocation evolution law allowed to reproduce the yield drop in simulations. Based on the interesting finding of [PAT 63] as well as the model of Alexander&Haasen [ALE 69], both experimental and numerical extensions were widely carried out throughout the years.

Yonenaga and Sumino [YON 78] performed a series of uni-axial tensile tests upon both intrinsic and extrinsic silicon single crystals. The well chosen crystallographic orientation ([123]) allowed to have easy glide (a single slip system is activated in earlier straining stage). This investigation recovered the influences of the temperature, the strain rate, the initial dislocation density and the dissolved oxygen concentration on the yield points. Over years, the experimental procedures varied, and the studies on multiple slip systems arose in the literature. Omri et al. [OMR 85] conducted uni-axial compression tests with different grain orientations as (123) crystals (single slip) (110) crystals (4 slips) and (001) crystals (8 slips). 4-point bending tests were also carried out by [WAL 00, CHE 99]. Due to the thermally activated nature of dislocation movement, the temperature effects received more detailed studies. In [OMR 87], the authors showed remarkable decrease of the yield point until their disappearance when increasing the temperature. Some studies determining the thermal activation energies with creep tests were reported in [TAY 72, WAL 00]. Moreover, the transition temperature was subjected to sophisticated investigations [SAM 89, BRE 92].

From the numerical point of view, the development of the microscale modeling like Molecular Dynamics (MD) and Discrete Dislocation Dynamics (DDD) allowed to take into account a single dislocation's mobility as well as the interactions between dislocations [MOU 99, DEV 06]. Based on these microscopic behaviors, extended macroscale constitutive law accounting for very complicated dislocation behaviors got a great advance. Moon et al. [MOO 01] modeled stepwise the straining in function of dislocation density. Recently, Cochard et al. [COC 10] proposed a well improved AH model in easy glide and then this work was extended to multiple slips in [COC 13]. These models need in fact a great support of experimental data for the parameter calibration and the model validation, as done in the three mentioned works.

However, the experimental support is not rich enough to be accessed by the modelers. The presented experiments held more or less drawbacks. In [YON 78], the authors only considered single slip configuration, which could not cover dislocation interactions. Besides, there existed a mounting block (with low stiffness) that obscured the real strain state in silicon specimen. Moreover, the applied strain rate on the silicon is no more constant upon the onset of plastic deformation, since the block undergoes a variant strain rate due to the non linear stress evolution. In [OMR 85], they found that a stage of easy glide seemed to appear in the crystal that supposedly underwent multiple slips. A common inconvenience for tensile and compression tests is the machine deformation under the high applied force. Concerning the bending loading in [WAL 00], the silicon plates were relatively thick so that localized plastic deformation appeared underneath the punch rollers. Due to this plastic collapse, the mean stress and strain fields were no more available.

In this study, we carried out 4-point bending tests at high temperature (600°C-1000°C) to enrich the experimental data base in the yield region. In order to avoid the localization problem, the studied specimens were obtained from very thin single crystalline solar grade silicon wafer—the thickness is around 190 μm . Investigations on the temperature and strain rate dependence were addressed, as will be presented below.

2 Specimens and experimental setup

The studied specimens are cut from single crystalline silicon wafer as showed in FIG. A.1, the dimension for all tested specimens is 50 mm \times 10 mm \times 195 μm . The crystallographic orientation is such as two [110] directions align with the length and the width while one [001] direction is perpendicular to the specimen's surface. Therefore, the firstly activated slip systems are $\langle -101 \rangle$ (111), $\langle 0-11 \rangle$ (111), $\langle 011 \rangle$ ($-1-11$) and $\langle 101 \rangle$ ($-1-11$), as depicted in FIG. A.2. The two slip plans make 70.5°. The two slip directions on each plan make 60°, while the crossing angle between two slip directions on different plans is either 60° or 90°. The interactions and the intersections between dislocations would take place as soon as the dislocations move.

The used silicon wafers are of very high purity (99.99999%), the precipitates and the dissolved oxygen concentrations are ignored. However, the initial dislocation density is unknown. In fact, this information are rarely available in the publications, but it is

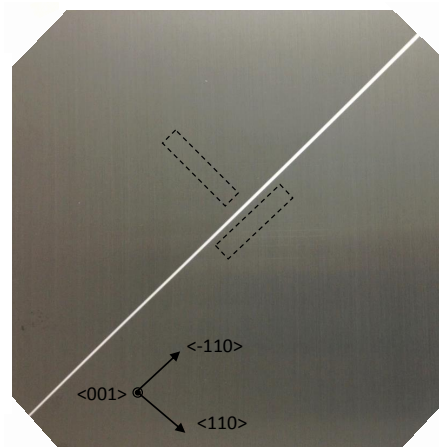


FIGURE A.1: Specimens cut from thin silicon wafer.

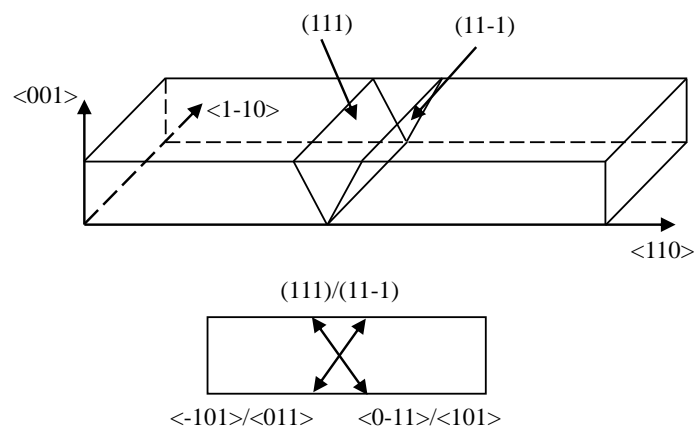


FIGURE A.2: Firstly activated slip systems.

widely accepted that the grown-in density is very low—in the most of cases in the order of magnitude of 10^8 m^{-2} [YON 78, SUM 80]. The measurement was based on etch-pit counting on the (111) surface to have an approximate quantity, then this estimated density was assumed to be identical in all other systems.

The experimental set up is presented in FIG. A.3. The left image shows the outside view of the furnace that allows to get the desired temperature, the right one highlights the inside mounting. Concretely, the bending apparatus possesses a punch and a support made of alumina. The inner contact span and the outer contact span are 18 mm and 40 mm, respectively. In order to avoid serve contact stress, the punch rollers are rounded by a diameter of 1 mm. The furnace is mounted on a LLOYD-Ametek LFPLUS electro-mechanical machine which is equipped of a moderate loading cell (0-10N) with low loading velocity (the lowest is 0.2 mm/min).

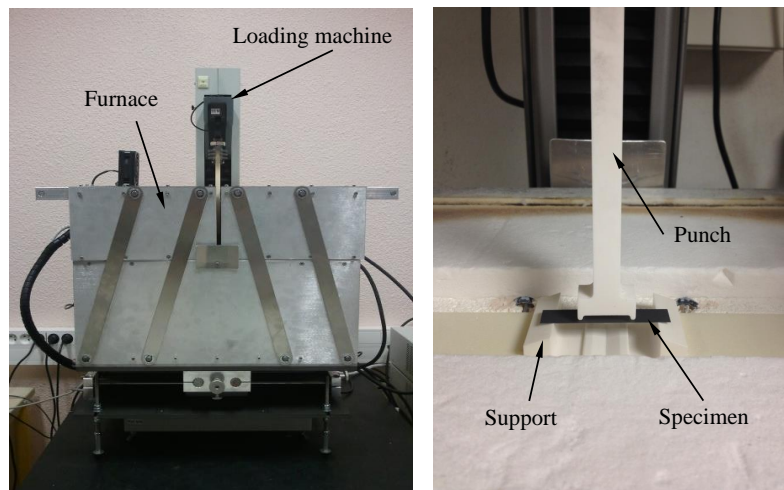


FIGURE A.3: Experimental set up at high temperature.

3 Experimental procedure and results

Firstly, the repeatability will be assessed, the aim is to confirm that the initial dislocation density is identical in the tested specimens. Also, the experimental result will be compared with the literature work under equivalent loading condition, the comparison will justify the necessity of our work. Then, two series of tests will be performed, the first is to vary the temperature and the second is to vary the applied strain rate, given that the yield stress depends on the temperature and the strain rate as found in experimental results [YON 78, SUM 99].

3.1 Reproducibility and comparison with existing results

As mentioned in the former section, the silicon single crystal specimens are cut from thin silicon wafers. In order to guarantee that the studies on the influences of other parameters like temperature and strain rate make sense, a preliminary investigation upon the consistency of the specimens was carried out. The called consistency concerns mainly the initial dislocation density that might vary from one specimen to another.

Logically, it consists of comparing the behaviors of two randomly chosen specimens stemming from different wafers. The same thermo-mechanical conditions were used. The testing temperature was fixed at 900°C and the applied loading velocity was fixed at 0.2 mm/min for this study.

The two force-deflection curves are presented in FIG. A.4. They are well superimposed with one to the other. Therefore, we can conclude that the initial dislocation density does not influence the mechanical behavior in our work. This indicates that parametric studies on temperature and strain rate can be fairly carried out.

Moreover, a comparison with existing results in the literature was conducted, particularly the bending results reported in [CHE 99, WAL 00]. In order to keep the same testing

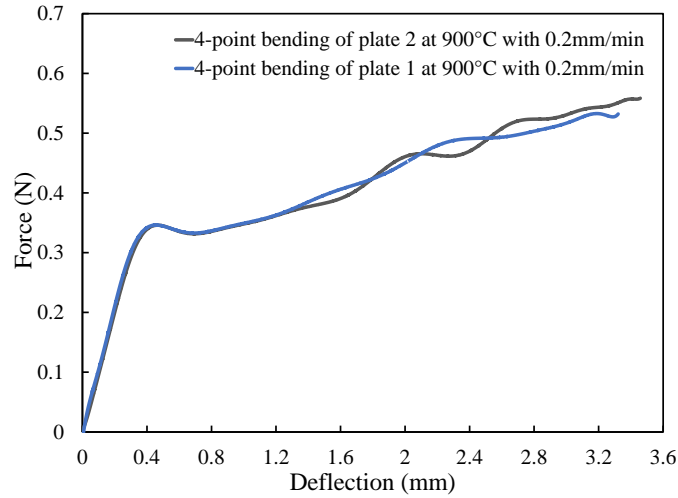


FIGURE A.4: Comparison between the specimens cut from two directions.

conditions, 800°C and 0.63 mm/min (equivalent strain rate $7.5 \times 10^{-6}/s$) were used. Also, to facilitate the comparison, the results are converted into strain stress relationship using the beam theory. One can observe in FIG. A.5 that there exists a great difference. In the linear elastic region, the Young's modulus of [110] direction can be deduced—105 GPa for the literature work while 163 GPa for our test. Taking into account the temperature effect, as reviewed in [MAS 12], the Young's modulus along [110] direction is approximately 160 GPa at 800°C. In the yield region, it can be noticed that the literature work presents a higher upper yield stress while a smaller lower yield stress with respect to our study. Moreover, the results in this study shows a much higher hardening rate. The difference in the yield region is due to the fact that the plastic deformation is localized in the contact zone in the literature work, as mentioned in [WAL 00] (see FIG. A.8), while it is more uniformly distributed in our test, see FIG. A.9. Thus, the result obtained with our experimental set up is more reliable.

3.2 Effects of temperature

The threshold temperature for silicon yielding depends on the strain rate as discussed in [SAM 89]. The experimentally revealed lowest temperature is around 550°C with respect to a low strain rate of $1.3 \times 10^{-6} s^{-1}$. On the other hand, extremely high temperature leads to the disappearance of the yield drop and involves in very complicated phenomena like diffusion. Omri et al. [OMR 85] reported that the stress peak only presented when at temperature below 1223 K i.e. 950°C in multiple slips case. However, the multiple yield points remained in the experiments performed by [YON 78] at 1223 K for single glide case.

In this work, we applied the lowest loading velocity i.e. 0.2 mm/min to obtain a relatively low strain rate, i.e. $2.33 \times 10^{-6} s^{-1}$ according to the beam theory. The chosen temperatures were 600°C, 650°C, 700°C, 800°C, 900°C and 1000°C. The results are presented

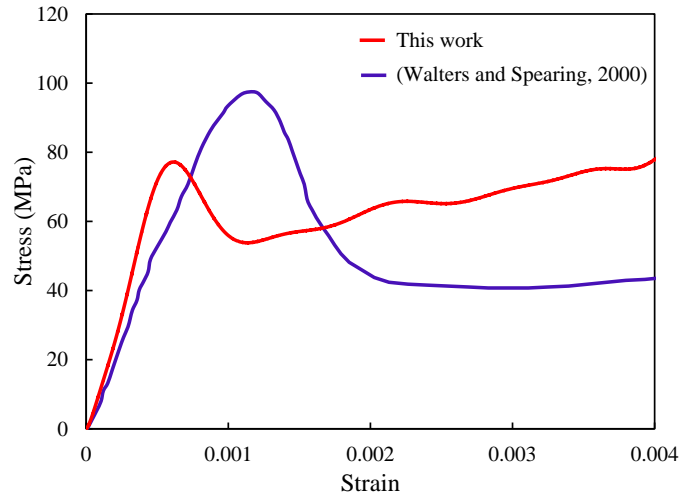


FIGURE A.5: Comparison between the results in the literature and in this study

in FIG. A.6. It should be noticed that the yield points move down as the temperature rises, and the yield drop becomes less and less remarkable consequently. Meanwhile, the yield drop phenomenon is still visible at 1000°C.

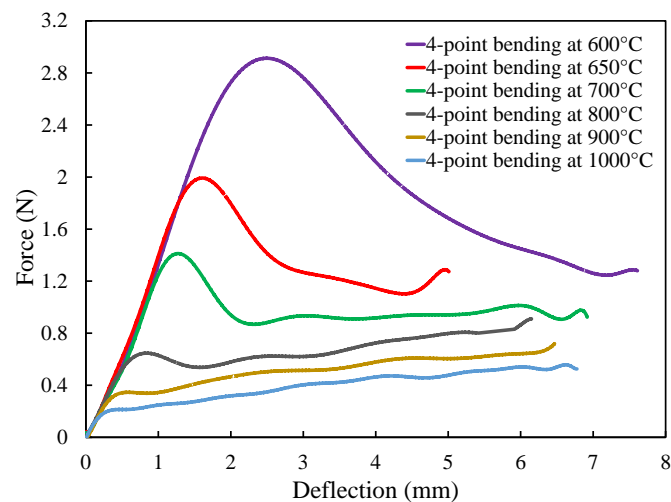


FIGURE A.6: Temperature effect.

3.3 Effects of strain rate

In microscale analysis, the dislocation mobility is mainly controlled by the temperature and the resolved shear stress, as highlighted in the mechanical behavior modeling [ALE 69, COC 13, MOO 01]. However, the macroscale yielding behaviors and latter hardening of silicon crystals are much affected by the imposed deformation rate. A higher

rate conducts to a higher yield point.

This parameter is somehow limited by the loading machine, the order of magnitude of $\times 10^{-7} s^{-1}$ or smaller is rarely encountered in the literature. As mentioned in the former section, the lowest strain rate in our study is fixed at 0.2 mm/min, which results in a strain rate of $2.33 \times 10^{-6} s^{-1}$. Starting from this value, 0.63 mm/min ($7.34 \times 10^{-6} s^{-1}$), 1 mm/min ($1.17 \times 10^{-5} s^{-1}$), 3 mm/min ($3.50 \times 10^{-5} s^{-1}$) and 6 mm/min ($6.99 \times 10^{-5} s^{-1}$) were applied at 800°C, respectively.

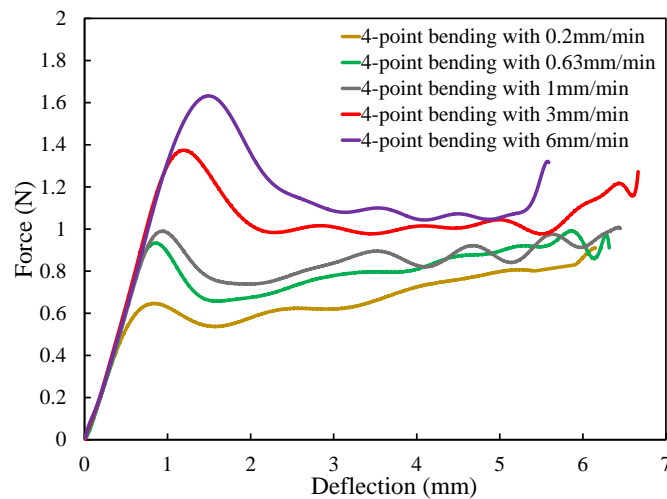


FIGURE A.7: Strain rate effect.

The results are displayed in FIG. A.7. The dependence on the imposed strain rate matches well the literature work, *i.e.* the elastic region is larger corresponding to a higher loading rate. This is also the typical characteristic of viscoplastic behavior. In fact, the dislocation velocity or macroscopic plastic strain rate is determined by the absolute shear stress on the slip plane. Considering a same stress state, the plastic strain rate occupies a relatively smaller part when the applied strain rate is important, compared to a case where the applied strain rate is small. Therefore, the yielding occurs at a higher stress state for an important loading rate than for a smaller loading rate case.

4 Discussion and conclusion

In bending tests, the deformation of the specimen is a result of local force that the punch rollers impose. Therefore, an important force might lead to a stress concentration in the contact region, where plastic deformation localizes and accommodates the global deflection of the specimen. This phenomenon has been encountered in the literature work, as presented in FIG. A.8.

In this present work, the specimens are quite thin, they deform more easily. For example, in FIG. A.5, corresponding to 80 MPa, the force in [WAL 00] is about 23 N, while it is approximately 1 N in this work. When looking at the deformed specimen, as

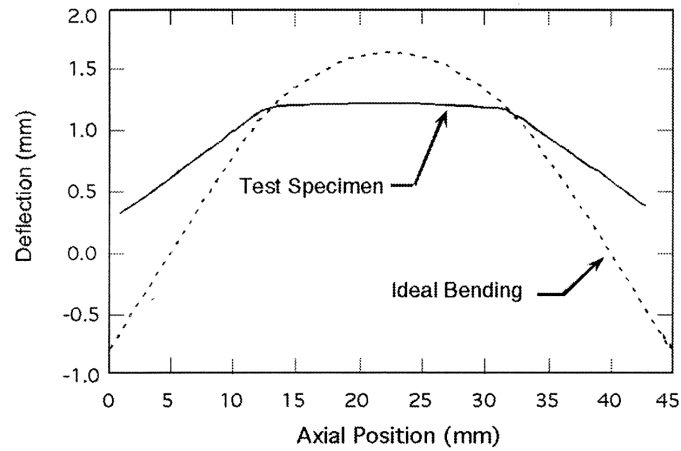


FIGURE A.8: Plastic deformation localized at the contact region in literature work [WAL 00].

presented in FIG. A.9, it can be noticed that no deformation localization is remarkable. Moreover, the slip bands can be observed on the cross section at the edge of the specimen. These slip bands are the traces of the dislocation movements on the slip plane, they are coherent with the multiple slip pattern predicted in FIG. A.2.

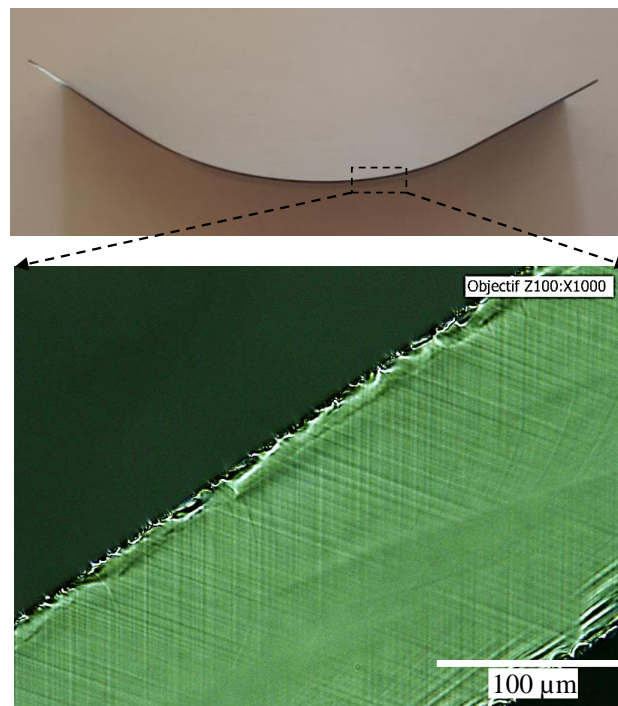


FIGURE A.9: Deformed specimen with a zoom on the cross section morphology.

The main disadvantage of bending tests is the relative sliding between the specimen

and the support rollers. The sliding will result in many oscillations on the curve, as can be seen in our experimental results, mainly in FIG. A.7. However, the oscillations occur mostly after the double yield points, in the hardening stage in other words.

Particularly, Moulin et al. [MOU 99] formulated the temperature and the strain rate dependence of the upper and lower yield stresses as highlighted in EQ. A.1.

$$\tau_{YP} \propto (\dot{\epsilon} \exp[Q/kT])^{1/3} \quad (\text{A.1})$$

where the symbol \propto indicates a proportional relationship, $\dot{\epsilon}$ represents the applied strain rate, which can be assimilated to the deflection velocity in bending condition, Q is the activation energy, k stands for the Boltzmann constant, and T denotes the temperature.

With our experimental results presented in section 3.2 and section 3.3, the dependence of the yield points (in terms of force) with respect to the temperature and the load rate (in terms of deflection velocity) is drawn in FIG. A.10, which follows the proportional tendency in terms of stress and strain rate highlighted in EQ. A.1. Hence, these experimental data can be used to calibrate numerical model that aims to capture the yield behavior for a multiple slip case.

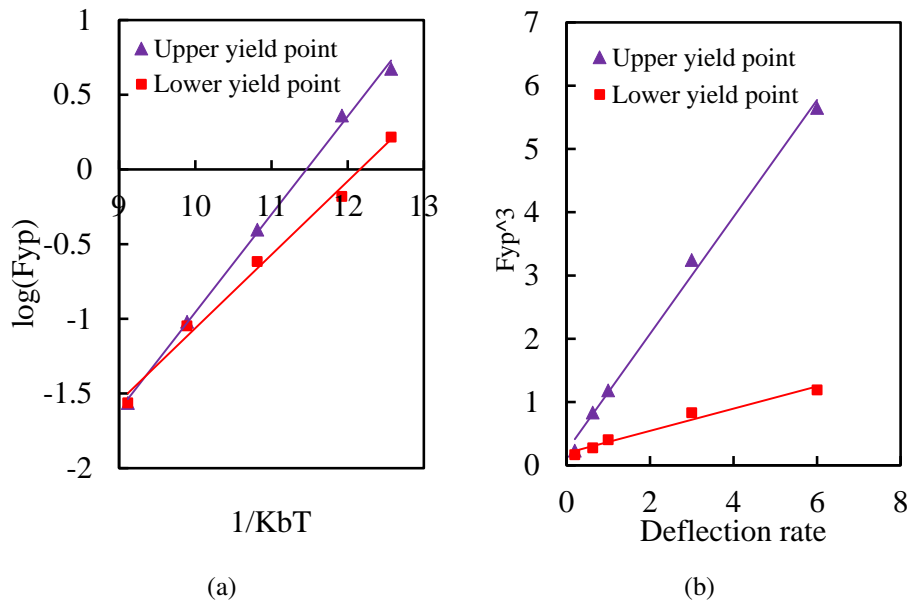


FIGURE A.10: Influences of the temperature (a) and the strain rate (b) on the yield points.

5 Perspectives

Crystal plasticity modeling of the viscoplastic behavior of silicon is of practical interest, since it allows to predict the dislocation motion and indicate the induced residual stresses under a given thermo-mechanical condition. This kind of prediction in turns helps

to guide new manufacturing processes in terms of solidification control in order to fabricate more reliable solar grade silicon wafers. In a future work, the modeling deserves a sophisticated investment, the better is to have a multi-scale constitutive law which is based on dislocation movement and evolution for macroscopic plastic flow determination.

Appendix B

Euler rotation matrix

The Euler angle triplet follows three rotations such that the first rotation is carried out around the axis z for an angle φ , the second rotation around the new axis x' for χ and the third one around the updated axis z' for ψ . The three corresponding rotation matrix are given below :

$$\underline{\underline{R}}_z(\varphi) = \begin{pmatrix} \cos \varphi & -\sin \varphi & 0 \\ \sin \varphi & \cos \varphi & 0 \\ 0 & 0 & 1 \end{pmatrix}$$

$$\underline{\underline{R}}_{x'}(\chi) = \begin{pmatrix} 1 & 0 & 0 \\ 0 & \cos \chi & -\sin \chi \\ 0 & \sin \chi & \cos \chi \end{pmatrix}$$

$$\underline{\underline{R}}_{z'}(\psi) = \begin{pmatrix} \cos \psi & -\sin \psi & 0 \\ \sin \psi & \cos \psi & 0 \\ 0 & 0 & 1 \end{pmatrix}$$

Thus, to express the parameters (vectors, tensors etc.) of the updated coordinate system in the original coordinate system, the equivalent rotation matrix is :

$$\underline{\underline{R}}(\varphi, \chi, \psi) = \underline{\underline{R}}_z(\varphi) \cdot \underline{\underline{R}}_{x'}(\chi) \cdot \underline{\underline{R}}_{z'}(\psi)$$

For a face-centered cubic crystalline structure, we have six equivalent orthogonal axis. For axis x or $\langle 100 \rangle$, one can have six possibilities, while for axis y or $\langle 010 \rangle$, only 4 choices can be made in order to be orthogonal to the first axis. The axis z or $\langle 001 \rangle$ is automatically fixed by the two chosen axis. Thus, we have $6 \times 4 = 24$ equivalent structures. This notation results from the product of the transformation matrix $\underline{\underline{S}}_i$ with $\underline{\underline{H}}$:

$$\underline{\underline{H}}_i = \underline{\underline{S}}_i \cdot \underline{\underline{H}}$$

where $i=1,2,3,4,\dots,24$ for cubic structure, $\underline{\underline{S}}_i$ allows to the cover the 24 possibilities, $\underline{\underline{H}}$ denotes the measured relative grain orientation.

Appendix C

Pole figures and inverse pole figures

1 Stereographic projection

The stereographic projection is initially elaborated to project a sphere onto a plane. In crystallographic domain, it is generalized to map a spatial direction (plane) onto the projection plane as a point (line) in order to elucidate more easily the crystallographic orientation.

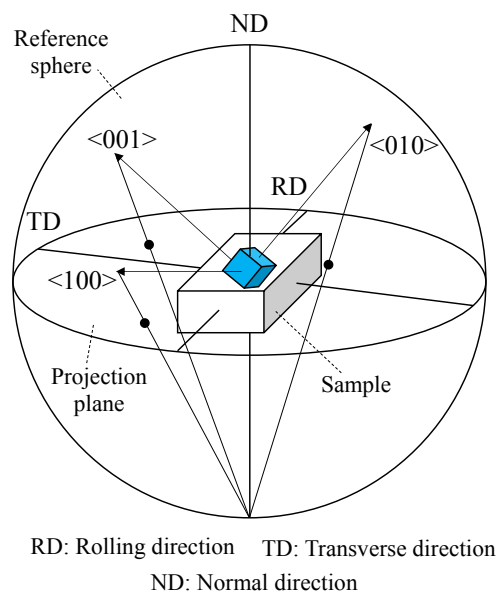


FIGURE C.1: Stereographic projection, example of $[100]$ directions.

As FIG. C.1 illustrates, the stereographic projection plane is defined with the equatorial plane of the reference sphere. The sample, associated with a sample's coordinate system, i.e. the rolling direction, the transverse direction and the normal direction, is placed at the center of the sphere such that the normal direction points to the north pole of

the sphere. To represent a direction, the first step is to extend the direction to intersect the sphere surface, then it consists to connect this first intersection point with the south pole of the reference sphere. The connection straight line will then cross the equatorial plane and leave a intersection point, which is the final stereographic projection point of the studied direction.

2 Pole figures

A pole figure is the result of the stereographic projection. In materials science, the pole figure is used to represent any crystallographic orientation of a grain with respect to the sample's coordinate system. In practice, one pole figure corresponds to one crystallographic orientation family, such as $[100]$ (see FIG. C.2), $[110]$, $[111]$ for a face centered cubic system.

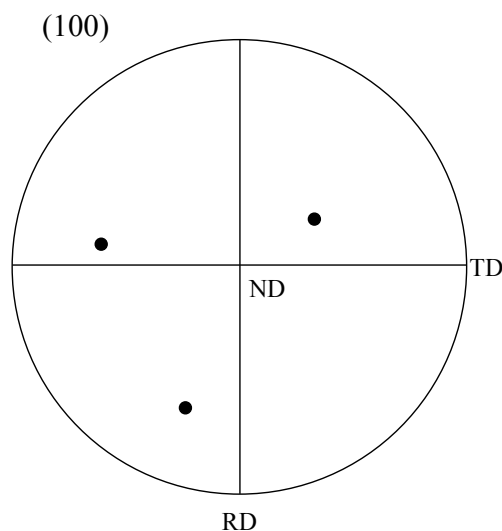


FIGURE C.2: Pole figure, example of $[100]$ poles.

3 Inverse pole figures and texture analysis

An inverse pole figure is also based on the principal of stereographic projection. However, the axes of the reference sphere are aligned with crystal directions. The directions to plot are that of the sample, either the normal direction (ND), rolling direction (RD) or transverse direction (TD).

For a face centered cubic crystal, the reference sphere takes three $[100]$ directions. Due to the cubic symmetry, the full inverse pole figure (full circle in FIG. C.3(a)) can be

divided into 24 equivalent "triangle" parts. In practice, we focus on only one of them, as the one fulfilled with yellow color in FIG. C.3(a). This triangle figure has three tops as one [100], one [110] and one [111] directions, three edges as one (100) and two (100) planes. Finally, the sample's coordinate system is represented with the chosen triangle figure, as shown in FIG. C.3(b).

The inverse pole figure can help visualize certain types of textures. Like the pole figure, the same direction is projected with all the grains of the sample, and the projection points will then be gathered in a same inverse pole figure. In this way, the projection points of the sample's coordinate system will be concentrated a small area when the texture is present.

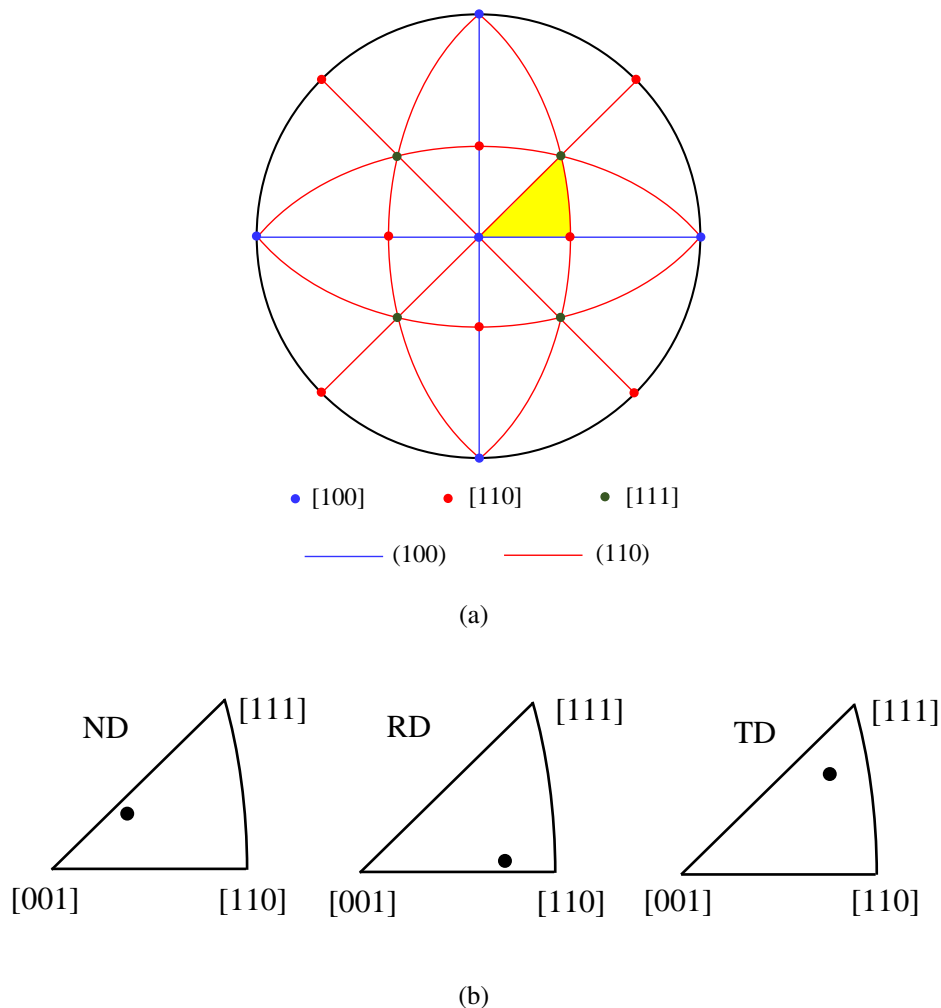


FIGURE C.3: Inverse pole figure. The full figure with 24 equivalent "triangle" parts (a) and the retained "triangle" figure representing the sample's coordinate system (ND, RD and TD) (b).

Appendix D

Fracture mode

According to the relationship between the external loading and the crack surface as well as the crack front, the fracture can be divided into three elementary modes, named mode I, mode II and mode III, see FIG. D.1. The presentation is as following :

Mode I–Opening mode. Only a tensile stress normal to the crack surface drives the crack propagation.

Mode II–Sliding mode also called in-plane shear mode. Only a shear stress parallel to the crack surface and perpendicular to the crack front drives the crack propagation.

Mode III–Tearing mode also called out-of-plane shear mode. Only a shear stress parallel to the crack surface and parallel to the crack front drives the crack propagation.

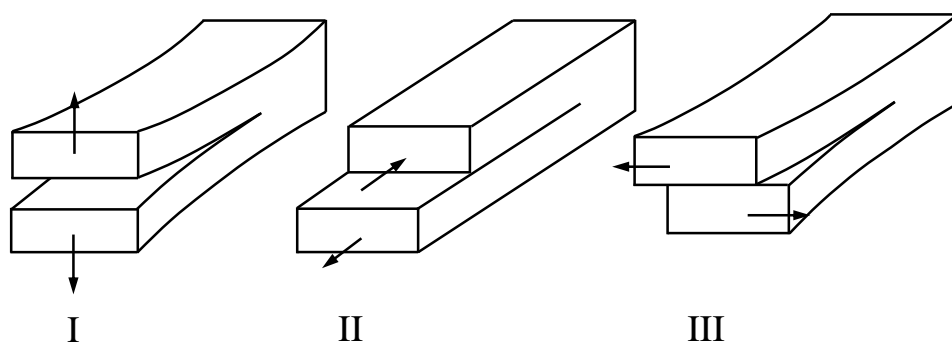


FIGURE D.1: Three elementary fracture modes.

Appendix E

Common crystallographic axis of both grains separated by grain boundary

We can define the euler angles which allows to rotate the crystalline coordinate system of one grain (first grain) into the crystalline coordinate system of the other grain (second grain). \underline{H} is then the corresponding rotation matrix. For a crystallographic axis in the second grain, $[uvw]'$, we can express it in the coordinate system of the first grain $[u^*v^*w^*]'$:

$$[u^*v^*w^*]' = \underline{H}.[uvw]'$$

In the mathematical point of view, $[uvw]'$ can be expressed in the coordinate system of the first grain as $\lambda.[uvw]'$, where λ is a constant. In this case, $[uvw]'$ and λ are in fact one eigenvector and one eigenvalue of the matrix \underline{H} , respectively. Since we have the form which corresponds to the definition of the eigenvalues as well as the eigenvectors of a matrix, as presented below :

$$\underline{R}.[uvw]' = \lambda.[uvw]'$$

Indeed, a 3×3 matrix has three eigenvalues and three eigenvectors, but for a general case of rotation matrix (all the three Euler angles are not zero neither $k\pi/2$, $k = 1, 2, 3, 4$), there exist only one real eigenvalue which equals to 1 (see the equation below) and the corresponding eigenvector has only real numbers. This unique real eigenvector represents the common crystallographic axis. Thus, we can define the grain boundary misorientation which brings the two grains in perfect matching by a rotation around this common axis.

Taking the rotation matrix presented in Appendix B., the below equation is used to compute the eigenvalue λ of this matrix :

$$(\lambda - 1)(\cos \varphi \cos \psi \cos \chi \lambda - \sin \varphi \cos \chi \sin \psi \lambda + \cos \varphi \cos \psi \lambda - \sin \varphi \sin \psi \lambda + \cos \chi \lambda - \lambda^2 - \lambda - 1) = 0$$

which shows that there is always an eigenvalue that equals to 1.

Bibliography

- [ABA 13] ABAQUS 6.13 DOCUMENTATION
Abaqus Analysis User's Guide. , 2013.
- [ALE 69] ALEXANDER H., HAASEN P.
Dislocations and plastic flow in the diamond structure. *Solide State Physics*, vol. 22, 1969, p. 27-158.
- [ARS 99] ARSDELL W. W. V., BROWN S. B.
Subcritical crack growth in silicon MEMS. *Journal of Microelectromechanical Systems*, vol. 8, 1999, p. 319-327.
- [ASH 70] ASHBY M. F.
The deformation of plastically non-homogeneous materials. *Philosophical Magazine*, vol. 21, 1970, p. 399-424.
- [AST] ASTM C 1161-02C
Standard test method for flexural strength of advance ceramics at ambient temperature.
- [ATR 11a] ATRASH F., HASHIBON A., GUMBSCH P., SHERMAN D.
Phonon emission induced dynamic fracture phenomena. *Physical Review Letters*, vol. 106, 2011, page 085502.
- [ATR 11b] ATRASH F., SHERMAN D.
Evaluation of the thermal phonon emission in dynamic fracture of brittle crystals. *Physical Review B*, vol. 84, 2011, page 224307.
- [ATR 12] ATRASH F., SHERMAN D.
Dynamic fracture instabilities in brittle crystals generated by thermal phonon emission : Experiments and atomistic calculations. *Journal of the Mechanics and Physics of Solids*, vol. 60, 2012, p. 844-856.
- [BAT 75] BATRA I. P., CIRACI S.
Effect of relaxation and reconstruction on the electronic-energy-level structure of the Si(111) surface. *Physical Review Letters*, vol. 34, 1975, p. 1337-1340.

- [BEL 99] BELYTSCHKO T., BLACK T.
Elastic crack growth in finite elements with minimal remeshing. *International Journal for Numerical Methods in Engineering*, vol. 45, 1999, p. 601-620.
- [BER 14] BERGMAN L. B., SHERMAN D.
Dynamic crack surface instabilities initiated at dopants. *Scripta Materialia*, vol. 75, 2014, p. 14-17.
- [BIT 15] BITZEK E., KERMODE J. R., GUMBSCH P.
Atomistic aspects of fracture. *International Journal of Fracture*, vol. 191, 2015, p. 13-30.
- [BLA 09] BLAKERS A. W., ARMOUR T.
Flexible silicon solar cells. *Solar Energy Materials & Solar Cells*, vol. 93, 2009, p. 1440-1443.
- [BON 03] BONAMY D., RAVI-CHANDAR K.
Interaction of shear waves and propagating cracks. *Physical Review Letters*, vol. 91, 2003, page 235502.
- [BRE 92] BREDE M.
The brittle-to-ductile transition in silicon. *Acta Metallurgica et Materialia*, vol. 41, 1992, p. 211-228.
- [BRO 03] BRODIE R. C., BAHR D. F.
Fracture of polycrystalline silicon. *Materials Science and Engineering : A*, vol. 351, 2003, p. 166-173.
- [BRU 62] BRUNEAU A. A., PRATT P. L.
The bending deformation of magnesium oxide. *Philosophical Magazine*, vol. 7, 1962, p. 1871-1885.
- [BRU 09] BRUN X. F., MELKOTE S. N.
Analysis of stresses and breakage of crystalline silicon wafers during handling and transport. *Solar Energy Materials & Solar Cells*, vol. 93, 2009, p. 1238-1247.
- [BUE 07] BUEHLER M. J., TANG H., VAN DUIN A. C. T., GODDARD W. A.
Threshold crack speed controls dynamical fracture of silicon single crystals. *Physical Review Letters*, vol. 99, 2007, page 165502.
- [CAR 08] CARDOSO R., YOON J., MAHARDIKA M., CHOUDHRY S., DE SOUSA R. A., VALENTE R. F.
Enhanced assumed strain (eas) and assumed natural strain (ans) methods for one-point quadrature solid-shell elements. *International Journal for Numerical Methods in Engineering*, vol. 75 (2), 2008, page 156-187.

- [CHE 80] CHEN T.-J., KNAPP W. J.
The fracture of single-crystal silicon under several liquid environments. *Journal of the American Ceramic Society*, vol. 63, 1980, p. 225-226.
- [CHE 99] CHEN K. S.
Materials characterization and structural design of ceramic micro turbomachinery. Thèse de doctorat, Massachusetts Institute of Technology, 1999.
- [CHE 07a] CHEN J., QIAO Y.
Mixed-mode cleavage front branching at a high-angle grain boundary. *Scripta Materialia*, vol. 56, 2007, p. 1027-1030.
- [CHE 07b] CHEN J., QIAO Y.
Secondary cracking at grain boundaries in silicon thin films. *Scripta Materialia*, vol. 57, n° 12, 2007, p. 1069 - 1072.
- [COCH 10] COCHARD J., YONENAGA I., GOUTTEBROZE S., M'HAMDI M., ZHANG Z. L.
Constitutive modeling of intrinsic silicon monocrystals in easy glide. *Journal of Applied Physics*, vol. 107, 2010, page 033512.
- [COCH 13] COCHARD J., YONENAGA I., M'HAMDI M., ZHANG Z. L.
A novel constitutive model for semiconductors : The case of silicon. *Journal of the Mechanics and Physics of Solids*, vol. 61, 2013, p. 2402-2432.
- [COFF 08] COFFMAN V. R., JAMES P. S.
Grain boundary energies and cohesive strength as a function of geometry. *Physical Review B*, vol. 77, 2008, page 144111, American Physical Society.
- [CON 92] CONNALLY J. A., BROWN S. B.
Slow crack growth in single-crystal silicon. *Science*, vol. 256, 1992, p. 1537-1539.
- [COU 94] COUFAL H., MEYER K., GRYGIER R. K., HESS P., NEUBRAND A.
Precision measurement of the surface acoustic wave velocity on silicon single crystals using optical excitation and detection. *The Journal of the Acoustical Society of America*, vol. 95, n° 2, 1994, p. 1158-1160.
- [COX 05] COX B. N., GAO H., GROSS D., RITTEL D.
Modern topics and challenges in dynamic fracture. *Journal of the Mechanics and Physics of Solids*, vol. 53, 2005, p. 565-596.
- [CRA 97] CRAMER T., WANNER A., GUMBSCH P.
Crack velocities during dynamic fracture of glass and single crystalline silicon. *Physica Status Solidi A : Applications and Materials Science*, vol. 164, 1997, page R5.

- [CRA 00] CRAMER T., WANNER A., GUMBSCH P.
Energy dissipation and path instabilities in dynamic fracture of silicon single crystals. *Physical Review Letters*, vol. 85, 2000, p. 788-791.
- [CZO 18] CZOCHRALSKI J.
Ein neues Verfahren zur Messung der Kristallisationsgeschwindigkeit der Metalle. *Zeitschrift für physikalische Chemie*, vol. 92, 1918, p. 219-221.
- [De 12] DE MORO F., FOCSA A., DERBOUZ K., SLAOUI A., AURIAC N., LIGNIER H., KELLER P.
Multicrystalline silicon solar cells from RST ribbon process. *Physica Status Solidi C*, vol. 9, 2012, p. 2092-2096.
- [DEV 06] DEVINCRE B., KUBIN L., HOC T.
Physical analyses of crystal plasticity by DD simulations. *Scripta Materialia*, vol. 54(5), 2006, p. 741-746.
- [DRU 01] DRUGAN W. J.
Dynamic fragmentation of brittle materials : analytical mechanics-based models. *Journal of the Mechanics and Physics of Solids*, vol. 49, 2001, p. 1181-1208.
- [EBR 99] EBRAHIMI F., KALWANI L.
Fracture anisotropy in silicon single crystal. *Materials Science and Engineering : A*, vol. 268, 1999, p. 116 - 126.
- [ECH 11] ECHIZENYA D., SAKAMOTO H., SASAKI K.
Effect of mechanical surface damage on Silicon wafer strength. *Procedia Engineering*, vol. 10, 2011, p. 1440-1445.
- [EIT 10] EITNER U., KÖNTGES M., BRENDL R.
Use of digital image correlation technique to determine thermomechanical deformations in photovoltaic laminates : Measurements and accuracy. *Solar Energy Materials & Solar Cells*, vol. 94, 2010, p. 1346-1351.
- [EMM 75] EMMETT W. W.
The channels and waters of the upper Salmon River area, Idaho. rapport, 1975.
- [FAL 00a] FALSTER R., VORONKOV V.
The engineering of intrinsic pointdefects in silicon wafers and crystals. *Materials Science and Engineering B*, vol. 73, 2000, p. 87-94.
- [FAL 00b] FALSTER R., VORONKOV V., QUAST F.
On the properties of the intrinsic point defects in silicon : a perspective from crystal growth and wafer processing. *Physica Status Solidi (b)*, vol. 222, 2000, p. 219-244.

- [FAR 02] FARKAS D., SWYGENHOVEN H., DERLET P. M.
Intergranular fracture in nanocrystalline metals. *Physical Review B*, vol. 66, 2002, page 060101.
- [Fra16] Photovoltaics report. rapport, 2016, Fraunhofer Institute for Solar Energy Systems.
- [FRÉ 90a] FRÉCHETTE V. D.
Failure analysis of brittle materials : advances in ceramics. American Ceramic Society, 1990.
- [FRE 90b] FREUND L. B.
Dynamic fracture mechanics. Cambridge University Press, 1990. Cambridge Books Online.
- [FUN 04] FUNKE C., KULLIG E., KUNA M., MÖLLER H. J.
Biaxial fracture test of silicon wafers. *Advanced Engineering Materials*, vol. 6, 2004, p. 594-598.
- [GAN 15] GANCHENKOVA M., NIEMINEN R. M.
Chapter 9 - Mechanical properties of silicon microstructures. TILLI M., , MOTOOKA T., , AIRAKSINEN V.-M., , FRANSSILA S., , PAULASTO-KRÄŨCKEL M., , LINDROOS V., Eds., *Handbook of Silicon Based {MEMS} Materials and Technologies (Second Edition)*, Micro and Nano Technologies, p. 253 - 293 William Andrew Publishing, Boston, second edition édition, 2015.
- [GEO 93] GEORGE A., MICHOT G.
Dislocation loops at crack tips-nucleation and growth-an experimental-study in silicon. *Materials Science and Engineering : A*, vol. 164, 1993, p. 118-134.
- [GER 90] GERBERICH W. W., DAVIDSON D. L., KACZOROWSKI M.
Experimental and theoretical strain distributions for stationary and growing cracks. *Journal of the Mechanics and Physics of Solids*, vol. 38, 1990, p. 87-113.
- [GRI 21] GRIFFITH A. A.
The phenomena of rupture and flow in solids. *Philosophical Transactions of the Royal Society of London A : Mathematical, Physical and Engineering Sciences*, vol. 221, n° 582-593, 1921, p. 163-198.
- [HAL 67] HALL J.
Electronic effects in the elastic constants of n-type silicon. *Physical Review*, vol. 161, 1967, p. 756-761.
- [HAU 99] HAUCH J., HOLLAND D., MARDER M. P., SWINNEY H. L.
Dynamic fracture in single crystal silicon. *Physical Review Letters*, vol. 82, 1999, p. 3823-3826.

- [HER 82] HERSCH P., ZWEIBEL K.
Basic photovoltaic principles and methods. Feb 1982.
- [HES 93] HESKETH P., JU C., GOWDA S.
Surface free energy model of silicon anisotropic etching. *Journal of The Electrochemical Society*, vol. 140, 1993, page 1080.
- [HIR 89] HIRSCH P. B., F.R.S., ROBERTS S. G., SAMUELS J.
The brittle-ductile transition in silicon. II. Interpretation. *Proceedings of the Royal Society of London. Series A, Mathematical and Physical Sciences*, vol. 421, 1989, p. 25-53.
- [HOL 98] HOLLAND D., MARDER M.
Ideal brittle fracture of silicon studied with molecular dynamics. *Physical Review Letters*, vol. 80, 1998, p. 746-749, American Physical Society.
- [HOR 58] HORNSTRA J.
Dislocations in the diamond lattice. *Journal of Physics and Chemistry of Solids*, vol. 5, 1958, p. 129-141.
- [HOR 07] HORCAS I., FERNÁNDEZ R., GÓMEZ-RODRÍGUEZ J. M., COLCHERO J., GÓMEZ-HERRERO J., BARO A. M.
WSXM : A software for scanning probe microscopy and a tool for nanotechnology. *Review of Scientific Instruments*, vol. 78, 2007, page 013705.
- [HUL 99] HULL R.
Properties of crystalline silicon. Institution of Electrical Engineers, 1999.
- [INF 14] INFUSO A., CORRADO M., PAGGI M.
Image analysis of polycrystalline solar cells and modelling of intergranular and transgranular cracking. *Journal of the European Ceramic Society*, vol. 34, 2014, p. 2713 - 2722.
- [JAC 63] JACCODINE R.
Surface energy of germanium and silicon. *Journal of The Electrochemical Society*, vol. 31, 1963, page 524.
- [JAG 16] JAGAILLOUX F., VALLE V., DUPRÉ J. C., PENOT J.-D., CHABLI A.
Applied photoelasticity for residual stress measurement inside crystal silicon wafers for solar applications. *Strain*, vol. 52, 2016, p. 355-368.
- [JOH 75] JOHN C. S.
The brittle-to-ductile transition in pre-cleaved silicon single crystals. *Philosophical Magazine*, vol. 32, 1975, p. 1193-1212.

- [JOU 12] JOUINI A., PONTHEINER D., LIGNIER H., ENJALBERT N., MARIE B., DREVET B., PIHAN E., CAYRON C., LAFFORD T., CAMEL D.
Improved multicrystalline silicon ingot crystal quality through seed growth for high efficiency solar cells. *Progress in Photovoltaics : Research and Applications*, vol. 20, 2012, p. 735-746.
- [KAJ 11] KAJARI-SCHRÖDER S., KUNZE I., EITNER U., KÖNTGES M.
Spatial and orientational distribution of cracks in crystalline photovoltaic modules generated by mechanical load tests. *Solar Energy Materials & Solar Cells*, vol. 95, 2011, p. 3054-3059.
- [KAU 14] KAULE F., WANG W., SCHOENFELDER S.
Modeling and testing the mechanical strength of solar cells. *Solar Energy Materials and Solar Cells*, vol. 120, Part A, 2014, p. 441 - 447.
- [KER 08] KERMODE J. R., ALBARET T., SHERMAN D., BERNSTEIN N., GUMBSCH P., PAYNE M. C., CSÁNYI G., VITA A. D.
Low-speed fracture instabilities in a brittle crystal. *Nature*, vol. 455, 2008, p. 1224-1227.
- [KER 13] KERMODE J., L.BEN-BASHAT, ATRASH F., CILLIERS J., SHERMAN D., VITA A. D.
Macroscopic scattering of cracks initiated at single impurity atoms. *Nature Communications*, vol. 4, 2013, page 2441.
- [KLU 14] KLUTE C., KAULE F., SCHOENFELDER S.
Breakage root cause analysis in as-cut monocrystalline silicon wafers. *29th European Photovoltaic Solar Energy Conference and Exhibition*, 2014.
- [KOH 14] KOHLER D., ZUSCHLAG A., HAHN G.
On the origin and formation of large defect clusters in multicrystalline silicon solar cells. *Solar Energy Materials & Solar Cells*, vol. 120, 2014, p. 275-281.
- [KÖN 11a] KÖNTGES M., KAJARI-SCHRÖDER S., KUNZE I., JAHN U.
Crack statistic of crystalline silicon photovoltaic modules. *26th European Photovoltaic Solar Energy Conference and Exhibition*, 2011.
- [KÖN 11b] KÖNTGES M., KUNZE I., KAJARI-SCHRÖDER S., BREITENMOSER X., BJØRNEKLETT B.
The risk of power loss in crystalline silicon based photovoltaic modules due to micro-cracks. *Solar Energy Materials & Solar Cells*, vol. 95, 2011, p. 1131-1137.
- [KÖN 14] KÖNTGES M., KURTZ S., PACKARD C., JAHN U., BERGER K., KATO K., FRIESEN T., LIU H., ISEGHEM M.
Performance and reliability of photovoltaic systems-Subtask 3.2 : Review of failures of photovoltaic modules. rapport, 2014, IEA-PVPS.

- [KOY 12] KOYAMA M., AKIYAMA E., TSUZAKI K.
Effect of hydrogen content on the embrittlement in a Fe-Mn-C twinning-induced plasticity steel. *Corrosion Science*, vol. 59, 2012, p. 277-281.
- [KOZ 07] KOZHUSHKO V. V., LOMONOSOV A. M., HESS P.
Intrinsic strength of silicon crystals in pure- and combined-mode fracture without pre-crack. *Physical Review Letters*, vol. 98, 2007, page 195505, American Physical Society.
- [KOZ 10] KOZHUSHKO V. V., HESS P.
Comparison of mode-resolved fracture strength of silicon with mixed-mode failure of diamond crystals. *Engineering Fracture Mechanics*, vol. 77, 2010, p. 193-200.
- [LAW 80] LAWN B. R., HOCKEY B. J., WIEDERHORN S. M.
Atomically sharp cracks in brittle solids : an electron microscopy study. *Journal of Materials Science*, vol. 15, 1980, p. 1207–1223.
- [LAW 81] LAWN B. R., MARSHALL D. B., CHANTIKUL P.
Mechanics of strength-degrading contact flaws in silicon. *Journal of Materials Science*, vol. 16, 1981, p. 1769-1775.
- [LAW 93] LAWN B.
Fracture of brittle solids. Cambridge solid state science series, 1993.
- [LEE 84] LEE E. H.
Extended growth of subgrain-boundary-free silicon-on-insulator via thermal gradient variation. *Applied Physics Letters*, vol. 44, 1984, p. 959-961.
- [LEJ 10] LEJČEK P.
Grain boundary segregation in metals. Springer-Verlag Berlin Heidelberg, 2010.
- [LI 05] LI X. P., KASAI T., NAKAO S., ANDO T., SHIKIDA M., SATO K., TANAKA H.
Anisotropy in fracture of single crystal silicon film characterized under uniaxial tensile condition. *Sensors and Actuators, A : Physical*, vol. 117, 2005, p. 143-150.
- [LIN 86] LIN I.-H., THOMSON R.
Cleavage, dislocation emission, and shielding for cracks under general loading. *Acta Metallurgica*, vol. 34, 1986, p. 187 - 206.
- [MAI 93] MAINPRICE D., LLOYD G. E., CASEY M.
Individual orientation measurements in quartz polycrystals-advantages and limitations for texture and petrophysical property determinations. *Journal of Structural Geology*, vol. 15, 1993, p. 1169-1187.
- [MAS 12] MASOLIN A., BOUCHARD P. O., MARTINI R., BERNACKI M.
Thermo-mechanical and fracture properties in single-crystal silicon. *Journal of Materials Science*, vol. 48, 2012, p. 979-988.

- [MÖL 05] MÖLLER H., FUNKE C., RINIO M., SCHOLZ S.
Multicrystalline silicon for solar cells. *Thin Solid Films*, vol. 487, 2005, p. 179-187.
- [MÖL 14] MÖLLER J., BITZEK E.
Fracture toughness and bond trapping of grain boundary cracks. *Acta Materialia*, vol. 73, 2014, p. 1-11.
- [MOO 01] MOON H.-S., ANAND L., SPEARING S. M.
A Constitutive Model for the Mechanical Behavior of Single Crystal Silicon at Elevated Temperature. *Symposium B Ő Materials Science of Microelectromechanical Systems (MEMS) Devices IV*, vol. 687 de *MRS Proceedings*, 2001.
- [MOR] MORRIS J. W.
Defects in crystals. <http://www.mse.berkeley.edu/groups/morris/MSE205/Extras/defects.pdf>.
- [MOR 98] MORRISSEY J., RICE J.
Crack front waves. *Journal of the Mechanics and Physics of Solids*, vol. 46, 1998, p. 467-487.
- [MOR 00] MORRISSEY J., RICE J.
Perturbative simulations of crack front waves. *Journal of the Mechanics and Physics of Solids*, vol. 48, 2000, p. 1229-1251.
- [MOR 03] MORITA K., MIKI T.
Thermodynamics of solar-grade-silicon refining. *Intermetallics*, vol. 11, 2003, p. 1111 - 1117.
- [MOU 99] MOULIN A., CONDAT M., KUBIN L. P.
Mesoscale modelling of the yield point properties of silicon crystals. *Acta Materialia*, vol. 47, n^o 1, 1999, p. 2879-2888.
- [MUH 01] MUHLSTEIN C., BROWN S. B., RITCHIE R. O.
High-cycle fatigue and durability of polycrystalline silicon thin films in ambient air. *Sensors and Actuators A : Physical*, vol. 94, 2001, p. 177-188.
- [MUH 02a] MUHLSTEIN C. L., STACH E. A., RITCHIE R. O.
Mechanism of fatigue in micro-scale films of polycrystalline silicon for microelectromechanical systems. *Applied Physics Letters*, vol. 80, 2002, p. 1532-1534.
- [MUH 02b] MUHLSTEIN C. L., STACH E. A., RITCHIE R. O.
A reaction-layer mechanism for the delayed failure of micro-scale polycrystalline silicon structural films subjected to high-cycle fatigue loading. *Acta Materialia*, vol. 50, 2002, p. 3579-3595.
- [MUL 15] MULAY S. S., BECKER G., VAYRETTE R., RASKIN J. P., PARDOEN T., GALCERAN M., GODET S., NOELS L.

- Multiscale modelling framework for the fracture of thin brittle polycrystalline films : application to polysilicon. *Computational Mechanics*, vol. 55, 2015, p. 73-91.
- [NAK 09] NAKAJIMA K., USAMI N., Eds. *Crystal growth of Si for solar cells*. Springer-Verlag Berlin Heidelberg, 2009.
- [NYE 53] NYE J.
Some geometrical relations in dislocated crystals. *Acta Metallurgica*, vol. 1, 1953, p. 153 - 162.
- [OHR 92] OHRING M.
The materials science of thin films. Academic Press, 1992.
- [OMR 85] OMRI M., MICHEL J., TETE C., GEORGE A.
Mechanical behavior of polycrystals and single crystals of silicon. MCQUEEN H. J., BAILON J. P., DICKSON J. I., JONAS J. J., AKBEN M. G., Eds., *Proceedings of the 7th International conference on the Strength of Metals and Alloys*, vol. 1, 1985.
- [OMR 87] OMRI M., TETE C., MICHEL J. P., GEORGE A.
On the yield point of floating-zone silicon single crystals I. Yield stresses and activation parameters. *Philosophical Magazine A*, vol. 55, 1987, p. 601-616.
- [PAG 13] PAGGI M., CORRADO M., RODRIGUEZ M. A.
A multi-physics and multi-scale numerical approach to microcracking and power-loss in photovoltaic modules. *Composite Structures*, vol. 95, 2013, p. 630-638.
- [PAG 14] PAGGI M., BERARDONE I., INFUSO A., CORRADO M.
Fatigue degradation and electric recovery in Silicon solar cells embedded in photovoltaic modules. *Scientific Reports*, vol. 4, 2014, page 4506, Macmillan Publishers Limited. All rights reserved.
- [PAG 16] PAGGI M., CORRADO M., BERARDONE I.
A global/local approach for the prediction of the electric response of cracked solar cells in photovoltaic modules under the action of mechanical loads. *Engineering Fracture Mechanics*, , 2016, page In Press.
- [PAR 77] PARKS D. M.
The virtual crack extension method for nonlinear material behavior. *Computer Methods in Applied Mechanics and Engineering*, vol. 12, 1977, page 353-364.
- [PAT 63] PATEL J. R., CHAUDHURI A. R.
Macroscopic plastic properties of dislocation free germanium and other semiconductor crystals. I. Yield behavior. *Journal of Applied Physics*, vol. 34, 1963, p. 2788-2799.
- [PEA 57] PEARSON G. L., READ W. T., FELDMANN W. L.
Deformation and fracture of small silicon crystals. *Acta Metallurgica*, vol. 5, 1957, p. 181-191.

-
- [PÉR 00a] PÉREZ R., GUMBSCH P.
An ab initio study of the cleavage anisotropy in silicon. *Acta Materialia*, vol. 48, 2000, p. 4517-4530.
- [PÉR 00b] PÉREZ R., GUMBSCH P.
Directional anisotropy in the cleavage fracture of silicon. *Physical Review Letters*, vol. 84, 2000, p. 5347-5350.
- [PIN 16] PINEAU A., BENZERGA A. A., PARDOEN T.
Failure of metals I : Brittle and ductile fracture. *Acta Materialia*, vol. 107, 2016, p. 424-483.
- [POP 11] POPOVICH V., YUNUS A., JANSSEN M., RICHARDSON I., BENNETT I.
Effect of silicon solar cell processing parameters and crystallinity on mechanical strength. *Solar Energy Materials & Solar Cells*, vol. 95, 2011, p. 97-100.
- [POP 13] POPOVICH V., RIEMSLAG A., JANSSEN M., BENNETT I., RICHARDSON I.
Characterization of multicrystalline silicon solar wafers fracture strength and influencing factors. *International Journal of Material Science*, vol. 3, 2013, p. 9-17.
- [QIA 07] QIAO Y., KONG X.
On size effect of cleavage cracking in polycrystalline thin films. *Mechanics of Materials*, vol. 39, 2007, p. 746-752.
- [QIA 08] QIAO Y., CHEN J.
Resistance of through-thickness grain boundaries to cleavage cracking in silicon thin films. *Scripta Materialia*, vol. 59, 2008, p. 251-254.
- [QUE 63] QUEISSER H. J.
Properties of twin boundaries in silicon. *Journal of The Electrochemical Society*, vol. 110, 1963, p. 52-56.
- [RAM 97] RAMANATHAN S., FISHER D. S.
Dynamics and instabilities of planar tensile cracks in heterogeneous media. *Physical Review Letters*, vol. 79, 1997, p. 877-880.
- [REI 16] REINOSO J., PAGGI M., AREIAS P.
A finite element framework for the interplay between delamination and buckling of rubber-like bi-material systems and stretchable electronics. *Journal of the European Ceramic Society*, vol. 36, 2016, p. 2371-2382.
- [ROU 01] ROUNDY D., COHEN M. L.
Ideal strength of diamond, Si, and Ge. *Physical Review B*, vol. 64, 2001, page 212103, American Physical Society.

- [SAM 89] SAMUELS J., ROBERTS S. G.
The brittle-ductile transition in silicon. I. Experiments. *Proceedings of the Royal Society of London. Series A, Mathematical and Physical Sciences*, vol. 421, 1989, p. 1-23.
- [SAN 13] SANDER M., DIETRICH S., PANDER M., EBERT M., BAGDAHN J.
Systematic investigation of cracks in encapsulated solar cells after mechanical loading. *Solar Energy Materials and Solar Cells*, vol. 111, 2013, p. 82-89.
- [SAT 90] SATO K., MIYAZAKI H., IKUSHARA Y., KURISHITA H., YOSHINAGA H.
Structure and strength of grain boundaries in Si bicrystals with $\langle 111 \rangle$ twist misorientations. *Materials Transactions-The Japan Institute of Metals*, vol. 31, 1990, p. 865-872.
- [SHA 01a] SHARON E., COHEN G., FINEBERG J.
Propagating solitary waves along a rapidly moving crack front. *Nature*, vol. 410, 2001, p. 68-71.
- [Sha 01b] SHARPE JR W. N.
Mechanical properties of MEMS materials. *Semiconductor Device Research Symposium, 2001 International*, 2001, p. 416-417.
- [SHA 02] SHARON E., COHEN G., FINEBERG J.
Crack front waves and the dynamics of a rapidly moving crack. *Physical Review Letters*, vol. 88, 2002, page 085503.
- [SHA 04] SHARON E., COHEN G., FINEBERG J.
Comment on "Interaction of shear waves and propagating cracks". *Physical Review Letters*, vol. 93, 2004, page 099601.
- [SHE 03a] SHERMAN D., BE'ERY I.
The shape and the energies of a dynamically propagating crack under bending. *Journal of Materials Research*, vol. 18, 2003, p. 2379-2386.
- [SHE 03b] SHERMAN D., BE'ERY I.
Velocity dependent crack deflection in single crystal silicon. *Scripta Materialia*, vol. 49, 2003, p. 551-555.
- [SHE 04a] SHERMAN D., BE'ERY I.
Dislocations deflect and perturb dynamically propagating cracks. *Physical Review Letters*, vol. 93, 2004, page 265501.
- [SHE 04b] SHERMAN D., BE'ERY I.
From crack deflection to lattice vibrations-macro to atomistic examination of dynamic cleavage fracture. *Journal of the Mechanics and Physics of Solids*, vol. 52, 2004, p. 1743-1761.

- [SHE 08] SHERMAN D., MARKOVITZ M., BARKAI O.
Dynamic instabilities in 111 silicon. *Journal of the Mechanics and Physics of Solids*, vol. 56, 2008, p. 376-387.
- [SHI 86] SHIH C. F., MORAN B., NAKAMURA T.
Energy release rate along a three-dimensional crack front in a thermally stressed body. *International Journal of Fracture*, vol. 30, 1986, page 79-102.
- [SHI 02] SHILO D., SHERMAN D., BE'ERY I., ZOLOTYABKO E.
Large local deflections of a dynamic crack front induced by intrinsic dislocations in brittle single crystals. *Physical Review Letters*, vol. 89, 2002, page 235504.
- [SØI 04] SØILAND A. K., ØVRELID E. J., ENGH T. A., LOHNE O., TUSET J. K., GJERSTAD Ø.
SiC and Si₃N₄ inclusions in multicrystalline silicon ingots. *Materials Science in Semiconductor Processing*, vol. 7, 2004, p. 39-43.
- [SON 06] SONG J. H., AREIAS P. M. A., BELYTSCHKO T.
A method for dynamic crack and shear band propagation with phantom nodes. *International Journal for Numerical Methods in Engineering*, vol. 67, 2006, p. 868-893.
- [STA 83] STALDER B., BEGUELIN P., KAUSCH H.
A simple velocity gauge for measuring crack growth. *International Journal of Fracture*, vol. 22, 1983, p. R47-50.
- [STO 09] STODDARD N., SIDHU R., ROZGONY G., WITTING I., DOLLEN P. V.
Monocrystalline cast silicon : a present and future technology. *Third International Workshop on Crystalline Silicon Solar Cells*, 2009.
- [STO 15] STOFFERS A., COJOCARU-MIRÉDIN O., SEIFERT W., ZAEFFERER S., RIEPE S., RAABE D.
Grain boundary segregation in multicrystalline silicon : correlative characterization by EBSD, EBIC, and atom probe tomography. *Progress in Photovoltaics : Research and Applications*, vol. 23, n° 6, 2015.
- [SUD 09] SUDANI N., VENKATAKRISHNAN K., TAN B.
Laser singulation of thin wafer : Die strength and surface roughness analysis of 80µm silicon dice. *Optics and Lasers in Engineering*, vol. 47, 2009, p. 850-854.
- [SUM 80] SUMINO K., HARADA H., YONENAGA I.
The origin of the difference in the mechanical strengths of Czochralski-grown silicon and float-zone-grown silicon. *Japanese Journal of Applied Physics*, vol. 19, 1980, p. L49-L52.
- [SUM 99] SUMINO K.
Deformation behavior of silicon. *Metallurgical and Materials Transactions A*, vol. 30A, 1999, p. 1465-1479.

- [TAY 72] TAYLOR T. A., BARRETT C. R.
Creep and recovery of silicon single crystals. *Materials Science & Engineering*, vol. 10, 1972, p. 93-102.
- [THO 71] THOMSON R., HSIEH C., RANA V.
Lattice trapping of fracture cracks. *Journal of Applied Physics*, vol. 42, 1971, p. 3154-3160.
- [TIL 15] TILLI M., HAAPALINNA A.
Chapter 1 - Properties of Silicon. *Handbook of Silicon Based {MEMS} Materials and Technologies (Second Edition)*, Micro and Nano Technologies, p. 3-17 William Andrew Publishing, Boston, second edition édition, 2015.
- [VAY 16] VAYRETTE R., GALCERAN M., COULOMBIER M., GODET S., RASKIN J.-P., PARDOEN T.
Size dependent fracture strength and cracking mechanisms in freestanding polycrystalline silicon films with nanoscale thickness. *Engineering Fracture Mechanics*, vol. 168, 2016, p. 190-203.
- [WAL 39] WALLNER H.
Linienstrukturen an Bruchflächen. *Zeitschrift für Physik*, vol. 114, 1939, p. 368–378.
- [WAL 00] WALTERS D. S., SPEARING S. M.
On the flexural creep of single-crystal silicon. *Scripta Materialia*, vol. 42, 2000, p. 769-774.
- [WEI 51] WEIBULL W.
A statistical distribution function of wide applicability. *Journal of Applied Physics*, vol. 18, 1951, p. 293-297.
- [WEN 12] WEN T. K., YIN C.
Crack detection in photovoltaic cells by interferometric analysis of electronic speckle patterns. *Solar Energy Materials & Solar Cells*, vol. 98, 2012, p. 216-223.
- [WIL 95] WILLIS J. R., MOVCHAN A. B.
Dynamic weight functions for a moving crack. I. Mode I loading. *Journal of the Mechanics and Physics of Solids*, vol. 43, 1995, p. 319-341.
- [WIL 97] WILLIS J., MOVCHAN A.
Three-dimensional dynamic perturbation of a propagating crack. *Journal of the Mechanics and Physics of Solids*, vol. 45, 1997, p. 591 - 610.
- [WIT 08] WITTING I.
Defect and impurity distributions in traditionally cast multicrystalline and cast monocrystalline silicon for solar substrates. Master's thesis, Raleigh University, 2008.

- [WU 13] WU H., MELKOTE S. N.
Effect of crystal defects on mechanical properties relevant to cutting of multicrystalline solar silicon. *Materials Science in Semiconductor Processing*, vol. 16, 2013, p. 1416-1421.
- [YAM 06] YAMAKOV V., SAETHER E., PHILLIPS D., GLAESSGEN E.
Molecular-dynamics simulation-based cohesive zone representation of intergranular fracture processes in aluminum. *Journal of the Mechanics and Physics of Solids*, vol. 54, 2006, p. 1899-1928.
- [YAN 08] YANG Z. P., ZHANG H. P., MADER M.
Dynamics of static friction between steel and silicon. *Proceedings of the National Academy of Sciences of the United States of America*, vol. 105, 2008, p. 13264-13268.
- [YON 78] YONENAGA I., SUMINO K.
Dislocation dynamics in the plastic deformation of silicon crystals. I. Experiments. *Physica Status Solidi A*, vol. 50, 1978, p. 685-693.

Scientific communications

- Articles
- L. Zhao, A. Maynadier, D. Nelias. *Stiffness and fracture analysis of photovoltaic grade silicon plates*. **International Journal of Solids and Structures**, 97–98, 355–369, 2016.
 - L. Zhao, D. Nelias, D. Bardel et al. *On the fracture of multi-crystalline silicon wafer*. **Journal of Physics D: Applied Physics**, 47, 475601, 2016.
 - L. Zhao, D. Bardel, A. Maynadier, D. Nelias. *Crack initiation behavior in single crystalline silicon*. **Scripta Materialia**, 130, 83–86, 2017.
 - L. Zhao, D. Bardel, A. Maynadier, D. Nelias. *Velocity correlated crack front and surface marks in single crystalline silicon*. **Under review**.
- Conference and seminars
- L. Zhao, A. Maynadier, D. Nelias. *Rigidity characterization and fracture analysis of the solar-grade multi-crystalline silicon plates at low temperature*. **ICM12**. 10-14 mai 2015, Karlsruhe (Germany).
 - L. Zhao, A. Maynadier, A. Saulot, D. Nelias. *Influence of the manufacturing process on the high temperature behaviour of Photovoltaic Silicon Wafer loaded in bending*. **CREEP2015**. 31 mai-04 juin 2015, Toulouse (France).
 - L. Zhao, A. Maynadier, D. Nelias. *Characterization of the rigidity and fracture of photovoltaic grade silicon plates*. **Workshop on Reliability of Solar materials and Systems-2015**. 26 mai 2015, Aix en Provence (France).
 - L. Zhao, A. Maynadier, D. Nelias. *Caractérisation de la rigidité et étude de la rupture de plaques en silicium de qualité photovoltaïque*. **22ème CFM**. 24-28 août 2015, Lyon (France).
 - L. Zhao, A. Maynadier, D. Bardel, D. Nelias. Seminar at Institut FEMTO-ST, Department of applied mechanics, 2016, Besançon (France).



FOLIO ADMINISTRATIF

THESE DE L'UNIVERSITE DE LYON OPEREE AU SEIN DE L'INSA LYON

NOM : ZHAO

DATE de SOUTENANCE : 08/12/2016

Prénoms : Lv

TITRE : On the fracture of solar grade crystalline silicon wafer

NATURE : Doctorat

Numéro d'ordre : 2016LYSEI134

Ecole doctorale : MECANIQUE, ENERGETIQUE, GENIE CIVIL, ACOUSTIQUE

Spécialité : Mécanique – Génie Mécanique – Génie Civil

RESUME : The solar grade crystalline Silicon occupies an important position in Photovoltaic (PV) technology. It is indeed the most common active material for electrical generation. The profitability of silicon solar cells is a critical point for the PV market and it requires improved electrical performance, lower wafer production costs and enhancing reliability and durability of the cells. Innovative processes are emerging that provide thinner wafers with less raw material loss. But the induced crystallinity and distribution of defects compared to the classical wafers are unclear. It is therefore necessary to develop methods of microstructural and mechanical characterization to assess the rigidity or mechanical operating performance of these materials. In this context, the detailed understanding of fracture behavior of cells and particularly of the brittle material that constitutes the wafer is crucial. Doing so, we will improve our knowledge of the causes and modes of cracking in the PV cells in order to finally be able to avoid them or at least to take them into account when designing the next solar cells generations. Nevertheless, the literature in this direction remains too rare and inaccuracies remain. For example, the community has not yet described with certainty the failure mode of multi-crystalline silicon (MCSi): does it break in a transgranular or intergranular way and why? In this work, 4-point bending tests were performed under quasi-static loading. This allowed to conduct both the stiffness estimation and the rupture study. A high speed camera was set up in order to track the fracture process thanks to a 45° tilted mirror. Fractographic analysis were performed using confocal optical microscope, scanning electron microscope and atomic force microscope. Electron Back-Scatter Diffraction and Laue X-Ray diffraction were used to explore the relationship between the microstructural grains orientations/textures of our material and the observed mechanical behavior. Jointly, finite element modeling and simulations were carried out to provide auxiliary characterization tools and help to understand the involved fracture mechanism. Thanks to the experiment-simulation coupled method, we have assessed accurately the rigidity of silicon wafers stemming from different manufacturing processes. A fracture origin identification strategy has been proposed combining high speed imaging and post-mortem fractography. Fracture investigations on silicon single crystals have highlighted the deflection free (110) cleavage path, the high initial crack velocity, the velocity dependent crack front shape and the onset of front waves in high velocity crack propagation. The investigations on the fracture of multi-crystalline wafers demonstrate a systematic transgranular cracking. Furthermore, thanks to twin multi-crystalline silicon plates, we have addressed the crack path reproducibility. A special attention has been paid to the nature of the cleavage planes and the grain boundaries barrier effect. Finally, based on these observations, an extended finite element model (XFEM) has been carried out which fairly reproduces the experimental crack path.

MOTS-CLÉS : Solar grade silicon wafer, 4-point bending, material rigidity, fracture, crack velocity, extended finite element model (XFEM)

Laboratoire (s) de recherche : Laboratoire de Mécanique des Contacts et des Structures
UMR CNRS 5259 - INSA de Lyon
20, avenue Albert Einstein
69621 Villeurbanne Cedex FRANCE

Directeur de thèse : Professeur Daniel NELIAS

Président de jury : Professeur Anthony GRAVOUIL

Composition du jury : Thomas PARDOEN Marco PAGGI Amal CHABLI Anthony GRAVOUIL
Tristan ALBARET Daniel NELIAS Anne MAYNADIER